TAMPEREEN TEKNILLINEN YLIOPISTO
TAMPERE UNIVERSITY OF TECHNOLOGY

Pavlo Molchanov

Radar Target Classification by Micro-Doppler Contributions

Julkaisu 1255 • Publication 1255

Tampere 2014

Tampereen teknillinen yliopisto. Julkaisu 1255
Tampere University of Technology. Publication 1255

Pavlo Molchanov

Radar Target Classification by Micro-Doppler Contributions

Thesis for the degree of Doctor of Science in Technology to be presented with due permission for public examination and criticism in Sähkötalo Building, Auditorium S3, at Tampere University of Technology, on the 20th of October 2014, at 12 noon.

Tampereen teknillinen yliopisto - Tampere University of Technology
Tampere 2014

ISBN 978-952-15-3390-7 (printed)
ISBN 978-952-15-3398-3 (PDF)
ISSN 1459-2045

Abstract

THIS thesis studies non-cooperative automatic radar target classification. Recent developments in silicon-germanium and monolithic microwave integrated circuit technologies allows to build cheap and powerful continuous wave radars. Availability of radars opens new applications in different areas. One of these applications is security. Radars could be used for surveillance of huge areas and detect unwanted moving objects. Determination of the type of the target is essential for such systems. Microwave radars use high frequencies that reflect from objects of millimetre size. The micro-Doppler signature of a target is a time-varying frequency modulated contribution that arose in radar backscattering and caused by the relative movement of separate parts of the target. The micro-Doppler phenomenon allows to classify non-rigid moving objects by analysing their signatures. This thesis is focused on designing of automatic target classification systems based on analysis of micro-Doppler signatures.

Analysis of micro-Doppler radar signatures is usually performed by second-order statistics, i.e. common energy-based power spectra and spectrogram. However, the information about phase coupling content in backscattering is totally lost in these energy-based statistics. This useful phase coupling content can be extracted by higher-order spectral techniques. We show that this content is useful for radar target classification in terms of improved robustness to various corruption factors.

A problem of unmanned aerial vehicle (UAV) classification using continuous wave radar is covered in the thesis. All steps of processing required to make a decision out of the raw radar data are considered. A novel feature extraction method is introduced. It is based on eigenpairs extracted from the correlation matrix of the signature. Different classes of UAVs are successfully separated in feature space by support vector machine. Within experiments or real radar data, achieved high classification accuracy proves the efficiency of the proposed solutions.

Thesis also covers several applications of the automotive radar due to very high growth in technologies for intelligent vehicle radar systems. Such radars are already build-in in the vehicle and ready for new applications. We consider two novel applications. First application is a multi-sensor fusion of video camera and radar for more efficient vehicle-to-vehicle video transmission. Second application is a frequency band invariant pedestrian classification by an automotive radar. This system allows us to use the same signal processing hardware/software for different countries where regulations vary and radars with different operating frequency are required.

We consider different radar applications: ground moving target classification, aerial target classification, unmanned aerial vehicles classification, pedestrian classification. The highest priority is given to verification of proposed methods on real radar data collected with frequencies equal to 9.5, 10, 16.8, 24 and 33 GHz.

Preface

THIS work has been carried out during 2010-2014 at the Department of Signal Processing, Tampere University of Technology, Finland.

I wish to express my gratitude to Prof. Karen Egiazarian for making it possible for me to start working on interesting topic of the dissertation, for his help, support and advice during the working process.

I am grateful to Prof. Jaakko Astola for providing a constant feedback and advice during my work. I wish to express my gratitude to Prof. Alexander Totsky, National Aerospace University, Ukraine, for introducing me to the world of radars, and providing a constant support during my studies.

I wish to thank pre-examiners of the thesis, Prof. Alexander Yarovoy, Delft University of Technology, the Netherlands, and Prof. Aleksandra Pizurica, Ghent University, Belgium, for careful evaluation and constructive comments that helped to improve the dissertation.

I would like to thank all members of Department of Signal Processing for sharing ideas and demonstrating high research level. Especially, I wish to thank Prof. Alessandro Foi, Prof. Vladimir Katkovnik, Prof. Atanas Gotchev, Dr. Aram Danielyan, Dr. Robert Bregović for sharing experience and making work-enjoyable environment. Thanks to Suren, Mikhail, Olli and Tatiana for cheering me up during long winter time.

Special thanks go to Ronny Harmanny, Thales, the Netherlands, and Dr. Jacco de Wit, TNO, the Netherlands, for exciting work on UAVs classification by radar systems. This collaboration have contributed to a number of papers and presented in the thesis as a Chapter 7. The work on automotive radar (Chapter 6) would not be possible without Prof. Alexey Vinel, Halmstad University, Sweden, Dr. Evgeny Belyaev, Tampere University of Technology, Finland and Svante Björklund, Swedish Defence Research Agency, Sweden. I am grateful to Prof. Ioan Tabus for collaboration on inventing novel feature selection algorithm presented in the Chapter 4.

I wish to thank administrative staff at Tampere University of Technology and especially Siltaloppi Ulla, Ruotsalainen Pirkko, Larmila Virve, Rotola-Pukkila Noora, Anttila Susanna, Pernu Johanna, Juha Peltonen, Elina Orava for helping me dealing with daily routines.

The financial support of the Graduate School in Electronics, Telecommunications and Automation (GETA), the Nokia Foundation and the Arvoisa Henry Fordin Säätiön is gratefully acknowledged. Especially I would like to thank Prof. Ari Sihvola and Marja Leppäharju for unforgettable experience being a part of Finnish graduate school.

I wish to thank my family for their encouragement on my way to PhD studies and constant support during my life way. My warmest thanks go to my wife, Iuliia, for being a special part of me, for her support, help, understanding and encouragement.

Pavlo Molchanov
Tampere, October 2014

Contents

Abstract iii

Preface v

Contents vi

List of Acronyms xi

List of Figures xi

List of Tables xviii

1 Introduction 1
- I Need of automatic target classification systems . . . 1
  - A) Sensors used for automatic surveillance . . . 1
- II Motivation and research objectivities . . . 2
  - A) Micro-Doppler phenomenon . . . 2
  - B) Radar target classification . . . 5
  - C) Joint time-frequency analysis . . . 7
  - D) Higher-order spectral analysis . . . 7
  - E) Unmanned Aerial Vehicle classification . . . 10
  - F) Joint usage of camera and automotive radar for overtaking assistance . . . 11
  - G) Frequency band invariant automotive radar system for pedestrian classification . . . 12
  - H) Feature selection . . . 13
  - I) Multiple target classification . . . 13
- III Outline of the Thesis . . . 14
- IV Publications and author's contribution . . . 15

2 Basics of radar signal processing 17
- I Continuous Wave (CW) radar . . . 18
  - A) Velocity estimation . . . 18
- II Frequency Modulated Continuous Wave (FMCW) radar . . . 19
  - A) Range estimation . . . 20
  - B) Range and velocity estimation . . . 22
  - C) Range-Doppler processing by 2D DFT . . . 24
  - D) Triangular wave . . . 25
  - E) Azimuth estimation . . . 27

3 Period estimation of micro-Doppler signature **31**
I Introduction . . . 31
II Suggested approach . . . 33
A) Problem statement . . . 33
B) Theoretical background . . . 33
C) Developed approach . . . 34
D) Correction of non-integer number of periods . . . 35
E) Optimal window length estimation . . . 35
F) Block diagram of the proposed algorithm . . . 35
G) Computational complexity analysis . . . 36
III Performance evaluation with simulated data . . . 36
IV Performance evaluation with measured data . . . 39
A) Human walking indoors . . . 39
B) Toy helicopter blade rotation . . . 40
C) Variations in target aspect angle . . . 40

4 Machine learning techniques and feature selection **45**
I General notations for the Chapter . . . 46
II Dimensionality reduction . . . 46
A) Linear discriminant analysis . . . 46
III Decision making techniques . . . 47
A) Statistical classifiers . . . 47
B) Maximum likelihood decision rule . . . 50
C) Support vector machine (SVM) . . . 50
D) Multilayer perceptron . . . 51
IV Techniques for performance evaluation . . . 52
A) Probability of correct classification . . . 52
B) K-fold cross validation . . . 52
C) Confusion matrix . . . 52
V Feature selection by information-based criteria . . . 53
A) Theoretical background . . . 54
B) Proposed algorithm . . . 56
C) Comparative analysis . . . 59
VI Summary . . . 64

5 Bispectrum-based features **67**
I Higher order spectral techniques . . . 67
A) Geometrical interpretation of frequency and phase coupling phenomenon in radar returns . . . 71
B) Micro-Doppler signature of human walking . . . 73
C) Bispectrum analysis for the human walking . . . 75
D) Bicoherence analysis . . . 78
II Classification of one, two and three walking humans . . . 81
A) Theoretical background . . . 82
B) Experimental data . . . 84
C) Analysis of classifier performance . . . 88
III Aerial target classification . . . 94
A) General classification scheme . . . 95

B) Feature extraction strategies . . . 96
C) Computer simulated data . . . 101
D) Results . . . 103
E) Discussions . . . 110
IV Summary . . . 111

6 Automotive radar 113
I Usage of automotive radar in application of video-based overtaking assistance . . . 113
A) Description of the proposed system . . . 114
B) ROI determination by a radar . . . 115
II Pedestrian classification by automotive radar via frequency band invariant features 120
A) General scheme . . . 121
B) Key observations . . . 122
C) Proposed approach . . . 125
D) Data collection . . . 128
E) Classification results . . . 129
III Summary . . . 135

7 Classification of small UAVs and birds by micro-Doppler signatures 137
I Introduction . . . 137
II Related work . . . 138
III Signal model . . . 139
IV Proposed approach . . . 140
A) General scheme . . . 140
B) Estimation of micro-Doppler signature . . . 141
C) Filtering . . . 141
D) Alignment of the micro-Doppler signatures . . . 142
E) Feature extraction . . . 144
V Rotor diameter estimation . . . 146
VI Data collection . . . 147
VII Classification results . . . 149
A) Classification by rotor diameter . . . 149
B) Classification by extracted features . . . 151
VIII Summary . . . 155

8 Classification of ground moving radar targets by using joint time-frequency analysis 157
I Introduction . . . 157
II Real radar data description . . . 157
III Problem Statement . . . 158
IV Feature Extraction Algorithms Suggested . . . 159
A) Bilik's approach . . . 159
B) Time-Frequency Distribution - Direction Features (TFD-DF) . . . 159
C) Time-Frequency Distribution - Singular Values Decomposition - Fourier Transform (TFD-SVD-FT) . . . 160
V Experimental setup . . . 162
VI Analysis of Experimental Results . . . 164
VII Summary . . . 170

Conclusions and Future Work **171**

Bibliography **174**

List of Acronyms

ADC	Analogue-to-Digital Converter
ANN	Artificial Neural Network
AWGN	Additive White Gaussian Noise
CV	Cross-Validation
CW	Continuous Wave
dB	decibel
DFT	Discrete Fourier Transform
FFT	Fast Fourier Transform
FMCW	Frequency Modulated Continuous Wave
IFs	Instantaneous Frequencies
ISAR	Inverse Synthetic Aperture Radar
HOS	Higher-Order Spectra
HOSI	Higher-Order Spectra Invariants
LBM	Local Binary Mask
LDA	Linear Discriminate Analysis
LRR	Long Range Radar
m-D	micro-Doppler
MI	Mutual Information
MIMI	Maximum Information Minimum Intersection
ML	Maximum Likelihood
MLE	Maximum Likelihood Estimator
MLP	Multilayer perceptron
MSE	Mean Squared Error
MR	Maximum Relevance
mRMR	minimum Redundancy Maximum Relevance
NBC	Naive Bayes Classifier
PCA	Principal Component Analysis
PDF	Probability Density Function
PSF	Point-Spread Function
RCS	Radar Cross Section
ROI	Region Of Interest
SNR	Signal-to-Noise Ratio
SRR	Short Range Radar
UAV	Unmanned Aerial Vehicle
WAVE	Wireless Access for Vehicular Environments

List of Figures

1.1 Nature of Doppler and micro-Doppler effects. Doppler effect arises with motion of rigid body object. Complex motion (e.g. translational and rotational motion) of rigid body, or motion of non-rigid body, causes unique frequency modulation of radar signal called micro-Doppler phenomenon. 3

1.2 Human locomotion as an example of non-rigid body motion which provokes micro-Doppler phenomenon. Human locomotion involves different body parts to move by a special law. Different activities have different motions of body parts. 4

1.3 Spectrogram of micro-Doppler signal provoked by walking human. The signal is simulated by software designed in [30] with wavelength $\lambda = 0.02$ m. 4

1.4 Example of the spectrogram of micro-Doppler phenomenon from rotating propeller (top view). 5

1.5 Different approaches to radar target classification 6

1.6 Analysis of the simulated radar backscattered signal of the human walking. Spectrogram (top left), squared magnitude short-time Fourier transform, represents time-frequency energy distribution. Phase plot (top right) shows phase distribution on the time-frequency plain. Phase plot is difficult to analyse and therefore is missed from analysis by many researchers. Bicoherence plot (bottom) shows phase coupling of the frequency components. Bicoherence estimate takes into account phase information in the short-time Fourier transform. 8

1.7 High range resolution profiles for three targets (AH-64, An-26 and B-52) depending on the variations of aspect angle (185^o, 190^o, 195^o). Range is horizontal axis, amplitude is vertical axis. 9

2.1 Structure of the CW radar, Ps - power splitter, Tx - transmitting antenna, Rx - receiving antenna, LPF - low pass filter, Amp - amplifier, ADC - analogue to digital converter. 18

2.2 Block scheme of FMCW radar. VCO - voltage controlled oscillator, Ps - power splitter, LPF - low pass filter, Tx - transmitting antenna, Rx - receiving antenna . 19

2.3 (Top) Instantaneous frequency of transmitted and received waves in case of a single stationary object. (Bottom) Resulting beat frequency. τ is a signal delay caused by wave travelling double distance to an object, T is a period of modulation, B is a bandwidth of modulation 22

2.4 (Top) Instantaneous frequency of transmitted and received waves in case of a single moving object. (Bottom) Resulting beat frequency. Doppler shift is denoted as f_d. 24

2.5 General scheme for range-Doppler processing by 2D DFT method. τ is maximum possible delay due to signal travelling to and from an object 26

2.6 FMCW waveform and beat signals in case of triangular wave modulation: $f_{b2} = f_f - f_s$, $f_{b1} = f_f + f_s$. 26
2.7 Angle of arriving estimation by two receiving antennas. 27
2.8 Angle of arriving estimation by phase comparison technique. For far-field ($r >> d$) we assume that $\angle dc = \theta$. 29

3.1 Block diagram of the proposed algorithm. 36
3.2 Function $D(i)$. The frequency content of the spectrogram illustrated in Fig. 1.3. The period of the spectrogram depends on the position of the second maximum. . 37
3.3 Bias (a) and MSE (b) of estimators depending on SNR level, computed for modeled micro-Doppler data of walking human. 38
3.4 Maximum value of function $D(i)$ depending on the length of window function L. . 38
3.5 Estimated period of human gait depending on the distance. The data for experiment were collected indoor in the 20 meters long corridor. 39
3.6 Experimental setup of micro-Doppler signal collecting from rotating blades of a toy helicopter. 40
3.7 Spectrogram of micro-Doppler signal from rotating blades of a toy helicopter. . . . 40
3.8 Period of micro-Doppler signature as a function of observed signal length, obtained from helicopter's blades and estimated by the suggested approach. The results for method without correction (Section D)) is shown as dashed line. The result after correction by (3.13) is shown as a solid line. 41
3.9 Spectrograms of micro-Doppler signal of walking human with aspect angle 0^o (a) and 90^o (b). The data is recorded by 24 GHz radar outdoor. 41
3.10 Experimental setup (top view) of micro-Doppler data collection of human walking at different aspect angles. 42

4.1 Feature extraction is a typical operation for machine learning. It is used to transform high-dimensional radar data into low-dimensional space, then features are used for classification, instead of radar data. 45
4.2 K-means clustering algorithm 49
4.3 Probability density function approximation by a two stage algorithm. First initial estimate is obtained from K-means algorithm and then the final one by GMM. . . 50
4.4 Classification by Naive Bayes Classifier (on the left) and SVM (on the right) for 2 dimensional feature space. 51
4.5 N-fold cross-validation as a method for performance estimation of a classification scheme for 2-classes problem 53
4.6 10-fold CV error rate on HDR (a), PIE (b), ARR (c) and PCMAC (d) data sets using MIMI, mRMR and MR features. 62
4.7 LOOCV error rate on AR (a) and LYM (b) data sets using MIMI, mRMR and MR features. 63

5.1 Analysis of random distributions by power spectrum density (top) and bispectrum (bottom). 70
5.2 Analysis of phase coupling by bispectrum analysis. Amplitude estimates are shown for signal with phase coupling (left) and without (right). 71
5.3 Scenarios for frequency coupling to exist. 72
5.4 Scenario for phase coupling to exist. 73
5.5 Scenario for the maximum phase coupling to be achieved. 73

5.6 Human walking models: (a) with 12 body parts, 3 translational trajectories and 14 rotation trajectories, image is taken from [166]; (b) time-velocity dependence of body parts involved in human walking, image is taken from [156]. 74

5.7 Analysis of the simulated radar backscattered signal of the human walking. Spectrogram (top left), squared magnitude short-time Fourier transform, represents time-frequency energy distribution. Phase plot (top right) shows phase distribution on the time-frequency plain. Phase plot is difficult to analyse and therefore is missed from analysis by many researchers. Bicoherence plot (bottom) shows phase coupling of the frequency components. Bicoherence estimate takes information of phase information in the short-time Fourier transform. 76

5.8 Analysis of real radar backscattered signal of the human walking. Spectrogram (top left), squared magnitude short-time Fourier transform, represents time-frequency energy distribution. Phase plot (top right) shows phase distribution on the time-frequency plain. Bicoherence plot (bottom) shows phase coupling of the frequency components. 76

5.9 Analysis of sinusoidal baseband signal by STFT and bicoherence. Spectrogram (top left), squared magnitude short-time Fourier transform, represents time-frequency energy distribution. Phase plot (top right) shows phase distribution on the time-frequency plain. Bicoherence plot (bottom) shows phase coupling of the frequency components. Because of a single component there are no phase coupling and bicoherence estimate doesn't have a pattern. 77

5.10 Bispectrum-based TFD computed simulated radar signal of human walking: (b) H, (c) IB, (d) DFB; compared to spectrogram (a). 78

5.11 Bispectrum-based TFDs computed for real radar data of human walking. 79

5.12 Contributions of the body part to the bicoherence estimate. One by one, body parts are removed from the simulator, spectrogram of the resulting signal is on the left. The contribution of the body part (by (5.21)) to bichorence estimate is shown on the right. 80

5.13 Bicoherence estimate of the radar return of human walking, with highlighted areas of contributions. 81

5.14 Comparison of contributions to bicoherence estimates of simulated and real radar data. 81

5.15 Structure scheme of a decision making concept applied in this study. A non-stationary signal can be divided into a series of quasi stationary segments. The features are extracted and conditional posterior probabilities are computed for those segments. Conditional probabilities are then multiplied and the maximum likelihood rule is applied 82

5.16 Scheme of the ATR system implemented in this work 83

5.17 Ground surveillance radar system used for experimental data collection. 85

5.18 Time-frequency radar signatures measured in vegetation clutter and represented by: (a) spectrogram; (b) bicepstrum-based features (5.19); (c) bicepstrum-based features (5.20). The spectrogram is computed in the form of the amplitude of the Short Time Fourier Transform (STFT), and the bicepstrum-based features are computed using IB (5.19) and DFB (5.20) 85

5.19 Bispectrum based features CDFB (5.23) belonging to one (a), two (b) and three (c) walking persons and their approximation (d) using the 3-order GMM at the level of 3 σ. The regions occupied by information features corresponding to different classes overlap; therefore, a sophisticated classifier strategy must be applied. 86
5.20 Histograms of the second bicepstrum/cepstrum coefficients related to the single (blue), two (red) and three (green) walking persons and computed using: (a) (5.23) and (b) (5.34). The histograms show that it is difficult to discern a single walking person from two or three persons by using only this one feature. 87
5.21 Inter-class similarity computed for the feature vector C (5.34) (dashed curve) and CIB (5.22) (straight curve). The correlation values are smaller for the bispectrum-based feature extraction technique, which means the latter technique possesses better orthogonality in its the features. 88
5.22 Scheme of the proposed ATR system. 89
5.23 Scheme of parameter estimation. An 11-fold cross-validation is applied for the performance evaluation of the ATR system, where a data mining is carried out and the optimal parameters are estimated. 89
5.24 Probability of correct classification as a function of the processing data length for the GMM classifier (a) and MLP classifier (b). Decision making interval is equal to 2 s. The regularity of the results does not depend on the classifier. 92
5.25 Probability of correct classification as a function of the processing data length for the SVM classifier. The decision-making interval is equal to 2 s. 93
5.26 Probability of correct classification as a function of the feature vector dimensionality. Parameters: the decision-making interval is equal to 2 s; the processing data length is 64 ms; the cepstrum-based technique; and the GMM classifier. 93
5.27 Elapsed time for feature extraction depending on the processing data length and method used. The processing time required for bispectrum-based techniques is significantly larger than for the cepstrum-based technique. Fortunately, real-time implementation is possible, because the processing time is smaller than the observation length. 94
5.28 ATR used in this study for evaluation of the feature extraction strategies 95
5.29 Effectiveness of the radar classification techniques depending on the aspect angle. Please note, that JEM effectiveness depends on the position and type of the jet, for example for turbine engine JEM will be more efficient for observing target from behind. 96
5.30 Generalization of considered feature extraction strategies. 97
5.31 Amplitude variations of micro-Doppler content extracted from the radar returns for aspect angle equal to 185^o. 98
5.32 Spectrograms of the micro-Doppler contributions for three aspect-angles of 185^o, 190^o, 195^o and three aerial targets: Ah-64, An-24 and B-52. 100
5.33 Bicoherence estimates of the micro-Doppler content in the radar returns for three aerial targets and three aspect angles. 101
5.34 Correct classification probability rates depending on the window length L (a) and the number of overlapping samples Q (b) computed using the BCH technique. 105
5.35 Feature spaces of data for Scenario 2, aspect angle is 185^o for training set, aspect angles are equal to 190^o and 195^o for testing data set. 105
5.36 Influence of SNR on classification performances, Scenario #1 108

5.37 Variability of aspect angle, roll and pitch under atmosphere turbulence. Radar data correspond to this parameters is used for testing, whereas clear data (without variations of angles) is used for training 108
5.38 Time elapsed for feature extraction depending on number of radar returns 110

6.1 The overtaking scenario examined 114
6.2 General structure of the proposed overtaking system 114
6.3 Designed waveform for overtaking assistance application. It consists of three segments: segment 1 - to estimate velocity and azimuth of an ongoing vehicle, segments 2 and 3 - to estimate range. 115
6.4 Periodogram of real life scenario at highway for scenario shown in Fig. 6.1. 117
6.5 Pinhole camera model of the considered application 118
6.7 Application of proposed frequency band invariant automatic radar classification system 121
6.8 General structure classification system 122
6.9 Examples of the Doppler spectrum computed for human walking with the parameters: (a) operating frequency 24 GHz, aspect angle 180^o (b) operating frequency 77 GHz, aspect angle 105^o (c); operating frequency 77 GHz, aspect angle 180^o. . . 124
6.10 Spectrograms of human walking collected by 24 GHz (a) and 77 GHz (b) radars. Despite the fact that at radar data of 24 GHz human was walking faster, spectrograms still look similar. 125
6.11 Main step to compute LBM descriptors of the Doppler spectrum (power spectrum density) 126
6.12 Training and testing procedures of a pedestrian classification system based on LBM 127
6.13 Description of HOSI feature extraction 128
6.14 Training and testing procedures of a pedestrian classification system based on HOSI 129
6.15 Considered scenarios: a) Sc1: One and two persons walking toward and away from the radar; b) Sc2: One person walking or running perpendicularly to the radar LOS; c) Sc3: Person walking at random path; d) Sc4: Vehicle driving towards and backwards the radar; e) Sc5: Vehicle driving perpendicularly to the radar LOS; f) Sc6: Vehicle turns left and goes away; g) Sc7: Vehicle maneuvering 130
6.16 Examples of spectrograms for each considered scenario 131

7.1 Block scheme of the proposed approach 140
7.2 Examples of the filtering for two cases (a) and (b): raw spectrogram is on the left hand side; result of the filtering is on the right hand side. 143
7.3 Examples of the averaged radar clutter estimated from data used in experiments. . 143
7.4 Examples of the alignment's results for flying birds: left - raw spectrogram and tracked motion; right - aligned spectrogram 145
7.5 Example of the spectrogram from small helicopter, on the left hand side. Result of the projection of spectrogram to frequency dimension, on the right hand side. Red line shows the threshold for bandwidth estimation 147
7.6 Examples of UAVs used for experimental study, from left to right, from top to bottom: YAK54 (class 1), EasyStar El-Sailor (class 2), Parrot AR.Drone (class 4), stationary rotors (classes 5-8), Mikado Logo 600 (class 9), Mikado Logo 400 (class 10), Align T-REX 450 (class 11). 148

7.7 Examples of filtered and aligned micro-Doppler signatures of 5 classes (first row); Eigenvectors corresponding to the largest eigenvalue (second row) and the second largest eigenvalue (third row) of Ψ for corresponding signatures. These eigenvectors are basis functions of the micro-Doppler signatures. 149
7.8 Probability density function of the rotor's diameter estimate, for (a) Mikado Logo 400 (class 10), true value 1.04 m; (b) Align T-REX 450 (class 11),true value 0.715 m. 150
7.9 Probability of correct classification for 11-classes problem depending on: (a) the number of Fourier coefficients in (7.13); (b) depending on the number of eigenpairs in (7.14) 151
7.10 Classification rate for 11-class problem depending on the dwell time 155
7.11 Classification rate depending on SNR, 11-classes problem 156

8.1 General structure of the *TFD-DF* feature extraction method for a test signal - sinusoidal baseband signal. It extracts features that depend on relevant information and parameters of the radar signal and irrelevant to not informative ones. 161
8.2 Block-scheme of classification algorithm 162
8.3 The decisions are made on local segments of radar date and then aggregated by majority voting. 163
8.4 Single walking human. Spectrogram (on the left) and first five left singular vectors with singular values (on the right). 164
8.5 Truck. Spectrogram (on the left) and first five left singular vectors with singular values (on the right). 165
8.6 Noise (clutter). Spectrogram (on the left) and first five left singular vectors with singular values (on the right). 165
8.7 Wheeled. Spectrogram (on the left) and first five left singular vectors with singular values (on the right). 165
8.8 Human running. Spectrogram (on the left) and first five left singular vectors with singular values (on the right). 166
8.9 Human crawling. Spectrogram (on the left) and first five left singular vectors with singular values (on the right). 166
8.10 A group of people walking. Spectrogram (on the left) and first five left singular vectors with singular values (on the right). 166
8.11 A group of people running. Spectrogram (on the left) and first five left singular vectors with singular values (on the right). 167

List of Tables

3.1 Bias of the proposed algorithm depending on the window length L 38
3.2 Estimated period (in ms) of human walking at different aspect angles 43

4.1 An example of a confusion matrix 53
4.2 Artificial data used for comparison. 58
4.3 Values of weighting vector at different stages 58
4.4 Results of feature ranking and selection of data provided in Table 4.2 60
4.5 Data sets used in comparison analysis 60
4.6 Error rates (%) obtained by wrapper feature selection. Smaller is better 64

5.1 The probabilities of correct classification given in percentages. Each cell situated in the intersection of the column corresponding to the window width (length of each segment) and row corresponding to the integration time parameter, is split onto three subcells. Each subcell corresponds to the feature extraction technique considered; from left to right: CIB (5.22), CDFB (5.23) and C (5.34) 91
5.2 Confusion matrices for the considered techniques with a data length of 512 ms and decision making time of 2 s. 92
5.3 Main characteristics of aerial targets used in the computer simulations 102
5.4 Data dimensions for Scenario #1 fixed aspect angle and single target 104
5.5 Correct classification probability rates computed in percentages. Scenario #1 . . . 106
5.6 Correct classification rates computed in percentages. Scenarios #2 and #3 106
5.7 Confusion matrices. Scenario #2 107
5.8 Classification rates computed in atmosphere turbulence environment 109

6.1 Classification probabilities obtained with LBM features, values represent the percentage of the data to be classified as pedestrian or vehicle, respectively. Training and testing sets are constructed from 24 GHz radar data 132
6.2 Classification probabilities obtained with HOSI features, values represent the percentage of the data to be classified as pedestrian or vehicle, respectively. Training and testing sets are constructed from 24 GHz radar data 133
6.3 Classification probabilities obtained with LBM features, values represent the percentage of the data to be classified as pedestrian or vehicle, respectively. Training set of pedestrian class contains simulated 77GHz radar echoes of human waling, testing sets is constructed from 24 GHz radar data 134
6.4 Classification probabilities obtained with HOSI features, values represent the percentage of the data to be classified as pedestrian or vehicle, respectively. Training set of pedestrian class contains simulated 77GHz radar echoes of human waling, testing sets is constructed from 24 GHz radar data 134

7.1 UAVs used for experimental verification of the proposed ATR system. Type 'P' is for Plane, 'H' is for Helicopter, 'Q' for quadrocopter, 'B' for birds, 'S' for stationary rotors. 148
7.2 Probability of correct classification obtained for 5 classes problem using 10-fold cross validation. Only rotor's diameter is used as a feature 150
7.3 Confusion matrix for non-linear SVM classifier (5 classes problem using 10-fold cross validation). Only rotor's diameter is used as a feature 150
7.4 Probability of correct classification obtained for 5-classes problem using 10-fold cross validation. 152
7.5 Probability of correct classification obtained for 11 classes problem using 10-fold cross validation. 152
7.6 Confusion matrix (in percentages) for linear SVM classifier, 11-classes problem . . 153
7.7 Classification of UAVs hidden from training procedure, 11-classes problem 153
7.8 Classification of the unseen for training classes, 5-classes problem 154

8.1 Accuracy of correct classification depending on decision making time. GMM classifier. 168
8.2 Confusion matrix. TFD-SVD-FT. $\tau = 4sec$. GMM classifier. 168
8.3 Confusion matrix. TFD-DF. $\tau = 4sec$. GMM classifier. 168
8.4 Confusion matrix. BA. $\tau = 4sec$. GMM classifier. 169
8.5 Accuracy of correct classification depending on decision making time. SVM classifier. 169
8.6 Confusion matrix. TFD-SVD-FT. $\tau = 4sec$ 170
8.7 Confusion matrix. TFD-DF. $\tau = 4sec$ 170
8.8 Confusion matrix. BA. $\tau = 4sec$ 170

Chapter 1

Introduction

I Need of automatic target classification systems

Knowledge and understanding of our surrounding environment is very important to protect ourself from external interference. For many years humanity has constructed defence systems to protect their goods. Surveillance of our surrounding environment is an important aspect of defence, as it helps protectors prepare helps for any unwelcome and sudden interference into their territory. Surveillance systems may also have many civil applications. For instance, fire preventing and extinguishing is more efficient if the number of persons and their positions are known inside buildings. Also, automatic (using sensors) door-opening and light switching devices could save resources. Observation of traffic conditions may help drivers avoid a collision. However, surveillance performed by humans may be inaccurate due to the "human factor", which may cause unpredictable consequences. Moreover, human sense of the surrounding environment is limited by personal abilities. The "human factor" may be reduced by auxiliary devices or assistant systems.

During the last 70 years, progress in electronics made it possible to build a computer, a device which utilizes logic and arithmetic-based operations. Further development helped to construct powerful computing units, which surpassed humans in logic and arithmetic calculations. One of the computer science branches, artificial intelligence, studies how to develop smart systems that could make a decision depending on input parameters. Success in artificial intelligence over last 30 years has made it possible to build semi- and fully automatic decision making systems. One of these systems is an automatic surveillance system which can detect, determine the class and estimate parameters of the objects around.

One of the advanced automatic surveillance technologies allows determination of the type of object, which is performed by automatic target classification. Such a system performs surveillance on large areas and for multiple target scenarios simultaneously. It can, for example, estimate the number and position of persons inside buildings, estimate traffic conditions, perform automatic door opening and light switching, warn of invasion to area etc. The "sensing", or environment understanding is done by devices called sensors. Some sensors can overcome human abilities in sensing and, therefore, such systems have high potential in automatic surveillance.

A) Sensors used for automatic surveillance

Information used by automatic surveillance and target classification about surroundings depends on the sensor type. Below is an overview of the advantages and disadvantages of several currently available sensors.

Visual/video camera sensors measure energy of optical light. Such sensors are low cost and can reconstruct a picture seen by the human eye. It makes easy to recognize objects in good light conditions and absolves obstacles. Systems based on camera sensors could be used for wide view, short-range surveillance or narrow view, far field surveillance. However, good performance is achieved with good weather conditions only. Fog or rain may reduce their efficiency. Moreover, powerful hardware is required due to processing of large data amount.

Infrared sensors estimate energy in infrared range. Their main advantage is capability to detect orthogonal (lateral, perpendicular) movements even at bad optical light. Disadvantages include poor detection of radial motions and poor performance at bad weather conditions such as rain. Also, it is difficult to estimate object parameters such as speed, distance, etc.

Ultrasound sensor is an active device which estimates time delay of transmitted and received waves, providing information of distances to objects. Disadvantages of such sensors are that they have short working distance, speckle and incapability of providing speed measurements precisely.

Radar sensor is based on reflection of electromagnetic waves. High frequency band allows it to estimate radial velocity of the target very precisely, together with accurate distance measurements. Other advantages of radar sensors include almost all weather and light condition operation, capability to penetrate through objects, and long operation distance. Disadvantages of the radars include worse 2D and 3D spatial resolution and possible interference with other high frequency electro magnetic waves and multiple reflections.

Furthermore, due to the long operation range and ability to measure moving parameters (distance, speed etc.), radar sensors have a high potential in automatic target recognition systems and considered in this Thesis.

II Motivation and research objectivities

A) Micro-Doppler phenomenon

The micro-Doppler content arises in radar returns due to the Doppler effect caused by micro-motions [30]. All motions in the scene affect the frequency of the radar's transmitted wave (as well as all other reflected waves) by changing it, with the value of the frequency shift proportional to the radial velocity. Time varying behavior of micro-motions forms a micro-Doppler signature in a form of Frequency Modulated (FM) multi-component signals.

Principle behind micro-Doppler phenomenon is illustrated in Fig. 1.1. All waves scattered from a moving object will be subject frequency shift, named Doppler effect. For radar it results in a shift of frequency of received wave in respect to transmitted one due to the motion of an object. Basically, the shift is caused by rapid phase changes of reflected wave. If an object is moving then distance to it changes from one successful wave crest to another; therefore, the phase of received wave is changing as well from one crest to another, with respect to transmitted wave. Regular phase changes result in a frequency shift.

Micro-Doppler phenomenon arises with motion of non-rigid body or a complex motion, when the global motion consists of several local micro-motions. As it is illustrated in Fig. 1.1, motion of the object illustrated at bottom consists of translational and rotational motion, resulting in frequency modulation of the reflected signal.

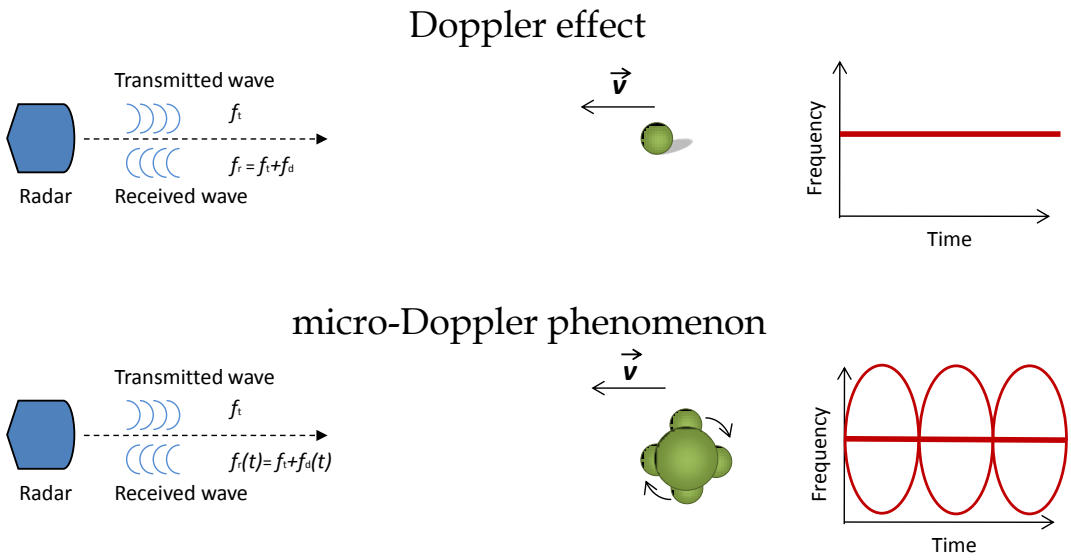

Figure 1.1: Nature of Doppler and micro-Doppler effects. Doppler effect arises with motion of rigid body object. Complex motion (e.g. translational and rotational motion) of rigid body, or motion of non-rigid body, causes unique frequency modulation of radar signal called micro-Doppler phenomenon.

Micro-Doppler signature is a characteristic of motion preserved for a special type of objects. Human activities, generally, involve different body parts with different motion structure. Therefore, these activities could be analysed by micro-Doppler signatures. Examples of human locomotions including walking and running are illustrated in Fig. 1.2.

A common technique for micro-Doppler analysis is the time-frequency representation [33]. Nowadays, conventional spectrogram defined as the square modulus of the short-time Fourier transform (STFT) is a widely spread tool used for time-frequency analysis of micro-Doppler content. Spectrogram is usually computed by using a sliding window truncating a received signal by the sequence of short-time segments and Fourier transform (FT) related to the short-time segmented signals. A larger window length provides higher frequency resolution in the STFT, however, as a consequence, poorer temporal resolution is observed at the same time.

Spectrogram of the simulated[1] radar return signal for continuous-wave radar is shown in Fig. 1.3. Each body part involved in walking has a sinusoidal-like change of the velocity during a gait, therefore, forming sinusoidal-like patterns at spectrogram. Human leg has the highest speed and stands out of a common group. The common group is formed by a human body motion and other body parts with a low motion, like shoulders, head etc.

Another source of the micro-Doppler phenomenon is a rotation of a propeller or a blade of flying objects. An example of the spectrogram of the rotating blade is shown in Fig. 1.4. Two key positions of the blade with respect to the radar line of sight (LOS) are marked as "1" and "2". In the position "1" the blade lies in the LOS plane, and therefore, an angle ϕ between the velocity vector and LOS is 90^o resulting in near zero Doppler shift. In the position "2", the blade is orthogonal to the LOS forming $\phi = 180^o$ between direction of the velocity vector and LOS. Moreover, in position "2", the blade reflects the signal from the multiple points between blade's

[1]Radar simulated data of a micro-Doppler signal of a walking human is developed in [22] and implemented in [30].

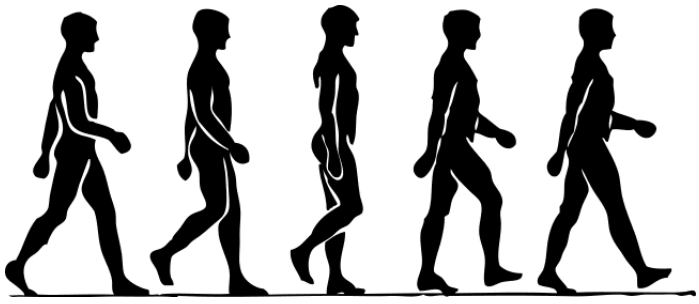

(a) Walking

(b) Running

Figure 1.2: Human locomotion as an example of non-rigid body motion which provokes micro-Doppler phenomenon. Human locomotion involves different body parts to move by a special law. Different activities have different motions of body parts.

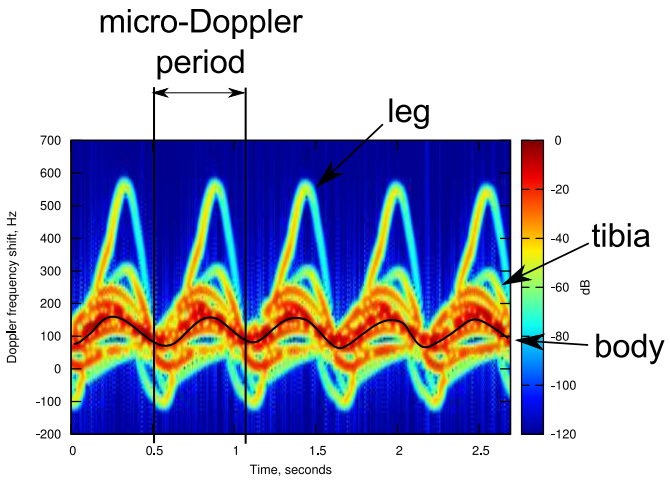

Figure 1.3: Spectrogram of micro-Doppler signal provoked by walking human. The signal is simulated by software designed in [30] with wavelength $\lambda = 0.02$ m.

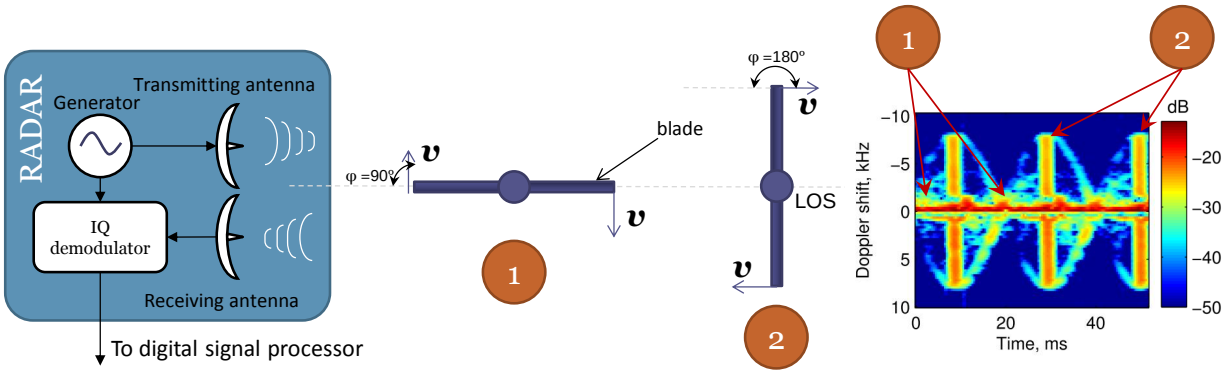

Figure 1.4: Example of the spectrogram of micro-Doppler phenomenon from rotating propeller (top view).

root and blade's tip, with a velocity from $-v$ to v (tip's velocity) introducing splashes at the spectrogram. Between positions "1" and "2" we can observe only reflections from the tip, which have a sinusoidal like pattern.

In case of repeatable action of the moving parts, the micro-Doppler signal becomes periodic. One of the main micro-Doppler parameters is a period. It characterises a human gait duration, walking speed, in case of human walking, and a number of propeller rotations per time unit in the case of a rotation blade. Most of the robust methods of period estimation [12, 35, 140, 143, 151, 159] require a prior knowledge of an object or a moving model. In contrast to them, we will propose in Chapter 3 a period-estimation method that requires no a priori knowledge about object and character of the motion. Moreover, the method adaptively estimates the window length for a time-frequency distribution estimation.

B) Radar target classification

Information retrieved from the radar returns could be used for a classification of an object on the scene. Many industrial radars have an output of the demodulated baseband signal which is in a audible range of frequencies. This allows to listen to the output directly by human. The person, called "listener", listen to the output and makes a decision about the presence of a moving objects in the areas of interest. Recently, researchers working on the problem of moving target recognition and classification by using ground surveillance Doppler radars have paid much attention to development of completely automated systems operating without any human-operator involvement. Advances in artificial intelligence allow to build radar-based automatic target recognition / classification (ATR) systems [157].

Generally, we could divide automatic radar target classification systems into three categories: template matching, model based and machine learning. This division is illustrated in Fig. 1.5.

The idea behind the template matching is to make a decision of a target type by matching the received signal with the predefined dictionary, which contains radar signals of all targets of interest. Generally matching procedure is performed with a radar signal transformed to another space, e. g. spectrum, spectrogram or other transforms. This method is used together with different time-frequency distributions [103] or using dynamic time wrapping [152] techniques. Disadvantage of this approach is a slow decision making process, because a dictionary is typically huge. The advantage of this approach is that only a small amount of information is lost during the transformation. Template matching could perform very good if the dictionary is constructed

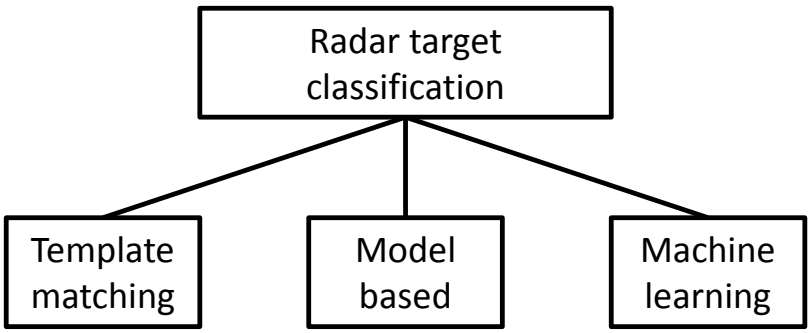

Figure 1.5: Different approaches to radar target classification

in an efficient way and contains all possible signatures of the target.

Model based approach of radar target classification allows to estimate the probability of the radar data to be of a predefined model. For example, models of human walking and running can be used to classify radar data of a human locomotion [65]. Model-based approach simulates the radar data (either in time or in transform domain, like spectrogram) with different input parameters of the model, like step length, height, speed etc. Then, the task is to find with which parameters the difference between the simulated and real radar data is minimal. The advantages of such a method include estimation of target parameters (e.g. like height and speed of a walking human). Disadvantages include a long decision making time, high system requirements on processing unit because of model recalculation for different parameters. Another drawbacks are requirements of a generalized model which uses target parameters (like kinematic parameters for human activity) and "curse of dimensionality", the problem of non-convergence because of a huge number of input parameters to the model (like velocity, height, aspect angle etc.)

Machine learning is a science of information retrieval from the data. It's primary goal to learn regularities, properties and rules with which data are formed. After the learning process, a decision making could be performed based on the learned rules. In such a way machine learning could be used to learn the radar data of different targets and then be used to predict a class label of unseen data. The concept of machine learning requires mainly computational power to discover the properties of the data, which is performed off-line during the training procedure, and the decision making by itself is very fast. Therefore, commonly, powerful computational units are used to learn the data, and then a micro-controller could perform a decision making. Disadvantage of such approaches is requirements of a feature extraction step prior to decision making. Feature extraction is a procedure to transform high-dimensional data into a low-dimensional space, called features, with preserving as much as possible useful information about the target and removing all irrelevant. Removing of irrelevant data is required to prevent the machine learning to lean the data based on the irrelevant features. Commonly, for high relevance of the features, data is transformed to another domain where the connection with real physical features is difficult to find. A number of studies have proven the relevance of this method for real radar data [17, 86, 102].

In the rest of the Thesis we will focus on radar target classification by machine learning approach. This method was chosen because of fast decision making which is important for surveillance of huge areas and operation in multiple target environment. Even though, a number of approaches have been proposed of radar target classification by machine learning [17, 86, 102], the research on this topic is still ongoing. This can be explained by a fact that it is difficult to define the best features. Moreover, existing system can not guarantee erroneousness operation

together with low complexity.

C) Joint time-frequency analysis

Joint time-frequency analysis of non-stationary radar signals backscattered by a moving ground target provides an information about time-dependent Doppler frequency variations and allows extracting unique recognition and classification features, i.e. the features that are definitely unique to radar target. In the recent years, number of approaches using different kinds of time-frequency distributions (TFD) for ground moving radar target detection, recognition and classification problems have been developed [10, 17, 29, 31, 79, 102, 104, 166]. These include linear transforms such as the TFDs based on the STFT [31]; the spectrogram defined as the square modulus of the STFT [166]; bilinear transforms such as the Wigner-Ville distribution (WVD) [104]; and bispectrum-based TFD [10]. The performances of different decision making concepts for ground moving radar target classification have been studied and include Gaussian mixture model (GMM) concept [17, 107]; hidden Markov model (HMM) [79]; neural network approach [102]; independent component analysis [29]; support vector machine (SVM) [128]; k-nearest neighbour classifier [152].

The disadvantages of time-frequency analysis include uncertainty about parameters for estimation (window length, overlapping) which results in frequency-temporal resolution trade-off. Another drawback is that target should be observed for period enough to capture temporal information. Separation of the multiple targets is also a problem if they have close velocity profile. Moreover, the phase information of Fourier transform is lost for spectrogram based analysis methods.

Features are extracted from time-frequency distributions for classification by machine learning. Researches have developed a number of feature extraction techniques which extract time-frequency behaviour of the micro-Doppler signature: based on cadence velocity diagram [19], smart generic features [86], Hermite S-method [127], Hough transform [35].

The majority of approaches referred to the moving object classification, unfortunately, do not take into account some interesting information features related to the target radial velocity time-evaluation. The main drawback of this approach lies in discarding of the time correlation between signatures. Assume that human gaits contain several steps. For the known methods dedicated to the pedestrian classification [17, 102], it does not matter in which sequence they are, i.e. Doppler signatures could be permuted. The researchers usually assume independence of the frequency profiles in spectrogram. In Chapter 8 two new methods of feature extraction from the spectrogram are proposed which use the time correlation information. Experimental results show effectiveness of the proposed methods when targets are observed longer than 0.5 seconds.

D) Higher-order spectral analysis

Moving person classification

Recently, approaches exploiting the m-D radar signatures for moving person classification have been reported in the literature [17, 28, 150, 151]. Most approaches deal with quadratic (spectrogram-based) TF analysis of non-stationary and multi-component backscattered radar signals. According to these approaches, discriminative features are extracted from the energy-based TF distributions, i.e. estimates of backscattered signal energy distribution per unit time per unit frequency. Unfortunately, phase and frequency relationships between certain Doppler spectral components in radar returns that contain important information about phase- and frequency-coupled m-D contributions are irretrievable lost in the energy-based TF radar signatures. Therefore, a common

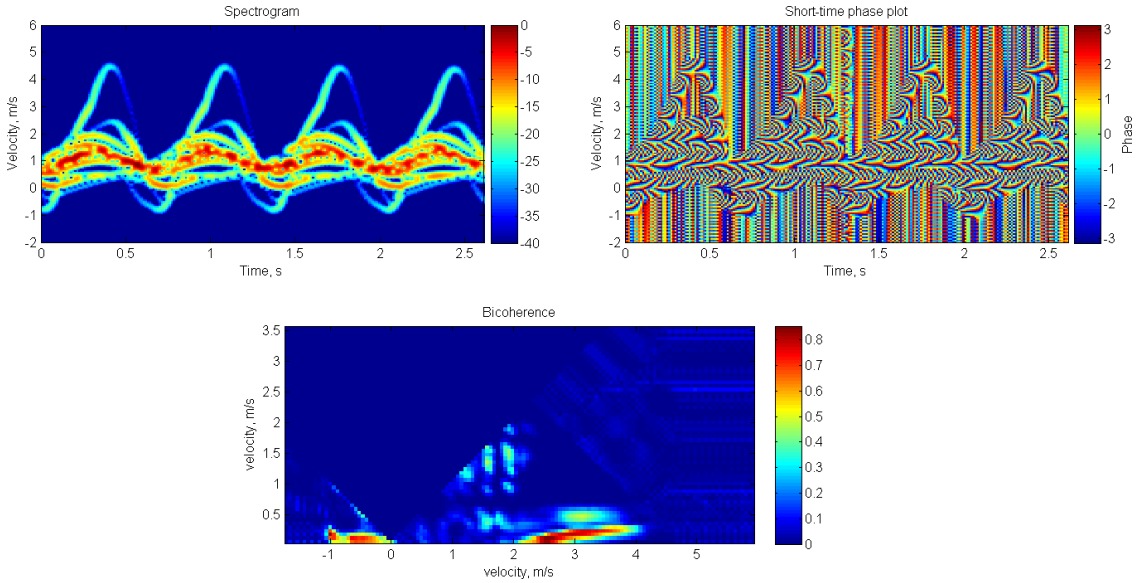

Figure 1.6: Analysis of the simulated radar backscattered signal of the human walking. Spectrogram (top left), squared magnitude short-time Fourier transform, represents time-frequency energy distribution. Phase plot (top right) shows phase distribution on the time-frequency plain. Phase plot is difficult to analyse and therefore is missed from analysis by many researchers. Bicoherence plot (bottom) shows phase coupling of the frequency components. Bicoherence estimate takes into account phase information in the short-time Fourier transform.

drawback of the energy-based TF analysis is the impossibility of retrieving additional particular information concerning frequency- and phase-coupling of instantaneous frequencies contained in the radar backscattering. Phase coupling contained in radar backscattering carries an important information about individual target properties. Extraction of the latter phase relationships from radar backscattering could provide additional insight into radar moving target classification and improve the classification probability rate compared with commonly used energy-based classification features such as power spectrum and cepstrum features.

Fig. 5.7 demonstrates the spectrogram, phase term of STFT and averaged bicoherence estimate, a measure of phase coupling of simulated radar return of human walking. We can see that spectrogram demonstrates clear repetitive behaviour of frequencies involved in a gait. Phase plot (Fig. 5.7 top right) demonstrates very stochastic behaviour which is difficult to analyse. However, bichorence estimate (Fig. 5.7 bottom) shows that there is very strong *phase coupling* (values higher than 0.5) between frequency components, letting us to assume that phase contains useful information that preserves information about the class. Latter in Chapter 5 we will analyse the contributions to the bicoherence estimate.

It will be shown in Chapter 5 that a sophisticated bispectrum-based signal processing can be used in ATR systems. It helps with extraction and use of phase coupled harmonics in raw radar backscattering contaminated by additive white Gaussian noise (AWGN) and vegetation clutter. The distinctive benefits of the bispectrum-based radar signature compared to a common energy-based spectrogram can be characterized as follows. First, the possibility of retrieving the phase coupled contribution, which common energy-based techniques are simply unable to provide. Second, the bispectrum tends to zero for a stationary zero-mean AWGN, which means that there are no phase coupled frequencies in a linear Gaussian process. Therefore, bispectrum-based

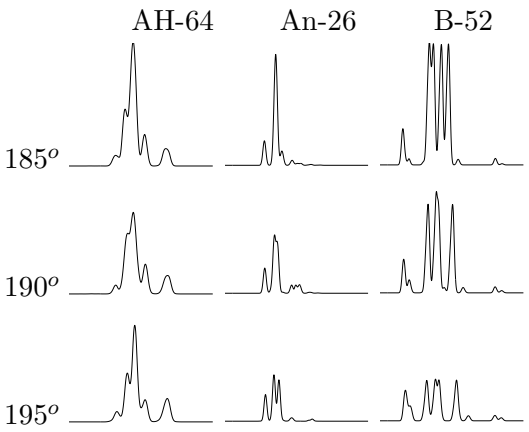

Figure 1.7: High range resolution profiles for three targets (AH-64, An-26 and B-52) depending on the variations of aspect angle (185^o, 190^o, 195^o). Range is horizontal axis, amplitude is vertical axis.

signal processing provides suppression of the AWGN contribution in the TF radar signature. As a result, powerful, (the phase coupled contributions unambiguously belonging to a moving target are emphasized) and the weak, (the phase independent spectral contributions belonging to vegetation clutter and AWGN) are diminished. Therefore, the bispectrum-based approach allows improved signal-to-noise ratio (SNR) in derivatives from the collected radar signatures and, hence, contributes to more accurate feature estimation.

Aerial target classification

Classification and identification of aerial targets by extracting features from the information contained in radar returns is a key task in air surveillance [69, 78, 122, 146, 149, 165, 181, 182].

Estimation of High Range Resolution Profile (HRRP) is one of the key techniques for aerial target analysis. HRRP can be considered to be the projection of the spatial intensity distribution of the backscattered electromagnetic field of the target onto the line of sight of the radar. HRRP, therefore, contains an information about the geometry of the aircraft. The contributions of rotating turbine or propeller blades to the radar backscattering in the form of a micro-Doppler phenomenon[2] [30] can contain additional classification information. Both HRRPs and Jet Engine Modulation (JEM) allow extraction of classification features conforming to the aircraft geometry and particular engine characteristics.

As a result of an aerial target travelling over a large azimuth angle, the HRRP measured and recorded during this travel are affected by three main factors: speckle, rotational range migration and translational range migration. Due to the speckle effect, HRRPs can fluctuate significantly even with only slight aspect variations (as little as tenths of one degree), i.e. only a slight change in elevation or aspect azimuth is enough to provoke a considerable variation in the intensity of peaks, while the location of the peaks may remain unchanged. Examples of intensity variability of HRRPs are presented in Fig. 1.7 for three different types of aircrafts (helicopter AH-64, and airplanes An-26 and B-52) and for aspect angles equal to 185^o, 190^o and 195^o. These HRRPs have been computed by using radio physical radar backscattering models developed in [146].

The micro-Doppler effect has been studied for a long time [23, 99, 144]. Concerning aerial

[2]For micro-Doppler phenomenon and JEM we mean the same

objects, researchers have mainly studied micro-Doppler effects generated by helicopters [159]. Assessing the performance of classification methods based on micro-Doppler discriminative features is of considerable interest.

The phase information generated by rotating engine blades and contained in the micro-Doppler contributions can provide additional information about the target. Unfortunately, this information which gives rise to a phase coupling of micro-Doppler harmonics, is irretrievably lost in HRRPs. In addition, the micro-Doppler content is less sensitive to aspect angle variations than the HRRP. It was mentioned above that even slight aspect variations that are equal to tenths of one angle degree can provoke considerable intensity fluctuations in the HRRP. At the same time, these aspect variations do not create strong variations in the micro-Doppler content caused by the rotating engine (helicopter) blades. This phase information can thus provide certain benefits over the HRRP-based approaches commonly used in ATR systems, and this problem is studied in Chapter 5.

E) Unmanned Aerial Vehicle classification

Unmanned Aerial Vehicles (UAVs) are a special type of aerial targets which have small physical size as they are pilotless. UAVs can be equipped with sensors and weapons for military or civil missions. Civil applications include telecommunication, weather and border monitoring, and remote sensing. Military applications include air reconnaissance, bombing and conducting air combats.

According to the analysis of the market performed by *M. Toscano* [162], the global market of the unmanned aerial systems is 11.3 billion US dollars on 2013 year. And over the next 10 years, the global market will increase up to 140 billions. Such a growth is of interest not only from the UAV manufacturers but also from developing of security systems.

The reason is that, UAVs could disturb official meetings, as it was in 2010 in Great Hall of the Binnenhof, The Hague, The Netherlands [89]. Another incident happened on September 15, 2013 when the mini quadcopter got very close to German Chancellor Angela Merkel before it crashed to the ground right in front of the Chancellor[138]. The incidents showed how it is important to be ready for such situations and that special systems should be developed to detect the UAV.

The detection and classification of the small UAVs can be performed by different sensors. The optical and infrared capturing sensors will be not the best solution due to the small size of the target, less than 0.1 m. The passive acoustic sensors will not perform good at long distances as well as the huge number of unwanted sources will corrupt the signal in urban environment. The best solution can be achieved by the radar sensors, and we are focused on this solution.

There are three main concepts in aerial target classification by the radar: High Resolution Range Profile (HRRP), Inverse Synthetic Aperture Radar (ISAR) images and micro-Doppler (m-D) signatures. Classification of UAVs by HRRP is problematic because sub centimetre resolution is required to capture a spatial structure of targets less than 100 cm in length; sub meter resolution can be achieved by systems with wide bandwidth, which are high-cost systems. The usage of ISAR is limited to the high resolution and long observation time requirements to get a reasonable image of the UAV. The m-D signatures provide distinguishing features of the rotating parts of the UAV, which are unique for special type of the UAV; moreover, this tool works with low-cost continuous wave radars. Due to the benefits, we recommend to use m-D signature concept for the classification of the UAVs.

The contributions of rotating turbine or propeller blades in radar backscattering in the form of micro-Doppler contents [30] can contain additional classification information about UAV characteristics. These micro-Doppler contributions are unique for different types of UAVs [43].

The UAV classification based on micro-Doppler signature is a novel topic, and the performance of such a system is of interest of the Chapter 7.

F) Joint usage of camera and automotive radar for overtaking assistance

Overtaking on roads may be dangerous when oncoming traffic is detected by the driver too late, or its speed is underestimated. Recently proposed cooperative overtaking assistance systems are based on real-time video transmission, where a video stream captured by a camera installed at the windshield of a vehicle is compressed, broadcast through the wireless channel and displayed to the drivers of vehicles driving behind. In such a system it is of ultimate importance to deliver video information about the opposite lane with low end-to-end latency and good visual quality.

We assume that in near future all road users will be equipped with IEEE 802.11p/1609 Wireless Access for Vehicular Environments (WAVE), which opens a broad range of automotive applications [83]. One of the applications includes an overtaking assistance based on real-time video transmission [172].

One of the disadvantages of video based overtaking assistance is that in case of many video transmission sources (e.g. urban environment) the interference become huge and video's bit-rate should be adapted accordingly. By other words, with increasing of the number of transmitting vehicles, video quality degrades significantly.

We propose reallocating the wireless channel resources in favor of the important part of the captured video frames to increase its visual quality. To achieve this goal we apply the automotive radar for the oncoming vehicle detection and use its relative position (of the vehicle with respect to the radar) as a region-of-interest (ROI) for the video rate control.

In order to determine ROI, azimuth and range of the oncoming vehicle should be estimated. This can be achieved by using K-band monopulse FMCW (Frequency Modulated Continuous Wave) radars [82, 175], which consist of one transmitter and two receivers installed on the overtaken vehicle.

Usage of the radar for the proposed cooperative VANET-enabled safety application is justified as follows:

- 24 GHz monopulse FMCW sensors are already available in modern cars for Adaptive Cruise Control application [134]; azimuth and range estimation of oncoming objects is merely an additional digital signal processing task [81];
- in contrast to other approaches for real-time vehicle detection, e.g. camera-based [172], a radar-based approach requires rather limited signal processing and is naturally suitable for the detection of oncoming objects without any a priori knowledge about their type and shape, weather conditions, etc.;
- although the geographical coordinates and velocity of the oncoming vehicle are contained in cooperative awareness messages, the mapping of the oncoming vehicle to the image plane of the camera using this information can be a more complex problem than radar-based mapping.

In Chapter 6 a system which reallocates the wireless channel resources in favour of the part of the captured video frame that contains the oncoming vehicle is proposed. To achieve this goal we apply the automotive radar for the oncoming vehicle detection and use the image of this vehicle as a region-of-interest for the video rate control. We present the theoretical framework, which describes the basics of such an approach and can serve as a useful guideline for the future practical implementation of the overtaking assistance systems.

G) Frequency band invariant automotive radar system for pedestrian classification

According to the statistics of United Nations Organization published in *"Global Plan for the Decade of Action for Road Safety 2011-2020"*, each year approximately 1.3 million people die in road accidents, which is more than 3000 deaths per day, and more than half of these people are not travelling in a vehicle [126]. Therefore, protection of vulnerable road users, such as bicyclists, two-wheelers and, foremost, pedestrians is an important challenge worldwide.

Up-to-date pedestrian protection systems rely on the *infrastructure enhancements* (improving roadway lightning, speed limits control, etc.), *passive safety systems* (design of vehicle body, pedestrian airbags, etc.) and *active safety systems* (based on sensors, cameras, etc.) [57]. Radar-based active pedestrian safety systems are a subject of intensive on-going studies [72] due to their following advantages [57]:

- system performance is independent of the weather conditions, time of the day and illumination intensity of the road;
- availability of the radar sensors on-board of the modern cars (e.g. those used for other driver assistance systems like parking assistant), which removes the need to install additional radars [64];
- complexity of the signal processing algorithms used in the radar-based systems is typically significantly lower than the one of video-based systems due to the lower dimension of the data.

Robust real-time algorithm for the classification of objects (normally pedestrians and vehicles) is a key component of radar-based pedestrian protection system [136, 160]. Even though, different sensors could be used for this purpose [57, 58, 92], the main advantage of the radar is a possibility of target parameters estimation like distance, azimuth angle, relative velocity etc. Typically, a decision about presence of targets in front of a vehicle is made by classification system using features extracted from raw data. As a classifier researches propose to use artificial neural networks [131], support vector machine [70], a polynomial classifier [90]. As features for classification a number of different target parameters have been considered: Doppler profile, range profile and radar cross-section [90, 131, 134]. With those features discrimination of pedestrian and vehicle can be performed with a probability above 90% [71, 131]. However, in this study we assume that only Continuous Wave (CW) radar is available, and therefore only Doppler information is available. This scenario put less costs to the radar system and supplemental hardware. This assumption arises because of availability of CW radar for authors only. Typically, vehicles are equipped with Frequency Modulated Continuous Wave (FMCW) radar with allows to estimate range and velocity simultaneously. The proposed classification algorithm can be applied on data from FMCW radar, where objects will be separated on range-Doppler map; with following classification based on velocity profile only.

However, using the radial velocity of the target as the classification feature has several drawbacks:

- a frequency shift of carrier frequency of the target due to the movement of the vehicle, where the radar sensor is mounted, which can be compensated (for example by interpolation, see Chapter 7) only if the exact speed of this vehicle is known;
- a lateral moving vehicle produces a low radial velocity and can be, therefore, miss-classified as a human if no additional information is available;

- the wavelength of the radar must be known[3] to estimate the radial velocity of the target.

In addition to the desired invariance of the classification method to the radar velocity, one of the ongoing challenges is to design a system with invariant property to the frequency band of the radar sensor [13], since due to the regulations, automotive radars have two different frequency bands: 24 GHz and 77 GHz [72]. Therefore, the objective of this study is to design a pedestrian classification scheme which will be invariant to the frequency band of the radar sensor and the velocity of the radar. Two solutions are presented in Chapter 6.

H) Feature selection

Working with machine learning tasks one can face a situation when a huge amount of features, possibly dependent, is available. Using all features to perform a classification can lead to a high computational complexity. To tackle this problem, there are two major techniques namely *feature extraction* and *feature selection* [80]. These techniques, also called *dimensionality reduction*, are reducing the amount of used features and, at the same time, are improving the classification performance. The *dimensionality reduction* approaches can work when class labels of training data are known (*supervised*) and when the class labels of training data are not known (*unsupervised*). The most popular feature extraction approaches are Principal Component Analysis (PCA), Linear Discriminate Analysis (LDA) and factor analysis. They show a good performance, however, they cannot be used for pinpointing the relevant features for the classification problem.

When we need to find the relevant features *feature selection* algorithms are used. The feature selection algorithms are divided into *filters* and *wrappers*. *A forward wrapper* calculates a classification error for each available feature and iteratively selects the ones with the smallest error. Then at each iteration, a new feature is selected, such that the new feature together with the already selected features minimizes the classification error. A *backward wrapper* initializes with a set containing all features and at each iteration the least relevant feature is deleted. A filter approach ranks the features according to some criterion and selects the relevant ones based on some other criterion. The most typical ranking criteria are correlation, mutual information [67], and kernel-based class separability measures [174].

In Chapter 4, we present a new feature selection approach for supervised classification from discrete data. The proposed approach can work as a criterion for the filter-based feature selection algorithm or as a prior stage for the wrapper. As a criterion function for feature ranking we will use Mutual Information (MI). Other information theoretic feature selection techniques have been proposed, e.g., see [67],[14] and [53]. The peculiarity of the proposed approach is estimating the probabilities involved in the criteria by weighting differently the data samples, according to their relevance to the classification problem.

I) Multiple target classification

One of the issues with machine learning based radar target classification is a presence of multiple targets simultaneously by the radar. For most of the studies in the Thesis this problem is not addressed and assumed to be solved in advance. Therefore, targets must be separated before applying the classification methods considered in the thesis. Separation could be performed based on velocity information (assuming two or more targets are moving with different velocities) for CW radar, or velocity and range for FMCW radar, or even velocity, range and angle for FMCW radar with antenna array. Once the targets are separated, the methods discussed in the thesis

[3] In the Thesis for classification of a pedestrian we assume that the wavelength of the radar is not known

should be applied to every separated target. In case when two or more targets could not been separated, the result of applying classification methods is not predictable and may be erroneous.

Only in the case of studied bicepstral features (Chapter 5 Section 5) the problem of classification multiple targets without prior separation is considered. However, in this case the multiple targets are considered as separated classes.

Therefore, the information about a priori target separation is essential for classification methods considered in the Thesis.

III Outline of the Thesis

Chapter 2. A brief overview of target parameter estimation by continuous wave and continuous wave frequency modulated radars is presented.

Chapter 3. A novel approach dedicated to estimation of a period in micro-Doppler radar signatures represented in the form of time-frequency distribution is suggested. The approach is based on the exploiting short-time Fourier transform (STFT) performed with window sliding along the micro-Doppler spectrogram. No a priori information about radar object under observation is required for estimation of a period. Modelled data of human walking is used both for performance evaluation of suggested and common approaches. Real-life micro-Doppler radar measurements of a walking human are collected for indoor environment and used for experimental examination of the proposed approach. It's robustness to aspect angle variations of moving human is estimated.

Chapter 4. A brief overview of the main techniques which are used for feature extraction and machine learning in the Thesis are introduced. Then a problem of feature selection is considered. Along with the problem introduction, a new method, called Minimum Interference Maximum Information, is proposed.

Chapter 5. Higher-order spectrum analysis of radar returns is performed. In Section I, background of higher order spectral techniques is introduced and it is shown that a phase information of the short-time Fourier transform is also important for radar data analysis. In Section II, a practical usage of bispectrum-based features in ATR system is discussed. Experimental real radar measurements demonstrated that it is quite feasible to distinguish three classes of humans (single, two and three persons) walking in a vegetation cluttered environment using novel bicepstrum-based classification features. In Section III a novel bicoherence-based method for the classification of aerial radar targets in ATR systems is proposed. The performance of the developed classification method is compared to the performance of common methods using high-resolution radar range profiles (HRRPs).

Chapter 6. Different applications of automotive radar are considered. In Section I, a new idea of joint usage of automotive radars, video encoding and vehicle-to-vehicle communication is presented. A system which reallocates the wireless channel resources in favour of the part of the captured video frame that contains the oncoming vehicle is proposed. To achieve this goal, we apply the automotive radar for the oncoming vehicle detection and use the image of this vehicle as a region-of-interest for the video rate control. In Section II, a problem of vulnerable road users classification by radars with different operating bands is considered. It is shown that scale invariant features could overcome the above mentioned problem.

Chapter 7. A new approach for unmanned aerial vehicles classification using continuous wave radar is proposed. We consider all the steps of processing required to make a decision out of the raw radar data. Then, classification features are extracted from micro-Doppler signature in order to represent an information about class at lower dimension space. Eigenpairs extracted from the correlation matrix of the signature are used as informative features for classification. The proposed approach is verified on real radar measurements collected with 9.5 GHz radar.

Chapter 8. Two novel algorithms for ground moving target classification using additional information features related to the radial velocity time-variability are proposed and studied. These approaches are compared with feature extraction method based on linear prediction model and cepstrum coefficients. Results of computer simulations performed by exploiting real-life radar backscattering signal records with different decision making concepts demonstrate the benefits of the proposed approach.

IV Publications and author's contribution

This Thesis is based on the following publications [16, 103, 106, 108–119].

The whole Thesis and publications by author [103, 106, 108–119] represent original work where the author has been the main contributor. In particular, for all papers, except [16], the author have proposed and developed all methods and algorithms. However, this work would not have been possible without the support, criticism, help and inspiration of co-authors. For the paper [16], the author contributed to the main idea, and the part related to the automotive radar.

Publications [105, 114] by the author are also related to the thesis subjects and were written during PhD studies, but are not included as a part of the thesis.

For paper [115] author of the Thesis received EuRAD Young Engineer Prize, it is equivalent to the best student paper award. The paper [108] got the best paper award at EuRAD 2011.

All co-authors have confirmed their agreement on the above statement.

Chapter 2

Basics of radar signal processing

Radar is an acronym for radio detection and ranging. The detection as well as ranging of moving objects is an important task in a number of industrial and civil applications.

History of radars started in 1886 when Heinrich Hertz proved the existence of electromagnetic waves by engineering instruments to transmit and receive radio pulses. Then, Christian Hülsmeyer in 1904 patented the first radar based experimental device for detection of ships wirelessly. First demonstration was at the Hohenzollern Bridge (Cologne) the same year. In 1934 in many countries, including the USSR, the USA, UK, Germany and France pulse radars were developed independently. Next contribution was with development of digital signal processing in 1970th. Millimeter wave radars where introduced in 1980th, and became a topic of interest up to now.

Millimeter wave radars become popular because of penetration through objects ability and high reflectivity from objects of millimeter size. However, water-vapor and oxygen are main absorbers of the waves in this band, and frequency 24 GHz was selected for industrial, scientific and medical (ISM) usage as the one with less attenuations and not used in telecommunication in order to avoid interference. Radars within this ISM band became popular because of decrease in production costs by gallium arsenide technology. Recently, advances in silicon-germanium technology, introduced in 1989 by IBM, allowed to build extremely cheap millimetre wave integrated circuits (MMICs). A number of companies such as Infineon Technologies even now produce MMICs with price near 15 EUR what makes it comparable to other sensing devices. Another Germany company, Innosent, is manufacturing radars for public use since 1999, and provides fully integrated sensors with price of tens of EUR. Especially for such public available radars most of the results in the Thesis are applicable.

By a waveform design, the radars have pulse or continuous waveform. A pulse radar emits short pulses and waits for a backscattered pulse. The distance between the radar and target could be estimated by processing the time between pulse transmitted and received. A pulse radar allows to work on higher distances, because energy is concentrated in a short period of time. The main disadvantage is that it has blind spots and high requirements on power of the transmitter.

The continuous wave radar emits and receives electro-magnetic (EM) waves simultaneously. The receiving antenna pattern collects reflected signal also simultaneously. The working distance is shorter comparing to the pulse radar, however, no blind zones occur. Therefore, the primary application of CW radars is short-range sensing.

The range measuring is an obvious task of the radars. In the case of CW radars, the range could be estimated if the transmitted signal is frequency modulated. Such radars are called FMCW (frequency modulated continuous wave) radars [135, 137].

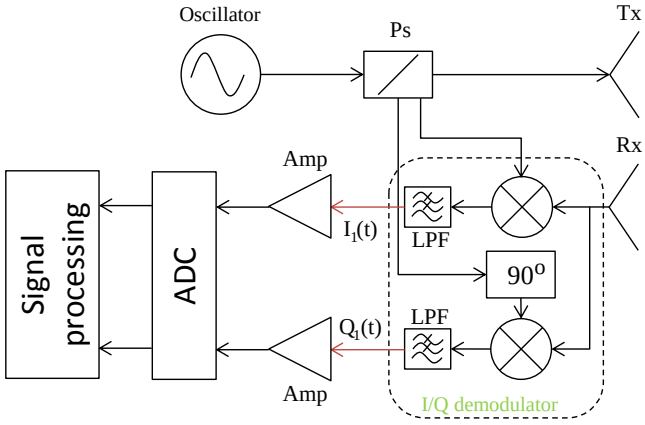

Figure 2.1: Structure of the CW radar, Ps - power splitter, Tx - transmitting antenna, Rx - receiving antenna, LPF - low pass filter, Amp - amplifier, ADC - analogue to digital converter.

In the Thesis we are mainly focused on CW and FMCW radars, therefore, their principals are discussed in details in the following sections.

I Continuous Wave (CW) radar

The main components of the continuous wave radar system are illustrated in Fig. 2.1. Radio frequency is generated in the oscillator, then the signal is transmitted by an antenna. The reflected signal is received by another antenna, then transmitted and received waves are passed through the I/Q demodulator. The I/Q demodulator mixes the transmitted and received wave as well as mixing shifted by 90^o transmitted wave and received wave. Resulting signals are then passed through low pass filters and come to analogue to digital converters, after which demodulated signals are ready for digital processing.

Monostatic CW radars can provide only velocity information, however, this information is enough to distinguish different targets in motion with help of micro-Doppler phenomenon.

A) Velocity estimation

A Doppler effect was discovered by Christian Doppler in 1842. The idea is in the change of frequency of a wave for an observer moving with the relative to the source of the wave. Due to the Doppler effect, the frequency of received wave is:

$$f_r = (\frac{c + v_r}{c + v_s}) f_0, \tag{2.1}$$

where c is a speed of light; v_r is a radial velocity of the receiver; v_s is a radial velocity of the source; f_0 is frequency of transmitted wave.

When the speed of source and of the receiver are much lower than the speed of EM wave, the difference in frequency can be written as:

$$f_d = -\frac{v_s - v_r}{\lambda_0}, \tag{2.2}$$

where $\lambda_0 = c/f_0$ is a wavelength of the transmitted wave.

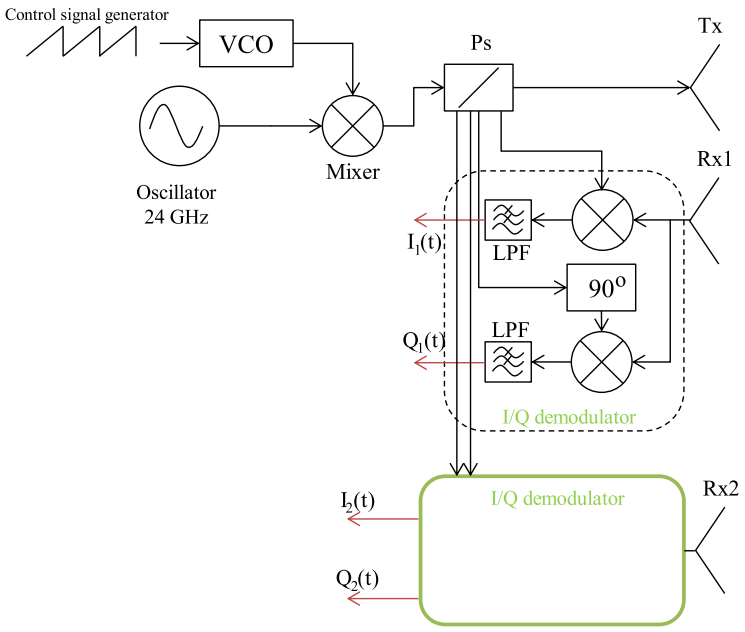

Figure 2.2: Block scheme of FMCW radar. VCO - voltage controlled oscillator, Ps - power splitter, LPF - low pass filter, Tx - transmitting antenna, Rx - receiving antenna

In the radar systems, the source and the receiver of the signal is the radar. In this case the wave travels to the moving object and then after reflection travels back to the radar, resulting in a double range. Therefore the frequency difference at the output of the radar is:

$$f_d = -\frac{2(v - v_r)}{\lambda_0}, \tag{2.3}$$

where v is velocity of target, v_r is velocity of radar.

For stationary radar $v_r = 0$, and therefore, Doppler shift became:

$$f_d = -\frac{2v}{\lambda_0}. \tag{2.4}$$

II Frequency Modulated Continuous Wave (FMCW) radar

Frequency Modulated Continuous Wave (FMCW) radars become popular in automotive sector and other industrial applications due to the usage of low cost components and providing range and Doppler information. Next, we are going to introduce signal processing behind FMCW radar for environmental sensing in terms of azimuth, range and velocity estimation of the objects.

Monopulse FMCW radar together with range and Doppler information can provide azimuth information as well. Typically, such radar consists of one transmitting antenna and at least two receiving antennas. Block diagram of monopulse FMCW system is illustrated in Fig. 2.2. Modulation signal is generated at control signal generator. Then this signal is sent to voltage controlled oscillator (VCO). RF signal generated at oscillator is frequency modulated at mixer and transmitted. Signal at receiving antenna is demodulated by I/Q demodulator, providing in-phase and quadrature-phase components of complex baseband signal. This complex signal is called beat signal in case of FMCW radar.

A) Range estimation

Frequency modulation is used in order to estimate range. General form of the FM signal is:

$$s(t) = A\cos\left(2\pi\int_0^t f(y)dy\right), \tag{2.5}$$

where $f(y)$ is an instantaneous frequency.

In the case of linear frequency modulation (chirp) the signal (2.5) takes the form:

$$s(t) = A\cos\left(2\pi\big(f_0 t + \frac{k}{2}t^2\big)\right), \tag{2.6}$$

where f_0 is the starting frequency, k is a chirp rate defined as:

$$k = \frac{B}{T}, \tag{2.7}$$

where B is bandwidth, T is period of the chirp.

Let us assume that a chirp with some phase shift (ϕ_0) is transmitted:

$$s_{tx}(t) = A_{tx}\cos(2\pi\big(f_0 t + \frac{k}{2}t^2\big) + \phi_0), \tag{2.8}$$

where A_{tx} is an amplitude of the transmitted wave.

If the object appears at distance r, then the received signal is delayed by τ:

$$\tau = \frac{2r}{c}, \tag{2.9}$$

where r is distance, $c = 3 * 10^8$ m/s is speed of light.

Due to a delay τ, which caused by signal travelling to stationary object and back, received signal has a form:

$$s_{rx}(t) = A_{rx}\cos(2\pi\big(f_0(t-\tau) + \frac{k}{2}(t-\tau)^2\big) + \phi_{rx}), \tag{2.10}$$

where A_{rx} is an amplitude of the received wave, ϕ_{rx} is phase of the received wave.

Received signal is then multiplied with transmitted one to demodulate it, resulting signal is

called in-phase component:

$$\begin{aligned}
\hat{I}(t) = s_{rx}s_{tx} &= A_{rx}\cos(2\pi\big(f_0(t-\tau)+\frac{k}{2}(t-\tau)^2\big)+\phi_{rx})A_{tx}\cos(2\pi\big(f_0t+\frac{k}{2}t^2\big)+\phi_0) = \\
&= A_b\Big(\cos(2\pi\big(f_0(t-\tau)+\frac{k}{2}(t-\tau)^2\big)+\phi_{rx}+2\pi\big(f_0t+\frac{k}{2}t^2\big)+\phi_0)+ \\
&+\cos(2\pi\big(f_0(t-\tau)+\frac{k}{2}(t-\tau)^2\big)+\phi_{rx}-2\pi\big(f_0t+\frac{k}{2}t^2\big)-\phi_0)\Big) = \\
&= A_b\Big(\cos(2\pi f_0t-2\pi f_0\tau+2\pi\frac{k}{2}(t-\tau)^2+2\pi f_0t+2\pi\frac{k}{2}t^2+\phi_0+\phi_{rx})+ \\
&+\cos(2\pi f_0t-2\pi f_0\tau+2\pi\frac{k}{2}(t-\tau)^2+\phi_{rx}-2\pi f_0t-2\pi\frac{k}{2}t^2-\phi_0)\Big) = \\
&= A_b\Big(\cos(2\pi f_0t-2\pi f_0\tau+2\pi\frac{k}{2}(t-\tau)^2+2\pi f_0t+2\pi\frac{k}{2}t^2+\phi_0+\phi_{rx})+ \\
&+\cos(2\pi f_0t-2\pi f_0\tau+2\pi\frac{k}{2}(t-\tau)^2+\phi_{rx}-2\pi f_0t-2\pi\frac{k}{2}t^2-\phi_0)\Big) = \\
&= A_b\Big(\cos(2\pi(2f_0)t+2\pi\frac{k}{2}(t-\tau)^2+2\pi\frac{k}{2}t^2+\phi_1-2\pi f_0\tau)+ \\
&+\cos(2\pi\frac{k}{2}(t-\tau)^2-2\pi\frac{k}{2}t^2-2\pi f_0\tau+\phi_2)\Big) = \\
&= A_b\Big(\cos(2\pi(2f_0)t+2\pi\frac{k}{2}(t-\tau)^2+2\pi\frac{k}{2}t^2+\phi_1-2\pi f_0\tau)+ \\
&+\cos(2\pi\frac{k}{2}t^2-2\pi kt\tau+2\pi\frac{k}{2}\tau^2-2\pi\frac{k}{2}t^2-2\pi f_0\tau+\phi_2)\Big) = \\
&= A_b\Big(\cos(2\pi t(2f_0-k\tau)+2\pi kt^2+\phi_1-2\pi f_0\tau)+ \\
&+\cos(\pi k\tau^2-2\pi kt\tau-2\pi f_0\tau+\phi_2)\Big)
\end{aligned} \tag{2.11}$$

where $A_b = A_{rx}A_{tx}/2$, $\phi_1 = \phi_{rx}+\phi_0$ and $\phi_1 = \phi_{rx}-\phi_0$.

After multiplication, signal $\hat{I}(t)$ is passed through a low pass filter. The first harmonic in signal is suppressed because it is centred near double of the carrier frequency ($2\pi 2f_0$). Resulting in-phase component to be in the following form:

$$I(t) = A_b\Big(\cos(\pi k\tau^2-2\pi kt\tau-2\pi f_0\tau+\phi_2)\Big) \tag{2.12}$$

Together with in-phase component, $I(t)$, a quadrature-phase component is computed as mixture of received signal and shifted by 90^o transmitted signal. Shifted by 90^o transmitted signal has the following form:

$$s_{tx}^{90}(t) = -A_{tx}\sin(2\pi\big(f_0t+\frac{k}{2}t^2\big)+\phi_0). \tag{2.13}$$

Similarly, quadrature-phase component, $Q(t)$, can be shown to be equal to:

$$\hat{Q}(t) = s_{rx}s_{tx}^{90} = -A_b\Big(\sin(2\pi t(2f_0-k\tau)+2\pi kt^2+\phi_1-2\pi f_0\tau)+\sin(\pi k\tau^2-2\pi kt\tau-2\pi f_0\tau+\phi_2)\Big). \tag{2.14}$$

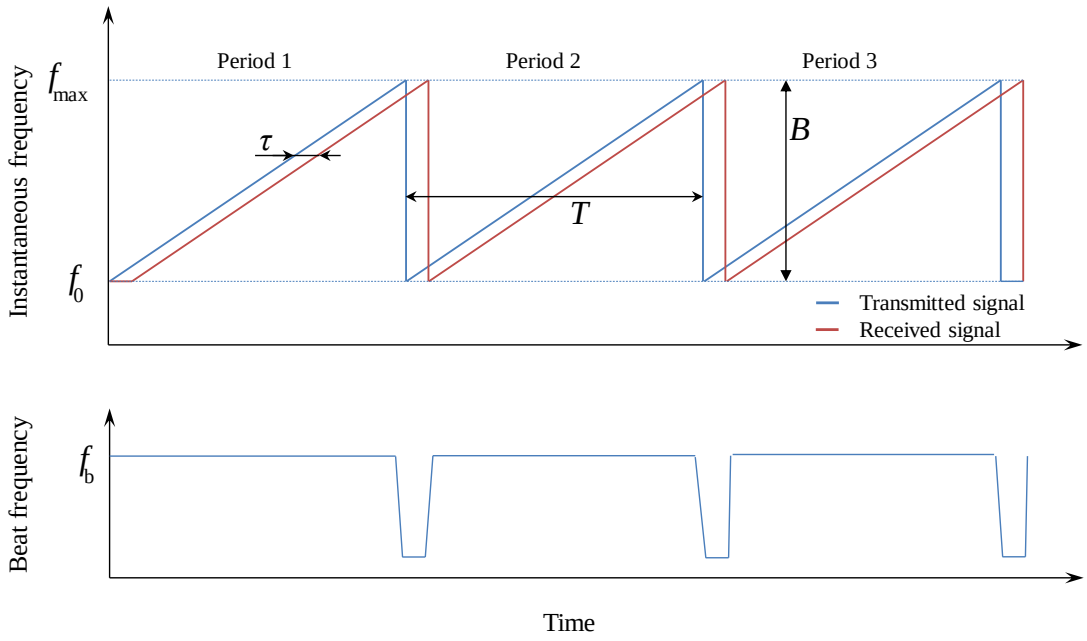

Figure 2.3: (Top) Instantaneous frequency of transmitted and received waves in case of a single stationary object. (Bottom) Resulting beat frequency. τ is a signal delay caused by wave travelling double distance to an object, T is a period of modulation, B is a bandwidth of modulation

After passing $\hat{Q}(t)$ through a low pass filter, the resulting signal has only one component:

$$Q(t) = -A_b \sin(\pi k\tau^2 - 2\pi kt\tau - 2\pi f_0\tau + \phi_2) = A_b \sin(-\pi k\tau^2 + 2\pi kt\tau + 2\pi f_0\tau - \phi_2). \quad (2.15)$$

Together, in-phase and quadrature-phase components form a complex signal called a beat signal:

$$s(t) = I(t) + jQ(t) = A_b e^{2\pi kt\tau - \pi k\tau^2 + 2\pi f_0\tau - \phi_2} = Ae^{\Psi(t)}, \quad (2.16)$$

where $\Psi(t)$ is a phase of the beat signal.

Instantaneous frequency is a derivative of the phase of the beat signal:

$$f_b = \frac{1}{2\pi}\frac{d\Psi(t)}{dt} = k\tau. \quad (2.17)$$

Taking into account (2.17) and (2.9), a distance could be estimated:

$$r = \frac{cf_b}{2k}. \quad (2.18)$$

Example of FMCW radar waveform in case of a chirp modulation and an object at distance $r = \tau c/2$ is depicted in Fig. 2.3.

B) Range and velocity estimation

The approach of range estimation, discussed in previous subsection, holds only for stationary objects. If the object is moving, then distance to it changes with the time:

$$\tau(t) = \frac{2(r + vt\cos\theta)}{c}, \quad (2.19)$$

where v is speed, θ is aspect angle between radar line of sight and object trajectory. Let us assume that target is moving only from one period (sweep, ramp) to another, standing without motion during the modulation period. Therefore we can rewrite (2.19) as:

$$\tau(n) = \frac{2(r + vnT\cos\theta)}{c} = \tau_0 + \frac{2vnT\cos\theta}{c}, \tag{2.20}$$

where τ_0 is initial distance to the object, T is period's length.

We need to clarify notations of time indexes n and t. The time inside one single sweep is called *fast-time* and denoted as t, whereas the period number, n, is called *slow-time*, to get it in time units it should be considered as nT. The idea behind assumption we made for (2.20) is that object is a slowly moving target ($c >> v$).

Let us to substitute (2.20) into (2.16) and consider only the phase component:

$$\begin{aligned}
\Psi(t) &= 2\pi kt(\tau_0 + \frac{2vnT\cos\theta}{c}) - \pi k\big(\tau_0 + \frac{2vnT\cos\theta}{c}\big)^2 + 2\pi f_0(\tau_0 + \frac{2vnT\cos\theta}{c}) - \phi = \\
&= 2\pi kt\tau_0 + 2\pi kt\frac{2vnT\cos\theta}{c} - \pi k\big(\tau_0 + \frac{2vnT\cos\theta}{c}\big)^2 + 2\pi f_0\tau_0 + 2\pi f_0\frac{2vnT\cos\theta}{c} - \phi = \\
&= 2\pi kt\tau_0 + 2\pi kt\frac{2vnT\cos\theta}{c} - \pi k\tau_0^2 - \pi k\frac{4\tau_0 vnT\cos\theta}{c} - \pi k\big(\frac{4vnT\cos\theta}{c}\big)^2 + 2\pi f_d nT\cos\theta - \hat{\phi} = \\
&= 2\pi kt\tau_0 + \frac{4\pi ktvnT\cos\theta}{c} - \pi k\frac{4\tau_0 vnT\cos\theta}{c} - \underbrace{\pi k\big(\frac{4vnT\cos\theta}{c}\big)^2}_{\text{tends to 0}} + 2\pi f_d nT\cos\theta - \hat{\phi} = \\
&= 2\pi kt\tau_0 + \frac{4\pi ktvnT\cos\theta}{c} - \pi k\frac{4\tau_0 vnT\cos\theta}{c} + 2\pi f_d nT\cos\theta - \hat{\phi},
\end{aligned} \tag{2.21}$$

where $\hat{\phi}$ absorbs all terms contributed to the linear phase.

Next we need to expand second term $\frac{4\pi ktvnT\cos\theta}{c}$, as it contains two time indexes. To eliminate non-linear phase term, a linear expansion is used with centring around central point ($t = T/2$ $nT = L\Delta T/2$) [96] (see (4.20)):

$$\frac{4\pi ktvnT\cos\theta}{c} \approx \frac{2\pi kv\cos\theta}{c}(LTt + Tn + \frac{L}{2}T^2), \tag{2.22}$$

where L indicates the number of periods were transmitted. Let us substitute 2.22 to (2.21):

$$\begin{aligned}
\Psi(t) &= 2\pi kt\tau_0 + \frac{2\pi kv\cos\theta}{c}(LTt + Tn + \frac{L}{2}T^2) - \pi k\frac{4\tau_0 vnT\cos\theta}{c} + 2\pi f_d nT\cos\theta - \hat{\phi} = \\
&= (2\pi k\tau_0 + \frac{2\pi kv\cos\theta}{c}LT)t + \left(\frac{2\pi kv\cos\theta}{c} - \pi k\frac{4\tau_0 v\cos\theta}{c} + 2\pi f_d\cos\theta\right)nT - \bar{\phi} = \qquad (2.23) \\
&= (2\pi k\tau_0 + \frac{2\pi kv\cos\theta}{c}LT)t + \left(\frac{2\pi v\cos\theta}{c}(\underbrace{k - k2\tau_o}_{<<2f_0} + 2f_0)\right)nT - \bar{\phi} = \\
&= (2\pi k\tau_0 + \frac{2\pi kv\cos\theta}{c}LT)t + \left(\frac{2\pi v\cos\theta}{c}2f_0\right)nT - \bar{\phi} = \\
&= (2\pi k\tau_0 + \frac{2\pi kv\cos\theta}{c}LT)t + \big(2\pi f_d\big)nT - \bar{\phi} \qquad (2.24)
\end{aligned}$$

Example of FMCW radar waveform for moving object in case of chirp modulation is depicted in Fig. 2.4.

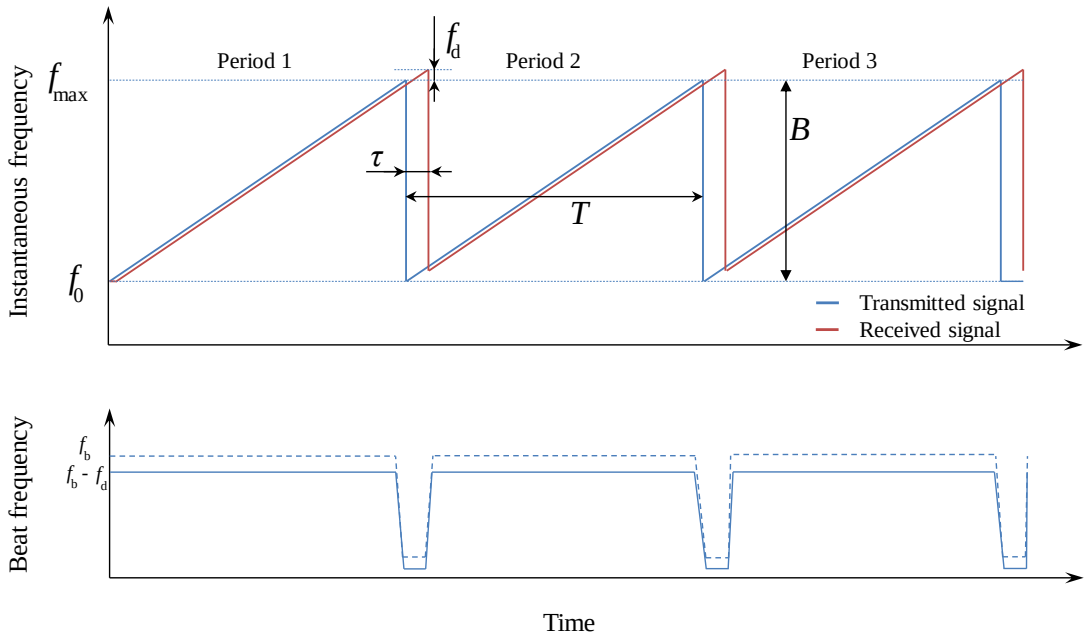

Figure 2.4: (Top) Instantaneous frequency of transmitted and received waves in case of a single moving object. (Bottom) Resulting beat frequency. Doppler shift is denoted as f_d.

C) Range-Doppler processing by 2D DFT

Phase term derived at (2.24) contains two frequencies $w_f = 2\pi k\tau_0 + \frac{2\pi kv\cos\theta}{c}LT$ and $w_s = 2\pi f_d$, therefore the 2-D Fourier transform is applied to signal in order to get estimates for two of them.

$$s(t) = A_b e^{\Psi(t)} = \hat{A}_b e^{(2\pi k\tau_0 + \frac{2\pi kv\cos\theta}{c}LT)t + (2\pi f_d)nT}, \tag{2.25}$$

where $\hat{A}_b$ is a complex coefficient including linear phase terms.

Next applying a two-dimensional Discrete Fourier Transform (2D DFT) we transform signal to frequency domain extracting information about frequencies:

$$S(p,q) = \sum_{q=1}^{L}\left(\sum_{t=\tau_m}^{T} s(t)e^{-j2\pi pt/(T-\tau_m)}\right)e^{-j2\pi qt/L} = \hat{A}_b\delta(p-w_f, q-w_s), \tag{2.26}$$

where δ is the Dirac delta function, τ_m is a maximum possible delay due to the signal travelling to and from an object, signal $s(t)$ is considered from start point $t = \tau_m$; w_f and w_s are equal to:

$$w_f = 2\pi f_f = 2\pi k\tau_0 + \frac{2\pi kv\cos\theta}{c}LT, \tag{2.27}$$

$$w_s = 2\pi f_s = 2\pi f_d. \tag{2.28}$$

For a single moving target, function $S(p,q)$ will have a single pick at frequencies w_f and w_s. As it can be seen from (2.28), Doppler frequency (and velocity) could be estimated directly from $S(p,q)$. After that, velocity term v is substituted into (2.27) and range is estimated.

In case when velocity v is not high and observation time LT in (2.27) is not long, the second term in w_f can be neglected, and frequency terms become:

$$w_f = 2\pi f_f = 2\pi k\tau_0, \tag{2.29}$$
$$w_s = 2\pi f_s = 2\pi f_d.$$

Ones angular frequencies w_f and w_s are estimated it is possible to estimate ordinary frequencies f_f, f_s and finally, range as well as velocity:

$$\begin{aligned} r &= \frac{cf_f}{2k}, \\ v &= \frac{f_s\lambda}{2}. \end{aligned} \tag{2.30}$$

For 2D Fourier transform based method of estimation, the resolution in range and velocity is determined as:

$$\begin{aligned} \Delta r &= \frac{c}{2B}, \\ \Delta v &= \frac{c}{2LTf_0}. \end{aligned} \tag{2.31}$$

This comes from frequency resolution: $\Delta f_f = 1/T$, and $\Delta f_s = 1/(LT)$.

Maximum unambiguous range and velocity are defined as:

$$\begin{aligned} r_{max} &= \frac{cT}{2}, \\ v_{max} &= \pm\frac{c}{4Tf_0}, \end{aligned} \tag{2.32}$$

General scheme for range-Doppler processing of beat signal by two dimensional DFT is shown in Fig. 2.5. The radar sends linear chirps repetitively, than received demodulated signal is used to form a 2-D data representation as in $S(p, q)$ (2.26). Then, 2D DFT is applied in order to estimate energy distribution per range and velocity cells.

D) Triangular wave

To estimate range and velocity of a single object at the scene one can use triangular modulation which results in two beat signals with frequencies:

$$\begin{aligned} f_{b1} &= f_f + f_s; \\ f_{b2} &= f_f - f_s. \end{aligned} \tag{2.33}$$

Fig. 2.6 shows the behaviour of instantaneous frequencies and beat frequency for triangular wave modulation. Resulting beat frequency is different for up- and down-chirp, which makes possible to separate contribution from time delay and Doppler shift.

From (2.33) it follows that:

$$\begin{aligned} f_f &= \frac{f_{b1} + f_{b2}}{2} \\ f_s &= \frac{f_{b1} - f_{b2}}{2} \end{aligned} \tag{2.34}$$

and range together with velocity are estimated from (2.30).

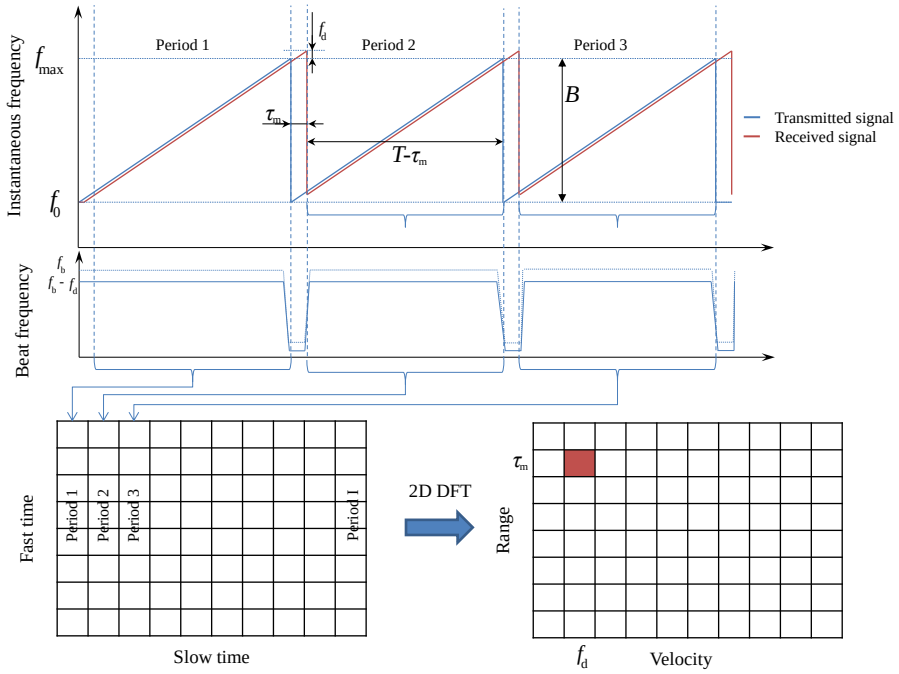

Figure 2.5: General scheme for range-Doppler processing by 2D DFT method. τ is maximum possible delay due to signal travelling to and from an object

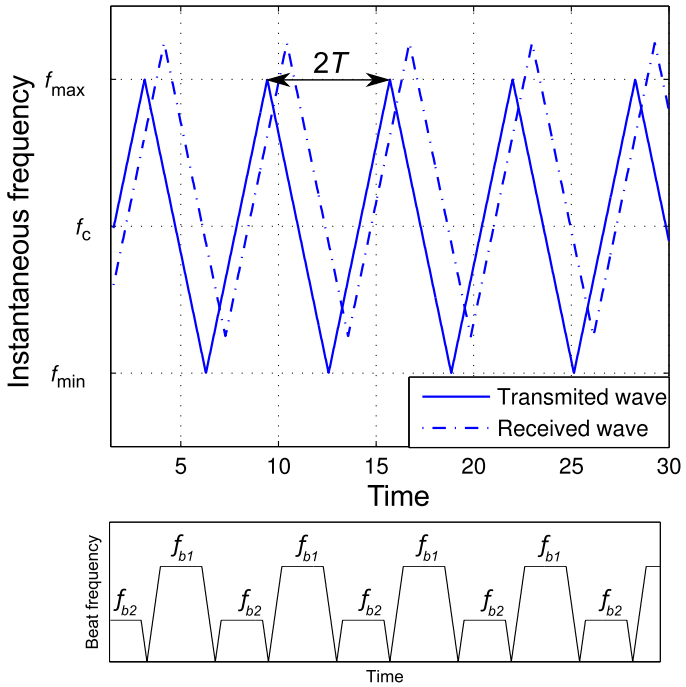

Figure 2.6: FMCW waveform and beat signals in case of triangular wave modulation: $f_{b2} = f_f - f_s$, $f_{b1} = f_f + f_s$.

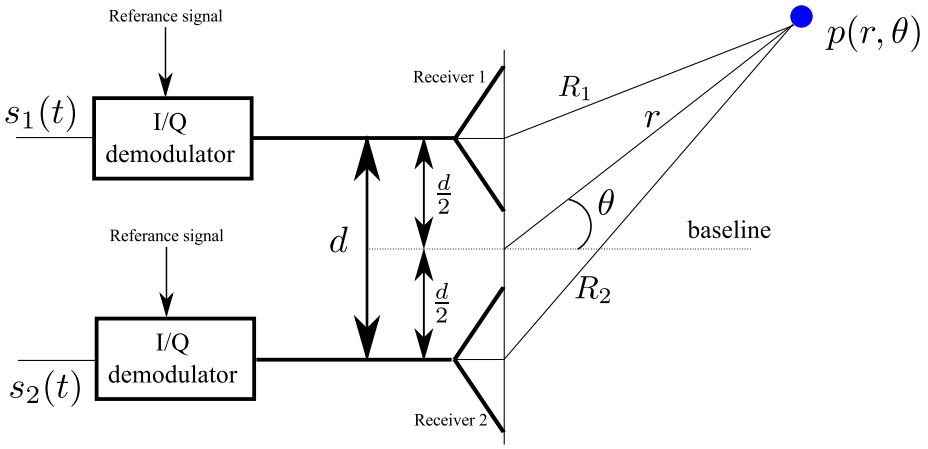

Figure 2.7: Angle of arriving estimation by two receiving antennas.

E) Azimuth estimation

Amplitude or phase difference in two receiving channels allow estimating of the angle of arriving. A distance from an object to two receiving antennas will be different, and the difference will determine the angle of the target. The difference is much smaller than the distance, and therefore phase measurements are used for angle estimation.

Fig. 2.7 illustrates principle behind angle estimation. Two receiving antennas are displaced by distance d. The task is to estimate angle θ between radar's baseline and direction to an object. Due to the displacement between radars, distances from an object to two receivers are:

$$R_1 = r - \frac{d}{2}\sin\theta \tag{2.35}$$

$$R_2 = r + \frac{d}{2}\sin\theta, \tag{2.36}$$

where r is a distance from an object to radar's baseline.

Signals at outputs of I/Q demodulators for receivers 1 and 2, respectively, can be written as:

$$s_1(t) = Ae^{j(wt+\phi_1)} \tag{2.37}$$

$$s_2(t) = Ae^{j(wt+\phi_2)}, \tag{2.38}$$

where A is an amplitude of signal at receiver, w is angular frequency which depends on the motion of the object, ϕ_1 and ϕ_2 are phase shifts at two receivers.

Phase terms ϕ_1 and ϕ_2 are equal to:

$$\phi_1 = \frac{R_1 2\pi}{\lambda} = \frac{2\pi(r - \frac{d}{2}\sin\theta)}{\lambda} \tag{2.39}$$

$$\phi_2 = \frac{R_2 2\pi}{\lambda} = \frac{2\pi(r + \frac{d}{2}\sin\theta)}{\lambda}. \tag{2.40}$$

Let us simplify a little around r:

$$\phi_1 = \frac{2\pi r}{\lambda} - \frac{\pi d}{\lambda}\sin\theta = L - \frac{\pi d}{\lambda}\sin\theta \tag{2.41}$$

$$\phi_2 == \frac{2\pi r}{\lambda} + \frac{\pi d}{\lambda}\sin\theta = L + \frac{\pi d}{\lambda}\sin\theta, \tag{2.42}$$

where $L = \frac{2\pi r}{\lambda}$.

Finally, two demodulated signals have the following form:

$$\begin{aligned} s_1(t) &= Ae^{j(wt+L-\frac{\pi d}{\lambda}\sin\theta)} \\ s_2(t) &= Ae^{j(wt+L+\frac{\pi d}{\lambda}\sin\theta)}, \end{aligned} \tag{2.43}$$

There are two typical ways to estimate angle θ from Eq. 2.43, named amplitude and phase comparison techniques.

Amplitude comparison technique

Amplitude comparison technique is based on comparison of amplitudes. We need to compute first a sum channel of two signals:

$$\begin{aligned} S(t) = s_1(t) + s_2(t) = Ae^{j(wt+L-\frac{\pi d}{\lambda}\sin\theta)} + Ae^{j(wt+L+\frac{\pi d}{\lambda}\sin\theta)} = \\ = Ae^{jwt}e^{jL}e^{-j\frac{\pi d}{\lambda}\sin\theta} + Ae^{jwt}e^{jL}e^{j\frac{\pi d}{\lambda}\sin\theta} = \\ = Ae^{jwt}e^{jL}(e^{-j\frac{\pi d}{\lambda}\sin\theta} + e^{j\frac{\pi d}{\lambda}\sin\theta}) = \\ = Ae^{jwt}e^{jL}\left(2\cos\left(\frac{\pi d}{\lambda}\sin\theta\right)\right) \end{aligned} \tag{2.44}$$

And a difference channel:

$$\begin{aligned} \Sigma(t) = s_1(t) - s_2(t) = Ae^{j(wt+L-\frac{\pi d}{\lambda}\sin\theta)} - Ae^{j(wt+L+\frac{\pi d}{\lambda}\sin\theta)} = \\ = Ae^{jwt}e^{jL}e^{-j\frac{\pi d}{\lambda}\sin\theta} - Ae^{jwt}e^{jL}e^{j\frac{\pi d}{\lambda}\sin\theta} = \\ = Ae^{jwt}e^{jL}(e^{-j\frac{\pi d}{\lambda}\sin\theta} - e^{j\frac{\pi d}{\lambda}\sin\theta}) = \\ = Ae^{jwt}e^{jL}\left(-2j\sin\left(\frac{\pi d}{\lambda}\sin\theta\right)\right) \end{aligned} \tag{2.45}$$

Taking into account Eq (2.44) and (2.47), angle θ could be estimated as:

$$\theta = \operatorname{asin}\left(\frac{\lambda}{\pi d}\arctan\left(\frac{j\Sigma(t)}{S(t)}\right)\right) \tag{2.46}$$

Let us verify solution given by Eq (2.46):

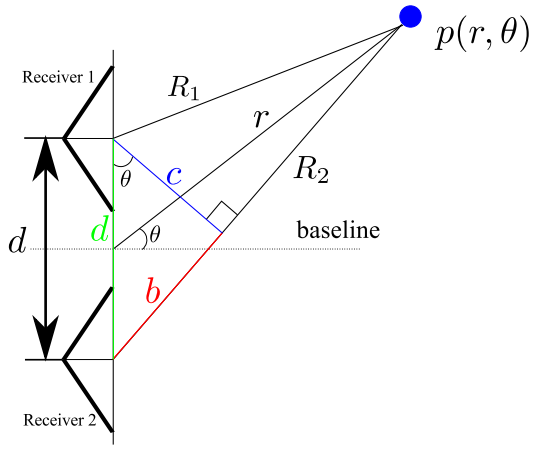

Figure 2.8: Angle of arriving estimation by phase comparison technique. For far-field ($r >> d$) we assume that $\angle dc = \theta$.

$$\theta = \arcsin\left(\frac{\lambda}{\pi d}\arctan\left(\frac{j\Sigma(t)}{S(t)}\right)\right) = \arcsin\left(\frac{\lambda}{\pi d}\arctan\left(\frac{jAe^{jwt}e^{jL}\big(-2j\sin(\frac{\pi d}{\lambda}\sin\theta)\big)}{Ae^{jwt}e^{jL}\big(2\cos(\frac{\pi d}{\lambda}\sin\theta)\big)}\right)\right) =$$
$$= \arcsin\left(\frac{\lambda}{\pi d}\arctan\left(\frac{-2jj\sin(\frac{\pi d}{\lambda}\sin\theta))}{2\cos(\frac{\pi d}{\lambda}\sin\theta)}\right)\right) =$$
$$= \arcsin\left(\frac{\lambda}{\pi d}\arctan\left(\frac{\sin(\frac{\pi d}{\lambda}\sin\theta))}{\cos(\frac{\pi d}{\lambda}\sin\theta)}\right)\right) =$$
$$= \arcsin\left(\frac{\lambda}{\pi d}\arctan\left(\tan(\frac{\pi d}{\lambda}\sin\theta)\right)\right) =$$
$$= \arcsin\left(\frac{\lambda}{\pi d}\left(\frac{\pi d}{\lambda}\sin\theta\right)\right) =$$
$$= \arcsin\left(\sin\theta\right) = \theta \tag{2.47}$$

Phase comparison technique

Fig. 2.8 illustrates geometry of angle estimation by phase comparison technique. For real situations where $r >> d$ we assume that $\angle dc$ is equal to θ. Therefore, the angle could be estimated as follows:

$$\theta = \arcsin\left(\frac{b}{d}\right) \tag{2.48}$$

Again, for real scenarios $r >> d$ and we assume that $b < \lambda$, therefore, b could be estimated by phase difference at receivers 1 and 2:

$$b = \frac{\lambda\big(\angle s_2(t) - \angle s_1(t)\big)}{2\pi}, \tag{2.49}$$

where $\angle s$ denotes a phase of the signal s.

Substituting (2.49) into (2.48) we get an estimate of θ by phase comparison method:

$$\theta = \arcsin\left(\frac{\lambda\big(\angle s_2(t) - \angle s_1(t)\big)}{d2\pi}\right) \tag{2.50}$$

In practise, phase difference is computed by multiplication the signal from one receiver with complex conjugated signal from second receiver with the following phase extraction.

Let us verify (2.50) by substituting phases of $s_1(t)$ and $s_2(t)$:

$$\begin{aligned}
\theta = \arcsin\left(\frac{\lambda\big(\angle(Ae^{j(wt+L+\frac{\pi d}{\lambda}\sin\theta)}) - \angle(Ae^{j(wt+L-\frac{\pi d}{\lambda}\sin\theta)})\big)}{d2\pi}\right) = \\
= \arcsin\left(\frac{\lambda\big((wt+L+\frac{\pi d}{\lambda}\sin\theta) - (wt+L-\frac{\pi d}{\lambda}\sin\theta)\big)}{d2\pi}\right) = \\
= \arcsin\left(\frac{\lambda\big(\frac{\pi d}{\lambda}\sin\theta + \frac{\pi d}{\lambda}\sin\theta\big)}{d2\pi}\right) = \\
= \arcsin\left(\frac{\lambda\big(2\frac{\pi d}{\lambda}\sin\theta\big)}{d2\pi}\right) = \\
= \arcsin\big(\sin\theta\big) = \theta
\end{aligned} \tag{2.51}$$

The assumption that $b < \lambda$ puts limits the angle estimation by phase comparison technique to be:

$$\theta_{max} = \pm\arcsin\left(\frac{\lambda}{2d}\right) \tag{2.52}$$

Analytical expression of resolution of amplitude and phase comparison methods could be find at [38] and is defined by:

$$\Delta\theta = \frac{0.45\phi}{\sqrt{S/N}}, \tag{2.53}$$

where ϕ defines 3 dB beamwidth of antenna, S/N is carrier signal to noise ratio. Beamwidth of the antenna at 3 dB could be approximated as $57.3d/\lambda$.

Analysis of the amplitude and phase comparison techniques has been performed in [38], according to it several conclusions could be pointed out:

- Phase measurements cause additional tolerance and degradation of the resolution;
- At short distances ($<$ 10m) additional tolerance is small, and therefore phase and amplitude comparison techniques provide comparable results;
- At long distances ($>$ 10m) additional tolerance due to the phase measurements become higher, and the amplitude comparison technique outperform the phase one.

Chapter 3

Period estimation of micro-Doppler signature

A novel approach dedicated to estimation of a period in micro-Doppler radar signatures is suggested in this Chapter. The approach assumes the form of frequency slices in STFT to be a superposition of pulses. The period of the pulses determines the period of the micro-Doppler signature. No a priori information about radar object under observation is required for estimation of period. Simulated data of human walking is used for performance evaluation of suggested and selected approaches. Real-life micro-Doppler radar measurements of a walking human are collected for indoor environment and used for experimental examination of suggested approach. Robustness of the proposed technique to aspect angle variations of moving human is estimated. Experimental radar measurements of toy helicopter rotating blades are executed and parameters of helicopter micro-Doppler radar signatures are studied. The benefit of suggested approach comparing to common approaches is demonstrated using the bias and mean squared errors of micro-Doppler period estimates computed in additive noise environment.

I Introduction

In case of a repeating action of moving parts, the micro-Doppler signal becomes periodic. One of the most important human movement parameters for activity classification is the period of micro-Doppler frequency variations in radar returns.

In a situation when the character of the motion is known a priori, the robust estimate of the motion parameters can be obtained by the Hough transform of the pseudo-Wigner-Ville time-frequency distribution [12, 35]. Using this technique, the micro-Doppler signature could be decomposed onto a set of simple oscillations. However, the exact type of the FM could be unknown. One more drawback is a computational complexity because the latter approach requires a grid search of parameters.

Wavelet decomposition can be applied for both processing of micro-Doppler signature of human walking and rotating blades [159]. If a priori knowledge of the motion parameters is given, then they could be estimated with better accuracy even at low SNR.

If the object under consideration is known then the motion parameters, including the period, can be estimated based on the model of the micro-Doppler signature. A number micro-Doppler signatures' models are available, including human walking for monostatic radar [22] or multistatic radar [151] as well as for horse running and blade rotation [30].

A number of Maximum Likelihood Estimators (MLEs) have been proposed for motion parameter estimation of the micro-Doppler signals [140, 143]. MLEs provide a robust estimate if the distribution of the noise as well as the model of the signal are known.

In contrast to the robust methods described above [12, 35, 140, 143, 151, 159] in this work we assume that no a prior knowledge is available about the object and character of the motion; therefore, none of the approaches described earlier can be applied.

The period of micro-Doppler can be estimated by comparing maximums of the similarity measure computed for time-frequency representation [41]. For better accuracy authors use parabola fitting to the maximums. The method does not require any a prior information about the motion type.

In this Chapter, a new approach for micro-Doppler signal period estimation is developed. The approach is based on the Fourier analysis of a periodic radar signature collected in the form of spectrogram. For this estimator we assume that a form of micro-Doppler signature is unknown. Noise corrupted signal is assumed to be independent and identically distributed process. The suggested approach is compared with two approaches corresponding to the above mentioned requirements.

The micro-Doppler signatures of the rotating blades of a fan [35] as well as helicopter [98] are also of a great interest. The period of the rotation is a paramount parameter of such a motion. Experimentally collected micro-Doppler signatures of rotating blades are analyzed in this paper.

The micro-Doppler signature of a human walking contains contributions from torso, legs, arms and other human body parts. All these parts have the same period [166].

Below we will consider and describe two approaches to period estimation which are close in spirit to the proposed technique and do not require a priori knowledge of a signal model.

The period of a micro-Doppler signature can be estimated by extracting the stride rate [155]. This algorithm is based on extraction of instantaneous frequencies from the spectrogram estimate with subsequent filtering by a median filter. The filtered data are then analysed by the Fourier transform in order to extract the period information.

Another technique for solving the considered problem can be found in [5] (Section 9.3). The approach is based on extraction of a behaviour of the spectrogram's energy in relation to the time for frequencies higher than the one corresponding to the contribution from the torso. This behaviour is then analysed by the autocorrelation function and period is defined by the location of the corresponding peak.

The advantage of the above mentioned approaches ([5, 155]) is their lower computational complexity comparing to the proposed approach. A difference between suggested and common approaches is that in the proposed strategy all frequency information contained in the spectrogram is used. On the contrary, the stride rate technique [155] uses frequency information caused by the torso only, and the technique presented in [5] uses frequencies higher than values provoked by torso.

The Chapter is organized as follows. First, in Section II, the problem is formulated with a further theoretical background consideration. Next, in Section III the suggested approach is compared with other estimators using simulated micro-Doppler data for human walking. Then, the approach is evaluated by real measurements of micro-Doppler signals caused by human walking as well as toy helicopter blade rotation.

II Suggested approach

A) Problem statement

Assume that a discrete periodic micro-Doppler signal is given as $s \in \mathbb{C}^I$ for K moving components with amplitude variations of $a_k(t)$, and it can be written as:

$$s(t) = \sum_{k=1}^{K} a_k(t) e^{j\theta_k(t)}, \tag{3.1}$$

where temporal phase variations are equal to:

$$\theta_k(t) = \theta_k(t + nT) = 2\pi t f_d(t)/F_s,$$

where $t = 0...I-1$, $n \in \mathbb{Z}$, T is a period of micro-Doppler and $f_d(t)$ is time varying Doppler shift, F_s is a sampling frequency.

The problem of a micro-Doppler period estimation is formulated as the estimation of a parameter T of a given multi-component signal s.

B) Theoretical background

Assume that the following three signals are given: an aperiodic discrete signal $x \in \mathbb{C}^T$; a signal $x_p \in \mathbb{C}^I$ contained N copies of x; and $x_z \in \mathbb{C}^I$ zero padded signal x given within length I. Then, the Fourier transforms X_p and X_z of signals x_p and x_z can be expressed, respectively as:

$$X_p(w) = \frac{I}{T} X_z(w) \sum_{b=-\infty}^{\infty} \delta(w - bT), \tag{3.2}$$

where δ is the Dirac function, $b \in \mathbb{Z}$.

Assume that the signal x has a form of a pulse with an amplitude of A, and width of K. Then, the magnitude of Fourier transform of the signal x is defined as:

$$|X(w)| = \left| \frac{AK \sin(\pi w K)}{\pi w K} \right| = \left| AK \ \mathrm{sinc}(\pi w K) \right|. \tag{3.3}$$

If the signal x has a pulse form, then the signal x_p contains N pulses, and from (3.2) and (3.3) it follows that the magnitude of Fourier transform of x_p is:

$$|X_p(w)| = \frac{IAK}{T} \left| \mathrm{sinc}(\pi w K) \right| \sum_{b=-\infty}^{\infty} \delta(w - bT) = AKN \left| \mathrm{sinc}(\pi w K) \right| \sum_{b=-\infty}^{\infty} \delta(w - bT). \tag{3.4}$$

It follows from (3.4) that the maximum of $X_p(w)$ with $w > 0$ can be estimated as:

$$\max_{w>0} |X_p(w)| = NAK \left| \mathrm{sinc}(\pi K T) \right| = |X_p(T)|. \tag{3.5}$$

From (3.5) it follows that the period T of a signal with the form of a pulse train can be estimated by the location of the maximum for $w > 0$. Latter we will show how the period of a pulse train relates to our problem of micro-Doppler period estimation.

C) Developed approach

The spectrogram of a given signal $s(t)$ is defined as:

$$S(f,n) = \left| \sum_{l=0}^{L-1} s(n-l)w(l)e^{-j2\pi fl/L} \right|^2, \tag{3.6}$$

where $0 \leq f \leq L-1$ is the frequency index; $0 \leq n \leq I-1$ is the time index; L is the length of sliding window $w(l)$.

To compensate the influence of the window length onto the spectrogram estimate, we define a normalized spectrogram $P(f,n)$ as:

$$P(f,n) = \frac{1}{2\pi||w||} S(f,n), \tag{3.7}$$

where $||w||$ is an Euclidean norm of the window function w.

The idea of the suggested approach is in the following. If the processed signal has a period T, then each micro-Doppler frequency at the spectrogram has the same period T. Therefore, the period of the signal can be estimated by the period of the spectrogram.

An example of a micro-Doppler spectrogram of simulated human walking process is illustrated in Fig. 1.3. The spectrogram has a repeating behaviour with some period called micro-Doppler period. It can be seen that the variation of the frequencies in the spectrogram is similar to repetition of pulse train. Every horizontal slice of the spectrogram illustrated in Fig. 1.3 has a form similar to pulse train with various amplitudes and pulse widths.

In order to estimate the period of frequency content in relation to the time index of the normalized spectrogram, the amplitude of Fourier transform is computed:

$$B(f,i) = \left| \sum_{t=0}^{I-1} P(f,t)e^{-j2\pi it/I} \right|, \tag{3.8}$$

where $i = 0, ..., I-1$.

The information about the periodicity of the frequency content in the normalized spectrogram is contained in the function $B(f,i)$ (3.8). This information should be averaged in order to obtain the following smoothed function:

$$D(i) = \frac{1}{L} \sum_{f=0}^{L-1} B(f,i). \tag{3.9}$$

An integer number of micro-Doppler periods in the signal are estimated in the following way:

$$\hat{N} = \arg\max_{i>0} D(i). \tag{3.10}$$

Period of the radar signature can be estimated as:

$$\hat{T}_{sug} = \frac{I}{\hat{N}}. \tag{3.11}$$

Suggested algorithm can be summarized as follows. First, a spectrogram $S(f,n)$ is computed by (3.6), then Fourier transform is applied to the spectrogram on the time axis by (3.8). Finally, the amplitude information is aggregated for all frequencies by (3.9). Period is estimated by (3.11) according to the index of a maximum peak for $i > 0$.

For a signal with period T the spectrogram also has period of T and thus contains I/T bursts. The Fourier transform will have a peak at the bin $\lfloor I/T+0.5 \rfloor$. Therefore, $\arg\max_i D(i) = \lfloor I/T + 0.5 \rfloor$ means that the bias of suggested estimator in case of noise free signal is equal to:

$$Bias(\hat{T}_{sug}) = T - \frac{I}{\lfloor I/T + 0.5 \rfloor}. \tag{3.12}$$

With an increase of the signal's length I the suggested estimator becomes asymptotically unbiased: $E\{T - \frac{I}{\lfloor I/T+0.5 \rfloor}\}_{I\to\inf} = T - \frac{I}{I/T} = 0$, where $E\{\}$ is the expectation.

D) Correction of non-integer number of periods

The proposed estimator has bias introduced in the (3.12). It can be explained by the fact that the Fourier analysis introduced in the previous section allows estimating an integer number of periods only. We propose to fit the Gaussian to the maximum of the function D and in this way to get the non-integer number. The location of the fitted Gaussian will determine the non-integer number of periods. The closed form solution of the location of the fitted the Gaussian function is:

$$\hat{N} = \frac{\ln\big(D(Q+1)\big) + \ln\big(D(Q-1)\big)}{2\left(2\ln\big(D(Q)\big) - \ln\big(D(Q-1)\big) - \ln\big(D(Q+1)\big)\right)}. \tag{3.13}$$

According to the correction of the $\bar{N}$ the final period is also recalculated as $\hat{T}_{sug} = I/\bar{N}$.

E) Optimal window length estimation

The accuracy of estimate of the period by the suggested approach depends on the window length L given in (3.6). Selection of this parameter relates to finding a trade off between temporal and frequency resolution in the spectrogram. Optimal window length L will correspond to the value which maximizes the function $D(i)$ in (3.9).

Assume a set $\{D_q, ..., D_Q\}$ is obtained by (3.9) with variation of the window length $L = q, ..., Q$. Then, the optimal window length can be estimated as:

$$\hat{L} = \arg\max_m(\max_i D_m(i)). \tag{3.14}$$

F) Block diagram of the proposed algorithm

Fig. 3.1 illustrates the main steps required for the proposed algorithm to estimate the period of the micro-Doppler (m-D) signal. Radar m-D signal arrives at the input of algorithm with no a priori information. First step is to estimate a time-frequency distribution of the signal by applying Short-Time Fourier Transform (STFT) with initial length of window function $L = 2$. As the result, function $S(f, n)$ is computed by (3.6). To compensate an influence of the window function, all values are normalized according to (3.7) and function $P(f, n)$ is computed. Next step is to apply the Fourier transform (3.8) resulting in the function $B(f, i)$. Averaging along the frequency is performed by (3.9) in order to evaluate a smoothed estimate. A possibility of applying longer window function is evaluated next. If it is possible, then the length of the window function is set to $L = 2^{1+\log_2 L}$. Next processing step is executed in the "STFT" block. If the function $D(i)$ is evaluated for all available values of L, then the optimal window length is selected by (3.14) and the period estimate is calculated by (3.11) with correction of non-integer number of periods (see Section E)).

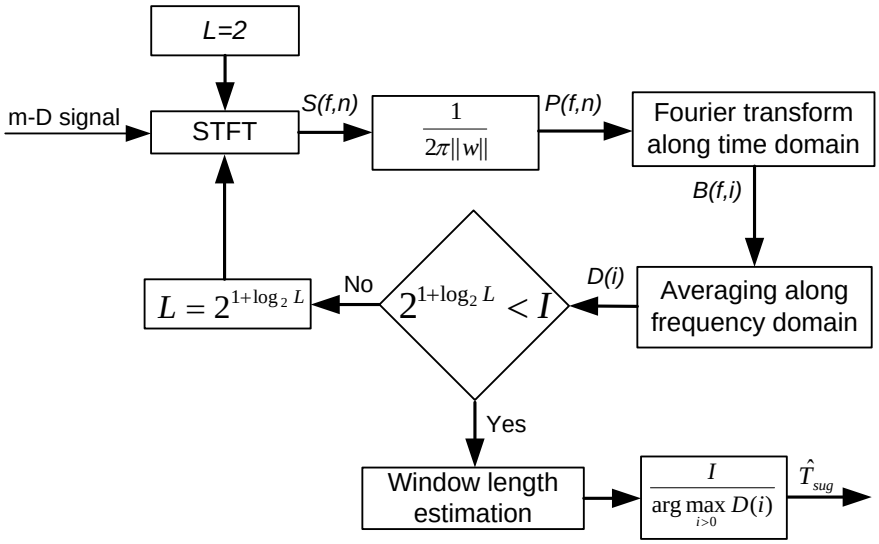

Figure 3.1: Block diagram of the proposed algorithm.

G) Computational complexity analysis

In this Subsection, a computational complexity of the proposed algorithm will be estimated. We assume that $L = 2^{\mu}, \mu \in \mathbb{N}$, making it possible to use the Cooley-Tukey algorithm for the fast discrete Fourier transform. If we assume that the optimal value of L is known or estimated before, then, for the proposed algorithm, the total number of complex procedures (multiplications and summations) is equal to:

$$\mathcal{O}(I) \approx (I - L + 1)(L(\log_2 L + 2) + \log_2(I - L + 1) + 1).$$

In the case when the optimal length of window function should be estimated according to (3.14), the total number of complex multiplications and summations is equal to:

$$\mathcal{O}(I) \approx \sum_{\mu=1}^{\lfloor \log_2 I \rfloor} (I - 2^{\mu} + 1)(2^{\mu}(\mu + 2) + \log_2(I - 2^{\mu} + 1) + 1).$$

III Performance evaluation with simulated data

In this subsection we will compare the suggested approach with several approaches introduced earlier. The common technique for the period estimation is based on autocorrelation analysis. After computation of autocorrelation function $R_{xx}(i)$, $i = -I + 1...I - 1$, the period is estimated by the index confirming to a peak with a shift parameter $i > 0$. However, this approach has a large bias value due to the fact that radar signal can contain a number of periodic components, as well as it is periodic itself. This peculiarity will be studied below.

Two micro-Doppler period estimators were proposed earlier by D. Tahmoush and J. Silvious in [155] and by M.G. Anderson in [5]. In further discussions they are referred as stride rate technique (SRT) and energy based technique (EBT), respectively. We will compare the performances of the suggested estimator with SRT and EBT.

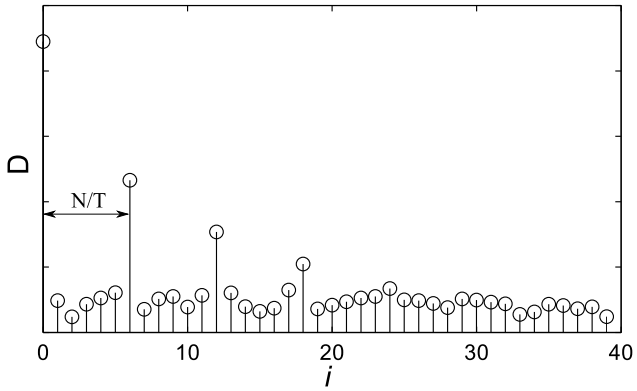

Figure 3.2: Function $D(i)$. The frequency content of the spectrogram illustrated in Fig. 1.3. The period of the spectrogram depends on the position of the second maximum.

The measures of period estimation error are selected to characterize the properties of the estimator. The first measure of estimator performance is a bias equal to: $Bias(\hat{T}) = T - E\{\hat{T}\}$. The second measure of estimator performance is a mean square error: $\mathrm{MSE}(\hat{T}) = E\{(T - \hat{T})^2\}$.

The performance of estimators is compared for simulated data of a micro-Doppler signal of a walking human developed in [22] and implemented in [30]. The period of gait is selected to be $T = 0.5384$ s corresponding to a walking velocity of 0.884 m/s. Sampling rate is equal to 1902 samples per second. Simulated micro-Doppler signal contains 5 periods (5120 samples) of human walking. The spectrogram is shown in Fig. 1.3. Fig. 3.2 demonstrates the behaviour of function $D(i)$ (3.9) calculated from the spectrogram illustrated in Fig. 1.3. Location of the second maximum peak defines the both periods of the bursts in spectrogram and micro-Doppler signal.

The length of the window function affects the final estimate of the period. In order to demonstrate this, Table 3.1 is presented. It is seen that the bias is large if the value of L is not selected properly.

For noise-free data both bias and MSE are equal to zero for the suggested approach as well as for both SRT and EBT. However, autocorrelation-based approach provides $Bias(\hat{T}_{ac}) = 0.528$ s and $\mathrm{MSE}(\hat{T}_{ac}) = 0.279$ s. These results show that the autocorrelation technique is not suitable for micro-Doppler period estimation of human walking. Therefore, in further comparison analysis it will be excluded from the consideration.

Additive white Gaussian noise (AWGN) corrupts the radar measurements. For example, when a target is far from the radar, and the power of the radar is rather low, whereas the received signal is considerably contaminated by AWGN. Therefore, the performance of estimators under AWGN influence should be compared. In the experiments below we will vary the variance of AWGN providing various signal to noise ratios (SNR). The SNR is computed as $10\log_{10}\left(\frac{P(s)}{P(AWGN)}\right)$, where $P(s)$ is the power of the signal, and $P(AWGN)$ is the spectral density of AWGN.

The bias of estimators depending on the SNR is illustrated in Fig. 3.3 (a). EBT provides unbiased estimate for SNR $\geq$ 2dB, and SRT for SNR ≥ -4dB. The best robustness against AWGN achieved by the suggested approach with priori estimated window length. It provides an unbiased estimate for SNR ≥ -10dB. Therefore, the benefit provided by the suggested technique is 12 dB comparing to EBT, and is 6dB comparing to SRT. It should be noted that all above mentioned approaches assume a prior knowledge of the optimal window length. When the optimal window length is not known a prior then the scheme for it estimation proposed in Section E) is applied.

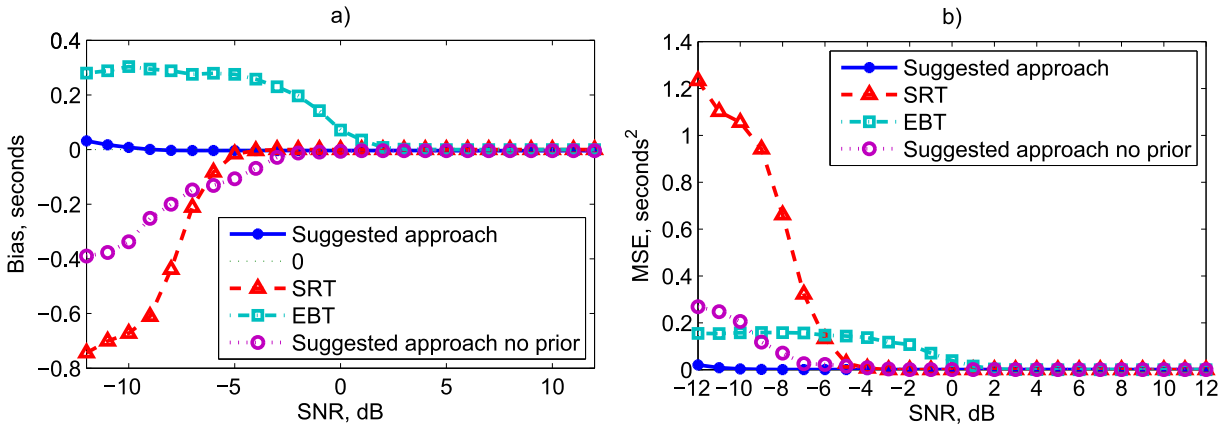

Figure 3.3: Bias (a) and MSE (b) of estimators depending on SNR level, computed for modeled micro-Doppler data of walking human.

Table 3.1: Bias of the proposed algorithm depending on the window length L

L	2	4	8	16	32	64	128	256	512	1024	2048	4096
$Bias(\hat{T}_{sug})$, s	0.5	0.4592	0	0	0	0	0	0	-0.1346	-0.1346	0.5172	0.523

The resulting bias for this case is illustrated in Fig. 3.3 by method called 'Suggested approach no prior'. Unbiased estimate is obtained with SNR > -2dB, and bias tends to decrease within increase of SNR.

The MSE values depending on the SNR are shown in Fig. 3.3 (b). It can be seen that the MSE provided by our approach has the smallest value comparing to other estimators. EBT provides MSE at level of 0.17 s^2 for SNR ≤ -4dB. SRT provides the highest MSE for SNR < -6dB. MSE provided by the suggested approach has the smallest value and it is on the level of 0.05 s^2 for SNR$=-12$ dB. MSE by suggested approach under uncertainty of motion type is at level of 0.3 s^2 for SNR $= -12$dB.

The window length is estimated for a noise-free signal and then applied for all SNRs in Fig.

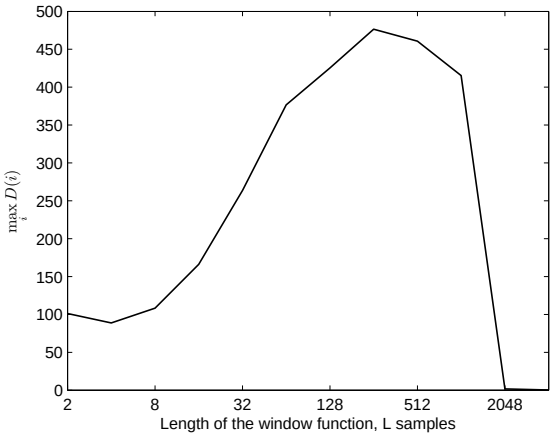

Figure 3.4: Maximum value of function $D(i)$ depending on the length of window function L.

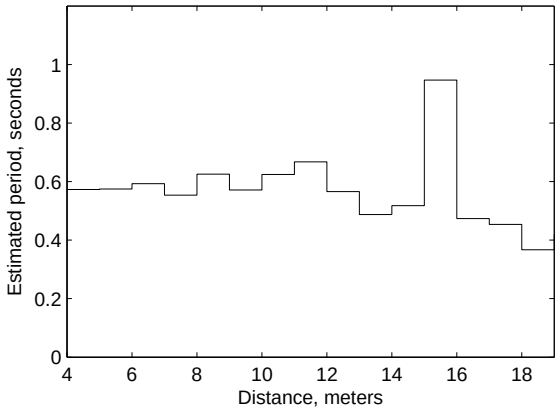

Figure 3.5: Estimated period of human gait depending on the distance. The data for experiment were collected indoor in the 20 meters long corridor.

3.3 for SRT, EBT and suggested approach. We have selected empirically the length to be 256 samples what corresponds to unbiased estimate in Table 3.1. Estimates provided by both EBT and SRT are computed using the same window length. Analysis of the performance of EBT and SRT using different window length indicates that the best result is obtained for value of 256 samples. In case of uncertainty of the window length the length is estimated according to the criteria $\max_i D(i)$ as it is described in section E). An example for noise free data is illustrated in Fig. 3.4 what demonstrates the dependence of $\max_i D(i)$ on the length of the window function; the optimal window length is estimated to be of 256 samples what corresponds to the unbiased estimate (see Table 3.1). In case of noise, for different values of SNR, the optimal window length is estimated again; therefore, the error is higher for suggested approach with no prior.

IV Performance evaluation with measured data

A) Human walking indoors

In reality, the contributions of the radar scatterers in the human micro-Doppler signature appear and disappear in the time-frequency domain due to a shadowing effect. The micro-Doppler signature is not so clear as it is illustrated in Fig. 1.3. Experimental data were obtained by 24 GHz continuous wave mono-static radar InnoSent IPS-146 [77] with the output power of 18 dBm and radiation pattern of 33^o in horizontal and vertical directions. The experiments were performed indoor in a 20 m long and 1.5 m wide corridor. A human moved towards the radar then returned and came back. In this way a number of experiments were recorded. Sampling frequency is selected to be equal to 2 KHz.

An estimated period of the human walking depending on the distance is shown in Fig. 3.5. A level of noise increases with an increase of a distance to the target, and, thus, a larger error of the estimator is observed. A signal recorded during the 4 last seconds was used to estimate the period of a gait for selected distance to the subject. From Fig. 3.5 it can be seen that for distance less than 13 m the estimator provides an unbiased estimate. It can be explained by high SNR at this observation segment. Moreover, the result is similar to the simulated data. For distances higher than 13 meters the estimator provides an error caused by a high noise level. For distances higher than 15 meters the bias is more than 0.3 seconds and the estimator is inapplicable.

Figure 3.6: Experimental setup of micro-Doppler signal collecting from rotating blades of a toy helicopter.

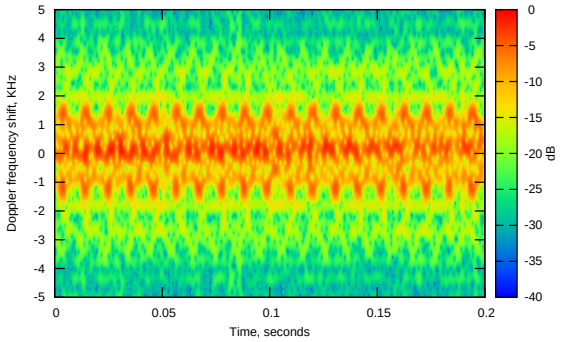

Figure 3.7: Spectrogram of micro-Doppler signal from rotating blades of a toy helicopter.

B) Toy helicopter blade rotation

Suggested approach was examined by the micro-Doppler signature measured for a toy helicopter blade rotation. Micro-Doppler signal of rotating blades was measured experimentally in the laboratory. Toy helicopter was used with two blades of 76 mm length and two smaller blades of 34 mm length. InnoSent IPS-146 radar was used with a sampling frequency 22050 Hz. The experimental setup is illustrated in Fig. 3.6. The distance between the radar and the helicopter was set to be 0.6 m.

The spectrogram of a micro-Doppler signal is shown in Fig. 3.7. It can be seen that the spectrogram contains the sequence of repeating bursts. Length of each burst corresponds to a half period of the helicopter's rotating blades. From a visual analysis it follows that the spectrogram contains 19 bursts repeated with the period of $\hat{T} \approx 0.2/19 = 0.0105$ seconds.

The estimated period depending on the length of an observed signal is demonstrated in Fig. 3.8. The figure shows how the bias of the proposed algorithm affects the estimate. It can be seen that with an increase of the signal's length the estimate tends to an unbiased value. In Fig. 3.8 the result of sub-integer number of periods correction can be observed.

C) Variations in target aspect angle

We performed a set of experiments to estimate the robustness of the proposed approach to variations in aspect angle of a moving target. Micro-Doppler signals of human walking at different aspect angles were recorded outdoor. Tested aspect angles are varied within the range from 0^o to 90^o and from 180^o to 270^o with a step of 15^o. It is well-known that the micro-Doppler signature varies extremely depending on the aspect angle variations. In order to demonstrate this, Fig. 3.9 shows spectrograms of micro-Doppler signal of human walking at different aspect angles. It is clearly seen that these two spectrograms considerably differ from each other.

The scheme of an experimental setup is illustrated in Fig. 3.10. All walking human paths are enclosed in a square area of 6 m width. A distance between the radar and the center of the square is equal to 9 m. A human is walking forward and backward along the path. The data were

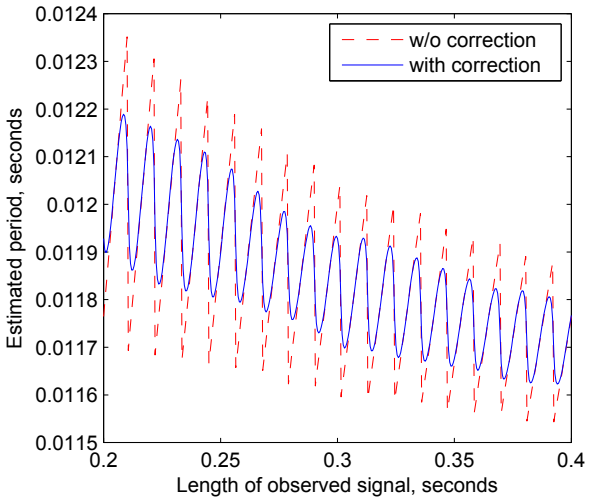

Figure 3.8: Period of micro-Doppler signature as a function of observed signal length, obtained from helicopter's blades and estimated by the suggested approach. The results for method without correction (Section D)) is shown as dashed line. The result after correction by (3.13) is shown as a solid line.

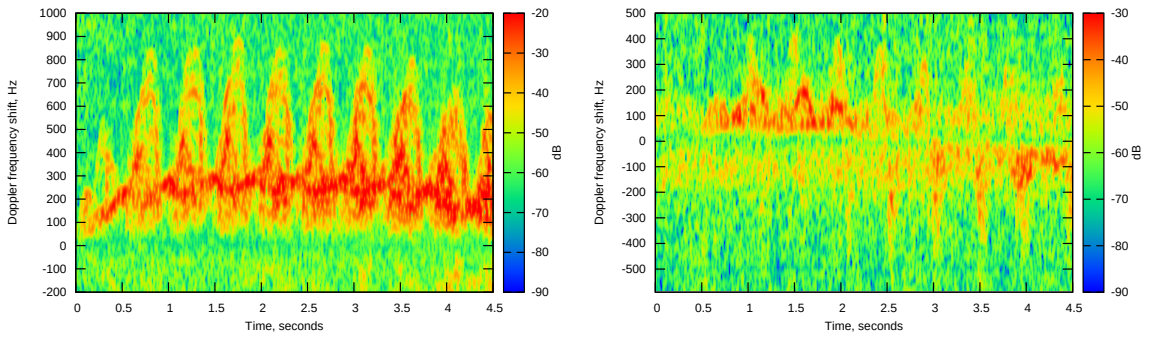

(a) 0^o (b) 90^o

Figure 3.9: Spectrograms of micro-Doppler signal of walking human with aspect angle 0^o (a) and 90^o (b). The data is recorded by 24 GHz radar outdoor.

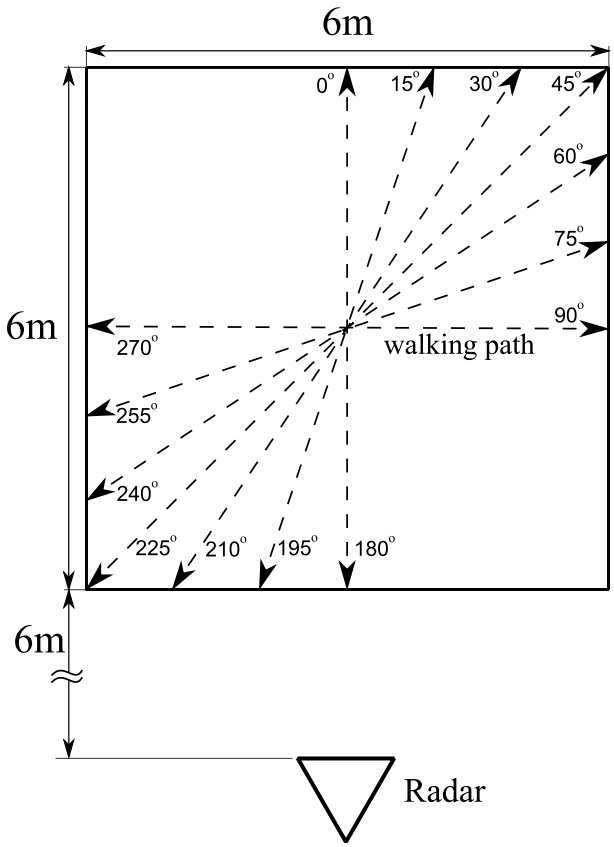

Figure 3.10: Experimental setup (top view) of micro-Doppler data collection of human walking at different aspect angles.

collected by the radar with a sampling frequency 2756 Hz and operating frequency of 24 GHz. For data collection two persons were involved: single woman and single man.

Estimated periods of a walking human depending on the aspect angle are shown in Table 3.2. Due to a human movement forward and backward along the same path twice, four records were collected for the same human. As a micro-Doppler signal of a person moving forward and backward along the same path is similar, the results are combined into the same column (as it 0^o (180^o)). A description for each set of experiments is given in the second column. The last column shows the median value of all estimates for a complete experiment.

Values in Table 3.2 show that estimated periods are close to the median value for most of the experiments. Estimated period of running activity is smaller than for a walking activity. A number of outliers occur in estimates, such as experiment 2.1 for aspect angles 60^o and 75^o, experiment 2.3 for aspect angle 60^o and etc. Those can be explained by the fact that the micro-Doppler signature of a person moving at the aspect angle near 60^o could contain the bursts with a period close to the double gait period. For this case contributions of the left part and right part of the human to the gait is different.

Obtained results indicate that it is possible to estimate the period of a moving person by the proposed approach even at aspect angles close to $90^o(270^o)$.

Table 3.2: Estimated period (in ms) of human walking at different aspect angles

Ex.	Description	Aspect angle							Median
		0^o (180^o)	15^o (195^o)	30^o (210^o)	45^o (225^o)	60^o (240^o)	75^o (255^o)	90^o (270^o)	
1.1	A woman moving with normal speed	564	529	493	520	499	522	523	501
1.2		542	520	478	476	466	480	491	
1.3		503	518	510	492	519	524	553	
1.4		528	509	482	477	467	480	496	
2.1	A woman moving with higher speed	477	484	474	461	1042	1188	476	469
2.2		452	476	471	431	438	410	478	
2.3		481	473	466	491	931	484	459	
2.4		468	457	468	438	438	431	449	
3.1	A woman running	409	324	315	295	314	387	363	339
3.2		309	303	345	434	373	419	367	
3.3		340	497	312	447	294	346	372	
3.4		334	300	282	416	364	623	281	
4.1	A man moving with normal speed	544	541	552	549	591	587	558	546
4.2		543	552	508	503	525	525	542	
4.3		537	521	543	1113	585	596	589	
4.4		536	552	544	517	507	525	576	
5.1	A man moving with higher speed	522	481	521	480	540	505	481	486
5.2		472	490	457	452	428	451	453	
5.3		489	483	533	466	552	681	475	
5.4		479	490	458	935	436	860	453	

Summary

A novel approach to micro-Doppler period estimation is proposed in this Chapter. It is based on the period estimation in time-frequency domain and uses Fourier transform as a tool for periodic radar signature analysis. The key benefit of the proposed approach is that no a priori information is required about the moving object or modulation parameters of the micro-Doppler signal.

In case of a priori uncertainty about a class of radar target, the correct estimate of a period is achieved for SNR $\geq$-2 dB. In the case of complete determination about moving radar target, the correct estimate of period is provided for SNR $\leq$-10 dB. Experiments on the real measurements collected for a human walking indoor in the corridor has indicated that this approach can be successfully applied to a real data even in presence of multiple reflections from the walls. Suggested approach was examined experimentally for rapidly rotating helicopter blades. The robustness of the approach to aspect angle variations has been demonstrated for a real micro-Doppler signal caused by a walking human.

Chapter 4

Machine learning techniques and feature selection

This Chapter introduces a brief overview of the main techniques of machine learning and performance evaluation of a decision making system used in the Thesis. In the Section V a problem of feature selection is considered. Then a new method called, Minimum Interference Maximum Information, is proposed and evaluated. The method is based on information criteria, and it ranks features according to the relevance for classification.

For successful radar target classification by machine learning approach, first, features should be extracted. Feature is a number, a value, that represents property of the object. Features must be extracted to contain most of the relevant information from the data, and be invariant to irrelevant information. Another idea behind feature extraction is transforming high-dimensional input radar data to low-dimensional space for faster convergence of the machine learning. For example, we want to classify different UAVs by spectrogram, if we will try to fit the whole spectrogram to machine learning algorithms, we will find that result could be not the best. This because the dimensionality of spectrogram is more than 20 000 points. Moreover, spectrogram contains irrelevant information such as an initial time shift, which will affect learning algorithm; imaging if we computed spectrogram 1 ms latter, than it will be shifted by 1 ms. Another irrelevant parameter could be power of the signal, because it is proportional to the distance from an object. And in order to have an effective machine learning we should add extra step, called feature extraction. Therefore, now instead of dealing with spectrogram we will deal with a feature vector - a number of features, see Fig. 4.1.

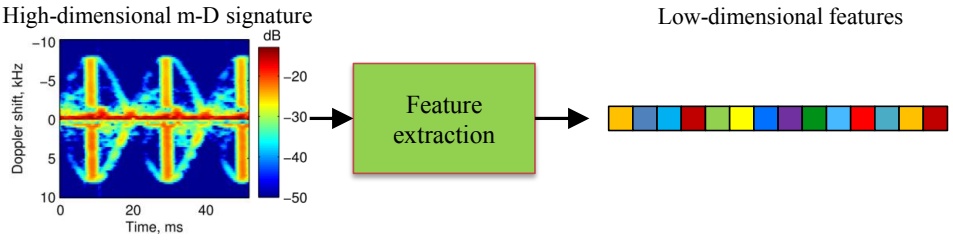

Figure 4.1: Feature extraction is a typical operation for machine learning. It is used to transform high-dimensional radar data into low-dimensional space, then features are used for classification, instead of radar data.

Features help people to make decisions. For example if we consider buying a house, than we look at parameters of an offer like price, place, condition etc. All these parameters are features which could be used by machine learning for a decision making. For radar target classification we are going to use features as well. They could link to physical parameters, like speed and size, or be artificial, like shape descriptors of Doppler spectrum etc. For a computer those two types of features are the same as it sees data by numbers, not by physical meaning.

By feature extraction we can resolve different problems for example make classification to be invariant to frequency band (Chapter 6), or to radar velocity, or to direction of the movement of the target. However, the "art" of feature extraction is to preserve as much relevant information as possible. For example if we want to make features to be invariant to all possible interferences, we could design feature extraction method which just multiplies radar data by zero, and for sure all irrelevant information is suppressed. However, it is straightforward, we will also lose all relevant information as well. Therefore, for feature extraction we should find a balance between removing irrelevant and preserving relevant information, and remember that with removing irrelevant information we lost some relevant as well.

After the features extraction step, features are separated by a classifier. Classifier is a set of logic, arithmetic operations and rules which can determine class label of the data. Process of defining rules and operations is called learning.

In radar target classification it is more important to have "good" features, and main research focus of research community is in this direction, rather than usage of different classifiers. In the Thesis we will compare results by several classifiers in order to show flexibility of the developed features.

I General notations for the Chapter

Assume given K objects, each of them is described by M different features $[1, ..., M]$, where a feature Z_j has k_j possible values, which for convenience we denote as $\{1, .., k_j\}$.

Let us define a data matrix X, having K columns (each represents an object) and M rows. Each object, k, is labelled with a class label, y_k, from the set $\{1, ..., k_y\}$. The number of classes is defined as C. We will also define a feature number j of an object k as $x_j^{(k)}$, such that it is true that $X_{:,j} = [x_j^{(1)}, ..., x_j^{(K)}]$.

We will use notations Z_j and x_j for a vector of the feature j, and $x^{(k)}$ for feature vector[1] k. By x we define a random feature vector.

II Dimensionality reduction

A) Linear discriminant analysis

Linear discriminant analysis (LDA) is a method of dimensionality reduction prior to the classification [50, 54, 100]. It finds a linear combination of features which separates classes.

Assume, that we have a C classes. First, a class covariance matrix S_{cc} must be computed of dimension $C \times C$:

$$S_{cc}(y_1, y_2) = \sum_{k=1}^{K} \left((x^{(k)})_{y_1} - \mu_i \right) \left((x^{(k)})_{y_2} - \mu_i \right)^T, \tag{4.1}$$

[1]Feature vector is a vector of all features associated to a particular object. Vector of a feature contains a set of values of the particular feature for different objects

where $(x^{(k)})_y$ is feature vector of object k of data associated with class y; μ_i is the mean vector of features for a class i.

Second, a between class covariance matrix is computed as:

$$S_{bc} = \sum_{i=1}^{C} (\mu_i - \mu)(\mu_i - \mu)^T, \tag{4.2}$$

where μ is the mean of class means.

Next, a matrix of eigenvectors V of product $S_{cc}^{-1} S_{bc}$ is calculated. The dimensionality of V is $M \times C - 1$.

Finally, a new training set is obtained applying the following transform onto all samples:

$$\hat{x}^{(k)} = V^T (x^{(k)} - \mu), \tag{4.3}$$

The same procedure is done for features from testing set.

III Decision making techniques

A) Statistical classifiers

Statistical classifier is a decision making technique which is based on the probability theory. The decision is based on the maximum of class conditional probability:

$$\hat{C} = \max_C P(C|x). \tag{4.4}$$

Naive Bayes classifier

A Naive Bayes classifier decides in favour of the class with the highest posterior probability, assuming that the features associated with each class are conditionally independent. Further reading include [50, 139].

Considering the Bayes' theorem and assuming the conditionally independent properties of features, the decision can be expressed as:

$$\hat{C} = \max_C P(C) \prod_{j=1}^{M} P(x_j|C), \tag{4.5}$$

where $P(C)$ is a prior probability of class C; $P(x_j|C)$ is the likelihood function.

The likelihood function $P(x_j|C)$ is estimated from the training data, assuming that x_j has normal distribution. Therefore each class is represented as the parameters of the Gaussian: vector of mean values, and covariance matrix.

Gaussian mixture models (GMMs)

Gaussian mixture models (GMM) could be used for likelihood function estimation and for classification when used together with maximum likelihood rule or similar [132, 133].

Generally, the GMM approximates the probability density function of a feature vector x as:

$$P(x|C) = \sum_{n=1}^{N} r_n \phi(x|\Lambda_{(C)}^{(n)}), \tag{4.6}$$

where N is the number of mixture components called the GMM order; r_n is the mixture weight of the n-th component, such that $\sum r_n = 1$; $\Lambda^{(n)}$ is the parameter referred to the distribution of component n; and $\phi(x|\Lambda^{(n)}_{(C)})$ is the probability distribution of x parametrized by $\Lambda^{(n)}_{(C)}$.

Each class C is described by a set of parameters $\Lambda^{(n)}_{(C)}$:

$$\Lambda_{(C)} = \{\Lambda^{(n)}_{(C)}\}_{n=1,\dots,N} = \{r^{(n)}_{(C)}, \quad \mu^{(n)}_{(C)}, \quad \Gamma^{(n)}_{(C)}\}_{n=1,\dots,N}. \tag{4.7}$$

These parameters are trained on the data from class C. For simplicity we will drop subscript (C) which indicates the class label.

The probability distribution of each component given in (4.6) can be written as

$$\phi(x|\Lambda^{(n)}) = \frac{(2\pi)^{-\frac{D}{2}}}{|\Gamma^{(n)}|^{\frac{1}{2}}} exp(-\frac{1}{2}(x-\mu^{(n)})^T \left(\Gamma^{(n)}\right)^{-1}(x-\mu^{(n)})) \tag{4.8}$$

where D is the dimension of the feature vector; $\Gamma^{(n)}$ is the covariance matrix of the component n; and $\mu^{(n)}$ is the vector of the mean values of component n.

There are few different ways of how to use covariance matrix, the simplest one is to use only diagonal elements of it, by using this technique trained time of ATR system is decreasing, but relationships of the different GMMs components are not considered, and as result worse quality of approximation is obtained. In this work full length covariance matrix is used.

Parameter estimation of GMM

Performing of unsupervised teaching is necessary to obtain parameters of GMM of data distribution. Expectation-maximization (EM) algorithm is used for this purpose [45]. The initial values for EM algorithm were generated by k-means algorithm. The main weakness of GMM is that a priori knowledge of the clusters' number is necessary. In this study the number of clusters is evaluated experimentally on the training data.

The idea behind parameter estimation of the GMM is to find parameters of the Gaussian mixture which will fit a given distribution. The final likelihood function of the training data X can be defined as:

$$P(X|\Lambda) = \prod_{k=1}^{K} P(x^{(k)}|\Lambda). \tag{4.9}$$

However, the estimation of likelihood function according to (4.9) is difficult due to non-linear dependence on the parameter Λ.

A set of parameters Λ could be estimated iteratively. The EM algorithm initializes with Λ (i.e. randomly or using unsupervised clustering like k-means) using an iterative algorithm estimates $\hat{\Lambda}$ using Expectation and Maximization steps:

E-step: Estimates the belongingness of the feature values to the components of the Gaussian mixture:

$$p(n|x^{(k)}) = \frac{r_n \phi(x^{(k)}|\Lambda^{(n)})}{\sum_{m=1}^{N} r_m \phi(x^{(k)}|\Lambda^{(m)})}, \tag{4.10}$$

where $\Lambda^{(n)}$ is a set of parameters for mixture model n.

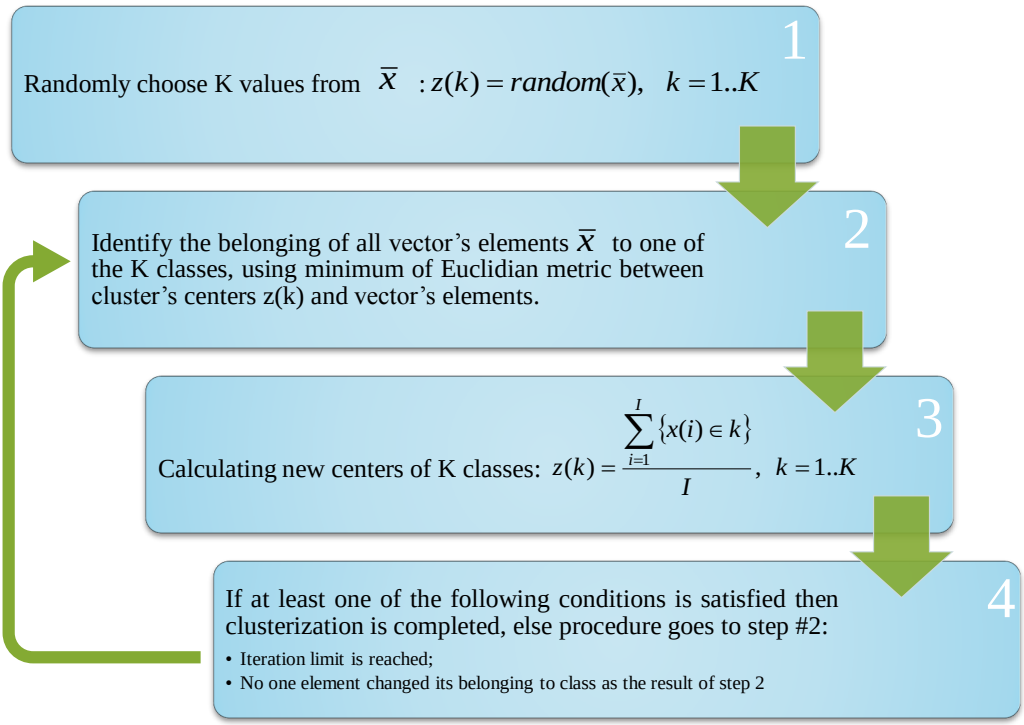

Figure 4.2: K-means clustering algorithm

M-step: Redefines the parameters of the components of the Gaussian mixture.

$$r_n = \frac{1}{K}\sum_{k=1}^{K} p(n|x^{(k)}); \tag{4.11}$$

$$\mu^{(n)} = \frac{\sum_{k=1}^{K}\left(p(n|x^{(k)})x^{(k)}\right)}{Kr_n}; \tag{4.12}$$

$$\Gamma^{(n)} = \frac{\sum_{k=1}^{K}\left(p(n|x^{(k)})(x^{(k)} - \mu^{(n)})(x^{(k)} - \mu^{(n)})^T\right)}{Kr_n}; \tag{4.13}$$

Initial values for EM-algorithm are obtained from the k-means clustering. The structure of k-means clustering is shown in Fig. 4.2.

The EM-algorithm is iterative, and it stops after a fixed number of iterations or when it convergences to global minimum (approximation error is too small).

Example of the GMM approximation is illustrated in Fig. 4.3. In this study we will use two stage algorithm for probability density function estimation $p(x|\Lambda)$. First, k-means algorithm is used to initialize parameters estimation Λ. Then using EM-algorithm the parameters Λ are iteratively updated to fit the distribution. This scheme has one disadvantage - the number of Gaussian functions must be known a prior. In the next chapters we will estimate this parameter using the training set.

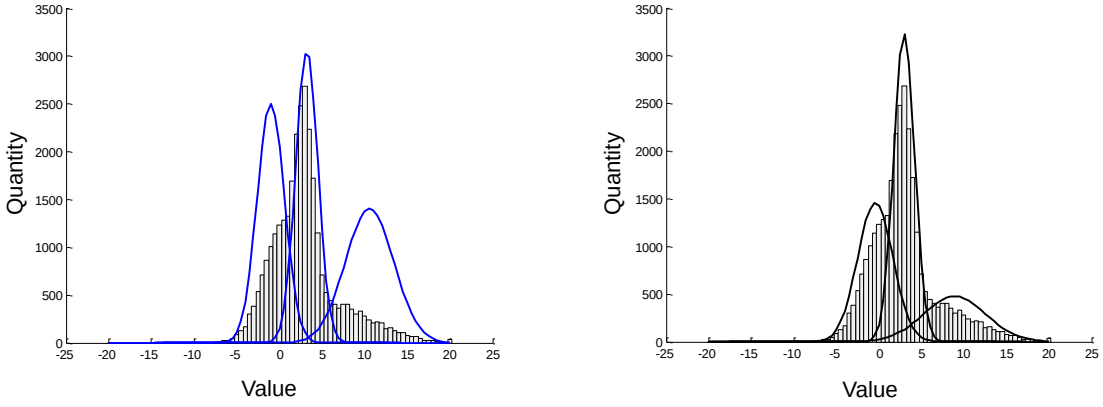

(a) K-means clustering result (b) GMM result

Figure 4.3: Probability density function approximation by a two stage algorithm. First initial estimate is obtained from K-means algorithm and then the final one by GMM.

B) Maximum likelihood decision rule

Commonly, the prior probability $P(C)$ from (4.5) is unknown and the equation is solved by maximizing the product of likelihood functions for GMM and naive Bayes classifier. Therefore, the decision rule is called the Maximum Likelihood (ML). The ML rule can be written as:

$$\hat{C} = \max_{C} \prod_{j=1}^{M} P(x_j|C). \tag{4.14}$$

For GMM the same decision making rule can be applied, in this case the likelihood function is approximated by Gaussian mixture:

$$\hat{C} = \max_{C} P(x|\Lambda_C), \tag{4.15}$$

where Λ_C are estimated parameters of the likelihood function for hypothesis of class C.

C) Support vector machine (SVM)

Support vector machine belongs to the non-probabilistic kind of binary classifiers [39, 169, 170]. In this study, we use the version of a support vector machine with soft margins proposed in [39]. Assuming the linearly separable classes, a hyperplane with maximal margins can be found to separate the classes with minimum error. The SVM can be extended to the multiple hypothesis classifier combining various SVMs using the one-against-one approach.

Assuming the training set of instance-label pairs $R_i = \{x_i, c_i \mid x_i \in \mathbb{R}^K; c_i \in \{1, -1\}\}$ is given, the support vectors are found by the solution of the following optimization problem:

$$\begin{aligned} \min_{w,b,\epsilon} \quad & \tfrac{1}{2} w^T w + S \sum_{i=1}^{I} \epsilon_i \\ \text{subject to} \quad & c_i(w^T \phi(x_i) + b) \geq 1 - \epsilon_i, \\ & \epsilon_i \geq 0, \end{aligned} \tag{4.16}$$

where ϵ_i is the degree of misclassification of the data x_i; w and b describe the separation hyperplane; S is the penalty parameter of the error term; $\phi(\cdot)$ is the function which maps the data x into a higher dimensional space.

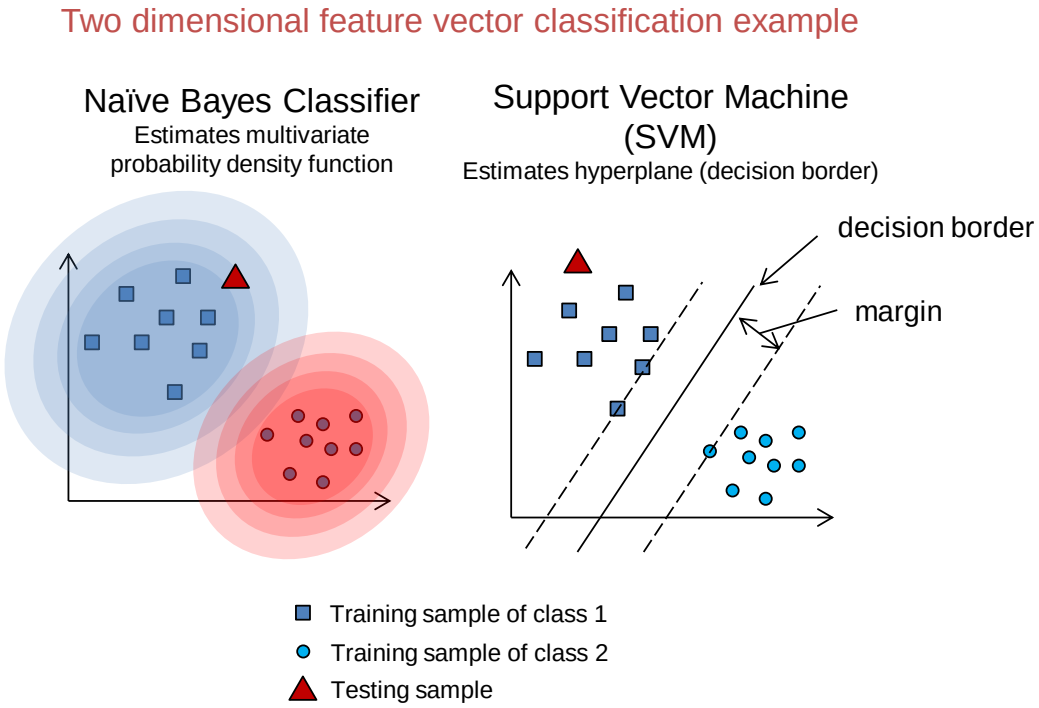

Figure 4.4: Classification by Naive Bayes Classifier (on the left) and SVM (on the right) for 2 dimensional feature space.

Actually, the SVM is a linear classifier. However, not all data are linearly separable in the data space. Therefore, the function $\phi(\cdot)$ is used for data mapping into a high dimensional space, where data is linearly separable with the minimum error (soft margin).

In this study, we use a radial basis function: $K(x_i, x_j) = exp(-\gamma||x_i - x_j||^2), \gamma > 0$. Thus, the function $\phi(\cdot)$ is selected to satisfy $K(x_i, x_j) = \phi(x_i)^T \phi(x_j)$.

A number of parameters are required to characterize the SVM classifier. The hyperplane which separates classes is described by a few support vectors (x_i). These selected support vectors are selected from the training set. The parameter γ of mapping function $\phi(\cdot)$, and the penalty parameter S are estimated using cross-validation procedure for the training set using grid search. The considered parameters of S are equal to $\{\exp(-5..5)\}$, and γ are $\{\frac{1}{2}\exp(2\sigma) \mid \sigma \in \{-4..4\}\}$.

D) Multilayer perceptron

Multilayer perceptron (MLP) is a machine learning technique which is inspired by a human brain [18, 68, 129]. The idea is that input data is mapped to the output by a set of layers, each layer contains activation functions (neurons) where input data distributed from minus infinity to plus infinity is transferred to range $[-1 \quad 1]$. It consists of an input layer (vector of features), a number of hidden layers, which define non-linear separation function of MLP, and an output layer (nodes with decision). The learning of MLP is a process of adapting parameters of neurons such that for input feature vector, required output will be obtained. Learning is done by a supervised method, when a number of input-output relations are given by means of training data.

MLP is very efficient on decision making process, however learning of the MLP is a very difficult problem [18]. Recently, the popularity of MLPs is increased because of advances in

GPUs which speed up the learning process.

In the Thesis, MLP is selected to be a feed-forward back-propagation Artificial Neural Network (ANN) with two hidden layers (ten neurons are contained in each hidden layer). Their transfer function is selected to be the tan-sigmoid. The output layer contains a number of nodes, correspond to a number of classes, with a purely linear transfer function. The mean squared error performance function is selected to estimate the ANN performance. The MLP is trained to estimate the class conditional posterior probability of the feature vector, such that for training data of the first class, the output of the first node is set to "1", others to "0"; then for training data from second class, the output of the second node is set to "1", where others to "0" and so on. These scheme is called one-against-all concept.

IV Techniques for performance evaluation

A) Probability of correct classification

The main evaluation parameter of a decision making system is a probability of correct classification. It is computed in percent as:

$$P = \sum_{c=1}^{C} \frac{Q_{cor}(c)}{Q_{total}(c)} p_a(c), \tag{4.17}$$

where C is the number of classes, $Q_{cor}(c)$ is the number of correctly classified objects referred to the class c; $Q_{total}(c)$ is the total number of tested objects referred to the class c, and $p_a(c)$ is a priori probability related to the class c. Unfortunately, it is impossible to evaluate a priori probability related to each separate class using experimental data. Because of this, we assume that each class has the same value of a priori probability. Therefore, the final formula takes the form:

$$P = \sum_{c=1}^{C} \frac{Q_{cor}(c)}{Q_{total}(c)}. \tag{4.18}$$

B) K-fold cross validation

The K-fold cross-validation technique is a technique for estimation of the classification performance (Fig. 4.5). The initial data under analysis are split into K subsets of the same length, and K-1 subsets are used as a training dataset, and the remaining one as a testing dataset. The cross-validation process is repeated K-1 times (K-1 folds) with each of the K subsets used as a testing dataset. The K results from the folds are averaged to get a single estimation. The cross-validation is applied in such a way that training and testing sets contain data from different trials(experiments). The cross-validation technique allows estimating the performance of the classification system under limited available data.

C) Confusion matrix

Commonly performances of classifier is analysed by confusion matrix. Table 4.1 shows an example confusion matrix for three classes. Confusion matrix shows the probability of declaring class c_j if input to the classifier was data with label c_i. Class label of the input data is shown on the left hand side of the matrix, whereas the declared class is listed at the top. The values on the main diagonal of the matrix show probability of correct classification when input class i is correctly

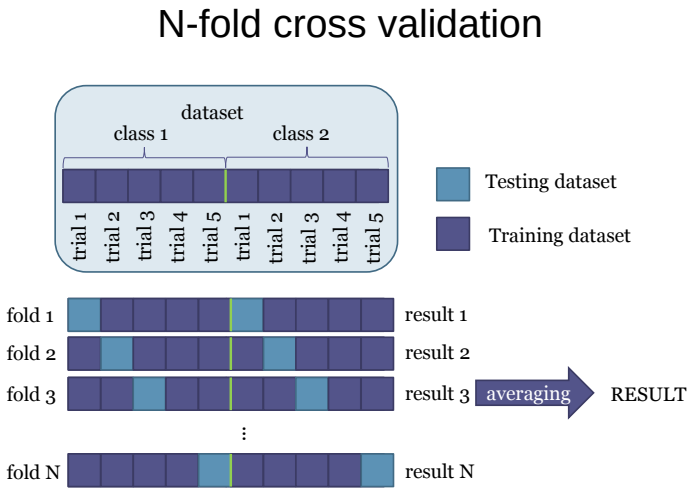

Figure 4.5: N-fold cross-validation as a method for performance estimation of a classification scheme for 2-classes problem

Table 4.1: An example of a confusion matrix

	Declared as		
Input	Class 1	Class 2	Class 3
Class 1	P_{11}	P_{12}	P_{13}
Class 2	P_{21}	P_{22}	P_{23}
Class 3	P_{31}	P_{32}	P_{33}

declared as i. Probability of classifying input data from class 1 being declared as class 1 in presents is defined as P_{11}. Probability of data from class 1 to be miss-classified as class 2 is defined as P_{12}.

V Feature selection by information-based criteria

In this Section, we present a new feature selection approach for supervised classification from discrete data, named as Maximum Information Minimum Intersection (MIMI). The proposed approach can work as a criterion for the filter based feature selection algorithm or as a prior stage for the wrapper. As a criterion function for feature ranking we will use Mutual Information (MI). Other information theoretic feature selection techniques have been proposed, e.g., see [67],[14] and [53].

The peculiarity of the proposed approach is estimating the probabilities involved in the criteria by weighting differently the data samples, according to their relevance to the classification problem. The proposed algorithm selects one new feature at each iteration based on their relevance, as measured by a weighted MI which also depends on a vector of weights, one for each data sample. After each iteration, this vector of weights is updated to account for the information just brought in by the new selected feature. The algorithm stops when none of the remaining features leads to a positive weighted mutual information.

Feature selection algorithms based on weight vectors have been already proposed [87, 153], where the weight vectors were applied for scaling each feature generating a weighted feature space. In contrast, in the proposed feature selection algorithm the weight vector changes the contribution

of each data sample when the conditional probabilities are estimated, accounting for the fact that the information added by a new feature is incremental, depending on the set of features which are already selected.

Our method is close in spirit with two well known approaches based on mutual information criteria: the Maximum Relevance (MR) and the minimum - Redundancy Maximum - Relevance (mRMR) [67], with which we compare our results in the experimental section. The MR approach ranks features based on the value of information contained about the class labels, without considering the possible correlation between the features. The mRMR introduces the concept of maximum relevance of a feature for a class label and ranks the features according to their maximum relevance and the mutual information between the already selected features and the considered one.

The section is organized as follows. In subsection A, a theoretical background of feature selection procedure based on the information theory is given. Next, in subsection B, the proposed approach is introduced and described. In subsection C, a comparison analysis is performed in order to evaluate the proposed algorithm.

A) Theoretical background

In this section we will use the terminology introduced in section I. Our goal is to find from the overall set of features, $\{Z_1, ..., Z_M\}$, a relevant subset of Q features $\{Z_{\gamma_1}, ..., Z_{\gamma_Q}\}$, with their indices collected in the vector γ, e.g., for the subset $\{Z_2, Z_4\}$ the index vector is $\gamma = [2\ 4]$. The relevant features will select out of the matrix X the submatrix $S = X_{\gamma,:}$ of data to be used for the classification task.

For each feature, Z_j, having an empirical entropy [40]:

$$H(Z_j) = -\sum_{l=1}^{k_j} p(l)\log(p(l)), \tag{4.19}$$

where the maximum likelihood estimate of the probability is

$$p(l) = \frac{\sum_{t=1}^{K} 1_{x_j^{(k)}=l}}{K} = \frac{n_l}{K},$$

and n_l is the count of symbol "l" in the vector $X_{j,:}$.

For the class label Y the available data is the vector $y = [y_1, ..., y_K]$ and the empirical entropy is:

$$H(Y) = -\sum_{b=1}^{k_y} p(b)\log(p(b)), \tag{4.20}$$

where

$$p(b) = \frac{\sum_{t=1}^{K} 1_{y_t=b}}{K} = \frac{n_b}{K},$$

and n_b is the count of symbol "b" in the vector Y.

The conditional entropy of Y given Z_j can be computed as

$$H(Y|Z_j) \quad = \quad \sum_{i=1}^{k_j} p(Z_j = i)H(Y|Z_j = i), \tag{4.21}$$

where $p(Z_j = i)$ is the estimated probability of having symbol "i" in the feature Z_j,

$$\begin{aligned} H(Y|Z_j = i) \quad &= -\sum_{b=1}^{k_y} p(Y = b|Z_j = i)\times \\ &\times \log(p(Y = b|Z_j = i)), \end{aligned} \tag{4.22}$$

and $p(Y = l|Z_j = i)$ can be computed from the counts of the joint event $x_j^{(t)} = i$ and $y_t = b$, for all $t \in \{1, ..., K\}$:

$$p(Y = l|Z_j = i) \quad = \quad \frac{\sum_{t=1}^{K} 1_{y_t=b} * 1_{x_j^{(t)}=i}}{K}.$$

The mutual information indicates the amount of additional information about the class label provided by the feature Z_j, and it can be given as [40]:

$$I(Y; Z_j) = H(Y) - H(Y|Z_j). \tag{4.23}$$

One can compute the I criteria values by (4.23) for all features Z_j and rank them from the highest value to the lowest. The rank of each feature will show the importance of the feature in solving the classification task. However, if one considers sets of features instead of one single feature, their joint effect on the class conditional distribution will be more subtle, and ranking will have to take into account joint distributions. In this vain, the relevant mutual information is given by:

$$\begin{aligned} &I(Y; S) = H(Y) - H(Y|S) = \\ &= H(Y) - H(Y|Z_{\gamma_1}, Z_{\gamma_2}, ..., Z_{\gamma_Q}), \end{aligned} \tag{4.24}$$

where Q is the predefined number of features to be selected.

The first term $H(Y)$ in (4.24) does not depend on a features, and can be computed easily. The second term can be expressed as:

$$H(Y|Z_{\gamma_1}, Z_{\gamma_2}, ..., Z_{\gamma_Q}) = \sum_{l_1}^{k_{\gamma_1}} ... \sum_{l_Q}^{k_{\gamma_Q}} p(Z_{\gamma_1} = l_1, ..., Z_{\gamma_Q} = l_Q) \times H(Y|Z_{\gamma_1} = l_1, ..., Z_{\gamma_Q} = l_Q), \tag{4.25}$$

where

$$H(Y|Z_{\gamma_1=l_1}, ..., Z_{\gamma_Q=l_Q}) = -\sum_{l=1}^{k_y} p(Y = l|Z_{\gamma_1=l_1}, ..., Z_{\gamma_Q=l_Q}) \times log(p(Y = l|Z_{\gamma_Q=l_1}, ..., Z_{\gamma_Q=l_Q})). \tag{4.26}$$

The total number of all possible subsets S, with a given parameter Q, is $\begin{pmatrix} M \\ Q \end{pmatrix}$, which is a huge number when M is large. As a result computing (4.24) for all possible subsets became a computational problem. Moreover, the multivariate density terms $p(Z_{\gamma_1} = l_1, ..., Z_{\gamma_Q} = l_Q)$ and $p(Y = l|Z_{\gamma_1=l_1}, ..., Z_{\gamma_Q=l_Q})$ in (4.25) and (4.26) tend to zero with increasing of Q, and the final value of $I(Y|S)$ becoming biased [154].

A number of techniques has been proposed in order to avoid high complexity of computing $I(Y|S)$ values for all possible subsets S. Some of these techniques are the incremental-based feature selection algorithms [67], [14], [53]. They are based on adding one more feature at each iteration. Also the proposed algorithm can be referred to this family of feature selection algorithms.

B) Proposed algorithm

In case of feature dependency, if some feature is selected then the entropy of the classes is reduced and, also, other features have different of previous values of conditional entropy. Therefore, if features provide a correlated information about the class label then a modified probability $\hat{p}_\gamma(y_k)$ should be computed instead of the simple probability $p(y_k)$, where γ is the vector of selected features' indexes.

Consequently we should rewrite (4.20) and (4.21) as:

$$\bar{H}_\gamma(Y) = -\sum_{b=1}^{k_y} \hat{p}_\gamma(b)\log(\hat{p}_\gamma(b)), \tag{4.27}$$

$$\bar{H}_\gamma(Y|Z_j) = \sum_{i=1}^{k_j} \hat{p}_\gamma(Z_j=i)\bar{H}_\gamma(Y|Z_j=i), \tag{4.28}$$

where

$$\bar{H}_\gamma(Y|Z_j=i) = -\sum_{b=1}^{k_y} \hat{p}_\gamma(b|Z_j=i)\log(\hat{p}_\gamma(b|Z_j=i)). \tag{4.29}$$

We define the conditional probabilities $\hat{p}_\gamma(b)$ and $\hat{p}_\gamma(Z_j = i)$ as:

$$\hat{p}_\gamma(b) = \frac{\sum_{k=1}^{K} D_k(\gamma)\times 1_{y_k=b}}{\sum_{k=1}^{K} D_k(\gamma)} \tag{4.30}$$

$$\hat{p}_\gamma(Z_j=i) = \frac{\sum_{k=1}^{K} D_k(\gamma)\times 1_{x_j^k=i}}{\sum_{k=1}^{K} D_k(\gamma)} \tag{4.31}$$

where $D \in [0,1]^K$ is a vector of weights which shows how much we are interested in improving the prediction of class label at object k, where each value D_k is between 0 and 1, as shown below. Now one can define the *weighted* mutual information criterion as:

$$wI(Y;Z_j,Z_\gamma) = \bar{H}_\gamma(Y) - \bar{H}_\gamma(Y|Z_j). \tag{4.32}$$

For a given set of features indexed by γ, the weighting vector D has the kth element given by

$$D_k(\gamma) = \prod_{j=1}^{Q}\left(p(Z_{\gamma_j}=X_{\gamma_j,k})\times\frac{H(Y|Z_{\gamma_j}=X_{\gamma_j,k})}{H(Y)}\right), \tag{4.33}$$

where $H(Y|Z_{\gamma_j}=X_{\gamma_j,k})$ is computed as in (4.22).

The reasoning behind the introduced weights is as follows. Assume that an already selected feature Z_j has a state $X_{j,k}$ which provides a complete information about the class label of the object k (it means that $H(Y|Z_j=X_{j,k})=0$). It will result that $D_k=0$ for object k and we are not interested in improving the prediction of class label for the object k. The value $D_k=0$ is obtained when the class label of the object k can be error-less predicted by the already selected

Algorithm 1 ; Maximum Information Minimum Intersection (MIMI) feature selection algorithm.
Input: $X = [x_1, ..., x_k] \in \mathbb{R}^{M \times K}$ {a matrix of training samples}
$Y \in \mathbb{N}^K$ {a class label vector}
Q_m {maximum number of features to be selected}
Output: $G \in \mathbb{R}^Q$ {vector of weighted mutual information criterion}
$\gamma \in \mathbb{N}^Q$ {indexes of selected features}
$Q \in \mathbb{N}$ {the number of selected features}

1: Discretize the columns of X to work with discrete data: $X \in \mathbb{N}^{M \times K}$
2: $D \leftarrow \mathbf{1}$ {the vector of weights $D \in [0\ 1]^K$}
3: $\gamma \leftarrow \varnothing$
4: $t \leftarrow 0$ {the number of already selected features}
5: Compute a vector of class conditional entropies $\bar{H}_{D(\gamma)}(Y|Z_j) \in \mathbb{R}^M$ by (4.28)
6: Compute weighted mutual information $wI \in \mathbb{R}^M$ by (4.32)
7: **if** $\max(wI) > 0$ **then**
8: $t \leftarrow t + 1$
9: **else**
10: $Q \leftarrow t$
11: go to step 19
12: **end if**
13: $G_t \leftarrow \max\left(wI(Y|Z_j, Z_\gamma)\right)$
14: $\gamma_t \leftarrow \arg\max_j \left(wI(Y|Z_j, Z_\gamma)\right)$
15: Update the vector of weights D by (4.33)
16: **if** $t < Q_m$ **then**
17: go to step 5
18: **end if**
19: **return** G, γ, Q

Table 4.2: Artificial data used for comparison.

Object		1	2	3	4	5	6	7	8	9	10	11	12	13	14	15
Class label		1	1	1	1	1	2	2	2	2	2	3	3	3	3	3
Feature #	1	1	1	1	1	0	0	0	0	0	0	0	0	0	0	0
	2	0	0	0	1	1	2	2	0	0	0	0	0	3	0	0
	3	0	0	0	0	0	2	2	2	2	0	0	0	0	0	0
	4	1	0	1	0	1	0	2	0	2	0	3	0	3	0	3
	5	0	0	0	0	0	0	0	0	0	0	0	3	3	3	3
	6	0	1	0	1	0	2	0	2	0	2	0	3	0	3	0
	7	1	1	0	0	0	2	2	0	0	0	3	3	0	0	0
	8	0	0	0	0	1	0	0	0	0	2	3	0	0	0	0
	9	1	0	1	0	1	0	2	0	2	0	3	0	3	0	3

Table 4.3: Values of weighting vector at different stages

Iteration	k														
	1	2	3	4	5	6	7	8	9	10	11	12	13	14	15
$D(\gamma = \varnothing)$	1	1	1	1	1	1	1	1	1	1	1	1	1	1	1
$D(\gamma = [4])$	0	0.4583	0	0.4583	0	0.4583	0	0.4583	0	0.4583	0	0.4583	0	0.4583	0
$D(\gamma = [4\ 6])$	0	0	0	0	0	0	0	0	0	0	0	0	0	0	0

features. The range of D_k is $[0, 1]$, where the value 1 is taken only at Step 0, when the set of features is empty. The algorithm is iterative, and after the feature selection on each iteration, the vector of weights D_k is updated by (4.33).

The initialization of the feature selection procedure should be done before the procedure starts, and the values of D_k should be defined. When the procedure starts there is no information available about the class labels and all elements of D are equally set to the maximum value, 1.

The procedure stops when none of the wI values (4.32) is larger than zero, what means that no additional information can be given by the remaining features.

The feature selection procedure, proposed in this paper, works only with discrete input values, and thus, before being applied to continuous data discretization should be performed.

Assume that the algorithm has selected $m-1$ features explained by a $\gamma \in \mathbb{N}^{m-1}$, then by the following equation the m-th feature with the index j^* is selected:

$$j^* = \arg\max_j (wI(Y; Z_j, Z_\gamma)). \tag{4.34}$$

The pseudo code is given in Algorithm 1 in order to detail the structure of the proposed method. The computational complexity of the iteration-based maximization (4.34) is $\mathcal{O}(Q \times M)$.

C) Comparative analysis

Algorithms

One of the simplest feature selection methods is called a maximum relevance (MR), it is based on mutual information. A new feature with index j^* is selected as:

$$j^* = \arg\max_j \big(I(Y|Z_j)\big). \tag{4.35}$$

According to the review in recent research in future selection field [93], the mRMR [67] algorithm is similar to the proposed one. The mRMR selects a feature wich maximazes the maximum relevance as well as minimazes the dependence with already selected features. The computational complexity of mRMR is $\mathcal{O}(Q \times M)$; which is exactly the same as for MIMI.

The mRMR maximizes the following criterion:

$$J(j) = (I(Y|Z_j) - \frac{1}{Q}\sum_{i=1}^{Q} I(Z_{\gamma_i}|Z_j), \tag{4.36}$$

and the feature with index j^* is selected:

$$j^* = \arg\max_j(J(j)). \tag{4.37}$$

It should be noticed, that if $\gamma = \varnothing$ (no features have been selected) then all three considered methods (MR, mRMR and MIMI) will provide the same result by (4.35).

Simulated data

To demonstrate how does the proposed algorithm work and how it differs from the others we consider the data[2] which is shown in Table 4.2. We will compare results of mRMR, MR approaches and the proposed one, MIMI. The task is to rank features #1-9 according to contained information about the class labels. We will use a trick, as one can see the features #4 and #9 take the same values.

The results of feature selection algorithms of data from Table 4.2 are listed in Table 4.4. The MR approach deals with the maximization of (4.35), and ranks features according to the I value, this approach doesn't take into consideration possible correlation of provided information by the features. As a result, according to the MR, the features #4 and #9 have the same importance for a classifier, but this is irrelevant because they provide exactly the same information. If only the feature #4 is used for self classification then the classification error will be 26.7 % (using any non-probabilistic based classifier); for error-less classification, according to MR, top three features are required: #4, #9, #6. The mRMR takes into account feature dependencies, and thus, features #4 and #9 have different importance. To self classify error-less the data in Table 4.2, the classifier should know the states of at least three features #4, #1 and #5 from rank list of mRMR, knowing just two of them (#4 and #1) will lead to classification error at level of 20 %. Considering the last approach, the MIMI, we can see only two selected features (#4 and #6.) The knowledge of the states of these two features is enough to classify correctly the class labels. The mRMR and the MIMI are iterative algorithms and thus slower than the MR. It should be noticed that the feature #6 has rank 2 by the MIMI but has large wI value than the feature #4, this can be

[2]The values of features are changed to be in region [0 3] rather than [1 4] for better visual perception

Table 4.4: Results of feature ranking and selection of data provided in Table 4.2

	MR		mRMR		MIMI	
Rank	I	Fea. #	J	Fea. #	wI	Fea. #
1	0.859	4	0.859	4	0.859	4
2		9	0.346	1	1.557	6
3	0.753	6	0.399	5		
4	0.634	7	0.399	3		
5	0.596	1	0.325	7		
6	0.596	5	0.282	6		
7	0.596	3	0.191	2		
8	0.538	2	0.219	9		
9	0.317	8	0.068	8		

Table 4.5: Data sets used in comparison analysis

Name	Multiple Features	The CMU PIE	AR	Arrhythmia	PCMAC	Lymphoma
Acronym	HDR	PIE	AR	ARR	PCMAC	LYM
Source	[55, 164]	[148, 180]	[101, 180]	[55, 66]	[91, 180]	[4]
Data type	handwritten numerals	images of faces	images of faces	medicine	text	gene
Instances	2000	210	130	452	1943	96
Attributes	649	2420	1000	279	3289	4026
Classes	9	10	10	16	2	9
Raw data type	real	integer	integer	real	integer	real
Preprocessing	discretized to 10 levels				-	discr. 3-states
Testing method	10-fold CV		LOOCV	10-fold CV		LOOCV

explained by iteration structure and by the fact that if classifier knows the states of feature #4 then with knowledge of the feature #6 classifier will know exactly the class labels of seven remain instances. In the considered example the MIMI worked as *filter* based *feature selection* approach.

Table 4.3 shows the values of weight vector D for all time samples depending on the set of already selected features γ.

Real data

After the experiments on the artificial data we consider a real-world data. First, we compare the sequential feature selection by the considered algorithms. For those tests, classification error is computed given the same number of selected features by different algorithms. Then, we compare classification accuracy given by wrappers whereas the initial subspace of features is selected by one of the algorithms.

Data sets. The six data sets corresponded to different types of data are used in experiments. They are widely used in feature selection studies [60, 67].

The CMU Pose, Illumination, and Expression data set [148] (PIE) contains images of faces captured in different situations and illumination. The total number of instances is 210, the number of features is 2420, the data is collected for 10 subjects (classes). The data set is a part of ASU repository [180]. A raw data, discrete 8 bit, were discretized to be 10 states.

The AR data set [101], denoted as AR, contains 210 images of faces of 10 subjects, each image is stored in 1000 integer values. The original data set has 2400 features represent each image, however, we use only first 1000 in experiments. The values were discretized to 10 levels. The data set is used in ASU benchmark [180].

The PCMAC dataset is generated from 20 newsgroups collection [91] and contains data from text records. The data set has 1943 instances with feature dimension of 3289 extracted for two classes. The data set as well as a source link are available at [180]. Each feature vector has less than 10 states and no discretization is applied.

The Multiple Features [164] data set, denoted as HDR, contains features extracted from the handwritten numerals "1"-"9". The data set has 9 classes and 2000 instances, each of them is represented by 649 attributes. The HDR is a part of UCI repository [55]. The raw data were discretized to be 10-state.

The Arrhythmia data set [66], denoted as ARR, contains data to detect the presence of cardiac arrhythmia and classify it in one of the 15 groups. The number of instances is 452 described by 279 features. Discretization is applied on raw data to be 10-state.

The Lymphoma data set [4], denoted as LYM, consists of DNA microarray measurements of nine human lymphoma types. A set of 4096 genes forms feature vectors which are available for 96 tests (instances). The raw data is discretized as 3 states.

The selected data sets allow performing experiments on data with huge range of features and instances. In some data sets the number of instances is bigger than the number of attributes, e.g. HDR. As well we consider data sets where the number of attributes exceeds significantly the number of samples (instances), such as in LYM data set.

The experiments are performed in different ways depending on the number of instances. For the data sets with less than 150 samples, such as AR and LYM, we apply Leave One Out Cross-Validation (LOOCV); for the others we apply 10-fold Cross-Validation (CV) repeated 100 times. The CV works in the following way. The initial data under analysis are split into K=10 subsets of the same length, and K-1 subsets are used as a training dataset, and the remaining one as a testing dataset. The cross-validation process is repeated K-1 times (K-1 folds) with each of the K subsets used as a testing dataset. The K results from the folds are averaged to evaluate a single estimation.

Comparison platform. All results shown bellow are obtained on MATLAB operating in 64 bit UNIX environment.

To perform analysis we use the Support Vector Machine (SVM) with soft margins implemented in [27]. For the SVM the radial basis function kernel is selected and a grid search method is applied for optimal parameter estimation.

During the CV procedure a data set is divided onto training and testing sets, and all feature selection algorithms are applied on the same data division.

Sequential feature selection. In this subsection we will compare the proposed feature selection algorithm with mRMR and MR in terms of obtained classification error with the selected feature subspaces of a fixed length. The number of features to be selected varies from 1 to 50 and the classification error is computed for selected feature subspaces.

Fig. 4.6 shows results of sequential feature selection and classification computed by 10-fold CV.

For the HDR data set, Fig. 4.6a demonstrates the error rate obtained with different feature dimension. Features selected by mRMR outperform those by MR and MIMI. On the same time

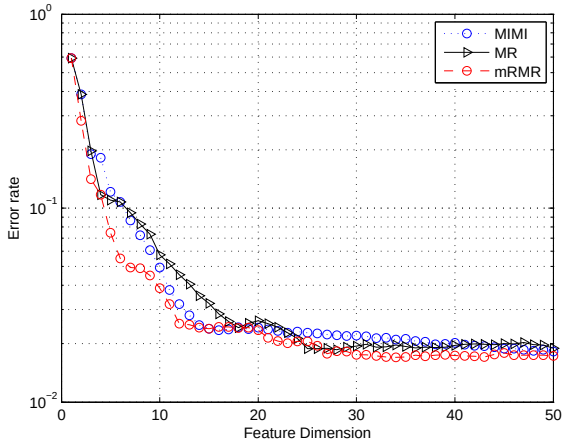

(a) HDR

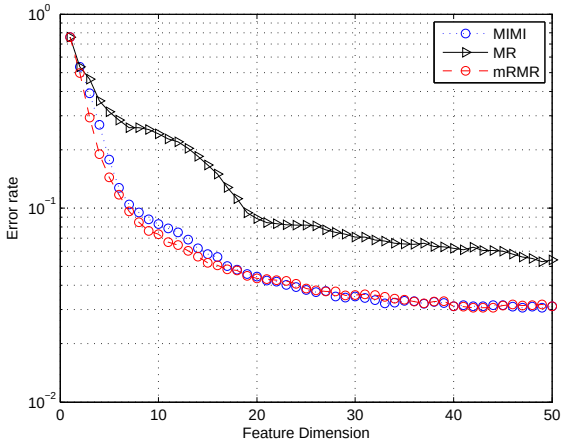

(b) PIE

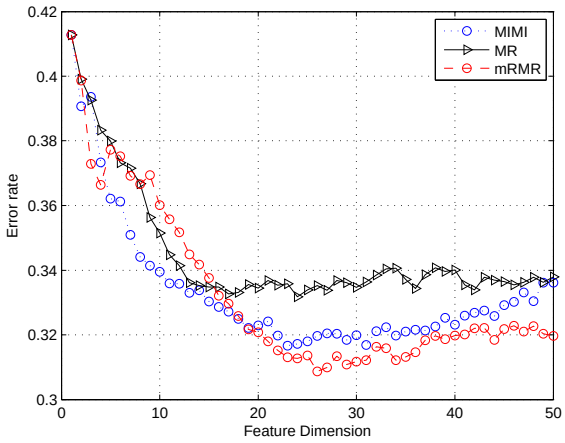

(c) ARR

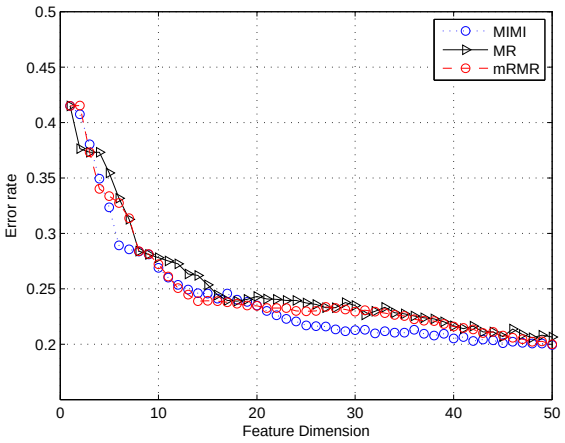

(d) PCMAC

Figure 4.6: 10-fold CV error rate on HDR (a), PIE (b), ARR (c) and PCMAC (d) data sets using MIMI, mRMR and MR features.

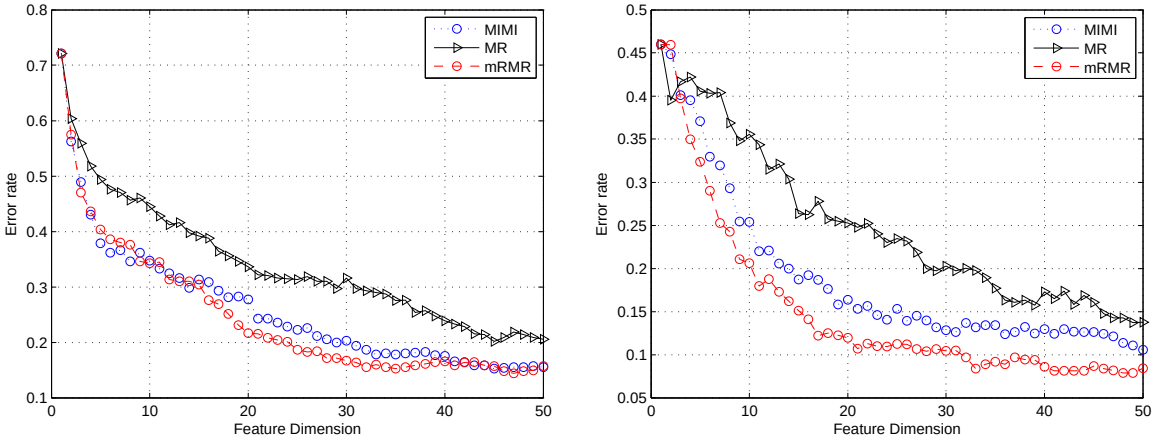

(a) AR (b) LYM

Figure 4.7: LOOCV error rate on AR (a) and LYM (b) data sets using MIMI, mRMR and MR features.

MIMI shows comparable results with MR. The lowers error achieved by MIMI features is 1.82%, by mRMR is 1.70% and by MR is 1.86%.

Fig. 4.6b shows error rates computed for PIE data set. Features selected by MIMI outperform those by MR at all ranges of feature dimension. The errors by MIMI and mRMR are comparable and very close to each other. The lowest error by MIMI features is 3.07%, by mRMR is 3.07% and by MR is 5.3%.

The results of 10-fold CV on ARR data set are shown in Fig. 4.6c. MIMI shows the best performance when feature number is from 5 to 19, then mRMR start to overcome. The lowest errors for ARR data set are: 31.67% by MIMI, 32.31% by mRMR and 33.18% by MR.

Fig. 4.6d shows error rates computed for PCMAC data set. Features selected by MIMI outperform those by MR and mRMR at all ranges of feature dimension. The level of benefit reaches 2 % for 29 features. The lowest error by MIMI features is 19.9%, by mRMR is 19.9% and by MR is 20.6%.

Error rates of LOOCV for AR and LYM data sets are shown in Fig. 4.7a and 4.7b. For AR data set, MIMI and mRMR features attain lower error rates than those by MR. All features show close result with feature dimension more than 42. Comparing mRMR and MIMI features we note that the performances are similar, however mRMR show better result.

For LYM data set results of LOOCV are shown in Fig. 4.7b. MIMI outperforms MR with features to be selected more than 2. However, we can notice that mRMR outperforms out method, MIMI, for any number of features. This makes MIMI to be in the middle between MR and mRMR.

Results in this section indicate that, for sequential feature selection, MIMI features outperform those by MR with significant advantage. They also show that MIMI is comparable to mRMR. However, for most of the datasets mRMR outperforms MIMI features.

Compact feature subsets selection The wrappers can be used to find a compact feature subset from the candidate features. The candidate features are selected from available data by different feature selection algorithms. The forward and backward schemes of wrapper are applied to calculate CV classification error. The length of candidate features subspace is selected to be

Table 4.6: Error rates (%) obtained by wrapper feature selection. Smaller is better

Data set	Approach	Wrapper	
		Forward	Backward
HDR	MIMI	2.33	1.97
	mRMR	**2.32**	**1.78**
	MR	2.47	1.95
PIE	MIMI	4.28	**3.07**
	mRMR	**3.99**	3.36
	MR	8.34	5.79
AR	MIMI	**29.75**	16.26
	mRMR	29.76	**15.98**
	MR	32.77	22.65
PCMAC	MIMI	21.41	**20.4**
	mRMR	**20.02**	20.72
	MR	21.79	20.89
LYM	MIMI	13.72	14.95
	mRMR	**8.32**	**14.67**
	MR	21.16	19.06
ARR	MIMI	33.31	33.02
	mRMR	**33.04**	**32.00**
	MR	33.85	33.53

maximum 50 features, as the previous section shows that classification errors are stable there.

Results of CV by forward and backward wrapper schemes are shown in Table 4.6. Feature selection of the wrappers is performed on training set by 2-fold CV.

We can notice that for 11 scenarios out of 12, MIMI based wrapper outperforms the one based on MR, only for HDR dataset and backward wrapper, the result is worse. Comparing to mRMR, MIMI shows better result only for 3 scenarios, for others, results are comparable. For cases when mRMR shows better result, the difference is near 0.3 %, and only for forward wrapper and PCMAC and LYM datasets, the difference is higher: 1.39% and 5.4% respectively.

Results in this section indicate that MIMI features provide the comparable performance for compact feature subset selection using both forward and backward wrapper schemes to state-of-the-art mRMR method, and outperform MR based method.

VI Summary

In this Chapter we briefly discussed the machine learning techniques used in the Thesis to build an intelligent radar systems. Then, we overview several methods used for performance evaluation of a decision making system.

In the second section we presented a novel approach for feature selection in task of classification. Given comparison analysis on real and artificial data shows the benefits of the proposed algorithm under the MR and mRMR approaches. The results obtained on simulated data show the difference between the approaches and a peculiarity of the proposed one. Experiments on the real data have been performed in terms of sequential and compact feature selection. Re-

sults of sequential feature selection have shown that MIMI features provide comparable result to mRMR features, and outperform MR based methods. Results obtained in compact feature selection by wrapper schemes indicate the advantage of the proposed algorithm over MR. The best performance is achieved in 3 cases out of 12, for others showing comparable results with mRMR.

Feature selection approach developed in this Chapter will be used in further ATR system.

Chapter 5

Bispectrum-based features

In this Chapter we will perform higher-order spectrum analysis on radar data. In the Section I, background of higher order spectral techniques is introduced and it is shown that phase information of the short-time Fourier transform is useful for radar target analysis. Section I contains definitions and introduction of bispectrum and bicoherence estimates, definitions of frequency and phase coupling. Then bispectrum and bicoherence analysis is performed on real and simulated continuous wave radar data of human walking.

In Section II a practical usage of bispectrum-based features in ATR system is discussed. Results on experimental real radar measurements demonstrate that it is quite feasible to distinguish three classes of humans (single, two and three persons) walking in a vegetation cluttered environment using novel bicepstrum-based classification features for data collected by continuous wave radar, where no range information is available.

In Section III a novel bicoherence-based method for the classification of aerial radar targets in ATR systems is proposed. The performance of the classification method developed is compared to the performance of common methods using high-resolution radar range profiles (HRRPs). The benefits achieved by using bicoherence-based classification features are demonstrated and discussed.

I Higher order spectral techniques

The majority of signal processing techniques developed for automatic target recognition (ATR) in surveillance radar systems are based on the second-order statistics estimation [19, 20, 47, 166]. In recent years, researchers are working on development of new informative features that are based on higher-order statistics analysis [10, 163]. One of the contributions of the thesis is in the development of an ATR system with features extracted using higher-order spectral techniques.

First, we will analyse frequency and phase coupling phenomena in application for micro-Doppler time-frequency analysis aimed for ATR radar systems. We will investigate these phenomena by using simulated backscattering, as well as real data measured by microwave surveillance Doppler radar.

Frequency coupling phenomenon is provoked by relations between harmonics contained in a multi-frequency process. Assume that the following multi-frequency process $s_1(t)$ is given as:

$$s_1(t) = \sum_{i=1}^{6} \cos(2\pi f_i t), \tag{5.1}$$

where f_1, f_2, f_4, f_5, f_6 are normalized frequencies, and $f_3 = f_1 + f_2$, i.e. the frequencies f_1 and f_2 are exhibit to be of frequency coupling.

Spectrum of the signal $s_1(t)$ shows the distribution over complex basis, and can be computed by the Fourier transform:

$$S(f) = \sum_{t=1}^{T} s_1(t) e^{-2\pi f t/T}, \tag{5.2}$$

where frequency index is $f = 1, \ldots, T$.

Power spectrum density allows to estimate energy distribution of the signal per frequency unit:

$$P(f) = S(f)S^*(f), \tag{5.3}$$

where * denotes complex conjugation

Conventional power spectral density $P(f)$ of the signal $s_1(t)$ contains contributions of all six frequencies in the form of six peaks observed in spectral domain. However, information referred to frequency coupling given in the signal $s_1(t)$ in the form of $f_3 = f_1 + f_2$ cannot be extracted from power spectral density $P(f)$. Therefore, it is impossible to answer the question by analysing the power spectrum $P(f)$: what spectral components in considered process are independent between each other and what frequencies are coupled?

As opposed to power spectral density, third-order spectrum called bispectrum is able to estimate the presence of frequency and phase coupling (will be introduced latter). In order to estimate frequency coupling contained in a process under study we should calculate the amplitude bispectrum (bimagnitude) $B(p, q)$ [123]:

$$|B(p, q)| = |S(p)||S(q)||S(p + q)|, \tag{5.4}$$

where $|S|$ indicates the magnitude extraction operation, $p = 0, \ldots, 2\pi$, $q = 0, \ldots, 2\pi$ such that $p + q \leq 2\pi$.

If harmonics f_1 and f_2 are frequency coupled then bimagnitude, B_m, will have only single peak located at the coordinates (f_1, f_2) in bifrequency plane.

One more interesting phenomenon which could be observed in the radar signal is a phase coupling. Assume that the following multi-frequency process is given:

$$s_2(t) = \sum_{i=1}^{6} \cos(2\pi f_i t + \phi_i), \tag{5.5}$$

Where f_1, f_2, f_4, f_5 are normalized random frequencies;$f_3 = f_1 + f_2$ and $f_6 = f_4 + f_5$; $\phi_1, ..., \phi_5$ are the initial phases that are supposed to be independent identically distributed random values varying within the interval of $[0,\ 2\pi]$ with the exception of phase coupling given as $\phi_6 = \phi_4 + \phi_5$. Frequency pairs f_1 and f_2, as well as f_4 and f_5 are frequency coupled. However, only frequency pair f_4 and f_5 is phase coupled.

The information about phase coupling is totally lost in power spectrum, because it does not contain information about the phase of a signal. Bispectrum estimate $B_t(p, q)$ for short-time period t contains information about phase coupling and it can be computed as:

$$B_t(p, q) = S_t(p)S_t(q)S_t^*(p + q), \tag{5.6}$$

S_t denotes Fourier transform of a signal correspond to short-time period t.

Bimagnitude $|B_t(p, q)|$ computed for process (5.5) tends to zero within the whole bifrequency plane apart from the single peak located in the frequency coordinates point of $(f_4,\ f_5)$. Therefore,

bispectrum can serve as the sensitive indicator of phase coupling. In other words, bispectrum is capable to emphasize the strong, i.e. phase coupled spectral components and, at the same time, suppress the contribution of weak, i.e. phase independent spectral components that are usually related to the interference in real-life signal processing.

Bispectrum estimate obtained by (5.6) together with information about frequency and phase coupled pairs contains all other components. These components have smaller amplitude, however, still exist due to the limited observation time.

In order to extract the information about phase coupled components only, another measure must be used, called bicoherence. The squared bicoherence is the quantitative measure of *phase coupling* [123]. The squared bicoherence $\hat{b}^2(p,q)$ can be interpreted as the proportion of signal energy at the frequency $(p+q)$ which is coupled to the spectral components at p and q as:

$$\hat{b}^2(p,q) = \frac{\left| \frac{1}{T} \sum_{t=1}^{T} B_t(p,q) \right|^2}{\hat{X}(p,q)\hat{P}(p+q)}, \tag{5.7}$$

where $\hat{P}(p+q) = \frac{1}{T} \sum_{t=1}^{T} \left| S_t(p+q) \right|^2$ is the power spectrum estimate averaged over T finite data samples; $\hat{X}(p,q) = \frac{1}{T} \sum_{t=1}^{T} \left| S_t(p) S_t(q) \right|^2$.

The bicoherence (5.7) takes values contained within the limits of $[0,1]$. If $\hat{b}^2(p,q) \neq 0$, some phase coupling related to the frequencies p and q will exist, but if $\hat{b}^2(p,q) = 0$ there is no phase coupling.

Phase coupling phenomenon regarding radar backscattering caused by moving human can be explained as follows. Both translation locomotion of human torso and swinging motion of legs and arms are not independent sources of Doppler frequency shifts because these human body parts are mechanically related between each other through the common "carrier", i.e through the human torso. Therefore, squared bicoherence 5.7 can serve us as a prospective and effective measure of phase coupling contained in the backscattering measured by Doppler surveillance radar and used for moving radar target classification.

Thus, extraction of target classification features by using bicoherence estimation makes possible to measure a novel class of statistical relations between Doppler instantaneous frequencies (IFs). Bicoherence can serve as a useful measure aimed for detection of interactions between spectral components and eliciting information on phase coupling. Furthermore, important feature of bispectrum referred to its low sensitivity to additive white Gaussian noise (AWGN) must be taken into account for ATR systems. It is well-known [123] that bispectrum tends to zero value for a zero-mean AWGN. It means that there are no phase coupled frequencies in a linear Gaussian process. Therefore, discrimination of phase coupled Doppler IFs from those that are not can be effectively provided by bicoherence estimation. In real-life situations, radar echo-signals are severely corrupted by AWGN of a priori unknown covariance. Signal-to-noise ratio (SNR) at the input of a radar receiver can vary within wide range and rate depending upon target velocity towards or away from radar, as well as time-varying characteristics of vegetation clutter. In such situation, performances of optimal signal processing technique based on estimation of information feature in the form of common second-order statistics, i.e. power spectra and correlation functions degrades. Hence, bicoherence estimation is a promising technique for ATR radar systems, firstly, due to the possibility of considerable suppression of AWGN in TFD and, secondly, extracting robust target classification features.

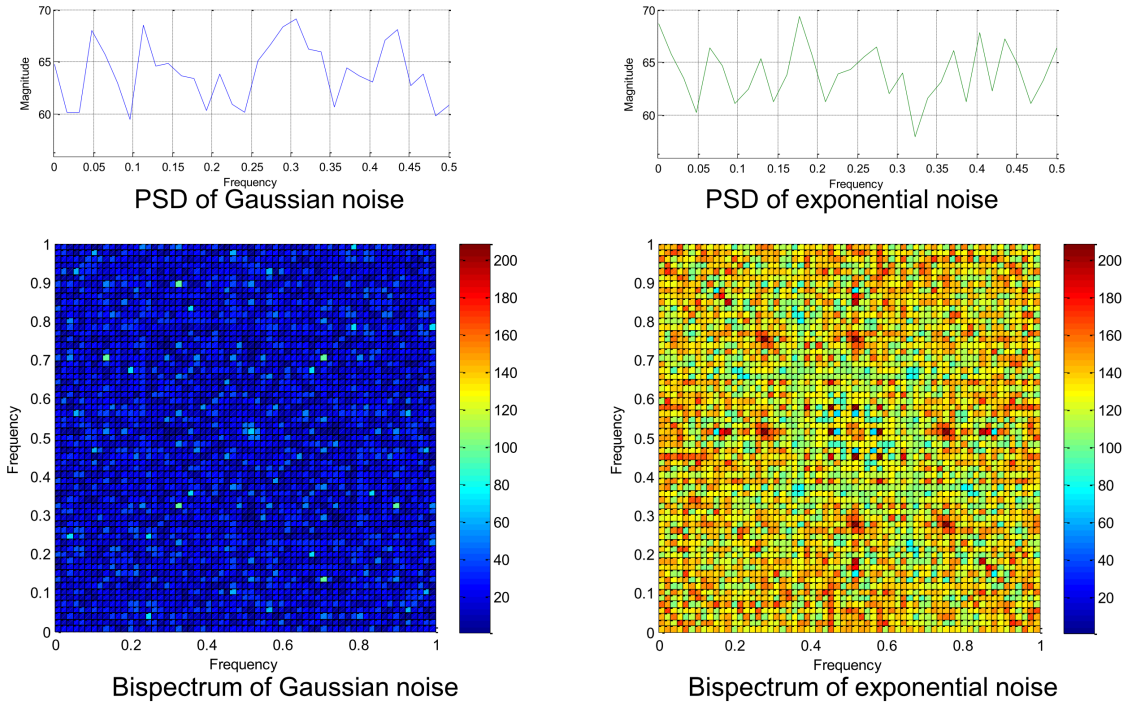

Figure 5.1: Analysis of random distributions by power spectrum density (top) and bispectrum (bottom).

To verify the noise robustness property of bispectrum we provide the following experiment. Let's assume given two random signals with different distributions: $\epsilon_{Gaussian}$ - white Gaussian noise, and ϵ_{exp} - exponential noise. Two signals have zero mean and unit variance. A set of $M = 256$ segments of realizations are generated, with length of $L = 64$ samples. First power spectrum densities are averaged over M segments. On the same time bispectrum estimates computed by 5.6 and averaged over M segments. The resulting power spectrum densities and amplitude of bispectrums are shown in Fig. 5.1. As it can be seen averaged bispectrum estimate tends to zero for Gaussian noise, where as power spectrum densities are of the same shape.

Quadratic phase coupling is a property of system arises when the system's input-output relation could be written as:

$$y(t) = s(t) + s^2(t), \tag{5.8}$$

where $s(t)$ is a multi harmonic signal. Let us assume, for example:

$$s(t) = \sum_{i=1}^{2} cos(2\pi f_i t + \phi_i) \tag{5.9}$$

Then according to (5.8), the output of the system will be:

$$\begin{aligned} y(t) = &\cos(2\pi f_1 t + \phi_1) + \cos(2\pi f_2 + \phi_2) + 1 + 0.5\cos(4\pi f_1 t + 2\phi_1) + \\ &+ \cos(2\pi(f_1 + f_2)t + (\phi_1 + \phi_2)) + \cos(2\pi(f_1 - f_2)t + (\phi_1 - \phi_2)) + \\ &+ 0.5\cos(4\pi f_2 t + 2\phi_2). \end{aligned} \tag{5.10}$$

Since relations between phases arise from quadratic non-linearity in the signal production mechanism (5.8), the signal (5.10) is said to exhibit *quadratic phase coupling.*

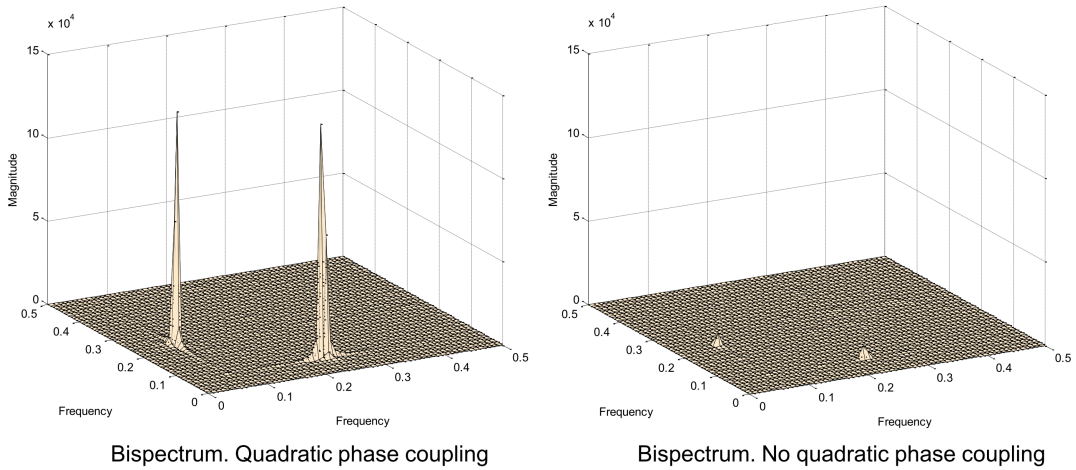

Figure 5.2: Analysis of phase coupling by bispectrum analysis. Amplitude estimates are shown for signal with phase coupling (left) and without (right).

In the next example we will test the property of emphasizing phased coupled components by bispectrum analysis. The signal of the following form is generated: $s_3(t) = \sum_{i=1}^{3} cos(2\pi f_i t + \phi_i)$, f_1, f_2 and ϕ_1, ϕ_2 are selected to be random, $f_3 = f_1 + f_2$. We will distinguish two types of signals:

signal with phase coupling: $\phi_3 = \phi_1 + \phi_2$;

signal without phase coupling: ϕ_3 is random.

A total of 256 segments of length of 128 samples are generated, the resulting amplitude of bispectrum estimates are shown in Fig. 5.2. From the Fig. 5.2 it follows that signal with phase coupling generates peaks of high amplitude. Please note that two peaks are present due to the symmetric properties of the bispectrum [179].

A) Geometrical interpretation of frequency and phase coupling phenomenon in radar returns

Frequency and phase coupling are properties of the signal. In radar terminology they could be explained in terms of geometrical interpretation. We will introduce the minimum required experimental set-up to generate a radar return with frequency and phase coupling phenomenon. We will consider continuous wave radar principle only, but it could be extended to pulse radar with high pulse repetition frequency.

Frequency coupling phenomenon arises when there are frequency coupled components in the spectrum of the signal. If we are looking for continuous wave radar than that means that radial velocities must be coupled. Fig. 5.3 shows two scenarios for which frequency coupling could exist. The scene should contain at least two scatterers which are moving with velocities v_1 and $v_2 = 2v_1$[1]; this will make the reflected signal to contains two frequency components f_1 and $f_2 = 2f_1$, see Fig. 5.3a. The latter relation will result in a peak of bispectrum estimate at frequencies (f_1, f_2). Another scenario for a frequency coupling to arise will be three scatterers with the following speeds: v_1, v_2, and $v_3 = v_1 + v_2$, see Fig. 5.3b. If such a regularity can be found than the frequency coupling is exist.

[1]In this subsection we will denote velocity as a projection onto the radar line-of-sight (radial velocity).

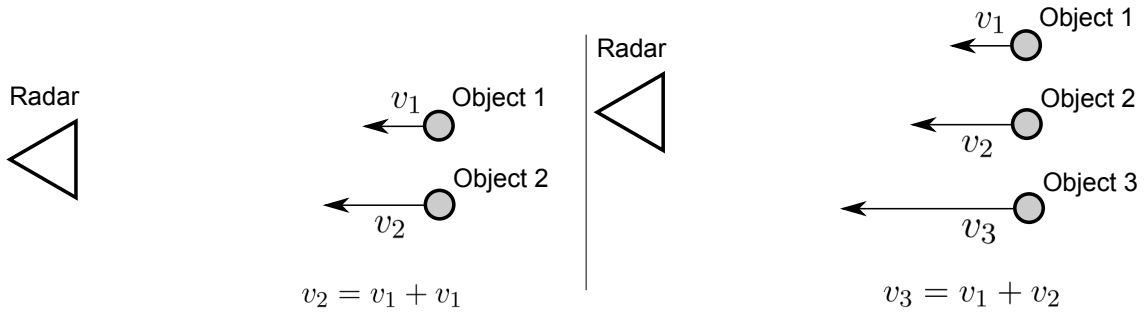

(a) Scenario with 2 scatterers (b) Scenario with 3 scatterers

Figure 5.3: Scenarios for frequency coupling to exist.

Phase coupling is more complex phenomenon which requires frequency coupling to exist with additional regularity in the phase of the demodulated radar signal. Let us assume that frequency coupling phenomenon exists for a particular radar return. The phase of the components in the return signal will correspond to the physical distance from the radar to objects. Let us consider a scenario with three moving scatterers, as it is illustrated in Fig. 5.4. The phases of three components are:

$$\phi_1 = d_1/k; \quad \phi_2 = (d_1 + d_2)/k; \quad \phi_3 = (d_1 + d_2 + d_3)/k, \tag{5.11}$$

where $k = 2\pi/\lambda$ is the wavenumber.

Assume that frequency coupling exists, therefore $v_3 = v_1 + v_2$. The bispectrum estimate is then will have a peak at position (f_1, f_2) where f_1 and f_2 are corresponding to v_1 and v_2 Doppler shifts. Then a bispectrum estimate, considering only phase component[2], is equal to:

$$B(f_1, f_2) = e^{i\phi_1} e^{i\phi_2} e^{-i\phi_3} = e^{i(d_1/k)} e^{i(d_1+d_2)/k)} e^{-i(d_1+d_2+d_3)/k} \tag{5.12}$$

Bispectrum is invariant to temporal shifts of the signal, which results in phase shift of all components. We will subtract the term $z = (d_1 + d_2)/k$ in order to shift the origin of the coordinate system. This results into:

$$B(f_1, f_2) = e^{i(d_1/k-z)} e^{i((d_1+d_2)/k-z)} e^{-i((d_1+d_2+d_3)/k-z)} = e^{i(-d_2/k)} e^0 e^{-id_3/k} = e^{i(-(d_3+d_2)/k)}. \tag{5.13}$$

Therefore, $B(f_1, f_2)$ has a maximum value when $d_2 = -d_3$. This scenario is shown in Fig. 5.5, for it the maximum of the bispectrum estimate will be achieved; moreover, bicoherence estimate will be equal to 1 for frequency pair (f_1, f_2). Other cases which result in maximum phase coupling include situation when at least one of the distances (d_1, d_2, d_3) is equal to zero.

Bicoherence estimate takes values in range [0 1]. Above we considered cases when it equals to 1, however smaller values than 1 are also of interest for analysis. Generally, phase coupling appears when frequency components f_1, f_2 and $f_3 = f_1 + f_2$ exist in a signal and their phases are looked. If we calculate bispectrum many times for different temporal segments of the signal, the bispectrum value $B_t(f_1, f_2)$ will remain the same. Because phases are locked, the bispectrum values will add from segment to segment, resulting in high amplitude and finally in non-zero value of the bicoherence. From other side, if phases are not locked, then resulting phase of the bispectrum at $B_t(f_1, f_2)$ will vary with segment number t. Finally, in case of non locked phases

[2]we do not consider amplitude component, because it will be normalized later in bicoherence estimate

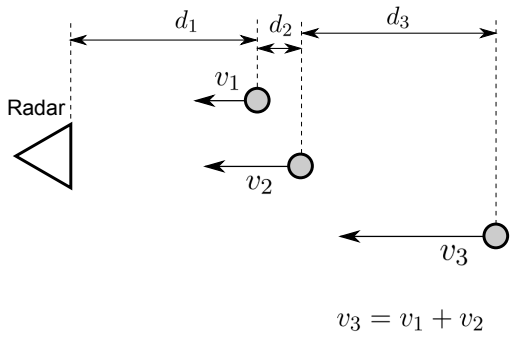

Figure 5.4: Scenario for phase coupling to exist.

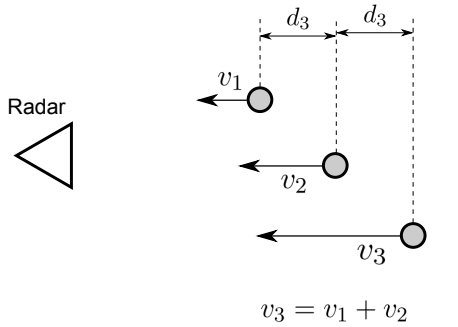

Figure 5.5: Scenario for the maximum phase coupling to be achieved.

of f_1 and f_2 averaged bispectrum value will be small, because averaging of values with random phases result in a cancellation; therefore, bicoherence estimate will be equal to 0.

Summarizing, we can notice that frequency coupling emphasizes regularities in the motion of a multi scatterer object, and it is high if there is a strong relation of scatterers motion and is low when all scatterers have independent motions. This feature emphasizes parent-child relations if human body parts during locomotion or another activity.

Phase coupling phenomenon emphasizes not only that motions have a strong pattern and depend on each other, but also geometrical relations between scatterers during the motion. Such geometrical relations could be important features of a propeller, or position of limbs during human activity.

B) Micro-Doppler signature of human walking

One of the most interesting scenarios to be analysed by micro-Doppler phenomenon is human locomotion [19, 59, 65, 141, 166–168]. Human locomotion consists of a number of scatterers which move by a special law. To show how complex the human locomotion is, we demonstrate two models by van Dorp [167] and Tahmoush [156] in Fig. 5.6. In both models at least 12 body parts are involved and they form interesting dependence of body parts' velocity within time.

Let us consider backscattering signal model focusing on the time-dependency of Doppler frequency behavior observed in a human gait analysis. Under assumption of periodical locomotion of a human legs (steps) and arms (swings), multi-component received signal $s(t)$ can be expressed

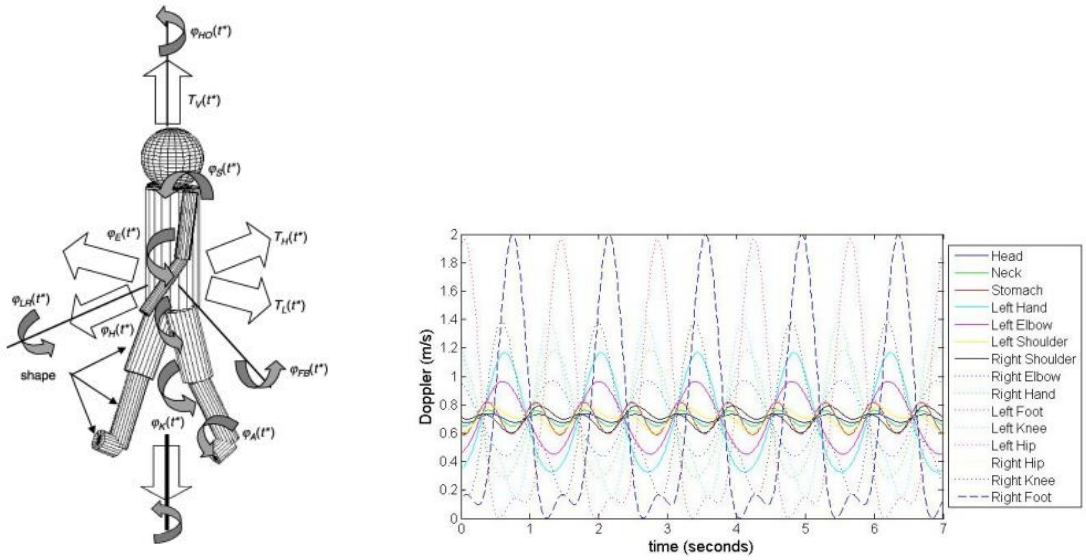

(a) After [167] (b) After [156]

Figure 5.6: Human walking models: (a) with 12 body parts, 3 translational trajectories and 14 rotation trajectories, image is taken from [166]; (b) time-velocity dependence of body parts involved in human walking, image is taken from [156].

as the following superposition of phase modulated contributions:

$$s(t) = \sum_{i=1}^{I} \exp(-\frac{j4\pi}{\lambda}(v_i t + \alpha_i \cos(2\pi t\theta_i + \phi_i) + r_i)), \tag{5.14}$$

where v_i is averaged velocity of i-th local scattering center; α_i, θ_i and ϕ_i are the parameters related to the radial velocity behaviour of i-th local scattering center; r_0 is a distance to the human root (body); r_i is a distance from radar to i-th scatterer; I is the total number of local scattering centres.

In the model (5.14) we assume only sinusoidal variations of the speed. Even-though the signal contains a number of non-stationary harmonic signals. Therefore we can assume that some of them exhibit *phase coupling* or *quadratic phase coupling*. Latter in this chapter we will investigate on simulated data which body parts provoke phase coupling, then we will verify results on real radar measurements, and finally we show how the phase coupling and frequency coupling could be used in ATR systems.

One of the most common ways to analyse radar data in the form of multicomponent non-stationary signals (like (5.14)) is short-time Fourier transform (STFT):

$$STFT(f,t) = \sum_{l=0}^{L-1} s(t(L-Q)-l)e^{-j2\pi fl/L}w(l), \tag{5.15}$$

where L is the length of the window function $w(l)$ (Hamming e.g.); Q is the number of overlapping samples; $f = 0, ..., L-1$ and $t = 1, ..., T$ are the IF and temporal shift indexes, respectively, $T = \frac{P-Q}{L-Q}$. The dimensionality of TF distribution (5.15) is defined as $TF \in \mathbb{C}^{L \times T}$. It should be noted that a modified version of the STFT is used in (5.15): the window is sliding with a step of $L - Q$.

Moreover, STFT is a complex function and it contains amplitude and phase which are time-frequency dependent:

$$STFT(f,t) = A(f,t)e^{\Psi(f,t)} = \left|STFT(f,t)\right|e^{\angle STFT(f,t)}. \tag{5.16}$$

Despite that the $STFT(f,t)$ contains amplitude and phase, researchers manly pay attention only to amplitude in form of *spectrogram estimate*:

$$Spectrogram(f,t) = \left|A(f,t)\right|^2 = STFT(f,t)STFT^*(f,t). \tag{5.17}$$

One of the research question we study in the thesis is: "Does phase component of the short-time Fourier transform of micro-Doppler have useful information for ATR?". And latter we will show that this information is useful, but first let's analyse radar backscattered signal of human walking.

Our analysis of human walking by micro-Doppler signature we start from the simulated radar data. For analysis we will use the simulator of the model developed in [22] and implemented in [30]. The continuous-wave (CW) radar data is modelled with the following parameters: radar wavelength $\lambda = 0.02$ m, sampling frequency $T_s = 1521$ samples/second, aspect angle $\theta = 180^o$ (direction straight to the radar).

Fig.5.7 demonstrates the spectrogram $\left|A(f,t)\right|^2$ (computed by (5.17)), phase term $\Psi(f,t)$ of STFT from (5.16) and averaged bicoherence estimate $\hat{b}^2(p,q)$ from (5.7). We can see that spectrogram demonstrates clear repetitive behaviour of frequencies involved in a gait. Phase plot (Fig. 5.7 top right) demonstrates very stochastic behaviour which is difficult to analyse (please note that noise was not simulated, so the phase plot is noise free). Probably, because of stochastic behaviour researchers are not using this information. However, bichorence estimate (Fig. 5.7 bottom) shows that there are very strong *phase coupling* between frequency components, letting us to conclude that phase information contains useful information. Latter we will analyse the contributions to the bicoherence plot. Bicoherence estimate is more effective when computed for a single period of the micro-Doppler signature; therefore, the STFT is divided onto 4 parts (because of 4 gaits), then bicoherence estimate is computed and finally averaged over 4 segments. For real data we should know how many periods do we have, and period estimator developed earlier is useful.

For real data, the phase noise is a main factor to corrupt the phase part of the STFT. Fig. 5.8 shows the analysis of the real radar data of human walking straight to the radar with wavelength $\lambda = 0.0088$ m. We can notice that spectrogram (Fig. 5.8 top left) represents useful information, pattern of the gait can be distinguished. The phase plot (Fig. 5.8 top right) seems to be noisy without any useful information, this is due to the phase wrapping and phase noise. However, when we look at bicoherence estimate (Fig. 5.8 bottom) we can notice that some components have phase coupling at level of 0.25. The signature is not that clear as for simulated data (Fig. 5.7), however, has a pattern.

Finally we want to emphasize that bicoherence is suitable only for multi-harmonic signals. On Fig. 5.9 the analysis of STFT and bichorence of simple single component sinusoidal baseband signal. Bicoherence estimate doesn't have a signature because there are only one component in the signal and phase coupling is possible.

C) Bispectrum analysis for the human walking

To analyse the bispectrum estimate for human walking we need to introduce bispectrum-based time-frequency distributions(TF). First, bispectrum-based TFD is obtained if for each short-time

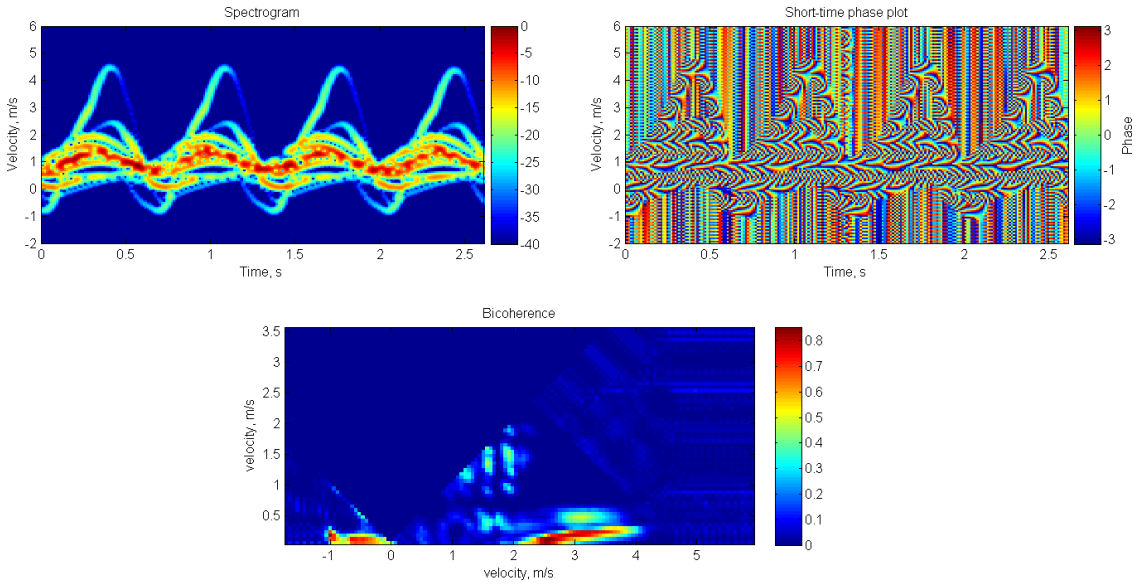

Figure 5.7: Analysis of the simulated radar backscattered signal of the human walking. Spectrogram (top left), squared magnitude short-time Fourier transform, represents time-frequency energy distribution. Phase plot (top right) shows phase distribution on the time-frequency plain. Phase plot is difficult to analyse and therefore is missed from analysis by many researchers. Bicoherence plot (bottom) shows phase coupling of the frequency components. Bicoherence estimate takes information of phase information in the short-time Fourier transform.

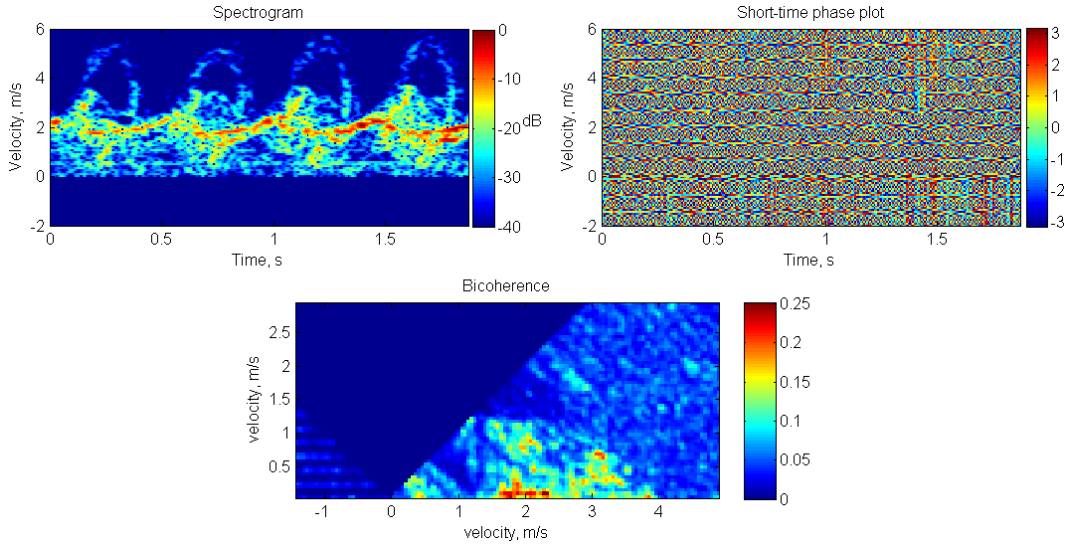

Figure 5.8: Analysis of real radar backscattered signal of the human walking. Spectrogram (top left), squared magnitude short-time Fourier transform, represents time-frequency energy distribution. Phase plot (top right) shows phase distribution on the time-frequency plain. Bicoherence plot (bottom) shows phase coupling of the frequency components.

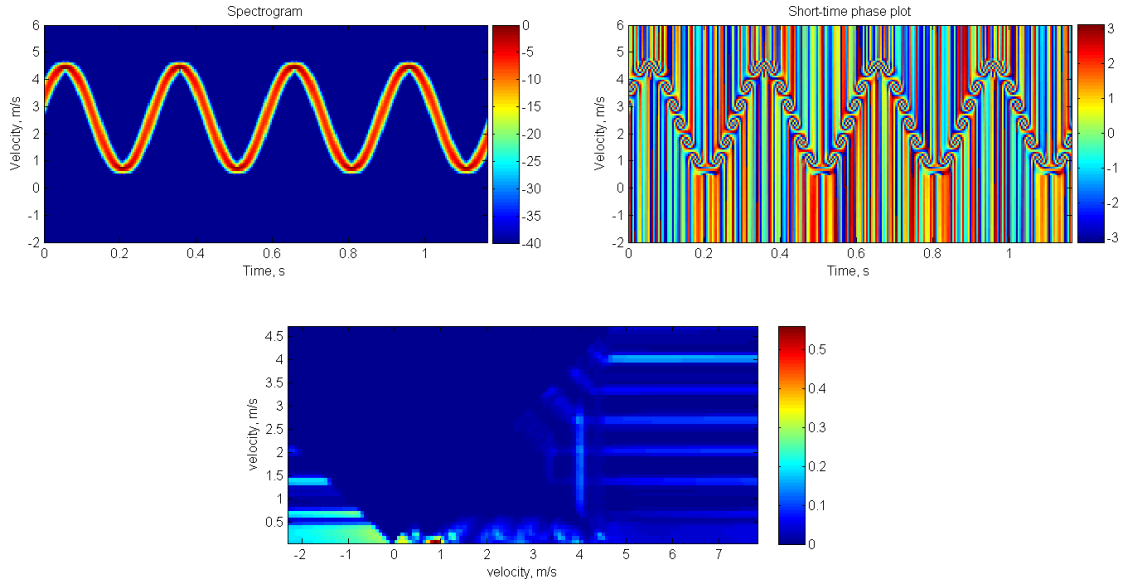

Figure 5.9: Analysis of sinusoidal baseband signal by STFT and bicoherence. Spectrogram (top left), squared magnitude short-time Fourier transform, represents time-frequency energy distribution. Phase plot (top right) shows phase distribution on the time-frequency plain. Bicoherence plot (bottom) shows phase coupling of the frequency components. Because of a single component there are no phase coupling and bicoherence estimate doesn't have a pattern.

bispectrum estimate we will consider only diagonal elements:

$$H(f,t) = |B_t(f,f)|, \tag{5.18}$$

where f is the normalized frequency belonging to the main diagonal of bispectrum. Another bispectrum-based TFD is proposed for speech recognition tasks in [120] and called integrated bispectrum (IB):

$$IB(f,t) = \frac{1}{L-f}\sum_{p=1}|B_t(f,p)|, \tag{5.19}$$

where L is the width of window in short-time Fourier transform (STFT); p is frequency under summation.

Another way to compute averaged bispectrum estimate has been proposed in [73]. We will call this technique as DFB, it deals with the averaging of the bispectrum samples in bifrequency domain along direction of a fixed frequency q:

$$DFB(f,t) = \frac{1}{K}\sum_{q=1}^{K}|B_t(f-q,q)|^{1/3}. \tag{5.20}$$

where K is a number of elements of q.

We will use bispectrum-based TFDs (5.18)-(5.20) in order to investigate evolutionary behaviour of frequency coupling during various phases of human gait by using computer simulated and measured in practice multi-component radar backscattering.

Analysis of the simulated data by bispectrum-based TFDs is performed in Fig. 5.10. TFD based on diagonal values of the bispectrum ($H(f,t)$ Fig. 5.10b) emphasizes components near

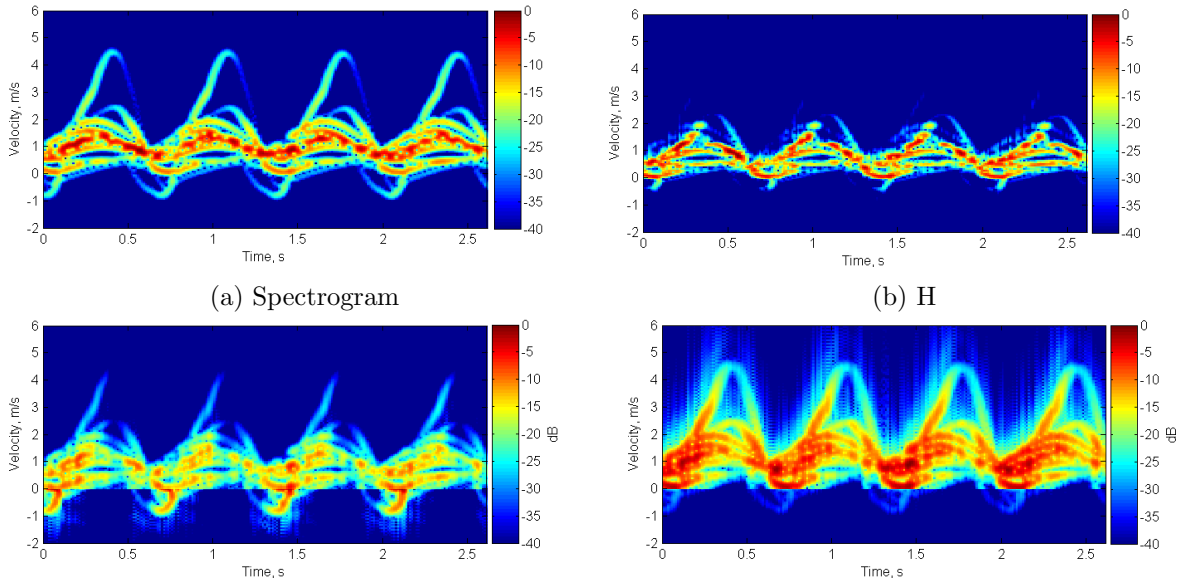

(a) Spectrogram (b) H

(c) IB (d) DFB

Figure 5.10: Bispectrum-based TFD computed simulated radar signal of human walking: (b) H, (c) IB, (d) DFB; compared to spectrogram (a).

body motion, extracting new signature of the human walking. The other two TFDs $IB(f,t)$ and $DFB(f,t)$ are similar to smoothing of the frequency profiles in the spectrogram with emphasize on components near the body.

Fig. 5.11 demonstrates bispectrum-based TFD for real radar data. We can notice the same features as for simulated data (Fig. 5.10). Bispectrum-based TFD, $H(f,t)$ (Fig. 5.11b) emphasizes components lower than the body. The other TFDs - $IB(f,t)$ and $DFB(f,t)$, again smooth the spectrogram.

Summarizing, we could say that bispectrum-based TFDs emphasize the frequency components correspond to the body, and lower frequencies, moreover, two of the considered TFD's - IB and DFB smooth (filter) the spectrogram based on frequency coupling phenomenon in the radar signal.

D) Bicoherence analysis

Earlier in this Chapter we have demonstrated the bicoherence estimates, which are non zero for radar return of human walking, in this subsection we are going to study the nature of contributions to the bicoherence.

To analyse bicoherence properties we should understand which human body parts cause the phase coupling. In order to study these, the following differential bicoherence value b^2_{dif} was computed:

$$b^2_{dif} = b^2_{ref} - b^2_b \tag{5.21}$$

where b^2_{ref} is the bicoherence value contained the contributions related to all human body parts; b^2_b is the bicoherence value without contribution of one of the body part. For example, we want to estimate contribution caused by a human foot. First, we have to compute b^2_b by using simulated data (we exclude contribution of the foot). After that, we compute b^2_{dif} according to (5.21) and, finally, we will understand which phase coupling contribution we lost without this human body part.

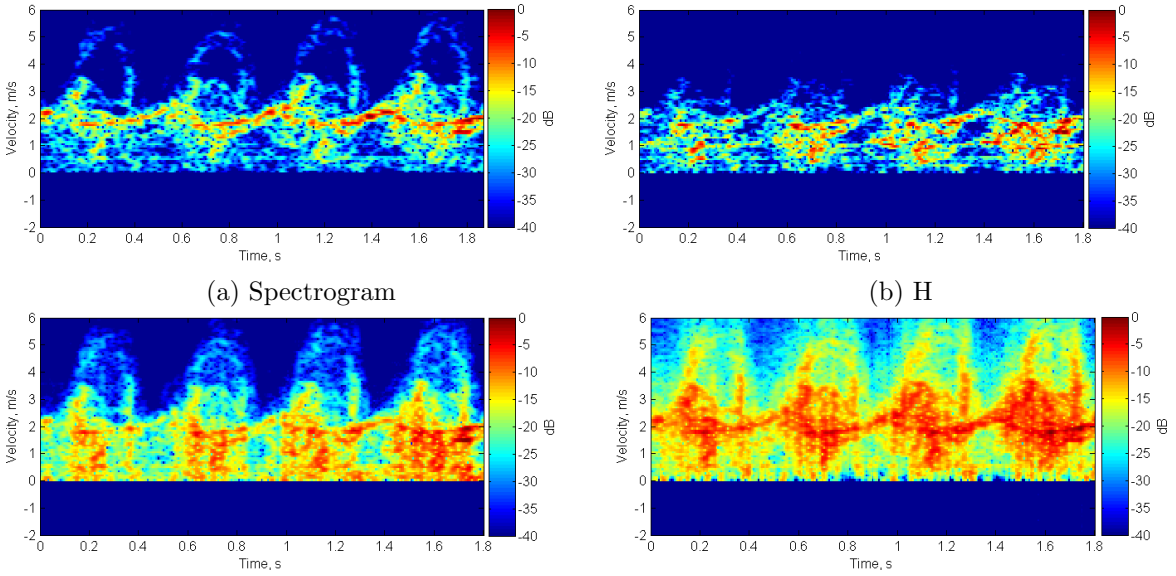

(a) Spectrogram (b) H

(c) IB (d) DFB

Figure 5.11: Bispectrum-based TFDs computed for real radar data of human walking.

Contributions of different body parts to the final bicoherence estimate are shown in Fig. 5.12. The contributions of head, shoulders, upper arm, lower arm, body, hip, upper leg, lower leg and foot were evaluated and the most informative are shown in Fig. 5.12. It can be noticed that the main contributors to the bicoherence estimate are human limbs, with the major contribution from foot and lower arm.

Based on the analysis of the contributions of different body parts from Fig. 5.12 we can identify contributions on the bicoherence estimate. Fig. 5.13 shows the division on regions of interest into areas A, B, C, D, E, and D. The detailed analysis showed that:

- Area A is provoked by motion of upper leg, foot and torso;
- Area B - by lower arm, foot and torso;
- Area C - by upper leg, lower arm and lower leg;
- Area D - by foot and lower leg
- Area E - by foot and lower arm.

The micro-Doppler contribution provoked by foot is a linking body part as it goes through all frequencies and maximally contributes to the *phase coupling*.

Finally we can compare contributions for simulated at real radar data. The bicoherence estimates are illustrated in Fig. 5.14, four similarities can be found. The strongest bicoherence values correspond to contributions from foot and lower leg are concentrated within the area D. The contributions provoked by foot and lower arm are concentrated within the area C. The contributions caused by torso, head and lower leg, as well as torso and other human body parts (foot, upper leg, lower arm) are located within the areas B and A, respectively.

Summarizing, bicoherence estimate has a pattern for radar return data if it has multiple moving parts contributing to micro-Doppler phenomenon. For human walking the main contributors to the bicoherence estimate are human limbs, with the major contribution from foot and lower

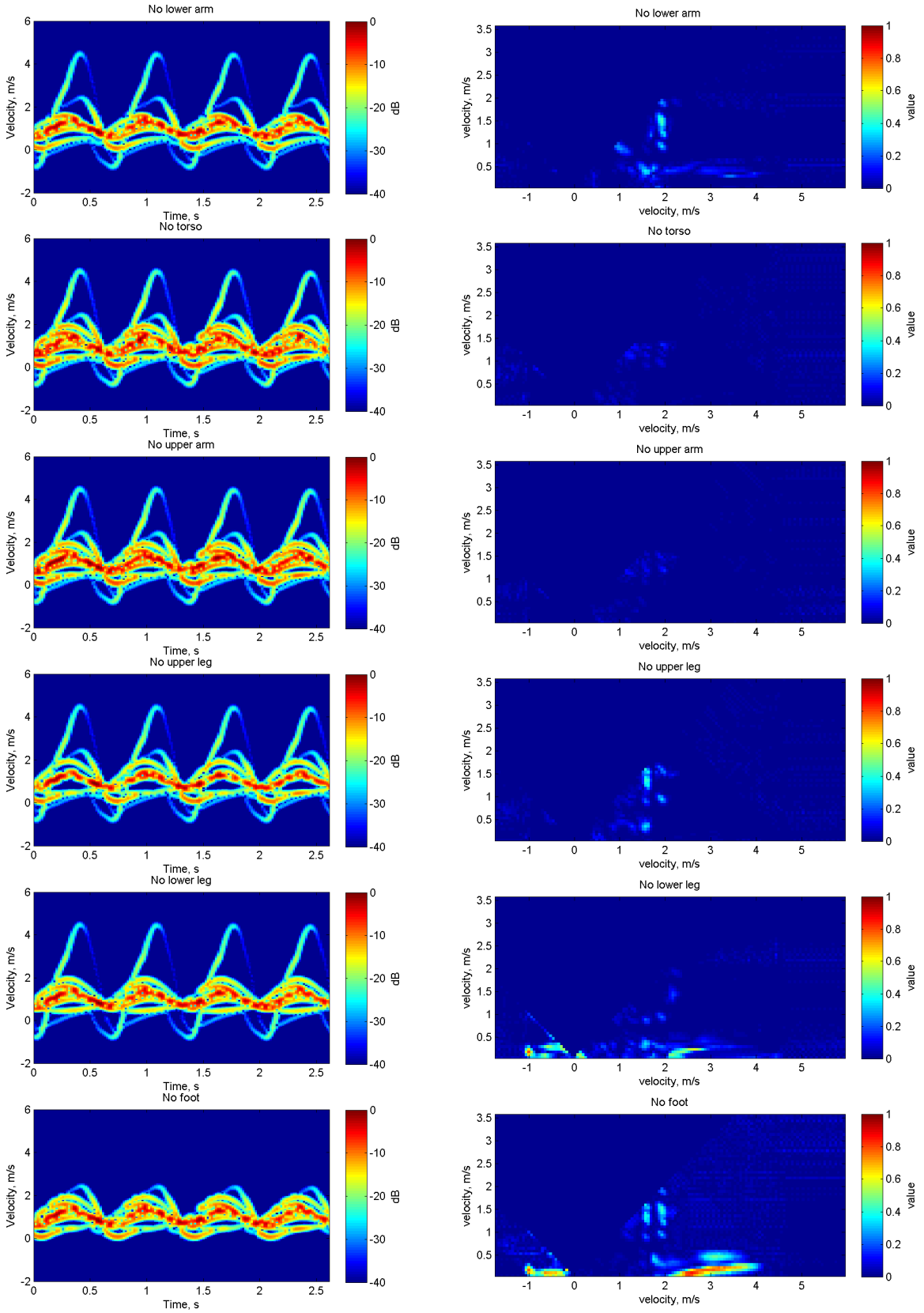

Figure 5.12: Contributions of the body part to the bicoherence estimate. One by one, body parts are removed from the simulator, spectrogram of the resulting signal is on the left. The contribution of the body part (by (5.21)) to bichorence estimate is shown on the right.

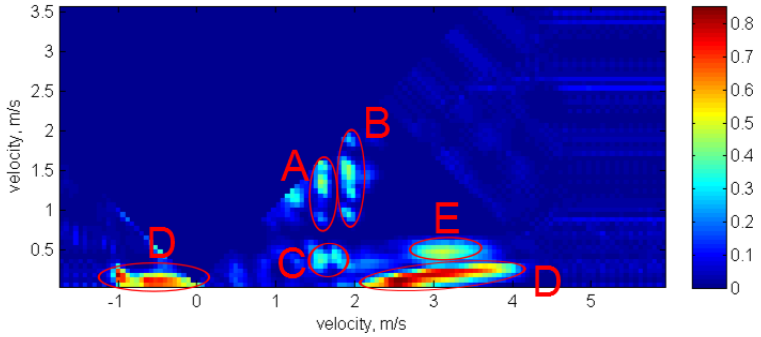

Figure 5.13: Bicoherence estimate of the radar return of human walking, with highlighted areas of contributions.

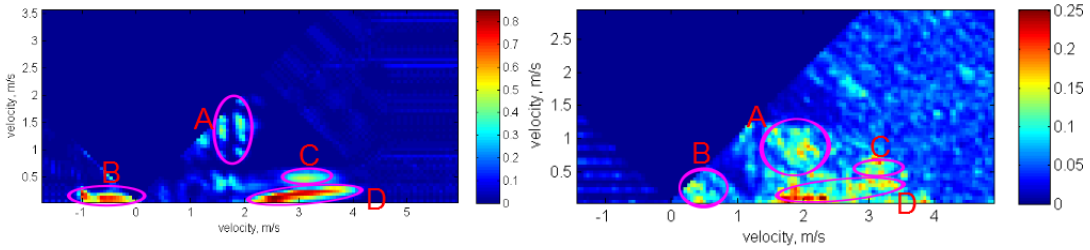

Figure 5.14: Comparison of contributions to bicoherence estimates of simulated and real radar data.

arm. Latter in this Chapter we will study how higher order spectral techniques could benefit to ATR systems.

II Classification of one, two and three walking humans

In recent years, radar analysis of human motion using measurements of evolutionary Doppler frequency variations has been under intensive study [9–11, 17, 28, 59, 150, 151, 166]. Recognition, identification and classification of persons moving in a vegetation cluttered environment using ground surveillance Doppler radar systems have a number of applications including security, military intelligence and battlefield purposes. One of the particular and effective discriminative features for the classification of moving persons is the micro-Doppler (m-D) contributions contained in the backscattering radar signature [17, 150].

In this Section, novel discriminative features computed in the form of bicepstral coefficients extracted by using bispectral estimation from radar echo-signals are suggested and studied. The performance of the suggested bicepstrum-based classifier is examined using experimental radar data processing for solving one of the most important and difficult problems in radar automatic target recognition (ATR) systems, which deals with discrimination and classification of a single walking person and group of walking persons in a vegetation clutter and AWGN environment.

The objective of this Section is a comparative study of ATR system performances evaluated by using the common spectrogram-based and suggested novel bicepstrum-based approaches.

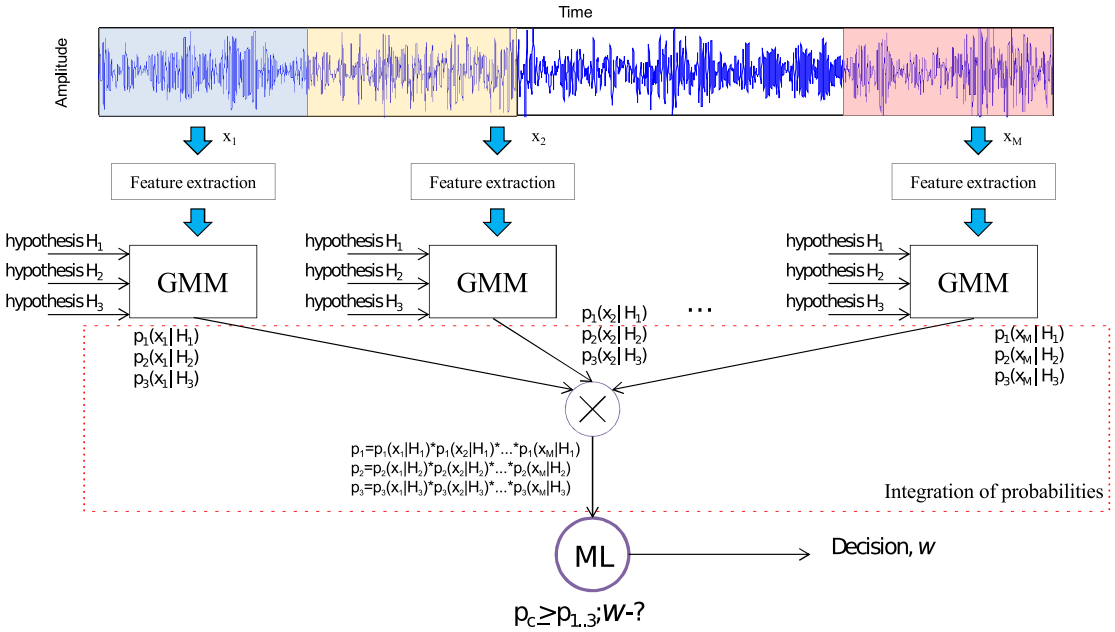

Figure 5.15: Structure scheme of a decision making concept applied in this study. A non-stationary signal can be divided into a series of quasi stationary segments. The features are extracted and conditional posterior probabilities are computed for those segments. Conditional probabilities are then multiplied and the maximum likelihood rule is applied

A) Theoretical background

The idea for the suggested approach deals with the well-known properties of the bispectral estimation method described in detail in [123]. Bispectral signal processing allows the assessment of the magnitude and phase of the correlation relationships between different harmonics. When a phase relationship exists, the phase-coupled harmonics contribute considerably to the bispectrum estimate in the form of corresponding peaks arising in the bifrequency plane. On the other hand, the bispectrum is identically zero for a stationary zero-mean AWGN. Therefore, unlike the energy spectrum, the bimagnitude, i.e. magnitude bispectrum estimate, contains the peaks in the bifrequency domain caused only by coherent contributions in the signal under study.

The Doppler frequency shift Δf_D observed in a radar signal backscattered by a moving person is equal to $\Delta f_D = 2v/\lambda$, where v is the velocity of target and λ is the radar emitted wavelength. For a person moving with normal speed of motion equal to 3-5 km/h, the Doppler frequency shift caused by translating the locomotion of the human torso, is equal to $\Delta f_D = 190 - 316$ Hz. The latter frequencies are within the audio signal band. Though swinging human arms provoke larger Doppler frequency shift values, they are also within the audio frequency band. Therefore, the received Doppler signal caused by backscattering from a moving person can be related to an audio signal. From this point of view, it is reasonable to consider two bispectrum-based algorithms that find applications in the analysis and recognition of human speech [120, 125].

The main concept of radar data processing implemented in this Section is shown in Fig. 5.15, where 1,...,M are the M input segments. In this manner, an entire non-stationary received signal s can be divided onto a series of quasi stationary segments $x_1, ..., x_M$ using a sliding window function ψ. The segment x_m is assessed as $x_m(k) = \psi(k) \cdot s\big((m-1)L + k\big)$, where L is the length of the window function expressed in the number of temporal samples. The features are

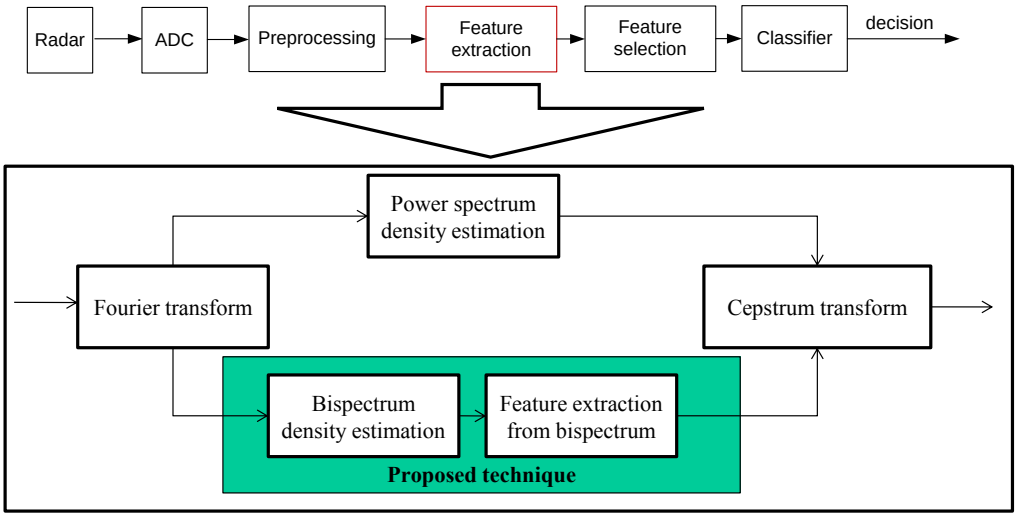

Figure 5.16: Scheme of the ATR system implemented in this work

then extracted and conditional posterior probabilities are computed for those segments.

Each segment is assumed to be independent from the others. Therefore, the conditional probabilities for each class of the entire sequence are equal to the product of the conditional posterior probabilities of each segment. The decision is made using the maximum likelihood rule.

Scheme of the ATR system used in this study is shown in Fig. 5.16. The main contribution are new features extracted in the form of bispectrum-based processing. We will consider IB and DFB features introduced earlier in (5.19) and (5.20), respectively.

A bicepstrum is the result of taking the inverse Fourier transform of the logarithm of the bispectrum. In this Section, the following bicepstral coefficients denoted below by CIB(f) and CDFB(f) are computed using the bispectral data IB (5.19) and DFB (5.20). These bicepstral values are exploited as the discriminative classification features as:

$$\mathrm{CIB}(f) = \Big|\frac{1}{K}\sum_{j=1}^{K} log(|\mathrm{IB}(j)|)e^{i2\pi fj/K}\Big|, \tag{5.22}$$

$$\mathrm{CDFB}(f) = \Big|\frac{1}{K}\sum_{j=1}^{K} log(|\mathrm{DFB}(j)|)e^{i2\pi fj/K}\Big|. \tag{5.23}$$

To evaluate and compare correctly the performance of the suggested bicepstrum-based classifier with the common power cepstrum-based classifier, the following power cepstrum coefficients C(f) are considered and computed in our survey as:

$$\mathrm{C}(f) = \left|\frac{1}{K}\sum_{j=1}^{K} log(|\mathrm{X}(j)|^2)e^{i2\pi fj/K}\right|^2. \tag{5.24}$$

A human operator can distinguish different targets listening to the baseband version of the received continuous wave radar signal [17, 102]. The cepstrum coefficients (5.34) are commonly used as features for speech and audio recognition [42, 46]. Taking into account the similarity in the signals used for speech recognition and ground moving target classification [102], the selection

of cepstrum coefficients for the comparison seems reasonable. Moreover, the cepstrum coefficients as a feature for ground target classification are of great interest to other researchers [17], and comparison with their research is sensible.

From the various existing approaches to radar target recognition and classification, the maximum likelihood (ML) rule and the Gaussian mixture model (GMM) are selected to evaluate the bispectrum-based classifier performance. Please see Chapter 4 for more details.

The posterior class conditional probability for the entire received signal s is the product of the posterior class conditional probabilities $p(x_m|w)$:

$$p(s|w) = \prod_{m=1}^{M} p(x^{(m)}|w), \tag{5.25}$$

where w is the class hypothesis, $x^{(m)}$ is a feature vector extracted from segment m, decision is made by considering M segments.

The decision-making rule exploited in the ATR system using the maximum likelihood (ML) method can be defined as follows:

$$\hat{w} = \arg \max_{w=1..W} p(s|w), \tag{5.26}$$

where $p(s|w)$ is a likelihood function conforming to the signal s referred to the classification hypothesis w.

B) Experimental data

Real radar data were collected by experimental measurement performed with a ground surveillance Doppler homodyne, monostatic, polarimetric and continuous wave radar.

The radar backscattering data relevant to three pedestrian classes were accumulated and recorded. The following scenarios were considered both in vegetation clutter and open space environments

1) Single moving person: Person walking towards or away from the radar at a velocity of 3-5 km/h;

2) Group of moving persons: Two persons walking towards or away from the radar at a velocity of 3-5 km/h

3) Group of moving persons: Three persons walking towards or away from the radar at a normal velocity of 3-5 km/h and either synchronously or asynchronously.

The ground surveillance radar system is shown in Fig. 5.17. The parameters of the radar are: wavelength - 8.8 mm; emitted radar microwave power - 15 mW; receiving/transmitting antenna beam width in both E and H planes - 60^o; level of side lobes in the horn antenna pattern - 24 dB; cross-polarization level $\leq$ -30 dB; receiver noise figure - 20.2 dB; two-channel 16 bit ADC; and a sampling rate in the digital records - 8 KHz. The averaged Signal-to-Noise Ratio (SNR) values are equal to 4 dB, 6dB and 11 dB for single, two and three moving persons, respectively.

The total length of all recorded wave-files is more than 23 minutes. The measurements were performed during the autumn period. Despite the radar being able to operate in both vertical and horizontal polarization modes, only the horizontal mode was considered for the classification.

Collection of the data for the dataset was performed as follows. The initial position of a target was fixed at a few meters from the radar. The person started to walk away from the radar

Figure 5.17: Ground surveillance radar system used for experimental data collection.

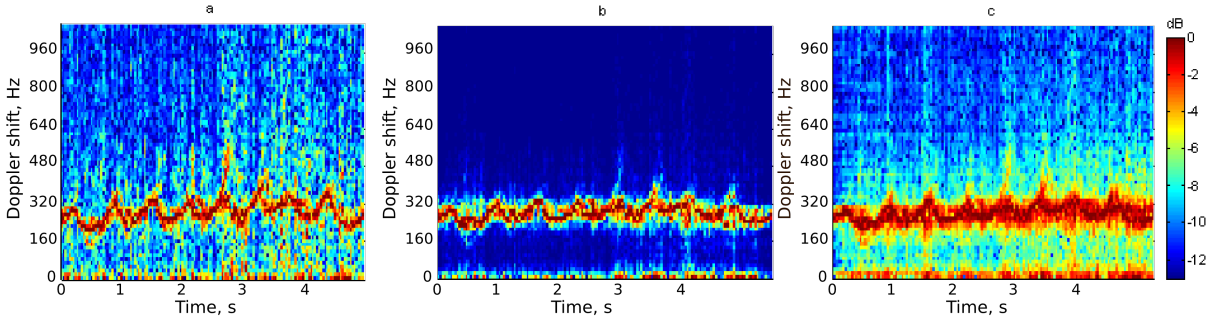

Figure 5.18: Time-frequency radar signatures measured in vegetation clutter and represented by: (a) spectrogram; (b) bicepstrum-based features (5.19); (c) bicepstrum-based features (5.20). The spectrogram is computed in the form of the amplitude of the Short Time Fourier Transform (STFT), and the bicepstrum-based features are computed using IB (5.19) and DFB (5.20)

for approximately 40 s, stopped for 2 s, turned around and came back, stopped for about 2 s and repeated the motion several times. Each considered class contained six sets of experiments performed with a person walking away from the radar and five sets of experiments with a person walking towards the radar. The same persons have participated in all experiments.

Examples of time-frequency radar signatures of a single person moving in vegetation clutter are shown in Fig. 5.18. Three types of TF distributions are shown: a spectrogram computed in the form of the amplitude of the Short Time Fourier Transform (STFT), and bispectrum-based radar signatures computed by IB (5.19) and DFB (5.20). The time-frequency distributions are computed with a Hamming window of length $L = 64$ ms, without overlap.

It can be seen from Fig. 5.18 that AWGN is suppressed better in the bicepstrum-based radar signatures plotted in both Fig. 5.18(b) and (c) compared to the spectrogram represented in Fig. 5.18(a).

It can be seen from the Fig. 5.18 that the analyzed signal does not contain frequencies higher than 700 Hz, therefore, a sampling frequency for the ADC equal to 8 KHz is a reasonable choice.

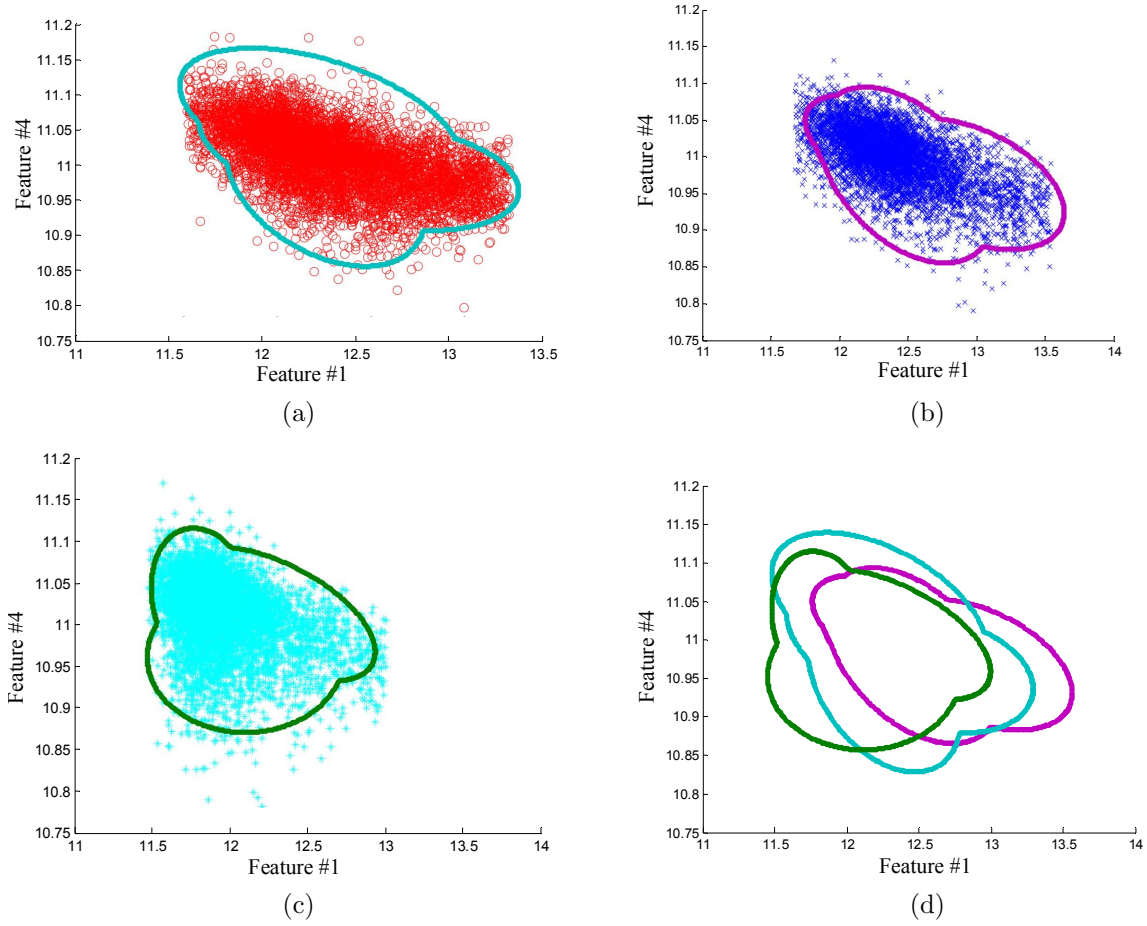

Figure 5.19: Bispectrum based features CDFB (5.23) belonging to one (a), two (b) and three (c) walking persons and their approximation (d) using the 3-order GMM at the level of 3 σ. The regions occupied by information features corresponding to different classes overlap; therefore, a sophisticated classifier strategy must be applied.

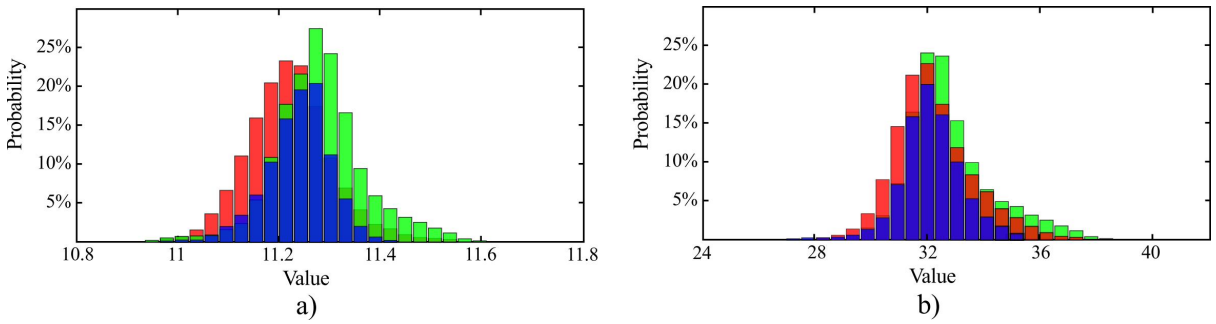

Figure 5.20: Histograms of the second bicepstrum/cepstrum coefficients related to the single (blue), two (red) and three (green) walking persons and computed using: (a) (5.23) and (b) (5.34). The histograms show that it is difficult to discern a single walking person from two or three persons by using only this one feature.

Dependencies between the values conforming to the first and fourth bicepstrum coefficients given in CDFB (5.23) and their GMM approximation represented by a 3-order model at a level of 3σ are illustrated in Fig. 5.19. As can be seen from Fig. 5.19, the regions occupied by information features corresponding to different classes overlap. Therefore, a feature space with a higher dimensionality is necessary to discriminate the classes.

Histograms illustrating the distribution laws for the second cepstral and bicepstral coefficients computed by using (5.34) and (5.23), respectively, are represented in Fig. 5.20. The histograms show that it is difficult to discern a single walking person from two or three persons using just this one feature. Both histograms in Fig. 5.20(a) and 5.20(b) referred to a single walking person but contain the overlapping domains corresponding to the histograms obtained for both two and three persons. However, classes belonging to two and three walking persons are more separated in the histograms plotted using bicepstral coefficients (5.23).

Classifier performance can be achieved using the features with lower inter-class similarity, i.e. when the same classifier but different feature vectors are used. To estimate inter-class similarity, the Euclidean metric has been computed for the sampled cross-correlation function. The similarity measure (SM) is evaluated as follows:

$$\mathrm{SM}(j) = \frac{1}{3K} \sum_{i=1}^{j} \sum_{\substack{k=1,2,3 \\ l=2,3,1}} ||\mathrm{XCF}\{Y_{k,i}, Y_{l,i}\}||, \tag{5.27}$$

where j is the number of used cepstral or bicepstral coefficients; XCF is the cross-correlation function; k, l are the indexes belonging to three classes; i is the cepstral/bicepstral coefficient number; and $Y_{k,i}$ is the set of cepstral/bicepstral coefficients number i belonging to the class k.

Dependencies of SM on the number of first cepstral/bicepstral coefficients are illustrated in Fig. 5.21. One can see the benefit of using the bispectrum-based strategy (see the straight curve in Fig. 5.21) compared to the power spectrum-based technique (dashed curve in Fig. 5.21). This benefit can be assessed by comparing the values belonging to the straight and dashed curves in Fig. 5.21. It is clearly seen that the correlation values are smaller for the bispectrum-based feature extraction technique, which means the latter technique possesses better orthogonality of its features. Therefore, a better classifier performance should be achieved for the bispectrum-based technique.

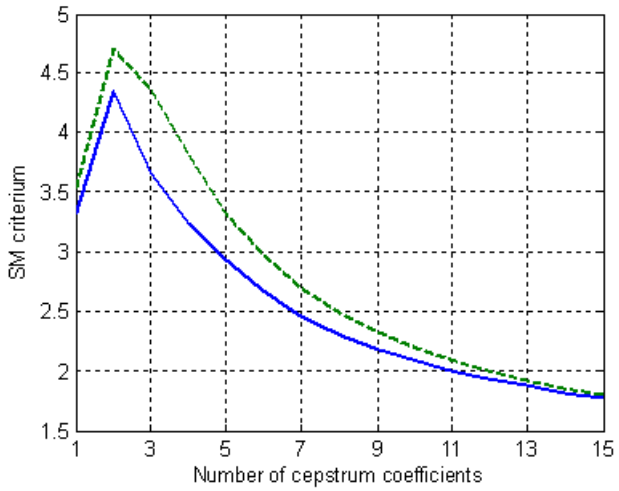

Figure 5.21: Inter-class similarity computed for the feature vector C (5.34) (dashed curve) and CIB (5.22) (straight curve). The correlation values are smaller for the bispectrum-based feature extraction technique, which means the latter technique possesses better orthogonality in its the features.

C) Analysis of classifier performance

Data separation

Commonly [17, 59], to evaluate classifier performance, the classification dataset is divided into two subsets of the same size. One subset is used as a training dataset and the other as a testing dataset. The disadvantage of such an approach is that the classification probability rates might vary if the small original dataset is split in a different manner. To obtain more accurate and reliable classification results, the K=11 cross-validation technique is applied (please see Chapter 4).

Eleven diverse experiments were performed for each of three radar target classes and the 11-fold cross-validation technique was exploited for target classification. This implies that the features have been extracted from the measured radar data ten times for the training dataset and once for the testing dataset during each experiment, i.e. 0.91 part of the data collected is used as a training dataset, and the remaining 0.09 part as the testing (validation) dataset for each fold.

Classification scheme

A scheme for the proposed classifier is shown in Fig. 5.22. The preprocessing block partitions the input signal into a series of frames of L samples length. The spectrum estimation block computes the spectrum of each frame using a Hamming window. The spectrum contains the frequencies higher than can be provoked by human gait, i.e. those frequencies that are higher than 900 Hz. Therefore, in the next block denoted as "Spectrum processing" they are removed by an ideal low pass filter. It can be seen from Fig. 5.18 that the maximum frequency in the signal under consideration is near 640 Hz, therefore, higher frequencies could be removed. Next, features are extracted from the spectrum at the block denoted as "Feature extraction". It could be one of the above-mentioned techniques C (5.34), CIB (5.22) or CDFB (5.23). The conditional posterior probabilities are computed at the block denoted as "GMM", and the decision is made using the

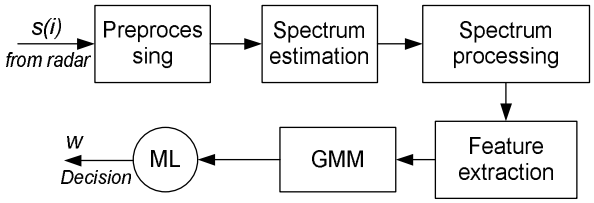

Figure 5.22: Scheme of the proposed ATR system.

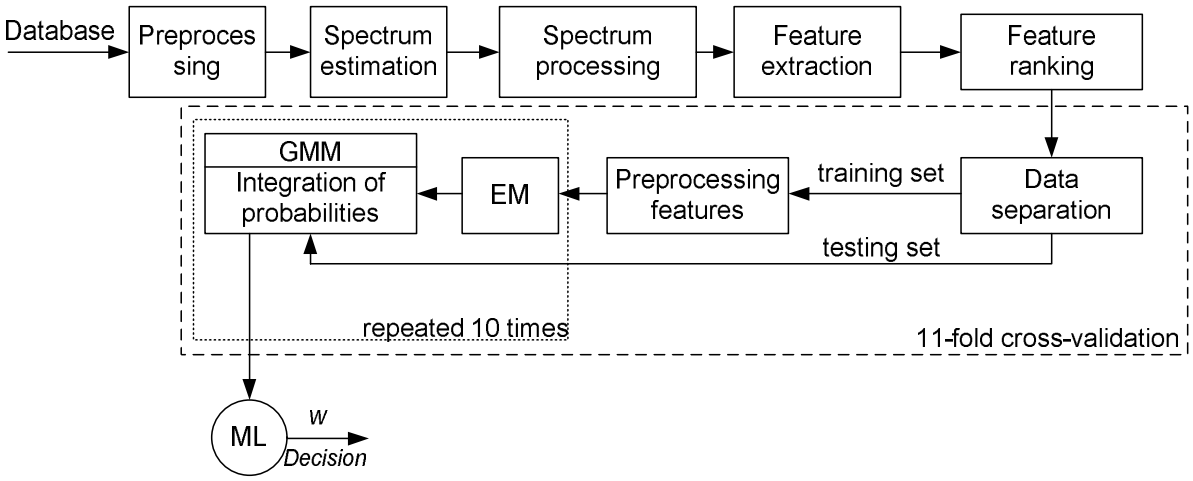

Figure 5.23: Scheme of parameter estimation. An 11-fold cross-validation is applied for the performance evaluation of the ATR system, where a data mining is carried out and the optimal parameters are estimated.

ML rule (5.26).

Some parameters such as the length of segment L, the number of GMM components and the number of used classification features must be defined a priori. The experimental system illustrated in Fig. 5.23 is presented for this purpose. An 11-fold cross-validation is applied for the performance evaluation of the ATR system, where data mining is carried out and the optimal parameters are estimated. The concept "optimal" means the parameters with which the best classification performance is obtained.

The scheme illustrated in Fig. 5.23 is used for performance evaluation. The block denoted "preprocessing features" removes the outliers from the training set, discarding 1% of the highest and lowest values. Next, the parameters Λ of GMM are estimated using the Expectation Maximization algorithm [44]. The initial estimate of the parameters is obtained by the k-means algorithm, and for statistical stability the results of 10 GMMs are averaged. Posterior class conditional probabilities extracted from the segments are multiplied to obtain the posterior class conditional probability of the entire received signal. The latter operation is performed in the block Integration of probabilities.

The optimal number of both power cepstrum (5.34) and bicepstral coefficients given by (5.22) and (5.23) has been estimated. From one side, if a small number of them is selected compared with the information containing in other coefficients, worse probabilities will be obtained. From the other side, the so called "curse of dimensionality" can arise if a large number of coefficients have been selected. We compute the probabilities of classification only for the training set changing the number of coefficients from 1 to 50% of their maximum number. Then, the number of coefficients

is selected according to the maximum value of classification probability. The estimated number of used coefficients depends on the segment length, and decision-making time. Therefore, it is unique for a fixed set of parameters. We consider 50 % features at most because of their symmetry (see (5.23), (5.22) and (5.34)). The maximum number of features is $z = L/9$.

Feature ranking is an important operation contained in classification algorithms. It ranks features according to certain information criteria and only the most informative features are used for classification. Here we use feature selection approach called MIMI developed in Chapter 4.

Empirically it was established that by varying the GMM order, the classification probability rates do not depend significantly on the GMM order. However, with increasing feature vector dimensionality, the GMM order should decrease. When only a few feature vectors are available GMM requires more components to achieve good approximation of the probability density function. However, when the ATR system operates with many feature vectors, a few components will be adequate. In the considered case, we deal with a few feature vectors. The processing data length is equal to 2 s (18 feature vectors are used for each class within one realization of cross-validation), and a large quantity of data are used when the data length is equal to 16 ms (2468 feature vectors for each class are used within one realization of cross-validation). The GMM order was defined empirically. When the processing data lengths were equal to 2 s, 1 s and 512 ms, the GMM order was selected to be equal to five. For the lengths of 256 ms, 128 ms and 64 ms, the GMM order was equal to four and, finally, for 32 ms and 16 ms it was equal to three.

Performance evaluation

The proposed classification scheme uses the integration of probabilities by dividing a non-stationary signal of length N into M segments of length L. As a result, a sequence of M quasi stationary signals is obtained.

The probability of correct classification is computed as:

$$P = \sum_{w=1}^{W} \frac{U_{cor}(w)}{U_{total}(w)} P_a(w), \tag{5.28}$$

where W is the total number of available classes; $U_{cor}(w)$ is the number of correctly classified instances related to the class w; $U_{total}(w)$ is the total number of classified instances related to the class w; and $P_a(w)$ is a priori probability related to the class w. Unfortunately, a priori probability is impossible to estimate using the available experimental data. Because of this, we assume that a priori probability related to each separate class is of the same value and equal to $P_a(w) = \frac{1}{W} \vee w$.

The probabilities of correct classification depending on the length of input signals and integration time are given in percentage terms in Table 5.1. Subcells containing the maximum value of probability obtained using different techniques with the same parameters are highlighted according to the technique used.

The comparative analysis data represented in Table 5.1 demonstrate the benefits of the bicepstrum-based techniques compared with the common cepstrum-based technique. The bicepstrum-based techniques provide better results with data lengths equal to or more than 64 ms. The conventional cepstrum-based technique outperforms the suggested techniques only when the data lengths are less than 64 ms and the integration time is more than 128 ms. However, the difference between the techniques under comparison is not very significant. The worst performance of the bicepstrum-based classifier is caused by low frequency resolution depending on the window width exploited in the STFT. The considered non-parametric estimation provides a frequency resolution equal to 63 Hz and 125 Hz for data lengths of 32 ms and 16 ms, respectively. To improve the

Table 5.1: The probabilities of correct classification given in percentages. Each cell situated in the intersection of the column corresponding to the window width (length of each segment) and row corresponding to the integration time parameter, is split onto three subcells. Each subcell corresponds to the feature extraction technique considered; from left to right: CIB (5.22), CDFB (5.23) and C (5.34)

Integration time \ FFT size (length of observed data)	16 ms			32 ms			64 ms			128 ms			256 ms			512 ms			1s			2s		
2 s	73	79	79	78	83	83	83	87	84	85	87	86	86	87	86	87	88	87	85	87	84	83	75	78
1 s	72	76	78	76	80	81	80	84	81	81	83	82	82	83	81	82	84	82	80	84	80			
512 ms	70	74	76	74	77	77	76	79	78	76	79	77	76	79	76	77	79	77						
256 ms	67	70	70	70	72	72	71	74	72	70	73	72	70	72	69									
128 ms	63	65	65	65	67	67	65	67	66	64	66	65												
64 ms	60	61	60	59	61	61	60	61	60															
32 ms	56	57	56	57	57	57																		
16 ms	53	53	52																					

The techniques given in each cell: CIB | CDFB | C

frequency resolution in ATR systems, the parametric bispectrum-based techniques [103] can be used.

It is well-known that the performances of ATR systems depend on the classifier, and may vary with different types of classifiers. All the above-mentioned results were obtained using the statistical-based classifier, GMM with the ML decision rule. Recently, the popularity of Neuron Networks (NN) and Multi Layer Perception (MLP) has increased in ATR systems. Therefore, it is reasonable to compare the obtained results with those obtained using MLP. The MLP is selected to be a feed-forward back-propagation Artificial Neural Network (ANN) with two hidden layers (ten neurons are contained in each hidden layer). Their transfer function is selected to be the tan-sigmoid. The output layer contains three output nodes with a purely linear transfer function. The mean squared error performance function is selected to estimate the ANN performance. The MLP is trained to estimate the class conditional posterior probability of the feature vector, and this is archived using three output nodes. The ANN is generated using standard Matlab functions.

Fig. 5.24 shows the dependences of the correct classification probabilities on processing the data length for a decision making interval equal to 2 s for two classifiers. The following peculiarities should be emphasized in the comparison of the results presented in Fig. 5.24:

- For both considered bicepstral classifiers, the CDFB technique (5.23) provides the best results with data lengths larger than 64 ms and less than 1 s;
- The common cepstrum-based technique C (5.34) outperforms the suggested techniques only when the data length is less than 64 ms;
- The best probability of correct classification for a data length of 2 s is obtained using the bicepstral CIB technique (5.22);
- Regularity of the results does not depend on the classifier.

Confusion matrices computed with a data length of 512 ms and decision making time of 2 s for all considered techniques are listed in Table 5.2:

- The best classification performance for a single walking person is achieved using the CDFB features with 90% of the correct classifications outperforming the other features by 2%;

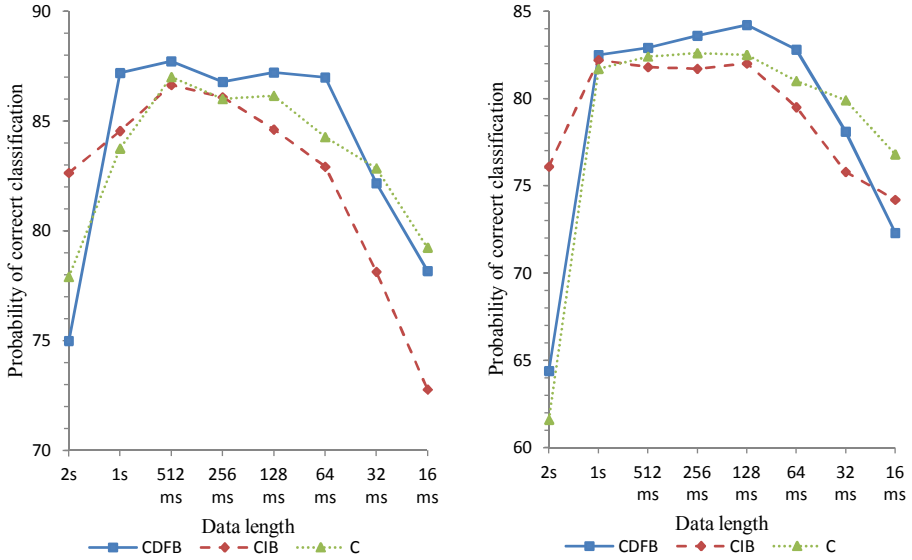

Figure 5.24: Probability of correct classification as a function of the processing data length for the GMM classifier (a) and MLP classifier (b). Decision making interval is equal to 2 s. The regularity of the results does not depend on the classifier.

Table 5.2: Confusion matrices for the considered techniques with a data length of 512 ms and decision making time of 2 s.

CDFB features

Number of persons	One	Two	Three
One	90	4	6
Two	6	82	12
Three	6	5	89

CIB features

Number of persons	One person	Two persons	Three persons
One	88	8	4
Two	5	83	12
Three	4	8	88

C features

Number of persons	One	Two	Three
One	88	7	5
Two	6	81	13
Three	4	7	89

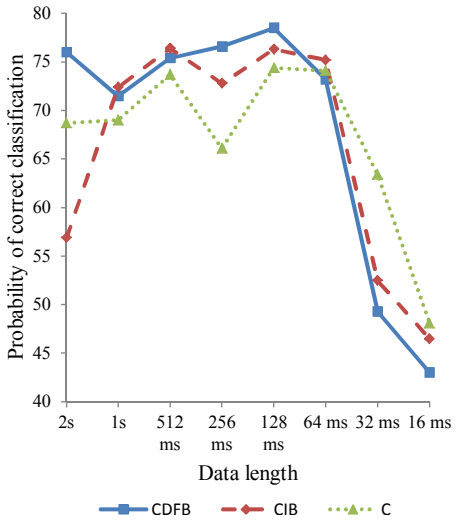

Figure 5.25: Probability of correct classification as a function of the processing data length for the SVM classifier. The decision-making interval is equal to 2 s.

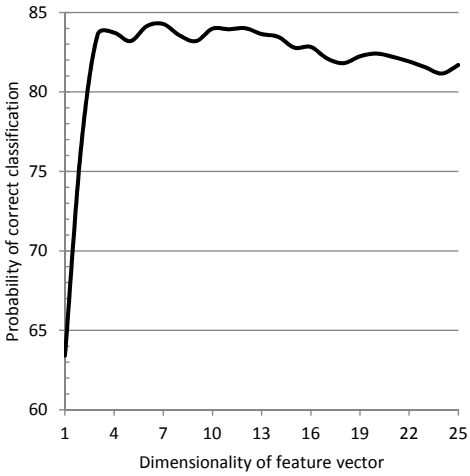

Figure 5.26: Probability of correct classification as a function of the feature vector dimensionality. Parameters: the decision-making interval is equal to 2 s; the processing data length is 64 ms; the cepstrum-based technique; and the GMM classifier.

- The class of two walking persons is the most complicated for all considered feature extraction techniques. The highest probability of correct classification, equal to 83%, is provided using the CIB features. The probabilities of correct classification equal to 82% and 81% are provided using the CDFB and C features, respectively;

- The last considered class of three walking persons is classified with a probability of correct classification at a level of 89% using the CDFB and C features. The CIB features provide 88% of the correct classifications.

Next, classification is performed using the Support Vector Machine (SVM) with a linear kernel. It is a non-probabilistic classifier, therefore, "integration of the probabilities" (5.25) could not be performed. This step is replaced by a majority voting method. The probabilities of correct classification are computed using 2-fold cross-validation.

The classification results computed by SVM are shown in Fig. 5.25. The results are similar to those obtained earlier. The cepstrum-based technique (C) outperforms other techniques when the data length is less than 64 ms. The bispectrum-based techniques outperform the cepstrum-based technique when the data length is higher than 64 ms, by 2-4%.

The probability of correct classification depending on the feature vector dimensionality is shown in Fig. 5.26. The curve is calculated for the cepstrum-based features and GMM classifier, with a processing data length of 64 ms and decision making time of 2 s. Before calculating the probabilities, the features are sorted according to the IG criterion and therefore, more of the informative features are used first. It can be seen in Fig. 5.26 that the function rapidly rises when there are fewer than four features. The function has a peak at number of features equal to seven, and corresponded features are selected to provide the classification result. The function then decreases with the increase in feature vector dimensionality.

It should be noted that bispectrum-based techniques require larger digital signal processing times because of additional computation for the 3-D-valued bispectral density. Therefore, it is

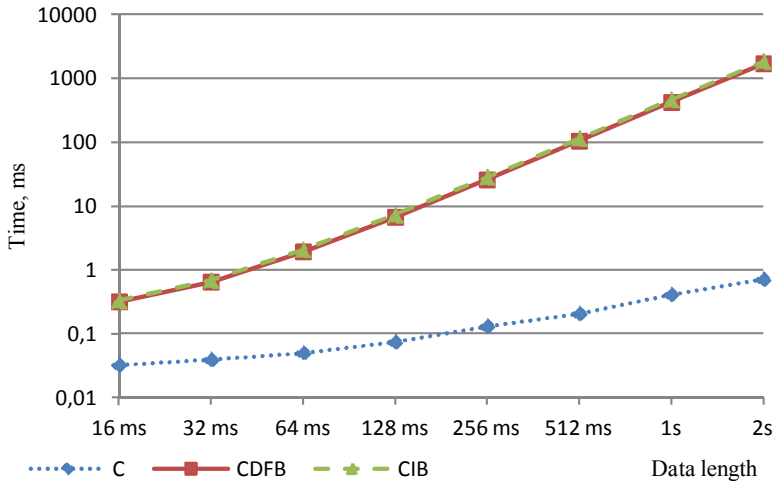

Figure 5.27: Elapsed time for feature extraction depending on the processing data length and method used. The processing time required for bispectrum-based techniques is significantly larger than for the cepstrum-based technique. Fortunately, real-time implementation is possible, because the processing time is smaller than the observation length.

of practical interest to estimate the computational time and compare it for all the techniques considered. Computations were performed by a computer with the following parameters: Intel Core 2 DUO CPU 3 GHz, 3.2 Gb RAM, operation system Windows XP SP 2, and Matlab R2010a.

Fig. 5.27 illustrates the time required for feature extraction using the three techniques considered. For all techniques and all available values of data length, the processing time is smaller than the data length. Therefore, a real-time implementation of all algorithms is possible. The processing time required for the bispectrum-based techniques is significantly larger than for cepstrum-based techniques. This is the cost of better classification performance. Fortunately, the signal processing time required for bispectrum-based techniques can be optimized using the symmetry properties of bispectra [123].

III Aerial target classification

High Range Resolution Profile (HRRP) can be considered to be the projection of the spatial intensity distribution of the backscattered electromagnetic field of the target onto the line of sight of the radar. HRRP, therefore, contains information about the geometry of the aircraft. A theory of radar target identification by HRRP is given in [149] where it is argued that HRRP offers the possibility of radar target recognition. In addition, the authors discuss a number of problems that occur when HRRPs are used.

Translational range migration is a known effect that causes translation shifts of the HRRPs related to the sequence of transmitted radar pulses. This effect must be taken into account if a sequence of HRRP is considered. The common way [184] of reducing the influence of the translation shift is to use an alignment method based on the maximum correlation between HRRPs. A more advanced method is the Time-Smoothed Zero Phase Representation proposed by Zwart [182] which provides the best performance when compared to other methods.

Proper transformations of the input processed data can enhance performance of radar target recognition. Nelson [122] has examined different families of wavelets used to transform the data. He found that no single wavelet transformation provides significant advantage over other wavelets

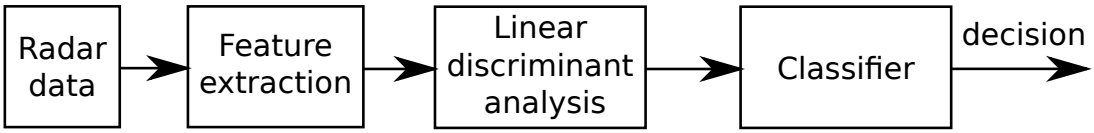

Figure 5.28: ATR used in this study for evaluation of the feature extraction strategies

in feature extraction for the radar classification task, and the simplest one, the Haar wavelet, can be used. The contribution of his work is in the new iterated wavelet transformation used to improve classifier performance.

A wavelet denoising method was developed by Huether [75] to increase classification rates of an ATR for aircraft classification based on HRRPs. A template matching procedure is used for decision making, the training set contains synthetic HRRPs and the testing set contains original HRRPs of 6 targets. Improvement of the classification rate from 72.9% to 94.8% is achieved by applying the wavelet denoising method to the series of HRRPs.

Zhou [181] proposed the spatio-temporal target identification method for HRRP identification. A sequence of HRRPs is used to model the signal generated by a hidden Markov model. Accuracy at a level of 93 % was obtained for classification of three original radar targets.

The potential for joint tracking and recognition using a simulated sequence of HRRPs was presented in [78]. For this purpose, a deterministic and a conditional Gaussian model for HRRPs were introduced, and the likelihood functions were compared for both L-band and X-band. The results demonstrated that the conditional Gaussian model provides improved performance compared to the deterministic model, and the benefit grows with increasing frequency.

A more robust statistical HRRP model was proposed by Du [49]. This model uses two distributions: The Gamma distribution and a Gaussian mixture distribution, that were successfully used in the Gaussian [78] and Gamma models [37]. To obtain the benefits given by the statistically-based radar HRRP classification, a large amount of training data is required to calculate the parameters of the model.

The Higher-Order Spectra (HOS) can be effectively exploited for HRRP classification due to their shift-invariance properties. Chandran [25] studied invariance properties of HOS for pattern recognition. Later, Zhang [179] and Du [48] proposed new features for HRRP classification based on HOS. Results obtained in [25, 48, 179] demonstrate that these features can provide aspect-angle and time-shift invariance.

The objective of this Section is twofold. Firstly, novel algorithms for extraction of cepstrum- and bicoherence-based classification features from a sequence of radar returns are proposed and studied. Secondly, the performance of state-of-the-art classifiers, using different decision making strategies, based on both the common classification features contained in the HRRPs and novel cepstrum- and bicoherence-based information features, are examined and compared.

A) General classification scheme

First, we will introduce the ATR system used in this section, it is illustrated in Fig. 5.28. For decision making we will use a feature-based approach. Radar data will be mapped onto lower dimensional space by feature extraction strategies. Extracted features are made to be invariant to irrelevant parameters of the signal (like averaged power), and on the same time to contain all the important information. As irrelevant parameters we will consider aspect angle of the target, noise and atmospheric turbulence effect. Once the features are extracted they are passed through linear discriminant analysis to reduce the dimensionality even more. Then machine learning approach

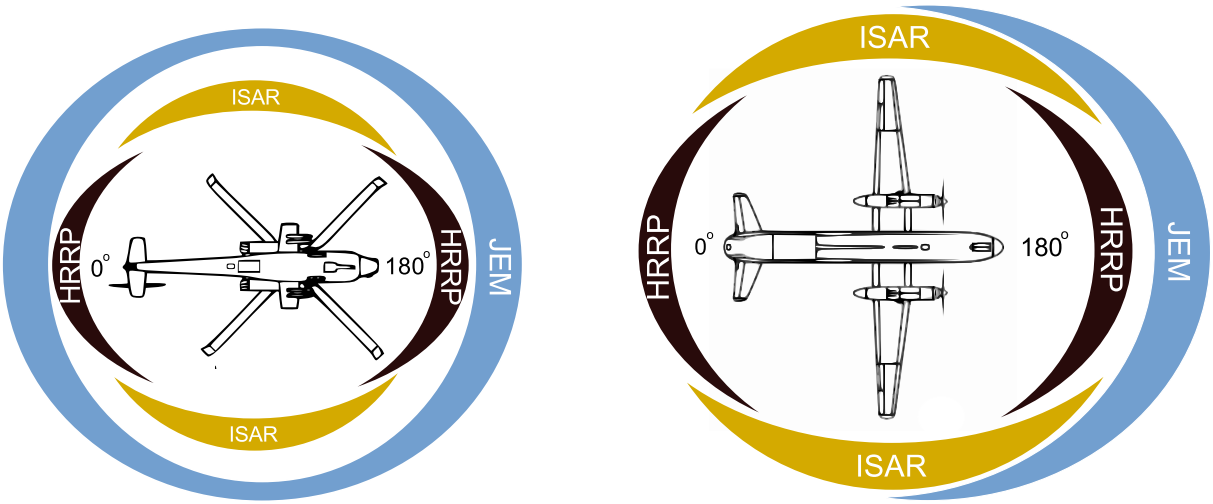

(a) Helicopter (b) Airplane

Figure 5.29: Effectiveness of the radar classification techniques depending on the aspect angle. Please note, that JEM effectiveness depends on the position and type of the jet, for example for turbine engine JEM will be more efficient for observing target from behind.

is used to map the features to the class label.

As it was pointed in the Introduction to the Thesis there are three main radar techniques for aerial target classification are HRRP, JEM and ISAR. These three technique are applicable when the target is observed at different aspect angles. The diagrams where these techniques could be applicable with the best effectiveness are shown in Fig. 5.29. We can notice the following peculiarities:

- HRRP shows the best performance when aspect angle is within range $\pm 30^o$ and 180 ± 30^o for helicopters and airplanes;
- ISAR is effective when the target is observed from the side. A long observation period is requited.
- JEM effectiveness depends on the type of the jet. For airplanes JEM is effective at those aspect angles where the blades are visible; for most of the cases this is for aspect angles $90^o - 270^o$. For helicopters the main rotor is visible from all aspect angles, and therefore JEM is effective for all aspect angles.

In this study we will work with radar returns obtained for aspect angles near 180^o - the situation when the target is approaching the radar. Therefore, we will consider only JEM and HRRP based strategies which are effective in this case. In the next section we describe the feature extraction techniques which are based on JEM or HRRP.

B) Feature extraction strategies

Four feature extraction approaches are considered: two of them provide feature extraction directly from the sequence of HRRPs measured during the tracking of the aircraft, while the other approaches use micro-Doppler contributions contained in time-frequency (TF) distributions of the

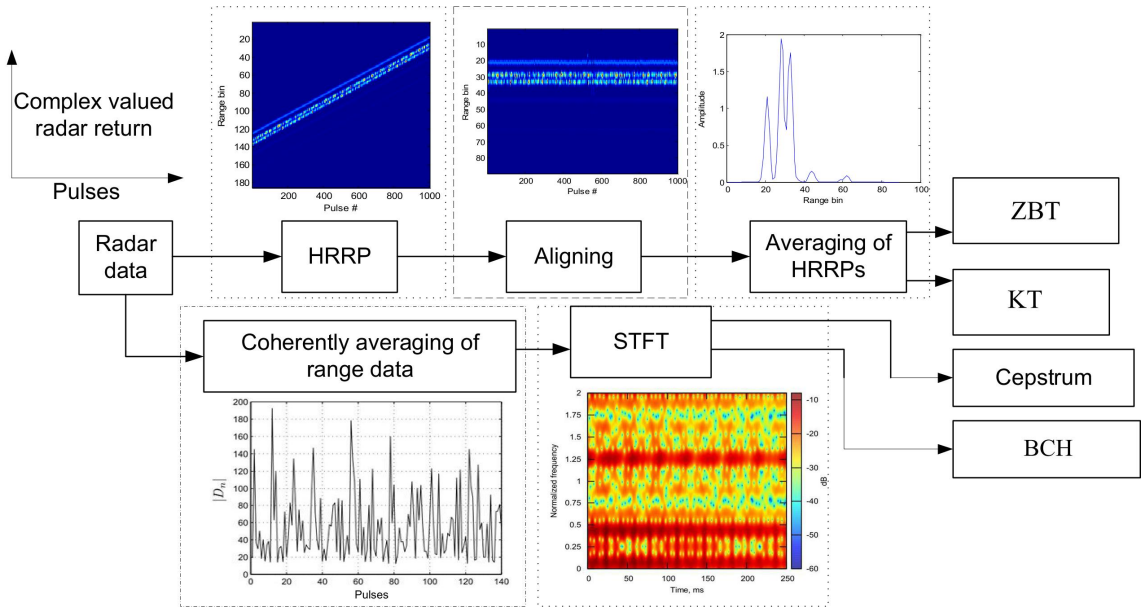

Figure 5.30: Generalization of considered feature extraction strategies.

radar echo-signals. All feature extraction methods could be generalized to scheme illustrated in Fig. 5.30. We will consider two feature extraction strategies based on HRRPs they are called ZBT and KT. We will also consider two strategies based on JEM, one of them is a proposed novel strategy denoted by BCH. Main steps of each of the algorithms are described in the following subsections.

Signal model

In this Section we deal with a classification of the aerial targets by processing a sequence of radar returns. Assume that the radar transmits a sequence of P pulses. After reflection from the target a sequence of radar returns $\{K_n\}_{n=1}^{P}$ will be received. Each radar return $K_n \in \mathbb{C}^M$ can be written as:

$$K_n(m) = y_n(m) + \epsilon_n(m), \tag{5.29}$$

where $y_n(m)$ is the target reflection in the m-th range bin for pulse n and $\epsilon_n(m)$ is the noise associated with the observation. Each n-th radar return contains M the in-phase (I) and quadrature (Q) samples, respectively.

A sequence of radar returns also forms a matrix $S \in \mathbb{C}^{M \times P}$, where each column is a radar return related to the n-th pulse, such that $S(m,n) = K_n(m)$.

Classification features extracted directly from the sequence of HRRPs

Based on our survey, the solution proposed by A. Zyweck and R.E. Bogner in [184] is the most cited reference in aircraft classifiers performance evaluation. We will refer to it below as the Zyweck and Bogner technique (ZBT). The ZBT contains the following signal processing steps:

1. Accumulation of the sequence of N HRRPs using the echoes related to the sequence of N radar pulses:

$$Y_n(m) = |K_n(m)|^2, \;\; n = 1, ..., P \quad m = 1, ..., M \tag{5.30}$$

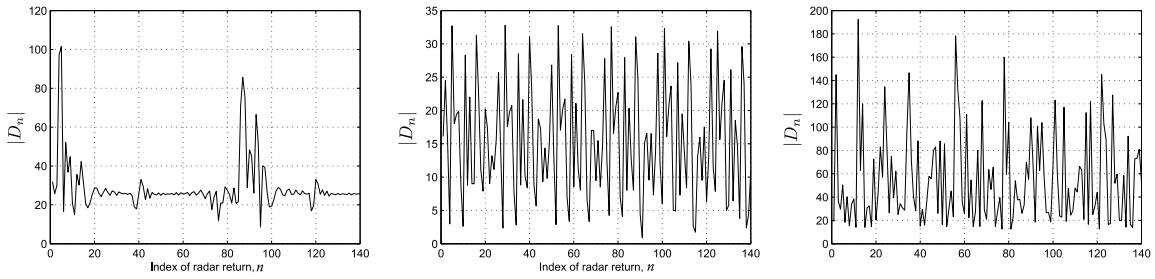

(a) AH-64 (b) An-26 (c) B-52

Figure 5.31: Amplitude variations of micro-Doppler content extracted from the radar returns for aspect angle equal to 185^o.

2. HRRPs must be normalized to provide intensity level invariance. The normalized HRRP is defined as $\hat{Y}_n$.

3. After aligning consecutive HRRPs (5.30) using a correlation-based procedure, the average of the aligned and normalized HRRPs is calculated:

$$R(m) = \sum_{n=1}^{P} \hat{Y}_n(m). \tag{5.31}$$

4. The averaged HRRP is then thresholded to remove the noise (for more details see [184]).

5. The direct discrete Fourier transform of the averaged HRRP (5.31) is calculated, and the magnitude of the Fourier spectrum is used for extraction of classification features.

Another approach based on the classification features extracted from HRRPs is the one proposed by K.-T. Kim et al (further referred to as KT) [85]. The main idea underlying the KT approach is to use the first 20 central moments as the features for aircraft classification. As the objective is to classify aircraft from a sequence of radar returns, this approach has been extended to utilize the given information. Therefore, the KT approach used in this study, encompasses the following signal processing steps:

1. Computation of the range profiles according to (5.30).

2. The aligning of consecutive HRRPs by using the correlation procedure and averaging of aligned range profiles according to (5.31).

3. Computation of the first 20 central moments of the averaged range profile which will be used as classification features.

Feature extraction from time-frequency distribution of radar echo-signals

In a real-life environment, micro-Doppler contributions can have non-stationary behaviour and intricate frequency modulations depending on aircraft acceleration and non-linear motion. In this situation, the common notion of frequency becomes meaningless, and the instantaneous frequency (IF) is usually taken into consideration. The Time-Frequency (TF) distribution is a tool widely used for evaluating the evolutionary behavior of the IFs.

The Short-Time Fourier Transform (STFT) can be used to obtain the joint TF distribution of the radar echo-signal:

$$STFT(f,t) = \sum_{l=0}^{L-1} D[t(L-Q)-l]e^{-j2\pi fl/L}w(l), \tag{5.32}$$

where

$$D[t(L-Q)-l] = D_n = \sum_{m=1}^{M} K_n(m), \tag{5.33}$$

L is the length of the window function $w(l)$; Q is the number of overlapping samples; $f = 0, ..., L-1$ and $t = 1, ..., T$ are the IF and temporal shift indexes, respectively, $T = \frac{P-Q}{L-Q}$. The dimensionality of TF distribution (5.32) is defined as $TF \in \mathbb{C}^{L\times T}$. A sequence of radar returns is obtained during a fixed time of the target tracking, and the TF representation can be considered because the index number of the n-th radar return is physically related to the time. It should be noted that a modified version of the STFT is used in (5.32): the window is sliding with a step of $L-Q$.

Behaviour of $|D_n|$ as a function of radar number return is shown in Fig. 5.31 for a fixed aspect angle equal to 185^o. These plots demonstrate the presence of micro-Doppler contributions.

According to the strategy suggested, STFT (5.32) is computed for the sequence of P complex-valued samples D_n (5.33), $n = 1, ..., P$. In turn, each single value D_n is computed by a corresponding sum of M samples belonging to I and Q components of an arbitrary n-th radar pulse.

Spectrograms estimated for three considered classes and three aspect angles used in this study are illustrated in Fig. 5.32. We can notice the following features:

- The micro-Doppler signature of the helicopters class (AH-64) shows robustness to the aspect angle, because only small variations are observed:
  - The contributions caused by main and tail helicopter blades can be distinguished. The front blade gives rise to a larger Radar Cross-Section (RCS) value, and in the position perpendicular to the radar line of sight excites harmonics throughout the spectrum.
  - The helicopter's tail blade gives rise to a smaller RCS value and excites harmonics with a narrower frequency bandwidth.
- Class of airplane has a micro-Doppler signatures which show high dependence on aspect angle, however, we can notice a pattern preserved for each class.

Cepstrum-based features possess the translation invariance property [108]. The cepstrum coefficients $C(f)$ are computed by using STFT (5.32) as:

$$C(f) = \left| \frac{1}{L} \sum_{k=0}^{L-1} \left(log_{10}(\frac{1}{T} \sum_{t=1}^{T} |STFT(k,t)|^2) \cdot e^{j2\pi fk/L} \right) \right|^2. \tag{5.34}$$

Also we will use a features based on the HOS techniques, like bicoherence. One of them, squared bicoherence, $\hat{b}^2$ was introduced in section I of this Chapter. It is computed for the whole STFT, averaging bispectrum estimates for each time slice.

The bicoherence estimate (5.7) depends on the target velocity. In order to provide an insensitivity to the velocity, the following bicoherence-based feature (referred to below as BCH) is proposed:

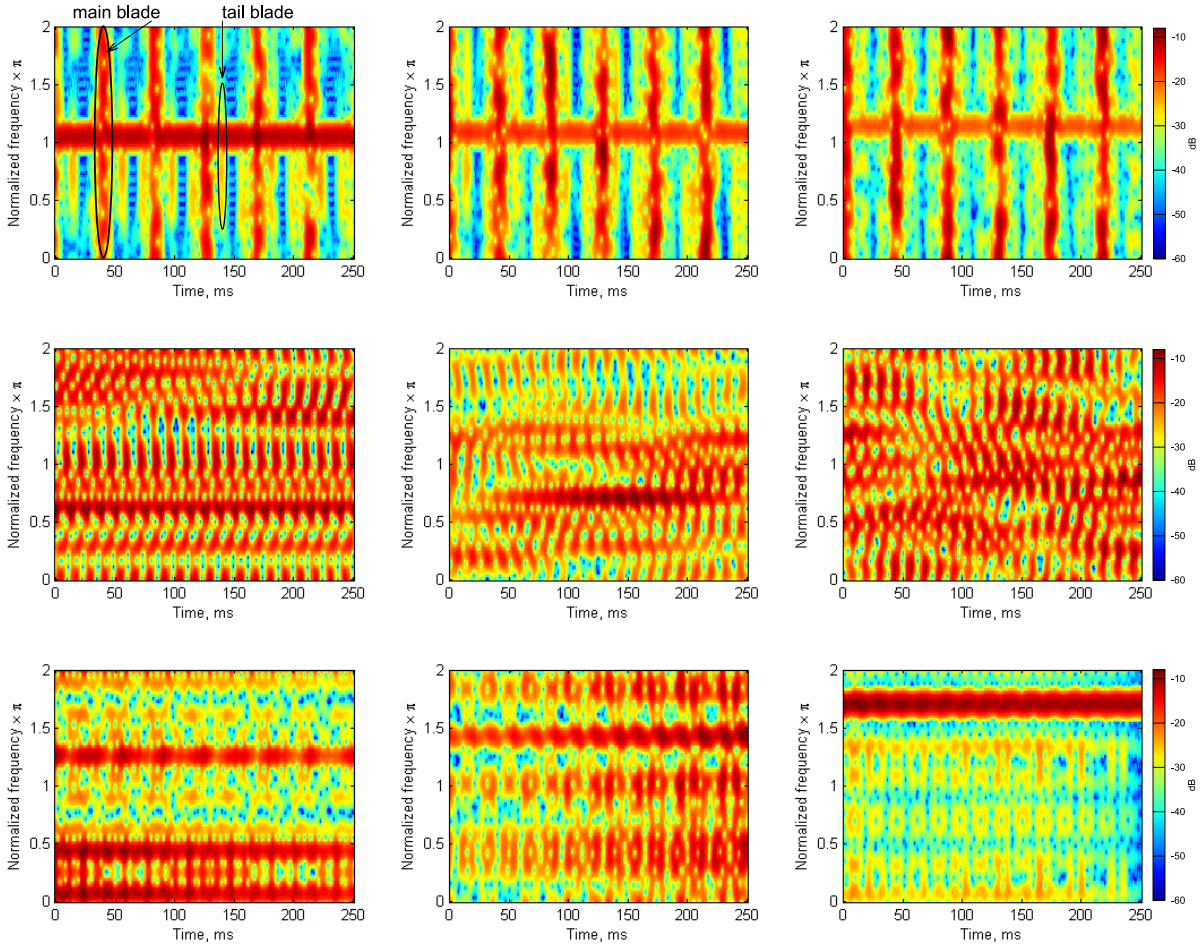

Figure 5.32: Spectrograms of the micro-Doppler contributions for three aspect-angles of 185^o, 190^o, 195^o and three aerial targets: Ah-64, An-24 and B-52.

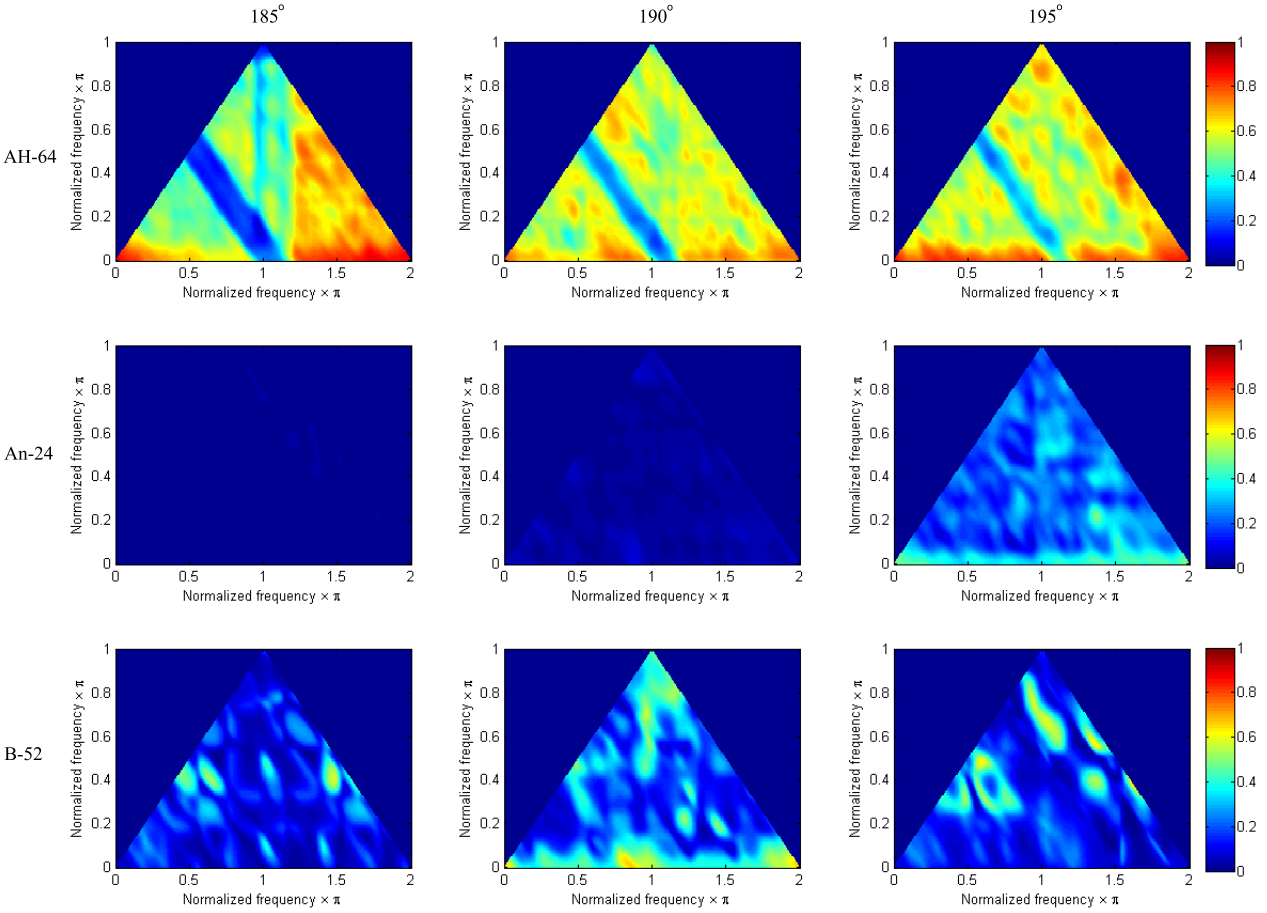

Figure 5.33: Bicoherence estimates of the micro-Doppler content in the radar returns for three aerial targets and three aspect angles.

$$BCH = |\mathscr{F}_{2D}\big(\hat{b}^2(f_1, f_2)\big)|, \tag{5.35}$$

where $\mathscr{F}_{2D}$ denotes the discrete 2-D Fourier transform.

Examples of bicoherence estimates (5.7) are illustrated in Figure 5.33. The bicoherence estimate computed for helicopter AH-64 shows the contribution of numerous phase coupled harmonics and $\hat{b}^2(f_1, f_2) \approx 1$ for a number of points in bifrequency plane. Moreover, we can notice small variations within the aspect angle. In contrast, the bicoherence estimate computed for An-26 has the lowest number of phase coupled harmonics for aspect angles 185^o and 190^o; for aspect angle 195^o the bicoherence estimate is larger, however still without large peaks. The bicoherence estimate computed for the B-52 contains a number of frequency coupled responses with phase coupling coefficients over 0.6.

C) Computer simulated data

Radar backscattered data are simulated in the form of I and Q samples using the approach proposed in [146]. A detailed explanation of modeling the backscattered secondary radiation used in this approach can be found in [63, 147]. The bandwidth of the chirp radar signal is equal

Table 5.3: Main characteristics of aerial targets used in the computer simulations

	Type	Speed	Altitude	Length	Height	Rotor
AH-64	Helicopter	160 km/h	200 m	17.73 m	3.87 m	main rotor - 4 blades of 7.315 m long tail rotor - 4 blades of 1.4 m long
An-26	Airplane	400 km/h	2000 m	23.80 m	8.58 m	2 pro. with 4 blades of 1.95m long
B-52	Airplane	800 km/h	2000 m	48.5 m	12.4 m	8 turbofans with diameter of 1 m

to $\Delta f = 150$MHz, which provides a range resolution of $R = \frac{c}{2\Delta f} = 1m$. The Pulse Repetition Frequency, PRF, and the central wavelength are equal to 2 kHz and 3 cm, respectively.

The data simulated by the approach proposed in [146, 147] are widely used for electro-magnetic backscattering field analysis of aerial targets [32, 48, 56, 173].

We consider aerial targets of three different types whose main characteristics are presented in Table 5.3. We study uniform motion of the targets towards the radar.

For each target, a set of data has been generated in the form of $N = 2000$ radar returns recorded within 1 second. Each radar return corresponds to the reception of $M = 1200$ I and Q digital samples. Three fixed values of aspect angles are equal to $A = \{185^o, 190^o, 195^o\}$. The aspect angle $a = 180^o$ corresponds the situation when the aircraft is flying directly towards the radar.

Three scenarios are used in this study:

- Under Scenario #1, half of the radar returns are related to each of three aspect angles and are used for training while the remaining half of the returns are used as test data.
- Under Scenario #2, the radar data associated with one of the three considered aspect angles, $A = \{185^o, 190^o, 195^o\}$, are used for training, and the records related to the other two aspect angles are used for testing. Step by step, the radar data associated with one aspect angle are used once for training and twice for testing.
- Under Scenario #3, the data generated for two aspect angles are used for training and the remaining set is used for testing. In this case, three combinations of testing and training sets are used in the study.

The final result for each scenario is evaluated by averaging of the probabilities of correct classification computed in percent (see Chapter 4 Section A)).

Initial data for simulation of the HRRPs

A backscattered signal model is developed using the simplest components method. This method is described in details in [146] (see the Sections 1.3, 1.4 and 1.5 pp. 9 - 55).

The main ideas used for development of the model are as follows: the object surface is represented by a number of the simplest components. Under "simplest component" one includes a surface described by equations of no more than second order: ellipsoid, paraboloid, hyperboloid and others. Approximate solutions related to radio waves backscattering are known from geometrical and physical optics. In addition, the edges, cockpits and the on board antennae are used as separate components. Empirical relations are used for two later structures.

Application of geometrical and physical optics methods introduce restrictions to the electrical size of the object. The latter must be considerably greater then the radar wavelength.

The interactions between the backscattering centres located on the target surface can be described as follows. The complex-valued echo-signal $y_k(i)$ observed at the output of range matched filter (MF) for an arbitrary k-th aspect angle can be expressed as

$$y_k(i) = \sum_{s=1}^{S} a_s(i) e^{j\beta_{ks}(i)},\ k = 1, 2, ..., K \tag{5.36}$$

where $a_s(i)$ and $\beta_{ks}(i)$ are the magnitude and phase spatial distribution under observation respectively; $i = 1, 2, , I$ and s are the range sample and s-th backscattering local center indices respectively. HRRP can be defined as the square of the envelope of the process (5.36) and can be written as

$$z_k(i) = \{Re[y_k(i)]\}^2 + \{Im[y_k(i)]\}^2 = \sum_{s=1}^{S} a_s^2(i) + 2\sum_{s=2}^{S}\sum_{n=1}^{S} a_s(i)a_n(i)\cos[\beta_{ks}(i) - \beta_{kn}(i)] \tag{5.37}$$

It follows from (5.37) that the intensity distribution in HRRP contains two terms. The first one is the sum of local backscattering center intensities whose value does not depend on the variations of target aspect angle. The other term is the sum of cross contributions whose values depend on the target aspect angle. Only this latter term generates HRRP variability.

D) Results

Two different types of classifiers are considered: the Support Vector Machine (SVM) with the Gaussian radial basis function as a kernel, a non-probabilistic linear classifier, and the Naive Bayes Classifier (NBC), a probabilistic one. Please see Chapter 4 for more details on classifiers.

The ZBT, the cepstrum-based, the bicoherence-based and the KT techniques are used for feature extraction. The dimensions of the feature vectors are M for the ZBT, L for the cepstrum-based technique and 20 for the KT approach. A $L \times L$ matrix is generated by the bicoherence-based technique. In order to reduce the dimension of the classifier inputs, Linear Discriminant Analysis (LDA) is applied to ZBT, cepstrum-based and bicoherence-based features [50]. As a consequence, the dimensions of the feature space is reduced to $U - 1$, where U is the number of classes. LDA finds linear combinations of features able to separate the classes considered. This technique is efficient when the dimensionality of the feature vector is much higher than the number of classes U. Therefore, the LDA is not applied to the KT feature set.

Let us consider in detail the operations performed with data processing for Scenario #1. The data processing steps are listed in Table 5.4. A set of $N = 2000$ pulses is simulated for one of the aerial targets flying at a particular aspect angle for 1 second. Radar returns are combined into one matrix $\Psi \in \mathbb{C}^{M \times N}$ where each pulse relates to M samples of the data received. Next, the radar returns are separated into training $\Psi^{(tr)} \in \mathbb{C}^{M \times N^{'}}$ and testing $\Psi^{(ts)} \in \mathbb{C}^{M \times N^{'}}$ data as follows: $\Psi^{(tr)}(m, g) = \Psi(m, g)$ and $\Psi^{(ts)}(m, g) = \Psi(m, g + N^{'})$, where $g \in [1, N/2]$ and $N^{'} = N/2$. For simplicity, assume that the data set Υ is either a training $\Psi^{(tr)}$ or a testing $\Psi^{(ts)}$ set. Next, we synthesize the overlapping sequences of radar returns from Υ as follows: $S_h(m, n) = \Upsilon(m, h + n - 1)\ \forall\ n \in [1, P],\ h \in [1, N^{'} - P]$, where h denotes the index number of the sequence.

The features are extracted according to the methods described above for each sequence of radar returns S_h from training and testing sets. In the next step, the extracted features, excluding KM features, are processed by LDA for reduction of dimensionality. When the classification is performed, the training and testing sets are permuted and classification is performed again, then the results are averaged and the probability of correct classification is computed.

Table 5.4: Data dimensions for Scenario #1 fixed aspect angle and single target

Description	Quantity
Pulses simulated	$N = 2000$
Radar returns in	
Training set	$N/2$
Testing set	$N/2$
Synthesised sequences of each set	$N/2 - P$
of radar returns	P
Number of features extracted from each sequence	ZBT: M KM: 20 C: L BCH: $0.5L^2$
Number of features after LDA	ZBT: 2 KM: 20 C: 2 BCH: 2

Interference-free case

In order to estimate the potential of ATR performance, an interference-free case is considered in this Subsection.

Two of the feature extraction approaches considered are based on the STFT (5.32). The window length L, and the number of overlapping samples Q must be defined. A compromise solution must be found taking into consideration that a larger window width provides higher frequency resolution while a smaller window width leads to better temporal resolution.

The values of L and Q are estimated separately for all Scenarios using the training data set with $P = 140$, where P is the number of radar returns to be processed for classification. This set is split and a twofold Cross-Validation (CV) procedure is performed using all possible values of L and Q. The probabilities of a correct classification rate are computed for SVM and NBC classifiers. The classification rates obtained for both classifiers are averaged to produce a single estimate for all sets of parameters. Finally, parameters L and Q are estimated according to the maximal classification rate.

Correct classification probability estimated for Scenario #1 as a function of the window length is shown in Fig. 5.34a. All possible values of Q are considered for a given value of L, and the maximum is stored. The maximum probability of correct classification is equal to 98.11% for $L = 70$ samples (radar returns). For $L = 70$ samples, the correct classification probability has been estimated for different values of Q (see Fig. 5.34b). A maximum value of 98.11% is achieved for $Q = 53$, so the optimal parameters can be calculated as $L = P/2$ and $Q \approx 0.76L$. It should be noted that these relationships are also valid for other values of parameter P.

For cepstrum features the results are similar. The maximum probability of correct classification is achieved for $L = P/2$, and $Q = 0.75L$.

The Hamming window and the following parameters are used for feature extraction algorithms

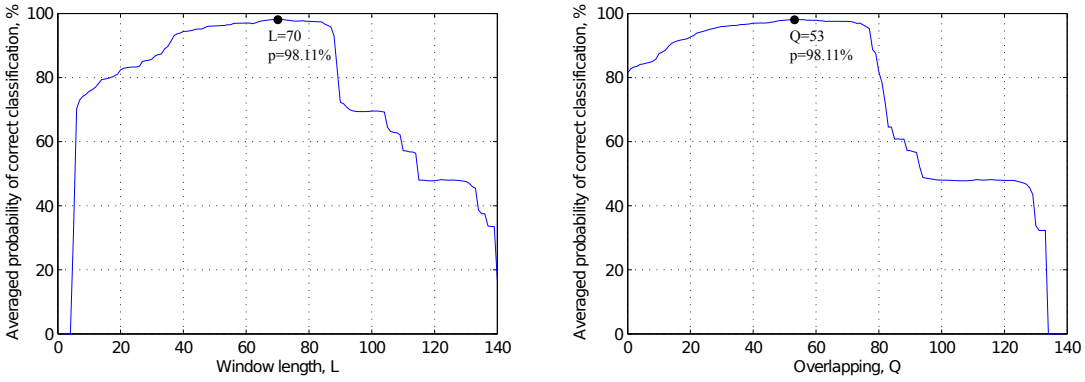

(a) L (b) Q

Figure 5.34: Correct classification probability rates depending on the window length L (a) and the number of overlapping samples Q (b) computed using the BCH technique.

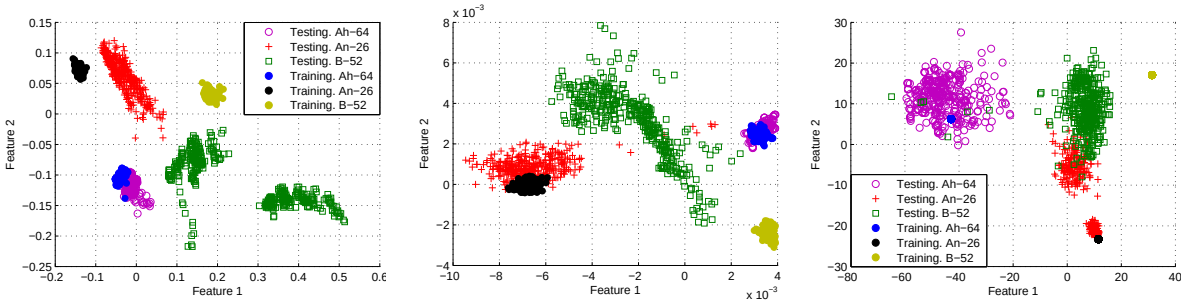

(a) KT features (b) Cepstrum features (c) BCH features

Figure 5.35: Feature spaces of data for Scenario 2, aspect angle is 185^o for training set, aspect angles are equal to 190^o and 195^o for testing data set.

based on the STFT (5.32): $L = 70$, $Q = 53$ and $P = 140$. These parameters are used for cases where the data set from Scenario #1 is used. For Scenarios #2 and #3, the parameters are estimated separately using only the training set from the corresponding Scenario. The dimensionality of the STFT (5.32) computed with parameters $L = 70$, $Q = 53$ and $P = 140$ will be $L \times T \approx 70 \times 5$.

Table 5.5 shows the results obtained for three-classes of aerial target classification under Scenario #1. Both SVM and NBC classifiers provide similar classification probability rates for ZBT and BCH methods. The best performance is achieved by ZBT and BCH techniques using an SVM classifier. These techniques outperform the KT approach and cepstrum-based techniques by 0.8% and 3.5%, respectively. For the NBC classifier, the best performance is achieved by the ZBT technique with a slight benefit over TF-based techniques. This benefit is equal to 0.3% and 0.5% compared to BCH and cepstrum-based techniques, respectively. The KT performance is the worst compared to the other three considered techniques.

The results obtained for the bicoherence-based method confirm the above mentioned hypothesis concerning the suitability of the phase coupling components contained in micro-Doppler contributions. The phase coupling components can therefore be recommended as fairly effective classification features for ATR radar systems. Note that the best performance is achieved by ZBT and BCH techniques with a slight advantage for the ZBT providing a correct classification

Table 5.5: Correct classification probability rates computed in percentages. Scenario #1

Classifier	Feature extraction technique			
	ZBT	KT	Cepstrum	BCH
SVM	99.52	98.72	96.01	99.50
NBC	99.95	93.5	99.45	99.61

Table 5.6: Correct classification rates computed in percentages. Scenarios #2 and #3

	Classifier	Feature extraction technique			
		ZBT	KT	Cepstrum	BCH
Scenario #2	SVM	73.24	76.36	71.67	**82.73**
	NBC	51.79	79.37	81.74	**84.06**
Scenario #3	SVM	83.33	85.39	85.60	**92.53**
	NBC	76.14	79.35	88.01	**89.19**

probability rate higher than 99.5%. Feature spaces related to Scenario #2 are depicted in Fig. 5.35. The testing data sets are rather good separated if KT or cepstrum-based features are used (see Fig. 5.35a and 5.35b). However, a variation of aspect angle leads to shifting of the features and later misclassification. On the other hand, the bicoherence-based features (see Fig. 5.35c) provide similar testing and training feature sets.

Aspect-dependence

In order to study the dependence on aspect angle, the data generated under Scenarios #2 and #3 are used. Table 5.6 shows the estimated correct classification probability rates. The best results are achieved using the BCH technique for both scenarios and classifiers. This allows us to conclude that the bicoherence-based classifiers are the most robust with respect to aspect angle variations among those considered. They provide correct classification probabilities at a level of 83-84% for Scenario #2, and 89-93% for Scenario #3. In the ranking of feature extraction techniques, the cepstrum features take second place with correct classification in the range from 72% to 88%. The worst results are obtained with the ZBT and the NBC. The correct classification probability of 52% obtained using the NBC classifier with the ZBT feature extractor can be accounted for by taking into consideration the sensitivity of the technique to aspect angle variations, as well as the poor approximation of the probability density function.

In fact, the correct classification probability is not the only parameter for measuring ATR system performance. In addition, the confusion matrix has to be estimated and analyzed for correct assessment of the classification performance. The confusion matrix indicates the probability of assigning a feature vector x to a class c_j if it actually belongs to class c_i.

Confusion matrices for four considered feature extraction techniques, SVM classifier and Scenario #2 are listed in Table 5.7:

- For all the techniques considered, class AH-64 is classified with the smallest error (for KT and Cepstrum techniques this class is classified errorless). Misclassification errors are equal to 0.2% and 13.6% for BCH and ZBT techniques, respectively.

Table 5.7: Confusion matrices. Scenario #2

ZBT features

	AH-64	An-26	B-52
AH-64	86.4	11.6	2
An-26	16.3	80	3.7
B-52	17.9	28.8	53.3

KT features

	AH-64	An-26	B-52
AH-64	100	0	0
An-26	0	86.1	13.9
B-52	17.5	39.5	43

Cepstrum features

	AH-64	An-26	B-52
AH-64	100	0	0
An-26	1.7	98.3	0
B-52	75.6	7.7	16.7

BCH features

	AH-64	An-26	B-52
AH-64	99.8	0	0.2
An-26	0.1	97.3	2.6
B-52	8.6	40.4	51

- The aerial target An-26 is predicted by the Cepstrum technique with the smallest error (1.7%) and the BCH technique provides a misclassification error equal to 2.7%. If the KT approach is used, 13.9% are misclassified as belonging to class B-52 instead to An-26. The worst probability of correct classification is provided by the ZBT, because only 80% of the patterns are predicted correctly and 16% are misclassified as belonging to class AH-64.

- Class B-52, is the most complex one for all considered feature extraction techniques. The highest probability of correct classification equal to 53.3% is provided by ZBT. The bicoherence-based features take the second place in classification performance providing a probability of correct classification of more than 51%. Similar conclusions can be pointed out from the results obtained for the KT feature extractor. The worst results are provided by Cepstrum-based features (only 17% of testing data are predicted correctly).

From the results presented in Table 5.6, we can conclude that the TF-based methods providing extraction of cepstrum-based and bicoherence-based features show the greatest robustness with respect to aspect angle variations. The results obtained for Scenario #2 prove that the information concerning phase coupling provides the best immunity with regard to aspect angle variations.

Influence of atmosphere turbulence

Clouds can corrupt aircraft range profile due to atmosphere turbulence, which influences aircraft aspect angle, pitch and roll randomly. It can lead to a decrease in correct classification probability rate. In order to study the influence of the atmosphere turbulence, random variability of aspect angles has been modelled introducing variable aircraft course, roll and pitch [146]. Example of how the parameters were varying is depicted in Fig. 5.37.

Following an approach similar to that proposed in Scenario #1, the training data set is constructed in the same way by using clear, i.e. computed under absence of the turbulence. The testing data set is constructed using the radar returns corrupted by the turbulence effect.

Correct classification probability rates estimated in atmosphere turbulence environment are presented in Table 5.8. The following peculiarities should be emphasized from the comparison of the results presented in Tables 5.5 and 5.8:

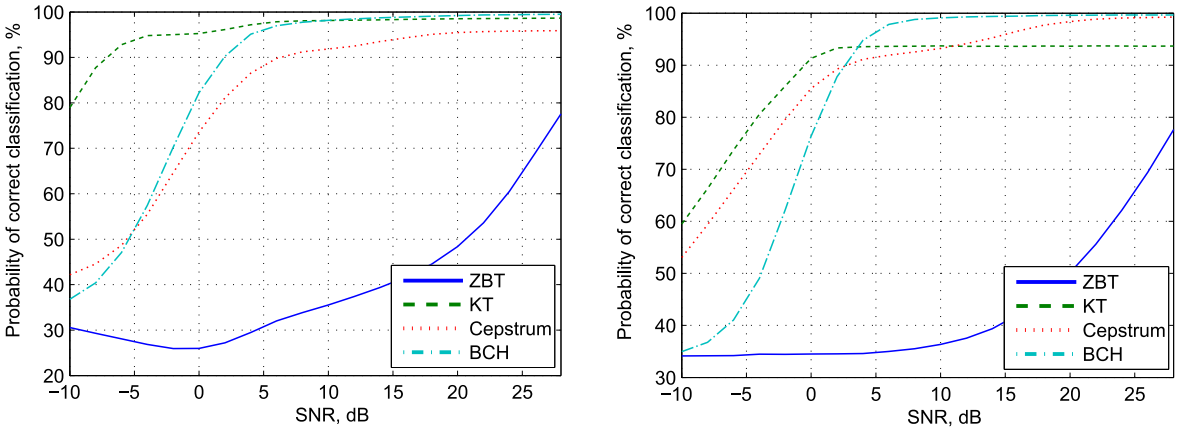

(a) SVM classifier (b) NBC

Figure 5.36: Influence of SNR on classification performances, Scenario #1

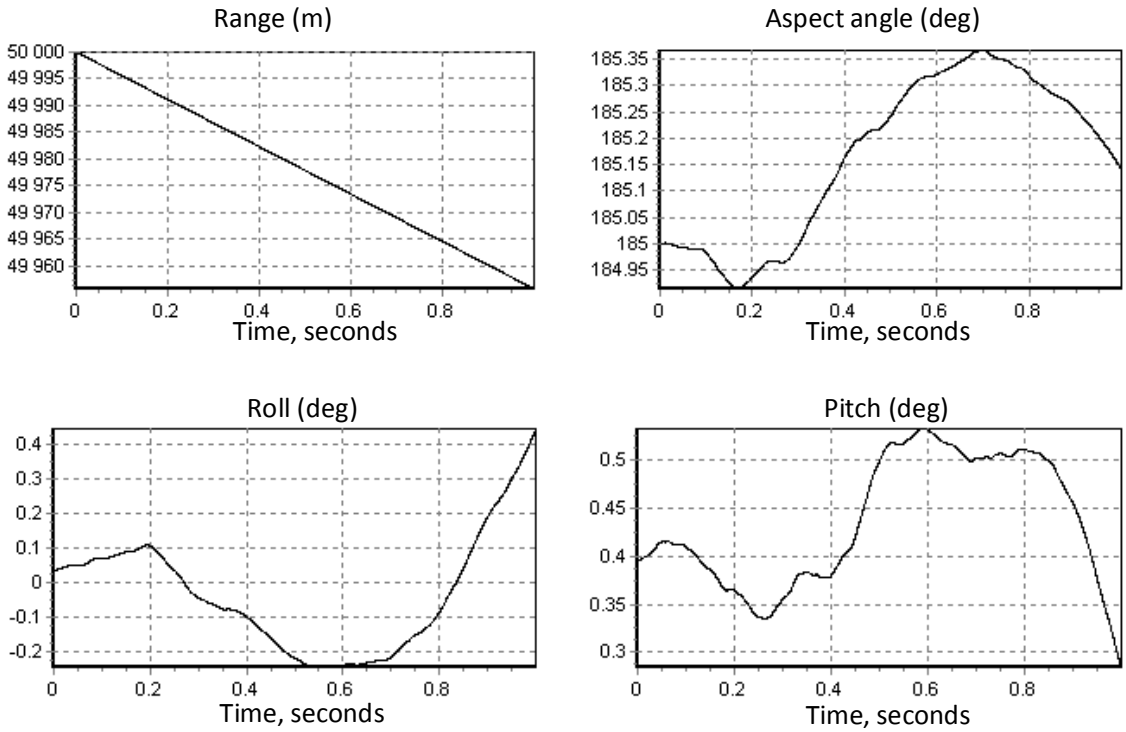

Figure 5.37: Variability of aspect angle, roll and pitch under atmosphere turbulence. Radar data correspond to this parameters is used for testing, whereas clear data (without variations of angles) is used for training

Table 5.8: Classification rates computed in atmosphere turbulence environment

Classifier	Feature extraction technique			
	ZBT	KT	Cepstrum	BCH
SVM	98.46	96.17	90.43	99.43
NBC	99.43	92.45	98.59	99.65

- Correct classification probability rates tend to decrease comparing to Scenario #1 (see Table 5.5).
- The best classification performance is achieved by the BCH technique. Therefore, this technique provides the highest robustness to the turbulence effect. It should be also noted, that the difference referred to Scenario #1 is less than 0.1%.
- The correct classification probability obtained by using ZBT is by 1% lower for SVM, and 0.5% for NBC, comparing to the values presented in Table 5.5.
- In the case of the KT features, the probabilities are by 2.5% and 1% lower for SVM and NBC, respectively.
- The highest influence of the turbulence is observed for the cepstrum-based features (correct classification probability decreases by 5.5% and 1% for SVM and NBC, respectively.

Influence of SNR onto classification performances

In real-life situations, radar records are commonly corrupted by Additive White Gaussian Noise (AWGN). A study of classification performance under the influence of AWGN is therefore of great practical interest. The noise ϵ in our signal model (5.29) is simulated as AWGN, with a variance of σ^2, and added to the observations.

In the experiments considered below the data sets from Scenario #1 are used, and the variance of AWGN is varied to provide the various SNRs. The SNR is computed as $10\log_{10}\left(\frac{W(y)}{W(AWGN)}\right)$, where $W(y) = \frac{1}{MP}\sum_{n=1}^{P}\sum_{m=1}^{M}|y_n(m)|^2$ is the power of the radar return y, and $W(AWGN) = \frac{1}{NM}\sum_{n=1}^{N}\sum_{m=1}^{M}|\epsilon_n(m)|^2$ is the power of the noise.

The classification performances estimated for the various SNRs are presented in Fig. 5.36. For the SVM classifier, the best performance is achieved by the KT technique (see Fig. 5.36a). This technique provides considerably better performance compared to the other three techniques considered for SNR$\leq$10 dB. The BCH technique performance is similar compared to that of the KT approach for SNR$\geq$10dB.

NBC demonstrates quite different results (see Fig. 5.36b). The KT approach provides worse results compared to SVM classifier. It is better than the other three techniques for SNR$\leq$3dB. For SNR$\geq$ 3dB, the BCH technique provides the best performance.

The worst probability of correct classification is provided by the ZBT in both classifiers, due to the huge feature space transformations caused by the AWGN.

It should be noted that the results demonstrated in this Section are obtained for a sequence of P radar returns. Therefore, the classification rates in Fig. 5.36 should be interpreted as the ones obtained not for a single pulse, but for a sequence of P pulses.

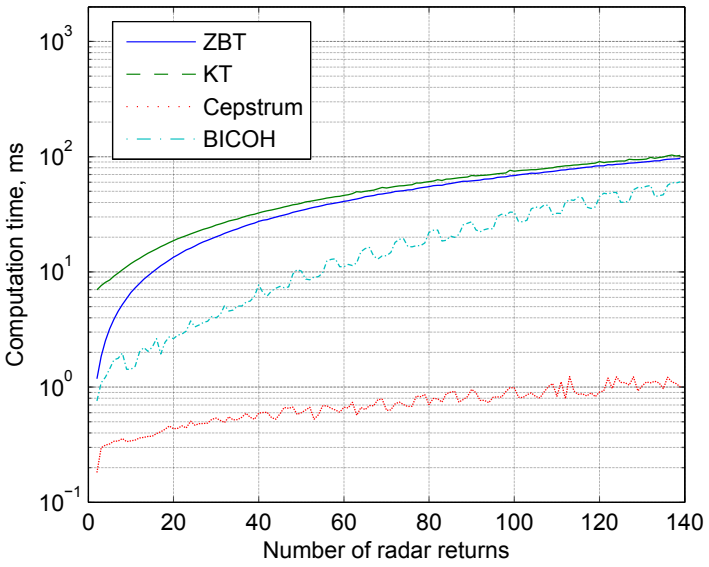

Figure 5.38: Time elapsed for feature extraction depending on number of radar returns

Analysis of computational complexity

The computational complexity of classification methods should be estimated for comparison reasons. The main difference between the approaches considered is in feature extraction. We will therefore, estimate the computational complexity of the classification methods considered in terms of the time required for feature extraction. The elapsed time was estimated on a computer equipped with 64-bit Redhat Enterprise CentOS Linux working on 2 x 3.0 GHz Quad-core Intel XEON CPU.

Fig. 5.38 shows the dependence of the elapsed time on the number of radar returns processed. The shortest feature extraction time is obtained for cepstrum features, it is equal to 1 ms for 140 radar returns. The time elapsed for feature extraction by HRRP-based approaches is the longest due to the aligning procedure: 100 ms are required to process 140 radar returns. The BCH method is of higher computational complexity than cepstrum-based technique, and lower than HRRP-based techniques. The time required to extract features from 140 radar returns by BCH technique is equal to 60 ms.

E) Discussions

A multi-component radar echo signal contains particular information related to both the underlying object shape and the micro-Doppler frequency content. Some underlying dependencies are therefore, contained in the recorded radar data. HRRP provides knowledge about object shape and geometry. Micro-Doppler contributions contained in radar echoes give us additional information about the number of engines as well as both the number of turbine or helicopter rotating blades or aircraft propellers and their angular velocities. In this Section, we are focusing just on the novel features physically caused by phase coupling between micro-Doppler frequencies and those caused by rotating target parts. Bicoherence is a quantitative measure providing an estimation of phase relationships (phase coupling), i.e. frequency-phase dependencies contained in backscattered radar data and used as particular discriminative features.

A distinctive property of the bispectrum-based signal processing is its robustness against additive Gaussian noise. Because of this, the performance of the bicoherence-based technique (coherent approach) could outperform the performance of an HRRP-based technique (non-coherent approach).

Speckle is a disadvantage in relation to HRRPs because speckle causes phase decorrelation between the signals related to different backscattering centers spatially distributed over the aircraft fuselage and hence it is aspect dependent.

In our suggested approach, we also use phase relationships, however they are physically caused not by speckle but by micro-Doppler contributions provoked by a rotating propeller, as well as by rotating turbine or helicopter blades. These micro-Doppler contributions depend largely on corresponding rotational velocities but not on the spatial distribution of backscattering centers located on the aircraft fuselage which move, depending on the aspect angle. Only the latter micro-Doppler contributions are used as distinctive classification features in our approach. This is the key difference between the common HRRP-based approach and our suggested bicoherence-based approach.

Three targets considered in our stufy differ from each other in size, shape, geometry and spatial structure. Therefore, one would expect good classification performance using conventional information features represented in the form of HRRPs. Hence, in the case when half of the available data is used for training, and the second half - for testing, probabilities of correct classification of over 99% are obtained for ZBT and BCH features. It should be stressed that micro-Doppler contributions extracted in the suggested form of novel bicoherence-based features are not dependent on the object size and shape. They are dependent on phase coupling caused by rotating turbine blades, rotating helicopter blades or rotating propellers. In this Section, we pay attention just to the classification performance referred not to the difference of object size and shape but to the difference of the bicoherence-based micro-Doppler radar signatures.

It should be noted that the number of possible real-life kinematic situations for consideration in the study is limited. Indeed, a helicopter landing, taking off, turning, and straight and level flight might have different BCH signatures for a single helicopter class. Practically however, the aircraft classification problem is commonly solved for the aerial targets flying within a radar surveillance scan sector. Landing and taking off manoeuvres are interesting from the point of view of target classification; however they were not considered in our study. Only straightforward flights executed far from the landing points of helicopter and airplanes were considered in our survey.

IV Summary

Section I contains theoretical background of higher-order spectral techniques, as well as analysis of micro-Doppler signature of human walking by these techniques. Frequency and phase coupling phenomena have been studied for radar backscattered signals of human walking. Presence of frequency and phase coupling has been investigated on modeled and real micro-Doppler radar backscattering related to human gait. Time-frequency distributions, as well as bicoherence-based signatures of non-stationary and multi-component radar returns have been demonstrated and compared between each other. Good similarity between simulated and experimental data have been shown. The reason for using suggested bicoherence-based information features extracted from radar measurements is twofold. First, bicoherence-based information features are robust regarding to additive Gaussian noise and, second, bicoherence-based features provide decreasing the capacity of training set comparing to common spectrogram and, therefore, reliability of classifier

can be improved.

In Section II a novel bispectrum-based feature extraction method from micro-Doppler radar signatures to classify moving radar targets has been proposed. Data were collected using ground surveillance Doppler radar for one, two and three moving persons. Pattern features have been extracted from integrated and averaged short-time bispectrum estimates of transient Doppler radar signals in the form of two types of bicepstral coefficients. Diverse scenarios have been considered and the 11-fold cross-validation test was employed to improve the classification accuracy. Experimental results demonstrate that it is quite feasible to recognize three classes of persons moving in a vegetation cluttered environment using the proposed bispectrum-based features extracted from micro-Doppler radar backscattering. Bispectrum-based pattern features extraction from radar backscattering provides additional insight into moving target radar classification that is superior to the commonly used energy-based information features. The experimental results obtained are useful from the point of view of practical recommendations for security and military ATR systems and open new possibilities for ground moving target recognition and classification.

The problem of aerial target classification has been considered in Section III. The performance of classifiers using information features contained in range profiles and micro-Doppler contributions has been studied. Novel cepstrum- and bicoherence-based classification features have been proposed and analyzed. Proposed classification methods are compared to two state-of-the art techniques using features extracted from HRRP. The influence of target aspect angle variations and SNR have been studied and estimated. The analysis of the influence of the target aspect angle variation demonstrates the advantages of using the cepstrum and bicoherence-based proposed classification features. Therefore, the bicoherence-based classification features can be recommended for modern ATR systems. Further studies could include analysis of joint features extracted from HRRP and TF distributions. This approach would provide a combination of advantages such as both invariance properties to target aspect angle variations and noise sensitivity.

Chapter 6

Automotive radar

In this Chapter we consider several applications of automotive radar. The architecture of the radar is assumed to be FMCW, which was discussed in detail in Chapter 2. In Section I, a new idea of joint usage of automotive radars, video codding and vehicle-to-vehicle communication is presented. Idea was originally presented in paper [16], where the author of the thesis contributed to part related to the automotive radar. We propose a system which reallocates the wireless channel resources in favour of the part of the captured video frame that contains the oncoming vehicle. To achieve this goal we apply the automotive radar for the oncoming vehicle detection and use the image of this vehicle as a region-of-interest for the video rate control. We present the theoretical framework, which describes the basics of such an approach and can serve as a useful guideline for the future practical implementation of the overtaking assistance systems.

The problem of Vulnerable Road Users (VRU) classification by radars with different operating bands is considered in Section II. It is shown that the Doppler spectrum estimated from the radars with lower operating frequency can be considered as a scaled version of the Doppler spectrum estimated from data with higher operating frequency. Two new feature extraction approaches are proposed. The first scheme is based on higher-order spectral invariants estimated from the Doppler spectrum. The second proposed feature extraction approach is named Local Binary Mask (LBM), it is fast and encodes the shape of the Doppler spectrum. The proposed feature extraction approaches are invariant to the averaged velocity of the vulnerable road users and the radar. The approaches are tested on real 24 GHz radar measurements and simulated 77 GHz radar measurements showing the robustness to operating frequency of the radar.

I Usage of automotive radar in application of video-based overtaking assistance

Recently proposed cooperative overtaking assistance systems are based on real-time video transmission, where a video stream captured by a camera installed at the windshield of a vehicle is compressed, broadcast through the wireless channel and displayed to the drivers of vehicles driving behind.

In this chapter we propose a system which reallocates the wireless channel resources in favour of the part of the captured video frame that contains the oncoming vehicle. To achieve this goal we apply the automotive radar for the oncoming vehicle detection and use the image of this vehicle as a region-of-interest for the video rate control. We present the theoretical framework, which describes the basics of such an approach and can serve as a useful guideline for the future

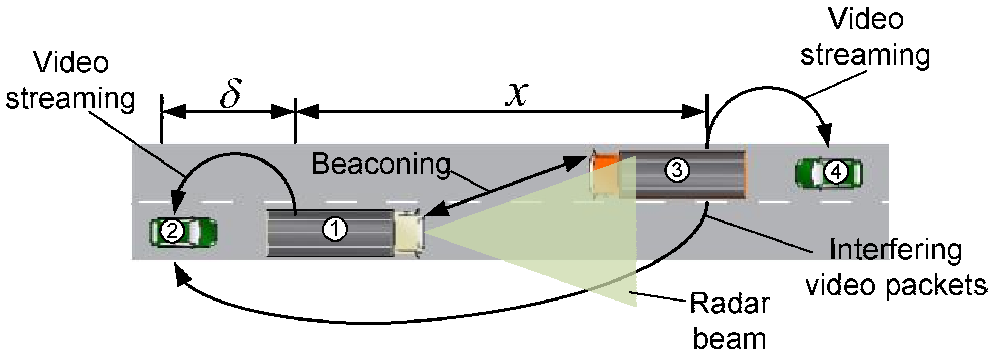

Figure 6.1: The overtaking scenario examined

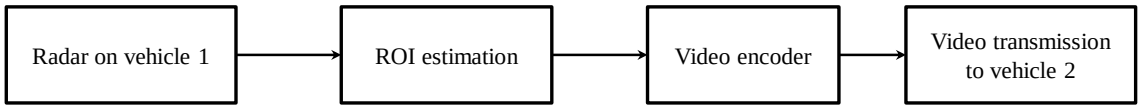

Figure 6.2: General structure of the proposed overtaking system

practical implementation of the overtaking assistance systems. In the rest of the section we will introduce the system and discuss how automotive radar could help.

In order to determine ROI, the azimuth and range of the oncoming vehicle should be estimated. This can be achieved by using monopulse FMCW (Frequency Modulated Continuous Wave) radars [82, 175], which consist of one transmitter and two receivers installed on the overtaken vehicle.

A) Description of the proposed system

Overtaking scenario studied is illustrated in Fig. 6.1. A rural road with a single lane in each direction with two platoons of vehicles approaching each other is considered. All vehicles are equipped with the IEEE 802.11p/WAVE wireless interfaces and permanently generate periodic broadcast cooperative awareness messages (beacons) to announce their presence. Information from video cameras installed in vehicles 1 and 3 are broadcast to vehicles 2 and 4 respectively. Since IEEE 802.11p random access channel is exploited for the video transmission, video packets from vehicle 3 might interfere with video packets from vehicle 1 leading to the increased packet losses at vehicle 2. In order to estimate azimuth and range between vehicles 1 and 3, vehicle 1 is also equipped with the automotive radar, whose radiation pattern matches the video camera field of view. The current distance between vehicle 1 and vehicle 3 is denoted as x, the one between vehicle 1 and vehicle 2 is δ.

The general structure of the proposed system is illustrated in Fig. 6.2. Radar on vehicle 1 is used to estimate ROI for video encoding. Then video is encoded preserving the maximum possible quality of the ROI and remain throughput for non-ROI. Finally, encoded video stream is transmitted to vehicle 2.

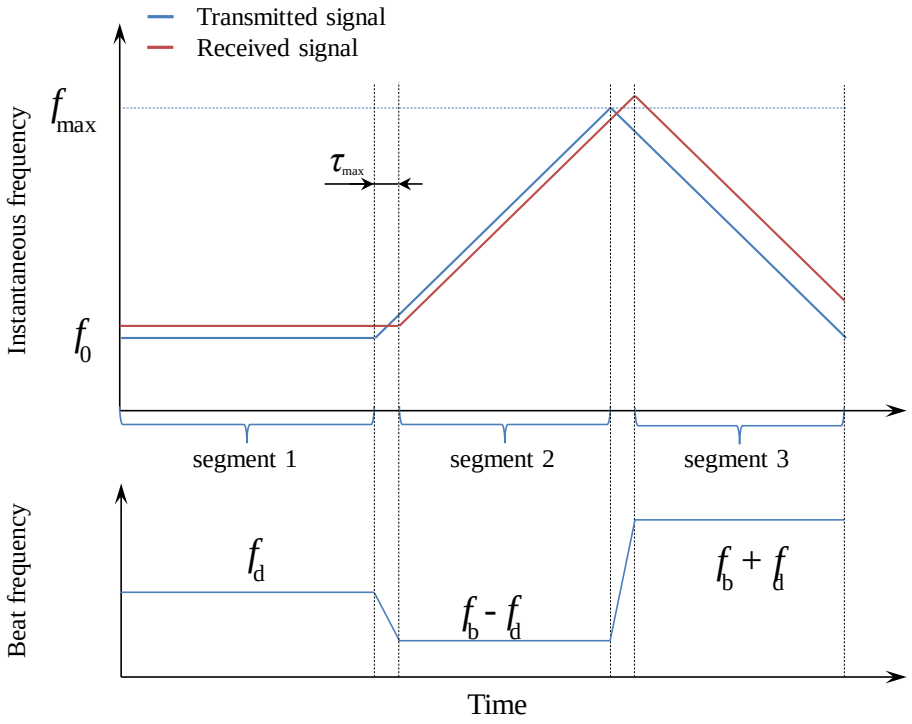

Figure 6.3: Designed waveform for overtaking assistance application. It consists of three segments: segment 1 - to estimate velocity and azimuth of an ongoing vehicle, segments 2 and 3 - to estimate range.

B) ROI determination by a radar

Waveform design

For the proposed system we should design a special waveform to meet requirements of low-complexity and high efficiency. We propose to use three-segment frequency modulation as it shown in Fig. 6.3. Three segments are used to estimate velocity and range without high ambiguity. In such a way, the first segment is used for velocity and azimuth estimation, it has beat frequency equal to Doppler shift. The second segment, is used to estimate range to the object. Similar approaches can be found in literature: [15, 88]. The advantage of the proposed three-segment waveform compared to standard triangular one, is in faster range and velocity estimation. The disadvantage is erroneous estimation of parameters when a number of targets having the same velocity; and high level of interference in case of incoming car and tress along the road. If the current velocity of the car is known than interference from trees and stationary object could be suppressed.

Velocity estimation

Assume we are working inside the first segment of waveform shown in Fig. 6.3. The output of the radar is a radio signal represented as a complex vector by quadrature baseband inphase I and quadrature Q components:

$$\omega(t) = I(t) + jQ(t). \tag{6.1}$$

Two components in (6.1) are used as the representation of the positive and negative frequencies

and they are defined as:

$$\begin{aligned} I(t) &= \sum_{k=1}^{K} A_k \cos(2\pi f_d^{(k)} t + \phi_k) \\ Q(t) &= \sum_{k=1}^{K} A_k \sin(2\pi f_d^{(k)} t + \phi_k), \end{aligned} \tag{6.2}$$

where K is the number of scatters at the radar line-of-sight, A_k is the gain of received signal from reflected k-th scatter, $f_d^{(k)}$ is Doppler frequency shift caused by motion of k-th scatter, ϕ_k is the phase shift caused by reflection from k-th scatter.

The difference between the frequency of transmitted wave and the received one is calculated as Doppler frequency shift:

$$f_d = \frac{2v_d}{\lambda_0}, \tag{6.3}$$

where $v_d = v_1 - v_3$ is a closing rate, v_1 is the velocity of vehicle 1 equipped by radar, v_3 is the velocity of vehicle 3, λ_0 is a wavelength of the transmitted wave.

Velocity estimation is done in three steps:

Step 1. A periodogram of the received signal $\omega(t)$ is calculated as:

$$\Omega(f) = \frac{1}{T}\left| \sum_{t=1}^{T} \omega(t) e^{-\frac{j2\pi ft}{T}} \right|^2, \tag{6.4}$$

where T is the length of $\omega(t)$.

Step 2. If such a value $v > v_1$ can be found that:

$$\Omega\left(\frac{2v}{\lambda_0}\right) \geq h, \tag{6.5}$$

where h is the decision-making threshold, then the decision about the presence of oncoming vehicle is made.

Step 3. If an oncoming vehicle is detected, then the closing rate is estimated as

$$\hat{v}_d = \arg\max_{v > v_1} \Omega\left(\frac{2v}{\lambda_0}\right). \tag{6.6}$$

The example of a periodogram of radar signal received during segment 1 of the waveform (see Fig. 6.3) frequency content is illustrated in Fig. 6.4. The data is obtained in real life scenario at highway for scenario shown in Fig. 6.1. Used analogue to digital converter has low accuracy and provides a low signal to noise ratio. A peak corresponding to closing rate 75 km/h indicates the velocity of a vehicle 1 with installed radar. This peak appears due to backscattering from stationary objects, such as tress and billboards etc. The speed could also be obtained by other devices, such as speedometer. The peaks at closing rate smaller than 75 km/h m/s correspond to ground clutter as well as to targets moving in the same direction but with the smaller speed. For the suggested approach they are considered as inessential targets, because, are not involved in process of overtaking. One more peak is present at speed of 155 km/h. This peak corresponds to the vehicle moving towards the radar and is in paramount importance for our application. If a wide peak appears with the speed higher than the speed of the radar, then the system make a decision about presence of the oncoming vehicle. For the above example, the decision threshold is chosen to be $h = -40$ dB.

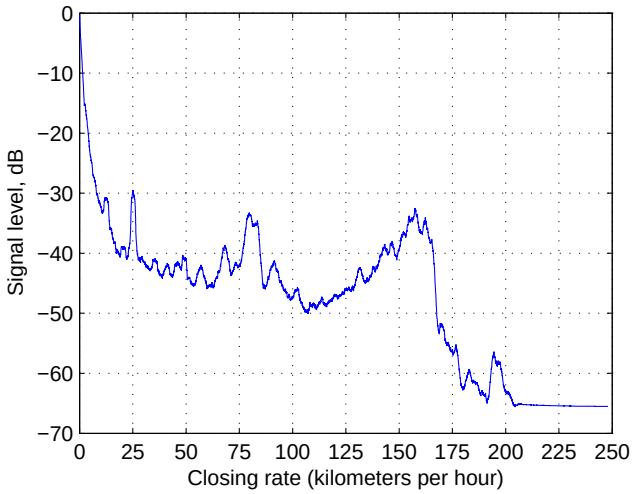

Figure 6.4: Periodogram of real life scenario at highway for scenario shown in Fig. 6.1.

Azimuth estimation

Two output signals from both radar receivers in the overtaken vehicle are given as $\omega_1(t)$ and $\omega_2(t)$ in the form shown in (6.1). From (6.2) it follows that the received signal can contain a number of contributions from scatters in the radar line-of-sight. Signals $\omega_1(t)$ and $\omega_2(t)$ are passed through the phase compensation stage and then filtered by the bandpass filter with the passband centered at frequency $2\hat{v}_d/\lambda_0$ in order to extract the contribution from oncoming vehicle only. Then the sum ω_+ and the difference ω_- patterns are computed

$$\begin{aligned} \omega_+(t) &= \omega_1(t) + \omega_2(t) \\ \omega_-(t) &= \omega_1(t) - \omega_2(t), \end{aligned} \tag{6.7}$$

and azimuth is estimated according to amplitude comparison technique as:

$$\varphi \sim \arcsin\left[\frac{\lambda_0}{\pi d}\arctan\left(\frac{|\omega_-|}{|\omega_+|}\right)\right], \tag{6.8}$$

where d is a distance between two receiving antennas, $|\omega_-|$ and $|\omega_+|$ are the amplitudes of difference and sum patterns, respectively.

Range estimation

The transmitted waveform is a frequency modulated signal with central frequency at f_c, upward modulated frequency at $f_{\max}$ and downward frequency $f_{\min}$. The received waveform is also a frequency modulated signal with shifted central modulated frequency and with time delay, which allows computing the range as [137]:

$$x = \frac{cf_fT}{2(f_{\max} - f_{\min})}, \tag{6.9}$$

where T is a period of the modulation signal, f_f is a beat frequency.

All parameters in (6.9) are known, except for f_f, which is estimated from beat frequency at segment 3 of our waveform (see Fig. 6.3) as $f_f = f_{b1} - f_d$.

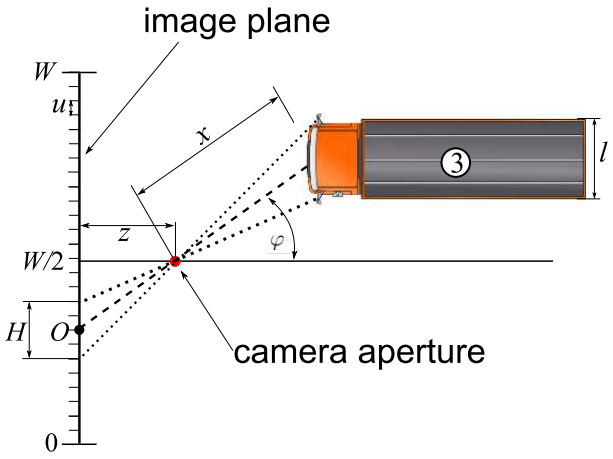

Figure 6.5: Pinhole camera model of the considered application

ROI determination

The pinhole camera model [62] is used for mapping the scene to image the plane of the camera. Let us define W as a width of the image plane in pixels, z as a focal length, u as a pixel pitch, l as a width of an oncoming vehicle. The focal length and the pixel pitch are based on the specifications of camera used. The width of a vehicle can be assumed equal to the width of the road lane. The mapping procedure of the oncoming vehicle into the image plane can then be done as illustrated in Fig. 6.5. In this figure, the middle point of ROI is calculated as

$$O = \left\lfloor \frac{z \tan\varphi + uW/2}{u} \right\rfloor, \tag{6.10}$$

and width of ROI as

$$H(x) = \left\lfloor \frac{lz}{u \cdot x \cos\varphi} \right\rfloor. \tag{6.11}$$

Finally, a pixel with coordinates (i, j) belongs to ROI, if

$$O - H(x)/2 < i < O + H(x)/2, \tag{6.12}$$

and the fraction number of region-of-interest pixels $\alpha(x)$ in a video frame at range (inter-platoon distance) x can be computed as

$$\alpha(x) = \frac{H(x)}{W}. \tag{6.13}$$

Fig. 6.6a shows an example of one frame captured by the camera of the overtaken vehicle. The corresponding frames received at the overtaking vehicle and displayed to its driver are shown in Fig. 6.6b–6.6c for the three systems considered above. Due to the high level of interference-induced packet losses, the system without beaconing is not acceptable in practice since error concealment algorithm copies slices from outdated frames, what leads to the fact that the oncoming vehicle is not displayed in a timely manner. In contrast, the systems with beaconing allow showing the opposite lane image with low transmission latency. Moreover, the usage of ROI coding permits better quality of the oncoming truck (one can compare its visual quality in Fig. 6.6d and 6.6c).

Thus, our results demonstrate that, in comparison to the state-of-the-art approaches [61] and [172], the proposed system significantly increases the visual quality of the frame region, which contains the oncoming vehicle. This helps the driver to detect the danger well in advance, what ultimately contributes to the road safety.

(a) Captured video frame

(b) Received video frame without beaconing and without radar-based ROI

(c) Received video frame with beaconing and with radar-based ROI

(d) Received video frame with beaconing and without radar-based ROI

II Pedestrian classification by automotive radar via frequency band invariant features

Robust real-time algorithm for the classification of VRU objects (normally pedestrians and vehicles) is a key component of radar-based pedestrian protection system [136, 160]. Even though, different sensors could be used for this purpose [57, 58, 92], the main advantage of the radar is possibility of target parameters estimation like distance, azimuth angle, relative velocity etc. Typically, a decision about presence of targets in front of a vehicle is made by classification system using features extracted from a raw data. As a classifier researches propose to use artificial neural networks [131], support vector machine [70], a polynomial classifier [90]. As features for classification a number of different target parameters have been considered: Doppler profile, range profile and radar cross-section [90, 131, 134]. With those features discrimination of pedestrian and vehicle can be performed with probability above 90% [71, 131]. However, in this study we assume that only continuous wave radar is available, and therefore only Doppler information is available. This scenario put less costs to the radar system and supplemental hardware.

One of the ongoing challenges is to design a system with invariant property to the frequency band of the radar sensor [13], since due to the regulations, automotive radars have two different frequency bands: 24 GHz and 77 GHz. Therefore, the objective of the chapter is to design a pedestrian classification scheme which will be invariant to the frequency band of the radar sensor and the velocity of the radar. The following contributions can be outlined:

- Two solutions for classification of pedestrians by data collected with different frequency bands are proposed. The first solution is encoding the Doppler spectrum by novel shape descriptors, named Local Binary Mask. The second proposed solution applies scale invariant features.

- A new approach of Doppler spectrum generation at given aspect angle is introduced. This approach allows classification of radar data from various frequency bands; and can be applied to any non scale invariant features.

- The proposed approaches are verified on the real radar measurements collected by stationary 24GHz radar and simulated 77GHz radar data.

The peculiarity of two proposed approaches is the ability to extract features from a Doppler spectrum obtained during short observation period (less than 40 ms, see [72]).

Scale-invariant features [94, 95, 142] are well known for computer vision tasks, however, not have not been used to provide radar frequency band invariant classification. However, these features have a high potential for providing different invariances for radar target classification. Idea of using scale-invariant features for radar target classification is not novel. Previously, researches have applied this concept for range profile classification of ships [74, 76, 183]. Performance of scale-invariant features on classification of Doppler profile has not been studied, and is a purpose of this section.

The proposed solution applies to two problems:

- Single intelligent radar system used for pedestrian classification by long range radar (LRR) and short range radar (SRR) operating at different frequencies (77 GHz and 24 GHz respectively). Intelligent radar system uses the same algorithm without a prior knowledge of the operating frequency. Fig. 6.7a illustrates the first application.

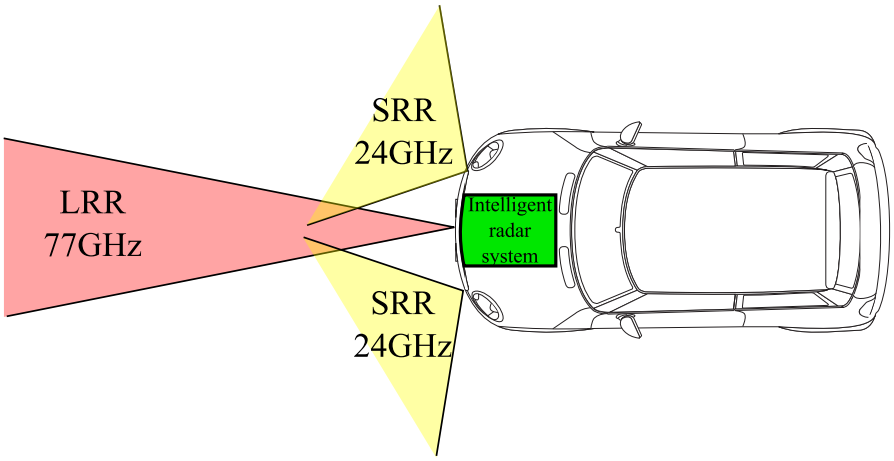

(a) Single intelligent radar system used for LRR and SRR

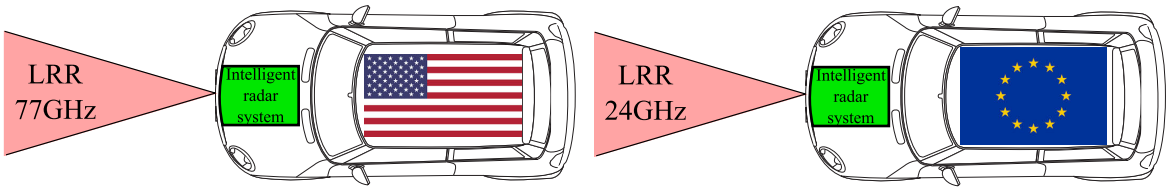

(b) Single intelligent radar system used independently of radar operating frequency

Figure 6.7: Application of proposed frequency band invariant automatic radar classification system

- Depending on targeting country, manufacturers change radar modules due to allowed frequencies to be used by radar. The proposed solution will allow using of a single intelligent radar system for different radar modules. Fig. 6.7b illustrates the second application.

The main idea of this section is to show that classification system could be trained only on data collected with the highest possible carrier frequency; then the system will classify radar data collected with any lower carrier frequency without tuning.

We will use two different directions at which target can move: longitude and lateral directions. The direction straight to / away from the radar is called longitude. As a lateral movement we mean motion at orthogonal direction to the radar, 90^o aspect angle.

A) General scheme

The overall scheme of the proposed system is illustrated in Fig. 6.8. Our task is to detect the presence of moving objects and determine the class of them (vehicle or pedestrian) using intelligent radar system equipped in a vehicle.

The intelligent radar system consists of the continuous wave Doppler radar, analogue-to-digital converter (ADC) and signal processing unit. The Doppler radar emits generated RF signal and receives a reflected signal. The received signal is demodulated using I/Q demodulator and the resulting signal is used for analysis. The signal at this points is a superposition of Doppler signals caused my motion of the scatterers in front of the radar.

The signal at the output of the Doppler radar is first digitized by ADC. Then, the amplitude Fourier spectrum is estimated. Next the spectrum is filtered to remove noise; we propose to use spectral subtraction algorithm [171] for filtering with the hard thresholding after. Detection of

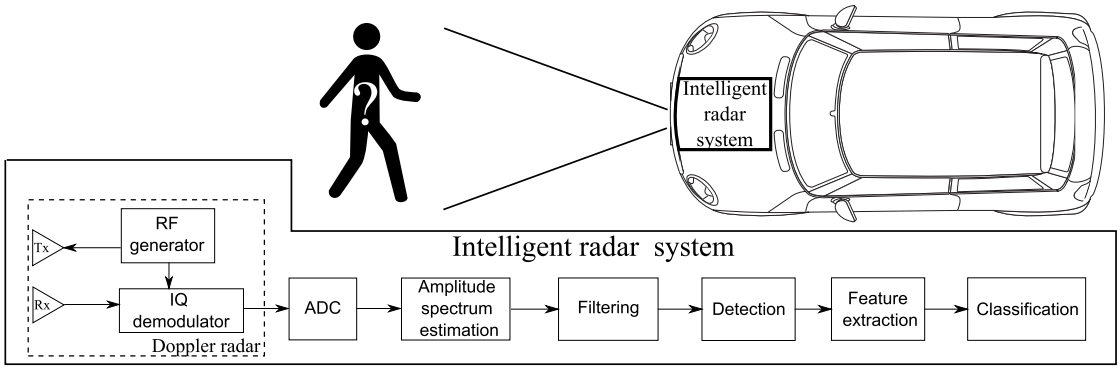

Figure 6.8: General structure classification system

the moving targets is performed by comparing the energy level of the filtered Doppler spectrum with the fixed threshold according to the Neyman-Pearson criterion [51]. The threshold is set according to the variance of the noise and given probability of false alarm; and it is selected to reject the clutter and stationary objects. Next step is feature extraction; the features are extracted by LBM or HOSI approaches (two proposed techniques). Finally, the features are passed through a classifier and the decision is obtained.

The automotive radar is already equipped into vehicles, and the central frequency is different depending on the country of use. Proposed approaches are robust to the frequency band of the radar, therefore, are robust to used automotive radar (considering only Doppler shift as information). However, the ADC is required to satisfy the NyquistShannon sampling theorem when the highest possible frequency band is used.

B) Key observations

Assume that $s \in \mathbb{C}^T$ is the output of the Doppler radar. The Doppler spectrum is defined as:

$$P(f) = \left| \sum_{t=1}^{T} s(t) e^{-j2\pi ft} \right|, \tag{6.14}$$

and

$$s(t) = \sum_{k=1}^{K} a_k e^{if_k t}. \tag{6.15}$$

Meanwhile, the Doppler shift is defined as:

$$f = -\frac{2v\cos\theta}{\lambda} \tag{6.16}$$

From (6.14) and (6.16) it hold that:

$$P(f) = \left| \sum_{k=1}^{K} a_k \delta(f - f_k) \right|, \tag{6.17}$$

where δ is the Dirac delta function.

Observation 1. *Given two radars with wavelengths $\lambda_1 > \lambda_2$, such an aspect angle θ_2 of the second radar could be found for which the Doppler spectrum of the first radar P_1 and of the second radar P_2 of the same target will relate as $P_1 = \alpha P_2$.*

Proof: Let's assume that an object is a multi-scatterer reflector, we will consider each scatterer independently. Doppler spectrum is a energy distribution of the Doppler shifts caused by those scatters over a fixed greed of frequencies[1]. Considering the observation for one point scatterer we will then generalize to the multi-scatterer object. For one point scatterer object moving towards the radar with velocity v and at aspect angle θ_1, the Doppler spectrum has a peak at $f_1 = -2v/\lambda_1 \cdot \cos\theta_1$:

$$P_{\lambda_1}(f) = \begin{cases} |a_1| & \text{if } f = f_1; \\ 0 & \text{if } f \neq f_1. \end{cases} \tag{6.18}$$

where λ_1 is the wavelength of the radar, $|a_1|$ is RCS of the scatterer, here we assume that no noise is present. The Doppler spectrum will have only a single pick for a one point scatterer. If two radars are available with wavelengths λ_1 and λ_2, such that $\lambda_1 > \lambda_2$, then the resulting Doppler spectrum will be:

$$P_{\lambda_2}(f) = \begin{cases} |a_2| & \text{if } f = f_2 = -2v/\lambda_2 \cdot \cos\theta_2; \\ 0 & \text{if } f \neq f_2. \end{cases} \tag{6.19}$$

where $|a_2|$ is RCS of the second target.

Then, an object moving at aspect angle θ_1 and velocity v at the radar with wavelength λ_1 will cause the same Doppler shift as an object at the radar with wavelength λ_2 at aspect angle:

$$\theta_2 = \operatorname{acos}(\lambda_2/\lambda_1 \cdot \cos\theta_1), \tag{6.20}$$

Substituting (6.20) into (6.19) we obtain:

$$P_{\lambda_2}(f) = \begin{cases} |a_2| & \text{if } f = f_2 = -2v\cos(\operatorname{acos}(\lambda_2/\lambda_1 \cdot \cos\theta_1))/\lambda_2) = f_1; \\ 0 & \text{if } f \neq f_2. \end{cases} \tag{6.21}$$

Next a normalization of Doppler spectrums is performed:

$$P_{\lambda_1}(f)/|a_1| = P_{\lambda_2}(f)/|a_2| \quad \forall f, \tag{6.22}$$

Therefore, the Doppler shifts observed in two radars are equal (f_1=f_2) if the above mentioned ratio (6.20) between aspect angles is satisfied. Taking into account the latter notice and (6.17), for Doppler spectrums P_1 and P_2 we will have a relation that $P_1(f) = \alpha P_2(f)$ where $\alpha = |a_1|/|a_2|$ is an attenuation factor depending on the aspect angle and operating frequency. For multi-scatterer object the observation holds if all scatterers are moving within the same aspect angle and separated in Doppler, which is true for moving vehicles and it is a rough approximation of human walking.

According to the Observation 1, the normalized Doppler spectrum of longitude (straight to the radar) moving object collected by the radar with 24 GHz operating frequency is equal to the normalized Doppler spectrum collected with 77 GHz operating frequency at the special aspect angle $\theta \approx 108^o$;

Observation 2. *Given two radars with arbitrary wavelengths λ_1 and λ_2, the Doppler spectrum of the first radar P_{λ_1} and of the second radar P_{λ_2} are scaled ($P_{\lambda_1}(f) = \alpha P_{\lambda_2}(\beta f)$), where β is a constant value depending on the wavelengths and aspect angles.*

[1]The grid of frequencies will be always fixed because ADC with fixed sampling frequency is used independently of the radar.

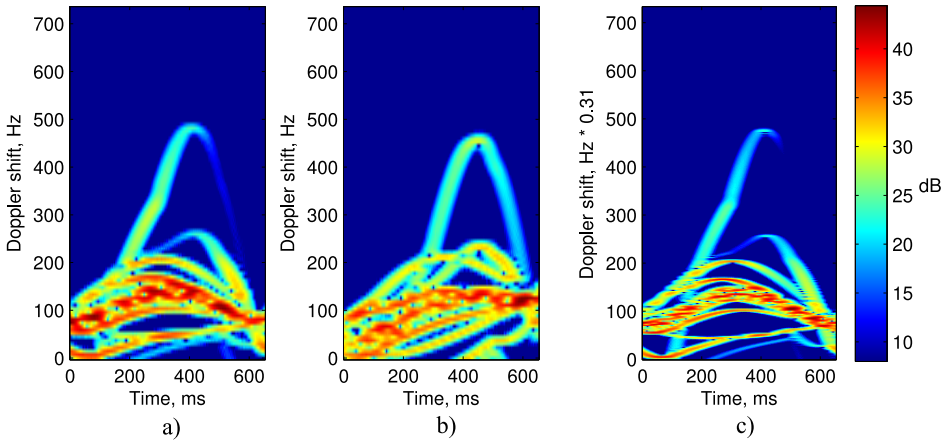

Figure 6.9: Examples of the Doppler spectrum computed for human walking with the parameters: (a) operating frequency 24 GHz, aspect angle 180^o (b) operating frequency 77 GHz, aspect angle 105^o (c); operating frequency 77 GHz, aspect angle 180^o.

Proof: Let's assume that an object is moving at constant velocity v and aspect angle θ, then the Doppler shift is $f = -2v\cos\theta/\lambda$. If two radars are available with different wavelengths (λ_1 and λ_2) and different aspect angles (θ_1 and θ_2) then $f_1 = -2v\cos\theta_1/\lambda_1$ and $f_2 = -2v\cos\theta_2/\lambda_2$. It can be shown that $f_2 = f_1\theta_2\lambda_1/\lambda_2\theta_1$. Therefore, the Doppler spectrums P_{λ_1} and P_{λ_2} obtained with two different wavelengths λ_1 and λ_2, respectively, are scaled by a factor λ_1/λ_2:

$$P_{\lambda_1}(f) = \alpha P_{\lambda_2}(\frac{\lambda_1}{\lambda_2}f) \tag{6.23}$$

According to *Observation 2* the Doppler spectrum collected with 77 GHz radar is a scaled version of the Doppler spectrum for 24 GHz data by the factor $l = \lambda_1/\lambda_2 \approx 0.31$.

Next we will analyse the Doppler spectrum of a walking pedestrian, collected by radars operating at 24 GHz and 77 GHz. For analysis we use the simulation of the human walking given in [30]. The radar data is simulated with sampling frequency of 5514 Hz for a human walking with velocity 0.88 m/s.

Fig. 6.9 illustrates examples of the Doppler spectrum computed for human walking. Fig. 6.9 (b) and (c) are obtained with operating frequency 77 GHz with aspect angle 105^o and 180^o, respectively. Fig. 6.9 (a) is obtained with operating frequency of 24 GHz and aspect angle 180^o. From a visual analysis it can be seen that the Fig. 6.9 (a), (b) and (c) are similar if we don't take into account the scaling factor. These similarities are the key components of the proposed techniques.

Fig. 6.10 show example of spectrograms collected by radars operating at 24 and 77 GHz. We can notice strong similarity in the patterns at spectrograms, this similarity is used in the Thesis to obtain frequency band invariant classification. Operating frequency 77 GHz provides higher separability of the body parts, therefore, spectrogram is more informative. That is why, the ATR system must be trained at data coming from higher operating frequency.

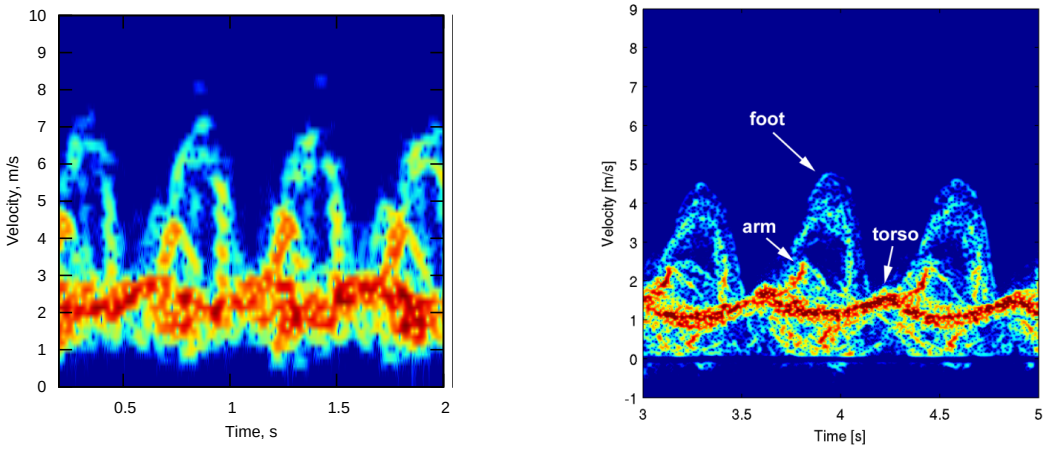

(a) 24 GHz real radar data

(b) 77 GHz real radar data, after [19]

Figure 6.10: Spectrograms of human walking collected by 24 GHz (a) and 77 GHz (b) radars. Despite the fact that at radar data of 24 GHz human was walking faster, spectrograms still look similar.

C) Proposed approach

Background

Two new feature extraction strategies are introduced for pedestrian classification based on the *Observations 1 and 2*.

According to the *Observation 1*, the training set of frequency band invariant ATR system should contain data with all aspect angles of the maximum possible operating frequency band. Data should be collected at all possible aspect angles to grantee the frequency band invariant classification. However, this is not suitable for many situations and we propose a scheme for generation of the Doppler spectrum at different aspect angles. After the generation procedure, non-scale-invariant features could be extracted from the Doppler spectrum. New features are called Local Binary Masks (LBM) they are similar to local binary patterns which show good results in computer vision classification [1–3, 97, 124]. The generation scheme and the LBM features are introduced latter in this section.

Based on the *Observation 2*, the Doppler spectrums obtained from radars with different operating frequencies are scaled versions of each other. Therefore, a scale invariant features could solve the problem of using different frequency bands. We choose the Higher-Order Spectrum Invariants (HOSI) [26] as scale invariant features due to several reasons. The HOSI are invariant to amplification, shift, scale transformations, and show good robustness to additive white Gaussian noise.

The idea behind the proposed features is to extract the shape information contained in the Doppler spectrum. The parameters that affect the features are the width the of Doppler spectrum, number of peaks and their relative position. The parameters that do not affect the features are maximum amplitude and initial shift.

Local Binary Mask (LBM)

We designed new descriptors of 1D signals with low complexity and required invariant properties. We named new descriptors as Local Binary Mask (LBM) which similar in spirit to Local Binary

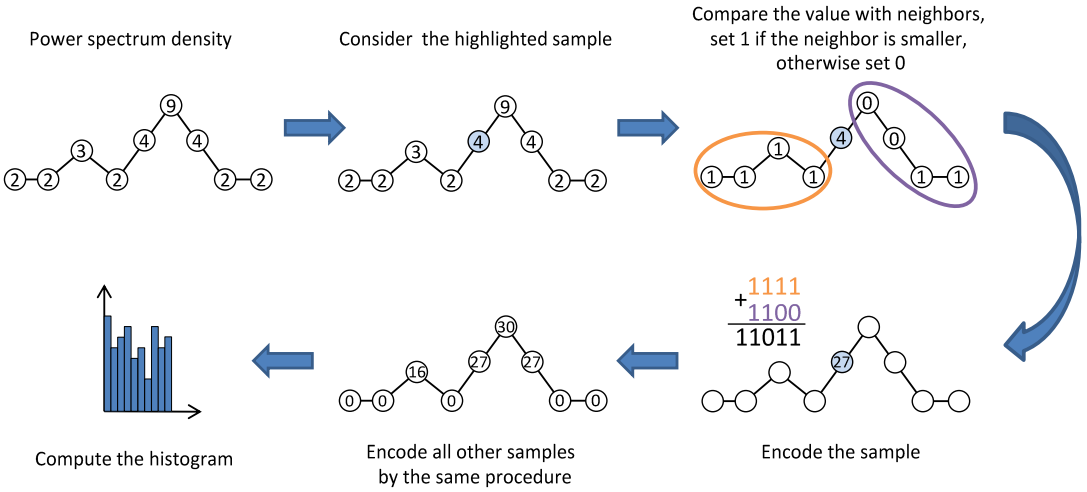

Figure 6.11: Main step to compute LBM descriptors of the Doppler spectrum (power spectrum density)

Pattern (LBP) [1–3, 97, 124].

The first step to calculate LBM features is encoding the input sequence by a binary mask. Given the log-scaled Doppler spectrum $P_{(db)} \in R^T$ it is transformed as:

$$L(n) = \sum_{k=-(K-1)/2}^{(K-1)/2} \{2^{|k|-1} \mid P_{(db)}(n+k) < P_{(db)}(n)\}, \tag{6.24}$$

where K is the length of the window.

In other words, each value in the Doppler spectrum is compared to local neighbours and weighted by distance function $d(k) = 2^{|k|-1}$ if the value is smaller.

After the Doppler spectrum has been encoded, the histogram is computed:

$$H_i = \sum_n \left\{ 1 \mid L(n) \in \left[ib, (i+1)b\right) \right\}, \; i = 0, 1, ...B, \tag{6.25}$$

where B is the number of bins, b is the width of the bin.

The LBM features are invariant to the global (macro) velocity of the target. The motion of the whole object causes a shift in frequency domain, and as the result shift of the Doppler spectrum.

The LBM features are invariant to the range to the target and radar cross section; this is achieved by the amplitude invariant property. Multiplication of the Doppler spectrum by a constant α causes the logic operator in (6.24) to be $\alpha P(n+k) < \alpha P(n)$ which is invariant to multiplication of both sides.

The main advantage of the LBM features is low computational complexity because of usage of only logic operators and summations. Fig. 6.11 summarizes new descriptors. As an input they take power spectrum density, then each sample is compared to neighbours and encoded by value that describes comparison analysis. After all samples being encoded, a histrogram is computed and used as final feature by the method.

Generation of the Doppler spectrum at given aspect angle

Unfortunately, the LBM features are not invariant to the scale factor of the Doppler spectrum. This leads to the fact that they are not invariant to the aspect angle of the target and to the

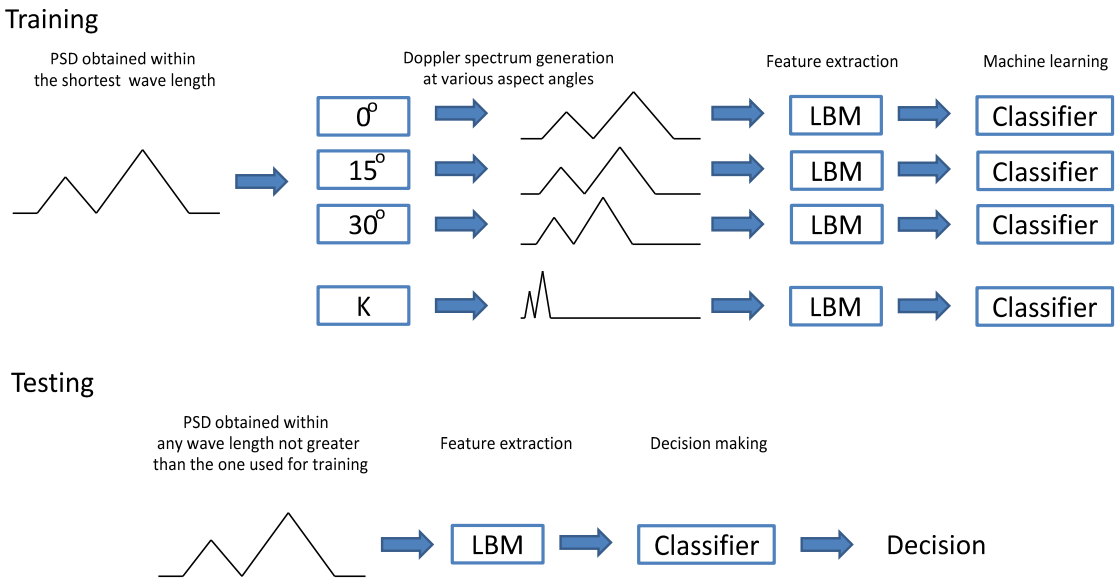

Figure 6.12: Training and testing procedures of a pedestrian classification system based on LBM

operating frequency of the radar. To overcome this problem we will use Observation 1 and will artificially generate the Doppler spectrums given the one at 180^o.

If the object is moving in the longitude direction (aspect angle 180^o) having velocity v, then at aspect angle θ the radial velocity can be estimated as $v_{(\theta)} = v \cdot \cos\theta$. Taking into account the linear relation between velocity and the Doppler shift we can note that: $f_{(\theta)} = f \cdot \cos\theta$. Hence, we can write: $P_{(\theta)}(f) = P(f/\cos(\theta))$. The LBM features are extracted from the discrete signal, and an integration of $P_{(\theta)}(f)$ is required:

$$P_{(\theta)}(f) = \sum_{k \in \left[\lfloor \frac{f}{cos\theta} \rfloor, \lfloor \frac{f+1}{cos\theta} \rfloor\right)} P(k). \tag{6.26}$$

A set of Doppler spectrums can be generated by (6.26) given a Doppler spectrum P of the longitude moving object. In this way, from the Doppler spectrum obtained by the radar with some particular operating frequency we will generate the Doppler spectrums equivalent to the Doppler spectrum obtained with smaller operating band.

The dependence of the radar cross section (RCS) on the aspect angle is not simulated, because LBM features are invariant to amplification of the Doppler spectrum and this step is irrelevant.

Finally, first solution to the problem of frequency band invariant target classification can be summarized as it is shown in Fig. 6.12. First a set of Doppler spectrums of should be obtained at highest possible carrier frequency. Then for each Doppler spectrum, the procedure of Doppler spectrum generation is applied. For each generated spectrum LBM descriptors are computed. Then all descriptors fit into classifier. The training step will be computational consuming, however the decision making is very fast, because we should extract LBM descriptors from the single Doppler spectrum only.

Integrated Bispectrum (IB)

It was mentioned in the Observation 2 that scale invariant features could overcome the problem of usage of the radars with different operating frequency. We choose higher-order spectral invariants

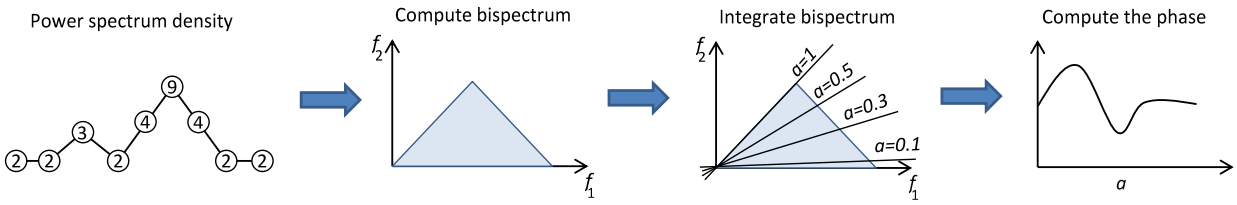

Figure 6.13: Description of HOSI feature extraction

(HOSI) [26] as a feature for Doppler spectrum classification. The HOSI is a shape descriptor based on phase information contained in the signal. Next we are going to overview briefly main steps of computing HOSI descriptors, for more detail information please see the original paper [26]. Steps required to compute HOSI descriptors include the bispectrum estimation, the integration procedure and phase estimation; these chain are illustrated in Fig. 6.13.

The first step is to estimate the bispectrum:

$$B(f_1, f_2) = X(f_1)X(f_2)X^*(f_1 + f_2), \tag{6.27}$$

where $X(f)$ is the Fourier transform of the Doppler spectrum P. In fact it is second Fourier transform of the signal, we took the first one with calculation of the Doppler spectrum.

Then, the bispectrum is integrated according to parameter a, $0 < a \leq 1$, as:

$$I(a) = \sum_{f=1}^{\lfloor (T/2-1)/(1+a) \rfloor} B(f, af), \tag{6.28}$$

where T is length of the Doppler spectrum P.

Finally, the HOSI features are obtained by taking the phase of the $I(a)$:

$$S(a) = \arctan\left(\frac{I_i(a)}{I_r(a)}\right), \tag{6.29}$$

where $I(a) = I_r(a) + jI_i(a)$, $I_r(a)$ and I_i are real and imaginary parts of $I(a)$, respectively.

The HOSI features are formed by computing a set of $S(a)$ values varying parameter a. In this study we choose $a = \{\frac{1}{19}, \frac{2}{19}, \frac{3}{19}, \ldots, 1\}$.

HOSI descriptors are invariant to translation, dc-level, amplification and scale. In addition as it was discussed in Chapter 5, due to the bispectrum transform, descriptors have high immunity to additive Gaussian noise.

Descriptors are calculated right from the the Doppler spectrum and, because of scale invariance, artificial generation of Doppler spectrum is not required. Therefore, training procedure is much easier than for LBM features. Usage of HOSI features in ATR system is illustrated in Fig. 6.14. To train a classifier, features must be extracted from the Doppler profiles obtained with the highest operating frequency, and after, a machine learning should be used to train the classifier. Then, any data from radar with the same or lower operating frequency can be classified with the trained classifier, after the feature extraction step.

D) Data collection

Two proposed approaches to overcome the problem of pedestrian classification by radars with different frequency bands are verified on real and simulated radar measurements. A set of measurements was performed in order to collect radar echoes from pedestrians and vehicles under a number of scenarios. All measurements were performed with the stationary radar only.

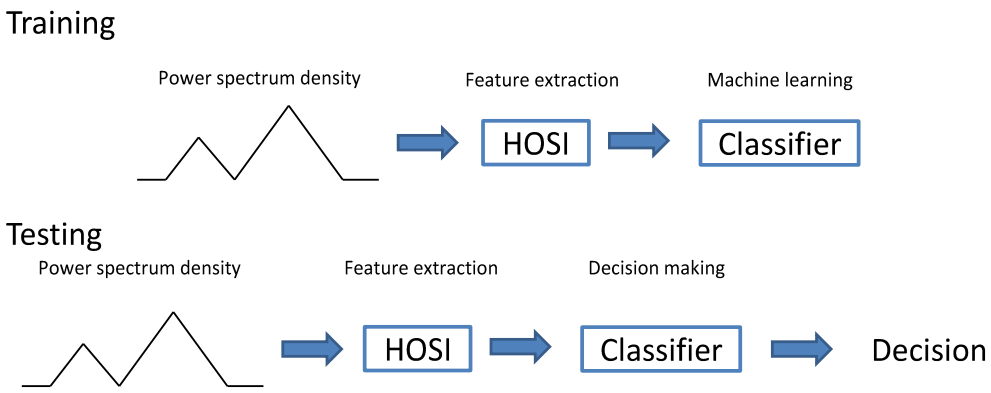

Figure 6.14: Training and testing procedures of a pedestrian classification system based on HOSI

Seven real-life scenarios are considered for data collection:

Sc1) Pedestrian walking at longitude direction. One and two walking persons are considered;

Sc2) Pedestrian walking and running at lateral direction;

Sc3) Pedestrian walking at random path;

Sc4) Vehicle moving at longitude direction;

Sc5) Vehicle moving at lateral direction;

Sc6) Vehicle turns left and goes away;

Sc7) Vehicle performs a manoeuvre;

Considered scenarios with distances to the objects are illustrated in Fig. 6.15.

It is known that a vehicle moving at longitude direction has the sparse Doppler spectrum with a single scatterer. Pedestrian walking at longitude direction has an extended Doppler spectrum with a number of scatterers. Therefore, Scenarios Sc1 and Sc2 can be distinguished easily using the particularity explained above, and it used in our features. When the object is lateral moving, the Doppler spectrums of pedestrian and vehicle are similar. Scenario Sc3 contains radar echoes of pedestrian moving at random path, and therefore, contains all possible aspect angles. Sc6 is interesting because of the turn and not direct path of the moving vehicle. Scenario Sc7 contains the radar echoes of a manoeuvring vehicle; in this case the Doppler spectrum is also extended as in the scenario Sc1, however, it has a different shape.

Radar echoes were collected by 24 GHz continuous-wave radar (InnoSent IPS-146). The parameters of the radar are the following: output power is 18 dBm, beam width in horizontal and vertical domains is 30^o, sampling frequency is 4410 Hz. The Doppler spectrum is estimated using window of length 40 ms (176 samples). Therefore, the frequency resolution is $\Delta f = 125Hz$.

E) Classification results

In this section we will test the two proposed approaches for frequency band invariant pedestrian classification. First, test is performed with training and testing datasets generated from data collected with the same frequency band. In this way we want to test that approaches are suitable

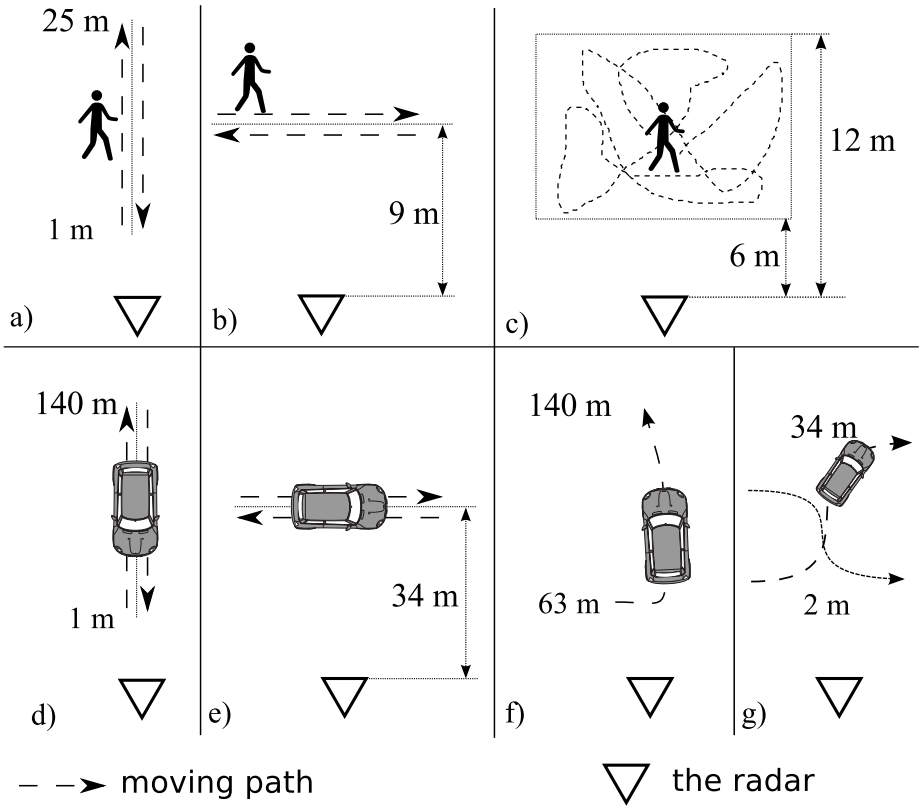

Figure 6.15: Considered scenarios: a) Sc1: One and two persons walking toward and away from the radar; b) Sc2: One person walking or running perpendicularly to the radar LOS; c) Sc3: Person walking at random path; d) Sc4: Vehicle driving towards and backwards the radar; e) Sc5: Vehicle driving perpendicularly to the radar LOS; f) Sc6: Vehicle turns left and goes away; g) Sc7: Vehicle maneuvering

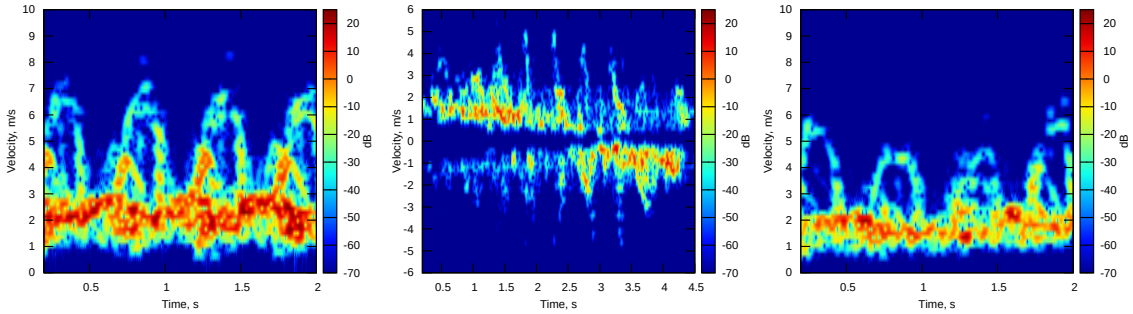

(a) Sc1: pedestrian, longitude (b) Sc2: pedestrian, lateral (c) Sc3: pedestrian, random

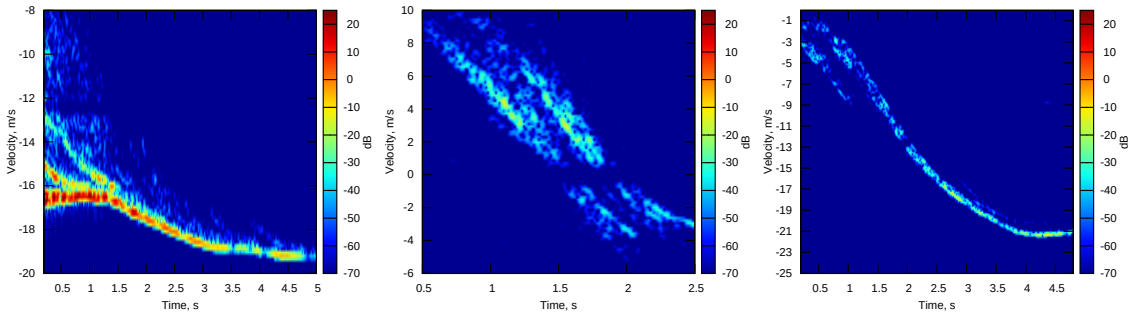

(d) Sc4: vehicle, longitude (e) Sc5: vehicle, lateral (f) Sc6: vehicle, turns left

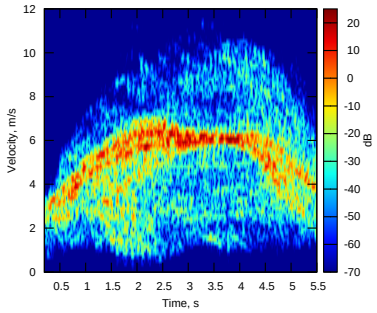

(g) Sc7: vehicle, manoeuvring

Figure 6.16: Examples of spectrograms for each considered scenario

Table 6.1: Classification probabilities obtained with LBM features, values represent the percentage of the data to be classified as pedestrian or vehicle, respectively. Training and testing sets are constructed from 24 GHz radar data

	Input sequence						
	Pedestrian			Vehicle			
Decision	Sc 1	Sc 2	Sc 3	Sc 4	Sc 5	Sc 6	Sc 7
Pedestrian	**93**	**99**	**94**	14	43	40	32
Vehicle	7	1	6	**86**	**57**	**60**	**68**

for VRU classification even with the same operating frequency of the radar. Then, during the second test, the robustness of the approaches to the frequency band will be tested in the following way. The training set will be constructed from the data obtained at one frequency band and the testing set from another.

To classify the object in front of the radar we will use a machine learning approach. First the features are extracted from the Doppler spectrum and then the decision is made by a "learned" system of rules. These rules are learned from the training data set. The classification performance is evaluated by counting the number of correctly classified instances from testing data set.

A support vector machine with soft margins [39] has been chosen as the classifier. The radial basis function is chosen as a kernel function.

24 GHz radar data

To perform the first test with the proposed approaches we construct the training and testing sets from the radar data obtained with the same operating frequency. Seven scenarios are considered as described in the previous section with the radar operating at 24 GHz.

The classifier is tested to distinguish two classes: pedestrian and vehicle. Stationary objects are not considered as a separate class, because they have been already rejected at the detection stage.

The training set is constructed in a simple way to show the effectiveness of the proposed approaches. The training set of pedestrian class contains a short record[2] ($\approx$ 20s) from Sc1 of longitude human walking. The training set of vehicle class contains 2 records (together $\approx$ 19s) from Sc4 and one record ($\approx$ 6s) from class Sc7. The testing set contains records of more than 600s in total for all classes.

The generation of Doppler spectrums at different aspect angles is not performed during the first test, because both sets, training and testing, contain data collected at the same frequency band.

Classification results obtained with LBM features are listed in Table 6.1. We can notice that pedestrians are classified with high probability. The reason why Sc1 has been classified less successfully compared to Sc2 and Sc3 is that the maximum distance to the target is higher. The class of vehicle is classified worse: Sc4 has 86% of data being categorized correctly. A lateral moving vehicle (Sc5) is classified correctly with the probability of 57%, which can be explained similarity if the radar echos from a vehicle in near distance and from a walking human. Results of Sc6 and Sc7 show that the LBM features can not classify manoeuvring vehicles with the high probability rate.

[2]One experimental trial

Table 6.2: Classification probabilities obtained with HOSI features, values represent the percentage of the data to be classified as pedestrian or vehicle, respectively. Training and testing sets are constructed from 24 GHz radar data

	Input sequence						
	Pedestrian			Vehicle			
Decision	Sc 1	Sc 2	Sc 3	Sc 4	Sc 5	Sc 6	Sc 7
Pedestrian	**97**	**100**	**96**	3	80	10	19
Vehicle	3	0	4	**97**	**20**	**90**	**81**

Classification results obtained with HOSI features are listed in the Table 6.2. The class of pedestrian is classified with high classification rate (above 96%). The longitude moving vehicle is recognized with probability of 97%. Lateral moving vehicle is classified correctly only for 20% of data. The class of manoeuvring vehicle is recognized with 81%.

24 GHz and 77 GHz radar data

In the next experiment we will test robustness of the proposed approaches to the operating frequency of the radar.

If the chosen feature extraction algorithm does not provide scale invariant property (e.g. as LBM) then the general scheme is the following. A training set is constructed from features extracted from the radar returns collected at the highest possible operating frequency and then Doppler spectrums at different aspect angles are artificially generated (see Section C)). Therefore, the training set will contain data captured at "all" lower operating frequencies. Then the system can be tested by radar data collected at any operating frequencies lower than the one used for training.

It should be mentioned that HOSI features provide scale invariant property, and thus the step of generation of Doppler spectrums is not included in the procedure.

Unfortunately, real data from 77GHz radar is not available, and we will use simulated data. Simulated 77 GHz radar returns of human walking is used to train classification system. The model used for simulation is described in details in [30]. The model contains motion of 17 body parts and obtained from real biomechanical experimental data.

Training and testing sets are generated in the following way. A training set of pedestrian class contains only 5 seconds of simulated radar (77 GHz operating frequency) returns of human walking toward the radar. A training set of vehicle class contains 2 records (together $\approx$ 19s) from Sc4 and one record ($\approx$ 6s) from class Sc7, all of them are obtained with 24 GHz radar. A testing set is the same as in the previous test and contains records from all scenarios (Sc1-Sc7) collected by 24 GHz radar.

We test LBM features with and without the step of generation of the Doppler spectrums at different aspect angles. The Doppler spectrums of human walking class for testing are generated at aspect angles $\{170^o\ 160^o\ 150^o\ 140^o\ 130^o\ 120^o\ 110^o\ 100^o\}$ given the one at 180^o.

Results of classification pedestrians and vehicles by LBM features are shown in Table 6.3. The classification without generation of the Doppler spectrums is biased to the class of vehicle; the class of pedestrian is recognized with probability at least twice smaller than a random guess (50% for 2-classes problem). The results in this case are not acceptable for VRU classification.

The results become acceptable when the scheme of Doppler spectrums generation is applied.

Table 6.3: Classification probabilities obtained with LBM features, values represent the percentage of the data to be classified as pedestrian or vehicle, respectively. Training set of pedestrian class contains simulated 77GHz radar echoes of human waling, testing sets is constructed from 24 GHz radar data

Without generating of Doppler spectrums

	Input sequence						
	Pedestrian			Vehicle			
Decision	Sc 1	Sc 2	Sc 3	Sc 4	Sc 5	Sc 6	Sc 7
Pedestrian	**26**	**15**	**28**	1	12	1	8
Vehicle	74	85	72	**99**	**88**	**99**	**92**

With generating of Doppler spectrums

	Input sequence						
	Pedestrian			Vehicle			
Decision	Sc 1	Sc 2	Sc 3	Sc 4	Sc 5	Sc 6	Sc 7
Pedestrian	**74**	**99**	**88**	10	45	25	27
Vehicle	26	1	12	**90**	**55**	**75**	**73**

Table 6.4: Classification probabilities obtained with HOSI features, values represent the percentage of the data to be classified as pedestrian or vehicle, respectively. Training set of pedestrian class contains simulated 77GHz radar echoes of human waling, testing sets is constructed from 24 GHz radar data

	Input sequence						
	Pedestrian			Vehicle			
Decision	Sc 1	Sc 2	Sc 3	Sc 4	Sc 5	Sc 6	Sc 7
Pedestrian	**93**	**100**	**95**	3	56	8	16
Vehicle	7	0	5	**97**	**44**	**92**	**84**

Obtained classification probabilities (see Table 6.3, lower part) are close to one obtained when both sets (training and testing) were generated from the same operating frequency data (see Table 6.1). The last note confirms Observation 1.

The classification probabilities obtained with HOSI features are shown in Table 6.4. The obtained results are mostly the same as obtained in Section E) for the same features. The only difference is in the scenario Sc5 which is now recognized with 44%, it could be explained by training with simulated noise-free data of pedestrian class, decreasing a miss-classification error of this class. The similarity of results obtained for different operating frequencies confirms the Observation 2, and concludes that data from radars with different operating frequencies can be cross-classified successfully by scale invariant features.

Results obtained in this study demonstrate that the method based on scale invariant features provides better performance for pedestrian classification rather than training the classifier with multiple variations of the radar data (frequency band, aspect angle etc).

III Summary

This Chapter discusses applications of automotive radar on video-based overtaking driver assistance system and on frequency band invariant pedestrian classification.

In Section I, a new idea of joint usage of automotive radars, video coding and vehicle-to-vehicle communication has been presented. Proposed system reallocates the wireless channel resources in favour of the part of the captured video frame that contains the oncoming vehicle. Automotive radar for the oncoming vehicle detection has been applied and the image of this vehicle as a region-of-interest for the video rate control is used. The proposed system significantly increases the visual quality of the frame region, which contains the oncoming vehicle. This helps the driver to detect the danger well in advance, what ultimately contributes to the road safety.

In Section II the problem of pedestrian and vehicle classification by automotive radar has been considered. Two new feature extraction strategies have been proposed with robust property to the radar operating band. The first proposed strategy is based on local binary descriptors, named Local Binary Mask (LBM). The second approach is based on proposed earlier Higher-Order Spectral Invariants (HOSI). The approaches are tested on real 24GHz radar measurements and simulated 77GHz radar measurements. The HOSI approach has been shown to be robust to operating frequency providing recognition of walking pedestrian at level of 96%; longitude moving vehicle at 97%, lateral at 20-44%, manoeuvring vehicle at 84%. The LBM strategy has shown not so good performance: pedestrian is recognized with 87%; longitude moving vehicle with 88%, lateral moving with 55%, manoeuvring vehicle with 84%.

Chapter 7

Classification of small UAVs and birds by micro-Doppler signatures

The popularity of the small UAVs is increasing. Therefore, the importance of security systems able to detect and classify them is increasing as well. In this Chapter we will show that UAVs could be classified and distinguished effectively by a low-cost radar sensors. We propose a new approach for unmanned aerial vehicles classification using continuous wave radar. We consider all the steps of processing required to make a decision out of the raw radar data. Before the classification, the micro-Doppler signature is filtered and aligned to compensate the Doppler shift caused by the target's body motion. Then, classification features are extracted from micro-Doppler signature in order to represent information about class at lower dimension space. Eigenpairs extracted from the correlation matrix of the signature are used as informative features for classification. The proposed approach is verified on real radar measurements collected with 9.5 GHz radar. Planes, quadrocopter, helicopters and stationary rotors as well as birds are considered for classification. Moreover, a possibility of distinguishing different number of rotors is considered. The obtained results show the effectiveness of the proposed approach. It provides capability of correct classification with a probability higher than 92%.

I Introduction

Unmanned Aerial Vehicles (UAVs) are a special type of aerial targets which have small physical size as they are pilotless. UAVs can be equipped with sensors and weapons for military or civil missions. Civil applications include telecommunication, weather and border monitoring, and remote sensing. Military applications include air reconnaissance, bombing and conducting air combats.

The reason of high importance is that, UAVs could disturb official meetings, as it was in 2010 in Great Hall of the Binnenhof, The Hague, The Netherlands [89]. Another incident happened on September 15, 2013 when the mini quadcopter got very close to German Chancellor Angela Merkel before it crashed to the ground right in front of the Chancellor[138]. The incidents showed how it is important to be ready for such situations and that special systems should be developed to detect the UAV.

One of the common inhabitant of the air space is a bird, and therefore, distinguishing between UAV and bird is of paramount importance for a security system. As it was mentioned, the UAVs have a number of military and civil applications. It makes also important to classify the type of the UAV for estimation of possible dangerousness.

The contributions of rotating turbine or propeller blades in radar backscattering in the form of micro-Doppler contents [30] can contain additional classification information about UAV characteristics. These micro-Doppler contributions are unique classification features for different types of UAVs [43].

In this Chapter we develop a system for classification of the UAV. We consider in detail all processing steps required for feature extraction after target has been detected. These steps include estimation and filtering of the micro-Doppler signature, alignment and the actual feature extraction. The alignment of the micro-Doppler signature is required in order to compensate the Doppler contribution of the target's body motion. We assess the robustness of the extracted features by feeding them to different types of classifiers. The assessment is performed using measured radar data of different types of targets such as aircraft, a quadrocopter, helicopters, stationary rotors and birds. Each target type induces a unique micro-Doppler signature depending on the velocity, orientation and direction of the motion.

The contributions of the Chapter can be summarized as follows:

- A system for classification of UAVs by m-D signatures is developed;
- New robust features in form of basis functions are introduced;
- Performance of the system is measured for real radar data;
- Sensitivity of the system is measured to observation time, SNR, and to rejection of the unknown target.

II Related work

Classification of the UAVs by the radar systems is a novel topic, therefore, in this section we focus on an overview of the aerial target classification by the radar systems.

In the Introduction three main concepts for aerial target classification were mentioned: High Resolution Range Profile (HRRP), Inverse Synthetic Aperture Radar (ISAR) images and micro-Doppler (m-D) signatures. We will consider each of them in detail.

A theory of radar target identification by HRRP is given in [149] where it is argued that HRRP offers promise for radar target recognition. In addition, the authors discuss a number of problems that occur when HRRPs are used. HRRPs have been used for helicopter classification by *Munoz-Ferreras et al.* [121], providing good performance on real radar data. For the continuous wave radar this method is applicable only when wide bandwidth is available, in our case it is not available.

ISAR is technique to represent moving object as a 2 dimensional high resolution image. Change of aspect angle of target over radar integration period used to provide a cross-range resolution. The 2-D images spatial images of the aircraft have been used for classification [21, 84]. *E. Botha* [21] showed that up to 92.18% of correct classification rate can be achieved when the target is observed from many aspect angles. *H. Essen et al.* [52] showed on experimental data, that ISAR technique could be used for imaging of the helicopters; which further usage of image based comparison algorithms for non cooperative classification. *P. Tait* [158] summarized in the review that there are two limits of the ISAR technique for classification: long dwell period required for short timeline engagements; and dependence upon target rotational motion.

The micro-Doppler content arises in radar returns due to the Doppler effect caused by micro-motions [30]. All motions in the scene affect the frequency of the radar's transmitted wave by changing it, with the value of the frequency shift proportional to the radial velocity. Time varying

behaviour of micro-motions forms a micro-Doppler signature in a form of Frequency Modulated (FM) multi-component signals projected onto time-frequency distribution. The micro-Doppler phenomenon has been studied for a long time [36], showing good performance in radar target classification [19]. The characteristics of the micro-motions are unique for each type of target, and they depend on the structure of the object.

B. Bullard and *P. Dowdy* [23] showed that main rotor configuration, rotor parity, tail rotor con figuration and hub configuration can be estimated using the return from a Doppler radar and appropriate frequency domain signal processing techniques. Letter, *L. Du et al.* [47] demonstrated that turbojet aircraft, prop aircraft and helicopter could be classified based on the jet engine modulation characteristics.

A common technique for micro-Doppler analysis is the time-frequency representation [33]. Analysing the time-frequency distribution, *S.-H. Yoon et al.* [177] showed how the number of blades and rotation frequency can be estimated. *A. Cilliers* and *W. Nel* proposed [34] another solution for helicopter parameter extraction using tomographic features. Their scheme contains the velocity compensation block which is also used in our method. A robust method based on the maximum likelihood for helicopter parameter estimation has been proposed by *P. Setlur et al* [145]. Even-though, a number of estimators were proposed for blade number and rotation frequency estimation, this information is not enough to distinguish different models from the same class of UAVs, and additional features are required.

The wavelet transform method incorporated with time-frequency analysis was applied for analysis and decomposition of the m-D signature by *T. Thayaparan et al.* [159]. The work showed that after the signal decomposition the motion parameters of the helicopter can be estimated with higher precision.

J. Park et al. [130] applied the Hilbert-Huang transform, a high-resolution time-frequency technique, on micro-Doppler signature of jet engine modulation. As a result, the decomposition of the signature into several signals was obtained.

Radar based systems for bird detection and analysis are of interest for researches. The bird detection and identification based micro-Doppler features has been proposed by *Q. Zhang et al.* [178]. He showed that beating frequency can be used for identification of the birds. *B. Torvik et al* [161] analysed the K-band radar signature of the a flying duck and showed that around half of the energy is coming from the wings. This studies describes our motivation in considering class of birds to be interesting for separation from UAVs.

We propose new robust features that can be extracted from the micro-Doppler signature. The proposed features are based on basis functions of the micro-Doppler signature and they can be extracted by applying Eigen or Singular Value Decompositions. The resulting features are orthogonal and unique providing essential and uncorrelated information about the target under consideration.

III Signal model

Assume $s \in \mathbb{C}^N$ is a received Doppler signal in the radar, where N is the length of the signal in number of temporal samples. The received Doppler signal is obtained by I/Q demodulation of the reflected radio wave. In the digital form it can be written as:

$$s(n) = \sum_{k=1}^{K} a_k e^{j2\pi n/F_s f_k(n)} + \epsilon(n), \tag{7.1}$$

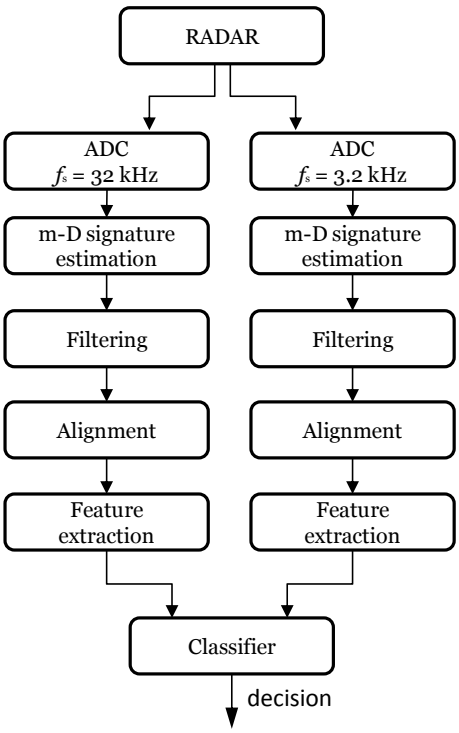

Figure 7.1: Block scheme of the proposed approach

where F_s is sampling frequency, $j = \sqrt{-1}$ is imaginary unit, K is the number of scatters, a_k is reflectivity of the k-th scatterer, $f_k(n)$ is Doppler frequency shift of the k-th scatterer, $\epsilon(n)$ is additive noise.

The micro-Doppler signature depends on the shape, tilt angle, length, number and rotation velocity of the blades. This dependence provides different signals for different jet types, and it is used as the main concept for the proposed approach.

IV Proposed approach

A) General scheme

Scheme of the proposed classification system is illustrated in Fig. 7.1. In order to discriminate objects with wide (helicopters) and narrow (birds, planes) Doppler bandwidth, the radar signal processed by using suggested approach is divided at two separate sampling rates: 32 kHz and 3.2 kHz. All information is contained in the branch of 32 kHz, however, to decrease the processing time we use a second sampling rate (3.2 kHz) with different parameters of feature extraction procedure. There is no practical need of the second ADC (3.2 kHz) as these information could be retrieved from the radar data sampled at 32 kHz followed by a down-sampler. Once the signal from radar is sampled, it passes through the m-D signature estimation, filtering, alignment, feature extraction and classifier blocks, then the final decision (with confidence score) is made. Let us consider all of these blocks in detail.

Micro-Doppler signature estimation To obtain micro-Doppler signature, the received signal must be transformed to time-frequency (TF) domain in order to obtain the energy distribution at

different frequencies per time. The simplest and effective way is to apply Short-Time Frequency Transform (STFT).

Filtering Environment, the radar and the analogue-to-digital converter (ADC) cause time-independent interference (noise pattern) to the true signal. This noise can be estimated by processing the signal-free record. When the noise pattern is estimated it can be removed from the short-time Fourier transform. Good robustness is shown by the "spectral subtraction" [171] method and it is implemented in this work.

Alignment of the micro-Doppler signature We want to classify targets by micro-Doppler signature, meaning by contribution from propellers and not from the target' body. The motion of the body must be estimated and compensated before extracting features from micro-Doppler signature.

Feature extraction The main contribution of the proposed ATR scheme is in extracted features from TF domain. The distinguishing features will be extracted in the form of basis functions of the spectrogram which are processed by amplitude of Fourier transform.

Classifier In this paper, three different types of classifiers are considered in order to evaluate the robustness of the proposed features. The first two classifiers are the linear and non-linear Support Vector Machines (SVMs) belonging to non-probabilistic classifiers, and the third one is the Naive Bayes Classifier (NBC) belonging to probabilistic linear classifiers.

B) Estimation of micro-Doppler signature

The micro-Doppler signature of the moving target is estimated as the magnitude of the spectrogram of the Doppler signal:

$$S(f,t) = \left| \sum_{m=0}^{M-1} w(m) s\Big(m + (t-1)(M-L)\Big) e^{-j2\pi f m/M} \right|, \tag{7.2}$$

where $w(m)$ is the smoothing window function of length M, for instance, Hamming window can be exploited; f is the frequency index; L is the overlap of successive Fourier lengths, expressed in samples ; the dimensionality of the spectrogram is $S \in \mathbb{R}^{M \times Q}, Q = \frac{N-L}{M-L}$.

C) Filtering

The noise ϵ could be removed from the observation s by the "spectral subtraction" noise reduction procedure [171]. The main idea of this approach is subtraction of an estimate of the average noise spectrum from the noisy signal spectrum. We assume that noise exhibits a static frequency profile with a varied gain (due to the adaptive gain control, which amplifies noise clutter).

The averaged noise spectrum is estimated by periodogram:

$$\Upsilon(f) = \frac{1}{Q} \sum_{t=1}^{Q} S^{(\epsilon)}(f,t), \tag{7.3}$$

where $S^{(\epsilon)}$ is a STFT of noise only signal ϵ.

Gain of noise is estimated as a normalized length of the projection of the noisy signal spectrum onto noise spectrum:

$$G(t) = \sum_{f=1}^{M} \frac{\Upsilon(f)S(f,t)}{||\Upsilon||^2}, \tag{7.4}$$

where $||\Upsilon|| = \sqrt{\Upsilon(1)^2 + \Upsilon(2)^2 + ... + \Upsilon(M)^2}$ is a Euclidean norm of the noise pattern. Values of noise's gain could be passed through low pass filter for better accuracy of the filtering procedure.

The noise can be removed from the signature as:

$$U(f,t) = S(f,t) - G(t)\Upsilon(f). \tag{7.5}$$

In order to make U of non-negative value:

$$U(\cdot) = \begin{cases} U(\cdot), & \text{if } U(\cdot) \geq \beta S(\cdot) \\ \beta S(\cdot), & \text{if } U(\cdot) < \beta S(\cdot) \end{cases} \tag{7.6}$$

The threshold is set to be at the level $\beta = 0.01$.

After the spectral subtraction, the signal is not transformed back to discrete time domain because features are extracted from the spectrogram. Due to this no processing of distortions is performed.

Examples of the filtering are shown in Fig. 7.2 for two cases of the class 10. Vertical lines in raw spectrograms correspond to radar interference, which is removed by filtering, also it is visible, that background noise is removed. The averaged noise spectrum $\Upsilon(f)$ is estimated from signal free data. Example of the average noise spectrum for data used in experiments is demonstrated in Fig. 7.3

D) Alignment of the micro-Doppler signatures

In order to extract behaviour of micro-Doppler features the motion of the target must be compensated. This can be done by tracking the change of velocity of the target's body.

It is logically to assume that target's body is a local separate scatterer with highest RCS. Therefore, the contribution of target's body will appear as the energy maximum at the STFT. We need to track this maximum and then compensate the motion. However, the contribution of the stationary clutter is not removed yet. For this purpose we propose to apply a weighting function before estimating the maximum:

$$h(f) = -\gamma e^{-\frac{f^2}{2\sigma^2}} \tag{7.7}$$

where $\gamma = 128000/F_s$, $\sigma = 7 \cdot (3200/F_s)^3$ and F_s is sampling frequency. It should be noticed that the weighting function h is obtained in dB scale.

As initial points to track the target's body motion, we take 10% of samples with the highest amplitude from the spectrogram. Then, an unsupervised clusterings is applied to reduce the number of initial points within the neighbour area. For each remain initial point, the maximum is tracked within local window with first increasing and then decreasing time index. In such a way we obtain a number of possible tracks. Then the track corresponding to the maximum accumulated energy is selected as the target's body track $V(t)$.

The tracked velocity $V(t)$ is approximated by a polynomial of order $p = 1$ to reduce the number of outliers. In such a way the track is assumed to be a simple line, meaning that motion

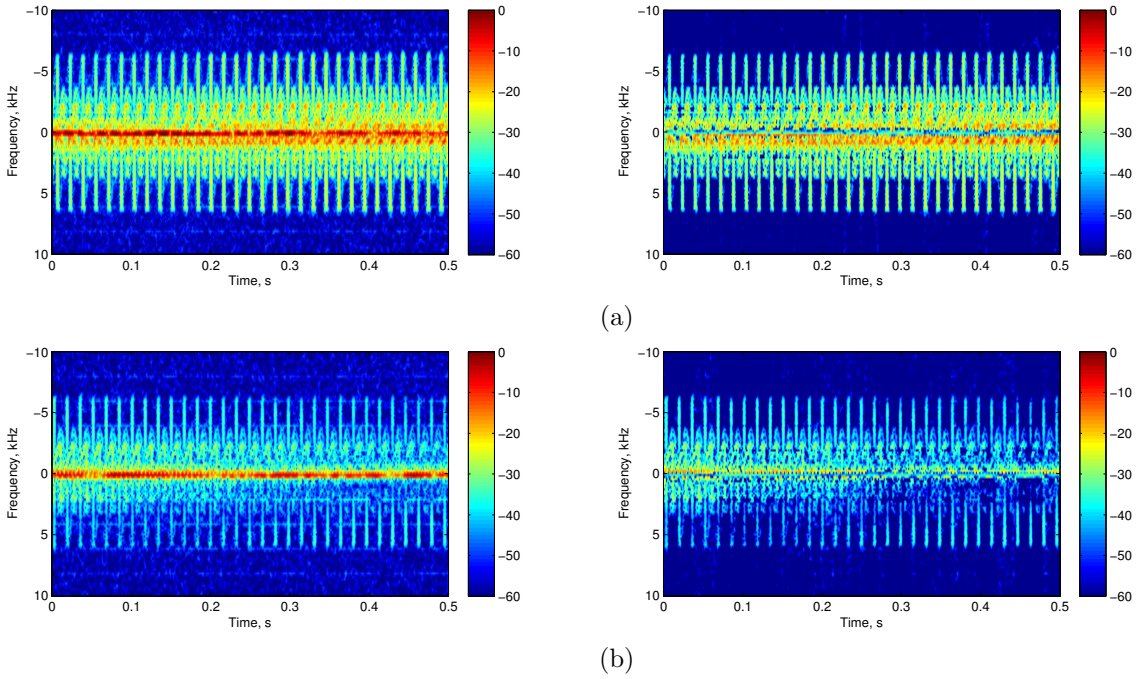

Figure 7.2: Examples of the filtering for two cases (a) and (b): raw spectrogram is on the left hand side; result of the filtering is on the right hand side.

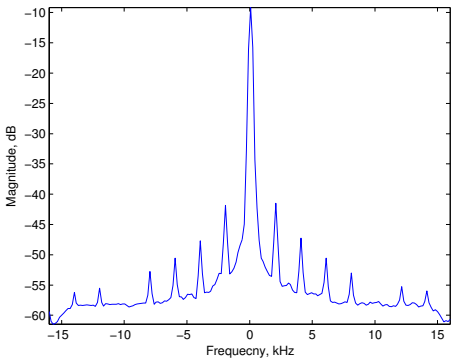

Figure 7.3: Examples of the averaged radar clutter estimated from data used in experiments.

can contain only linear acceleration.

$$\hat{V}(t) = \sum_{l \in [0,p]} \frac{c_l t^l}{l!} = Hc, \tag{7.8}$$

where c_l is the polynomial coefficient of order l, $c = [c_0\ c_1\ ...\ c_p]^T$, and

$$H(t,l) = \frac{t^l}{l!}.$$

The coefficients $c_{0:p}$ are estimated by least square method:

$$c = (H^T H)^{-1} H^T V. \tag{7.9}$$

The micro-Doppler signature is shifted then:

$$\hat{U}(f,t) = U\Big(f + \hat{V}(t), t\Big). \tag{7.10}$$

The last procedure is done by linear interpolation. Examples of successful alignment of the the micro-Doppler signatures are illustrated in Fig. 7.4. For these examples longer observation time was selected: 2 seconds, and polynomial order in (7.8) is selected to be $p = 4$. Fig. 7.4 (a)-(d) show result of alignment for a single flying bird, whereas, Fig. 7.4 e) shows the result for a flock of birds.

Finally, the micro-Doppler signature is prepared for feature extraction.

E) Feature extraction

Micro-Doppler signature contains the bases that have to be extracted for obtaining the classification features. These bases are orthogonal to each other and contain essential information about the rotating parts of the target. After the alignment we assume that the spectrogram can be viewed as a low rank matrix.

First we need to compute the correlation between different frequency components. Correlation matrix is computed as:

$$\Psi(f_1, f_2) = \sum_{t=1}^{Q} \hat{U}(f_1, t)\hat{U}(f_2, t). \tag{7.11}$$

Second step is to estimate eigenpairs $\{v_r, \lambda_r\}$, where v_r is r-th eigenvector and λ_r corresponds r-th eigenvalue, such that $\lambda_1 > \lambda_2 > ... > \lambda_r$. Each eigenpair satisfies the following equality:

$$\sum_{f_2=1}^{M} \Psi(f_1, f_2) v_r(f_2) = \lambda_r v_r(f_1) \tag{7.12}$$

Eigenvectors are orthogonal and unique forming the basis functions of the signal's spectrum. Eigendecomposition of Ψ or Singular Value Decomposition of $\hat{U}$ can be used for estimation of eigenpairs. The steps (7.11) and (7.12) are similar to Principal Component Analysis (PCA) with only small difference. For PCA the data must be mean centred before calculating the correlation matrix. In our case the first (and the most important) eigenvector corresponds to the mean vector of the spectrogram.

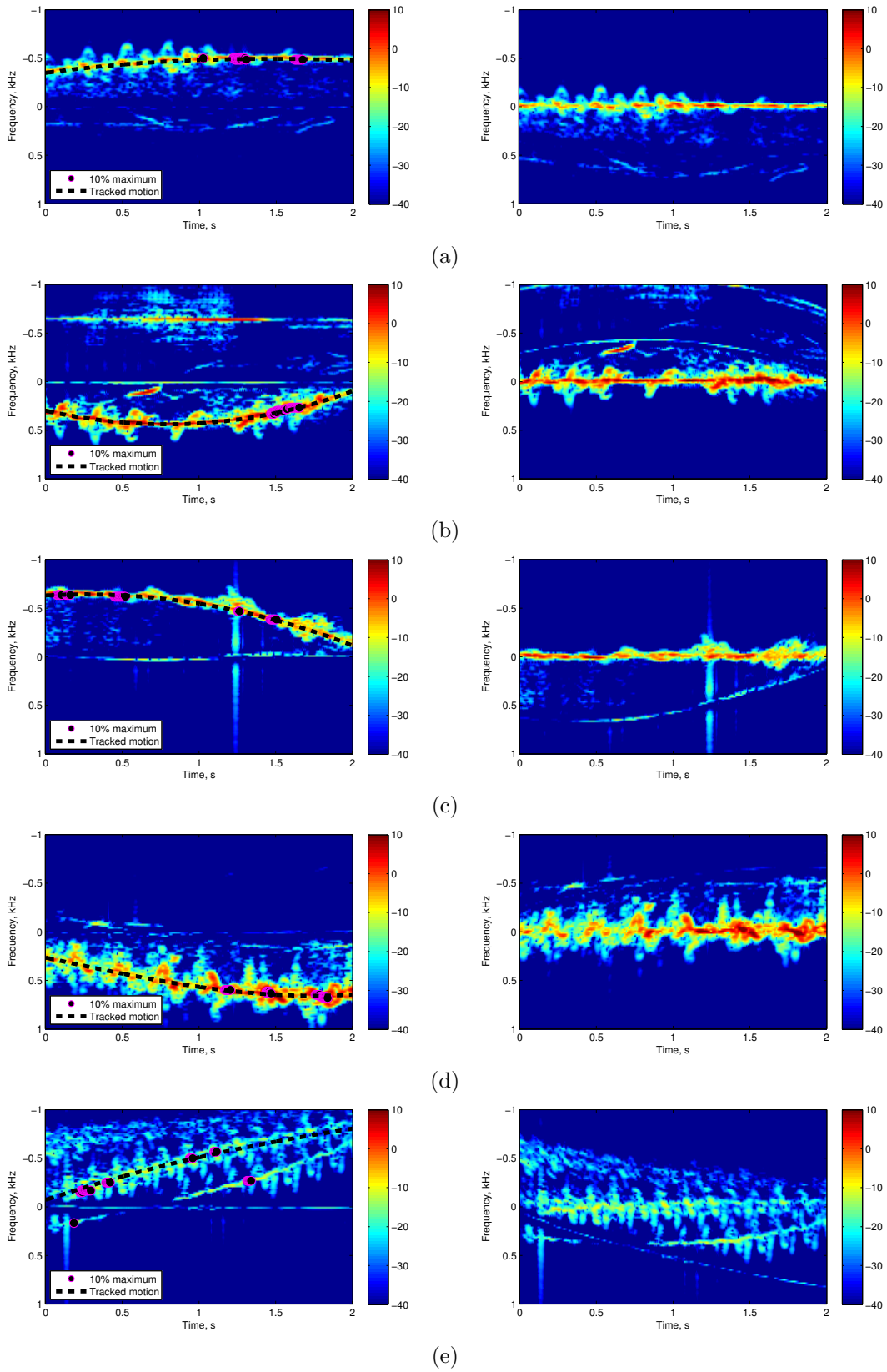

Figure 7.4: Examples of the alignment's results for flying birds: left - raw spectrogram and tracked motion; right - aligned spectrogram

Next, the Fourier transform of the eigenvectors is computed to obtain features with strong "energy compaction" property, i.e. the features where most of the signal information is concentrated. Typically, the signal information is contained in just a few low-frequency components. Due to this property we can calculate only the I first (low-frequency) coefficients to represent the data:

$$y_r = \bigcup_{i=1}^{I} \left\{ \left| \sum_{f=1}^{M} v_r(f) e^{-j2\pi fl/M} \right| \right\}. \tag{7.13}$$

Finally, the feature set is obtained by combining the first Z transformed eigenvectors and Z eigenvalues:

$$F = \bigcup_{r=1}^{Z} \{y_r, \lambda_r\}. \tag{7.14}$$

V Rotor diameter estimation

Different types of UAV have different length of the rotor. As a reference method for classification we suggest to use this feature. Therefore, in this section we are going to consider estimator for the diameter of the rotor.

The diameter of the rotor will be estimated from the spectrogram. For the used estimator we assume that flying object has two blades. From the spectrogram we will estimate velocity of the tip and number of rotations of the rotor per second (to get rotation velocity). Then the rotor diameter is estimated as:

$$D = \frac{VT}{\pi}, \tag{7.15}$$

where V is velocity of the tip in m/s, T duration of one rotation cycle.

The duration of the one rotation cycle is estimated by period estimation of the micro-Doppler signature proposed in Chapter 3. Due to the assumption that rotor has two blades, the estimated period must be divided over 2, because, one blade cause two splashes: one at positive frequencies, then after half of rotation a second at negative frequencies.

The velocity of the blade's tip is estimated through the bandwidth of the Doppler spectrum, considering the width of the splashes. We use the fact that splash happens when a blade is position perpendicular to the LOS, as it was shown angle between rotation velocity and the LOS is $\phi = \pm\pi$. Therefore, the Doppler shift is equal to $f(n) = 2V/\lambda$. The highest radial velocity corresponds to blade's tip, therefore, we propose the following way of tip's velocity estimation:

$$V = \frac{B\lambda}{4}, \tag{7.16}$$

where $\lambda = 0.0316$ m for the used radar system. The half of a bandwidth is used, because the full bandwidth corresponds to splash from two blades.

To compute the bandwidth B first a projection of the spectrogram onto frequency domain is estimated. The projection is estimated by picking the maximum value from from a spectrogram for each frequency index. Then the bandwidth is estimated as width of the projection at -44 dB, the value was found experimentally. An example of the spectrogram and its projection together with the threshold are shown in Fig. 7.5.

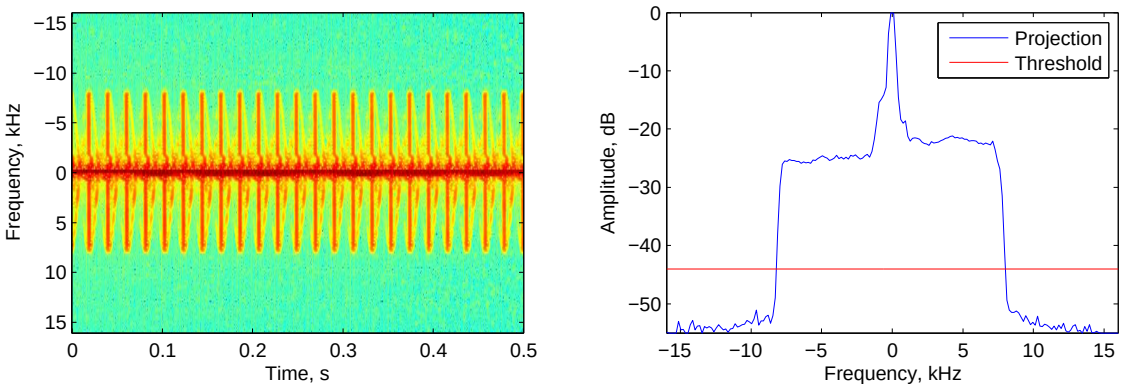

Figure 7.5: Example of the spectrogram from small helicopter, on the left hand side. Result of the projection of spectrogram to frequency dimension, on the right hand side. Red line shows the threshold for bandwidth estimation

VI Data collection

The proposed ATR system is evaluated on real radar measurements. The radar data have been collected with a continuous-wave radar operating in X-band at radio frequency of 9.5 GHz. These radar measurements have been performed within the framework of D-RACE, the Dutch Radar Centre of Expertise, a strategic alliance of Thales Nederland B.V. and TNO. The measured data have been made available for the present study.

The UAVs considered for classification by the proposed technique are listed with their characteristics in Table 7.1. Different types of the UAVs are considered: two planes, a quadrocopter and three helicopters. For comparison, stationary rotating rotors with different number of blades as well as diverse types of birds are considered for classification. At least 30 seconds were recorded of each class. The data were recorded at open space with the distance to target less than 30 m. The aspect angle, distance and velocity were varying as within the real situation. Images of the UAVs are shown in Fig. 7.6.

For classification we formulate two problems:

11-classes problem where each class corresponds to different model of the UAV, and the goal is to determine the correct the type as well as the model.

5-classes problem where each class consists of the data from the same type of aerial object, and the goal is to determine only the type of the flying object.

The radar signal is divided onto a number of non-overlapping segments of fixed length, by processing these segments a decision about the class label is made. The length of one segment is set to 0.5 s. To compute the STFT we use a sliding Hamming window of length $M = 128$ samples $=$ 4 ms with overlapping of $L = 90$ corresponding to $0.9 * 4 = 3.6$ ms. Finally, the features extracted for the two different sample rates are concatenated to one feature vector.

Examples of micro-Doppler signatures of the considered classes are illustrated in Fig. 7.7. The classes can be separated even visually. The features we extract are based on eigenvectors of the signature and the first two of them are shown in Fig. 7.7.

Table 7.1: UAVs used for experimental verification of the proposed ATR system. Type 'P' is for Plane, 'H' is for Helicopter, 'Q' for quadrocopter, 'B' for birds, 'S' for stationary rotors.

Class	Name	Type	# of rotors	Rotor, mm
1	YAK54 plane	P	1	100
2	EasyStar El-Sailor	P	1	108
3	Birds	B	-	-
4	Parrot AR.Drone	Q	4	200
5	1 rotor	S	1	203
6	2 rotor	S	2	203
7	3 rotor	S	3	203
8	4 rotor	S	4	203
9	Mikado Logo 600	H	2 (main, tail)	1350 (main)
10	Mikado Logo 400	H	2 (main, tail)	1040 (main)
11	Align T-REX 450	H	2 (main, tail)	715 (main)

Figure 7.6: Examples of UAVs used for experimental study, from left to right, from top to bottom: YAK54 (class 1), EasyStar El-Sailor (class 2), Parrot AR.Drone (class 4), stationary rotors (classes 5-8), Mikado Logo 600 (class 9), Mikado Logo 400 (class 10), Align T-REX 450 (class 11).

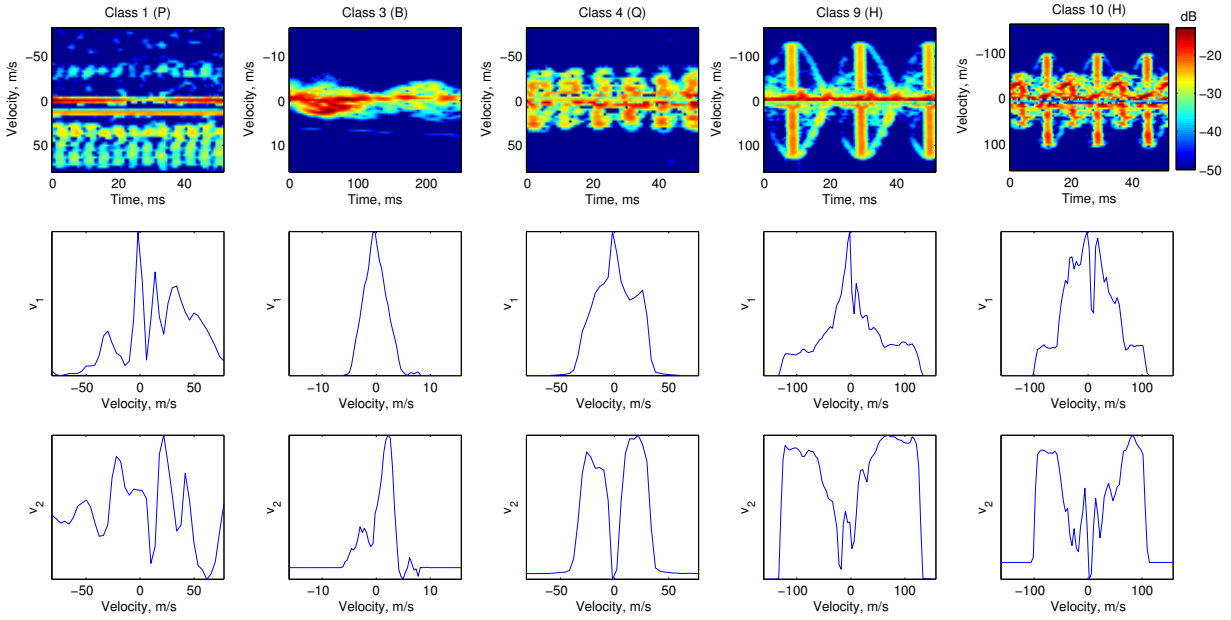

Figure 7.7: Examples of filtered and aligned micro-Doppler signatures of 5 classes (first row); Eigenvectors corresponding to the largest eigenvalue (second row) and the second largest eigenvalue (third row) of Ψ for corresponding signatures. These eigenvectors are basis functions of the micro-Doppler signatures.

VII Classification results

To classify the type of UAV we will use the machine learning approach. All available segments are divided into training and testing sets without overlapping. The decision about class membership is made by a predefined system of rules. The process of defining the system of rules is called learning; it is performed on the training set. The number of correctly classified segments determines the probability of correct classification as ratio to the total number of segments from the testing set.

The K=10 cross-validation technique is applied to obtain robust classification rates (see Chapter 4 Section A) for details).

A) Classification by rotor diameter

Performance of the estimator can be examined by probability density function (PDF). For classes 10 and 11 the PDFs are demonstrated at Fig. 7.8. As it can be seen, the estimator has high accuracy providing the bias at level of -0.0145 m and MSE at level of 0.0165 m for class 10, and bias -0.0166 m and MSE 0.001 m for class 11.

First we will analyse classification performance given by physical features such as rotor diameter. From Table 7.1 it can be seen that types of the UAVs are different by diameter of the rotor. Results of classification by this feature are given in Table 7.2. The highest probability of correct classification is achieved by non-liner SVM classifier at level of $\approx 60\%$.

Confusion matrix for non-linear SVM classifier in case when only diameter is used as a feature is shown in Table 7.3. By this feature, probability to distinguish the helicopter class is at 95%, stationary rotor at 79%, quadrocopter at 70% and planes at 52%; however, class of birds has a

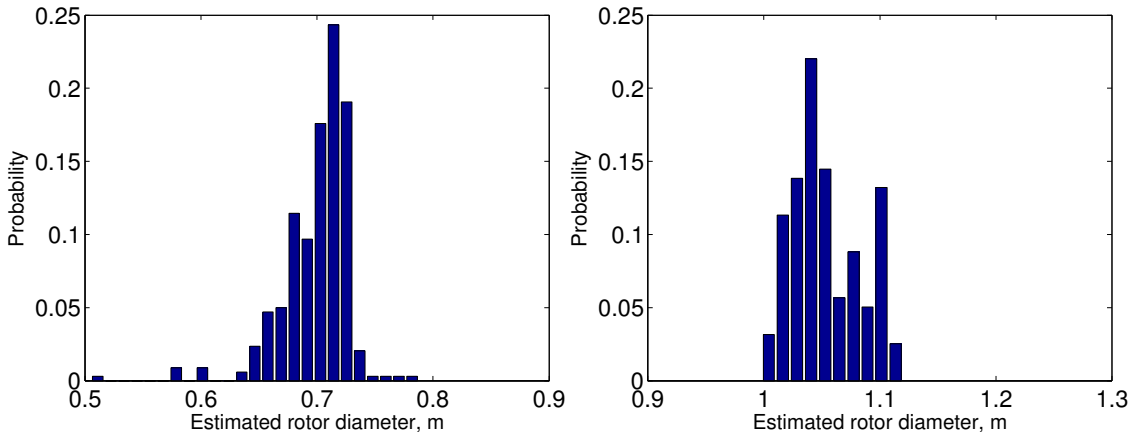

(a) (b)

Figure 7.8: Probability density function of the rotor's diameter estimate, for (a) Mikado Logo 400 (class 10), true value 1.04 m; (b) Align T-REX 450 (class 11),true value 0.715 m.

Table 7.2: Probability of correct classification obtained for 5 classes problem using 10-fold cross validation. Only rotor's diameter is used as a feature

SVM linear	SVM non-linear	Naive Bayes
21.98 %	59.95 %	51.82 %

lot of errors and probability of correct classification is less than 3%.

The reason of non-satisfactory performance by physical feature, such as a diameter of rotor, is that any estimator is optimal under a number of assumptions. These assumptions concern noise model, specification of the blades etc. Moreover, the objects used for experiments (7.1) have the same or similar diameter of the rotor (classes 4-8, or classes 1,2). Therefore, a more sophisticated features are required for satisfactory result of classification. The features proposed in this section are based on descriptors of the Doppler spectrum of the radar return.

Table 7.3: Confusion matrix for non-linear SVM classifier (5 classes problem using 10-fold cross validation). Only rotor's diameter is used as a feature

Class	P	S	B	Q	H
P	**52.27**	0	2.27	10.23	35.23
S	7.92	**79.21**	0	5.94	6.93
B	34.09	9.09	**2.27**	0	54.55
Q	10.48	12.38	0	**70.48**	6.67
H	3.48	0	1	0	**95.52**

B) Classification by extracted features

It is important to study the influence of the feature extraction parameters on the classification result. Therefore, the number of eigenpairs in (7.14) was varied as Z = 1,2,...,14 and the number of calculated Fourier coefficients in (7.13) was varied as I = 1,2,...,40. Total number of 560 classification results were obtained using 10-fold cross-validation for all possible pairs of Z and I. Then, the classification rates were averaged for all values of Z and I, to show the dependence on these variables in Fig. 7.9. Analysing the dependences we conclude the following:

- With increasing the number of Fourier coefficients, SVM classifiers show increase in the performance;
- For Naive Bayes Classifier, the performance reaches the pick with 16 Fourier coefficients, with larger number the performance degrades due to the "curse of dimensionality" phenomenon;
- For non-linear classifiers, such as non-linear SVM, with increasing the number of eigenpairs, the performance degrades; the best result is obtained for only 1 eigenpair extracted.
- For linear classifiers, such as linear SVM and naive Bayes classifier, the best performance is reached when several eigenpairs are extracted: For linear SVM, 4 eigenpairs provide the best performance, for naive Bayes classifier - 5 eigenpairs.

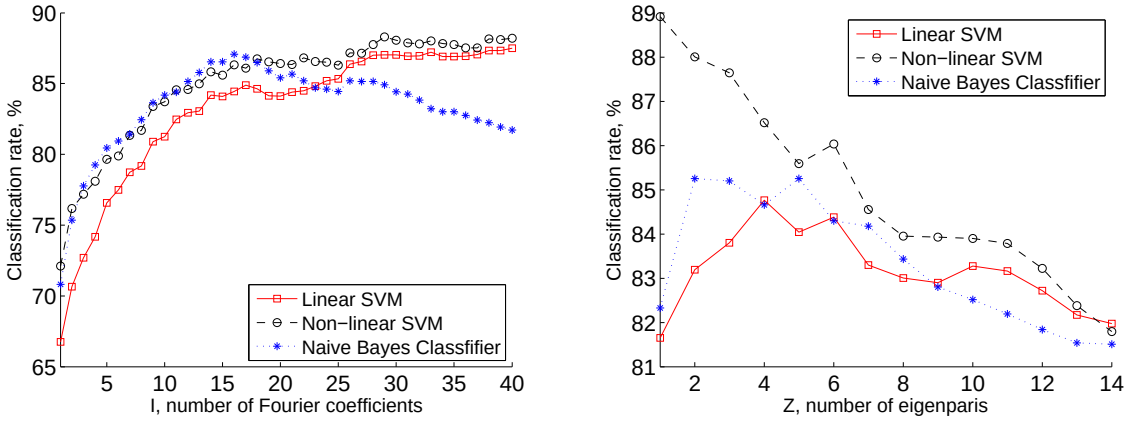

Figure 7.9: Probability of correct classification for 11-classes problem depending on: (a) the number of Fourier coefficients in (7.13); (b) depending on the number of eigenpairs in (7.14)

According to the analysis we selected the following parameters:

- Non-linear SVM: Z = 1, I = 29;
- Linear SVM: Z = 4, I = 33;
- Naive Bayes: Z = 5, I = 16;

Classification results for 5-classes problem and a full feature set are demonstrated in Fig. 7.4. The probability of correct classification ranges from 92.03% by Naive Bayes classifier up to 96% by non-linear SVM. Comparing to the results by rotor's diameter feature (Table 7.2), the benefit of new features is 74% for linear SVM, 36% for non-linear SVM, 40% for Naive Bayes classifier.

Table 7.4: Probability of correct classification obtained for 5-classes problem using 10-fold cross validation.

SVM linear	SVM non-linear	Naive Bayes
95.77 %	96.47 %	92.03 %

Table 7.5: Probability of correct classification obtained for 11 classes problem using 10-fold cross validation.

Sampling type	SVM linear	SVM non-linear	Naive Bayes
3.2 kHz	73.79%	74.75%	69.22%
32 kHz	86.3%	86.14%	88.28%
32 kHz and 3.2kHz	89.86%	92.3%	88.42%

Computed probabilities of correct classification for 11-classes problem are shown in Table 7.5. The results are shown for different sampling frequencies of the signal: 3.2 kHz, 32 kHz and when two of them are applied. The results in Table 7.5 allow us to conclude the following:

- For all classifiers the best results are obtained when two sampling frequencies are used;
- The benefit of processing the signal sampled at two sampling frequencies, compared to the best result out of one sampling frequency, is: SVM linear 3.56%; SVM non-linear 5.85%; Naive Bayes 0.14%;
- The best result is obtained with SVM nonlinear classifier: 92.3%.

Confusion matrix for non-linear SVM with applied 10-fold cross-validation is shown in Table 7.6 to estimate the intra class distribution of classification rates. It can be seen that all targets, except classes {1 2 7 8}, are classified with probability of correct classification higher than 95%. The first two classes have more errors due to the fact that blades are small and their micro-Doppler signatures are similar. The results for classes 5 to 8 show the capability to distinguish different number of rotors. The class #7, three stationary rotors, shows misclassification at level of 15% with the class of four stationary rotors and helicopters class.

In order to show the flexibility of the proposed ATR scheme and classify different types of the UAVs, the following classes were removed from the training set: 1, 5, 6, 7, 9, 10. In this way for each type of the UAVs (plane, birds, stationery rotors, quadrocopter and helicopter) only a single class is used for training. The removed classes are then used to test the system. The results of classification by linear SVM classifier are listed in the Table 7.7. The class of stationary rotating rotor, and the class of helicopters are classified correctly with 100%; the data from class 1 is classified correctly as a class of plane with probability of 86%. We can claim that proposed ATR scheme is robust to variations inside the class, and therefore with high probability, other UAVs with similar flying concept will be classified correctly.

For ATR system it is important to reject an unknown target which class significantly differs from the ones used for training. To reject the unknown target a confidence threshold can be set. By confidence threshold we mean a minimum value of the class conditional probability (posterior probability) for which the decision is assumed to be true, otherwise the target is marked as unknown. Even for non-probabilistic classifiers, such as SVM, it is possible to estimate the

Table 7.6: Confusion matrix (in percentages) for linear SVM classifier, 11-classes problem

class	1	2	3	4	5	6	7	8	9	10	11
1	**70**	22	4	2	0	0	0	0	0	0	2
2	17	**79**	2	2	0	0	0	0	0	0	0
3	0	5	**95**	0	0	0	0	0	0	0	0
4	1	0	3	**96**	0	0	0	0	0	0	0
5	0	0	0	0	**100**	0	0	0	0	0	0
6	0	0	0	0	0	**100**	0	0	0	0	0
7	0	0	0	0	0	0	**85**	8	7	0	0
8	0	0	0	0	0	0	4	**96**	0	0	0
9	0	0	0	0	0	0	0	0	**99**	1	0
10	0	0	0	0	0	0	0	0	2	**98**	0
11	0	1	0	0	0	0	0	0	0	0	**99**

Table 7.7: Classification of UAVs hidden from training procedure, 11-classes problem

Class	P	B	Q	S	H
1	**85**	11	4	0	0
5	0	0	0	**100**	0
6	0	0	0	**100**	0
7	0	0	0	**100**	0
9	0	0	0	0	**100**
10	0	0	0	0	**100**

Table 7.8: Classification of the unseen for training classes, 5-classes problem

Class	Unknown	B	Q	S	H
P	**83**	0	13	5	0
B	0	**100**	0	0	0
Q	16	0	**84**	0	0
S	9	0	0	**91**	0
H	0	0	0	0	**100**

approximated posterior probability based on distances to the hyperplanes [176]. If we set the confidence threshold to 0.85 then with high probability targets from classes not used for training will be rejected. To demonstrate this Table 7.8 is shown. The following classes were removed from training set: [1 2 5 6 7 9 10]. Classes 1 and 2 are removed, the classifier has no data to train the class of plains, and these classes are assumed to be from class of unknown target. According to Table 7.6, 83% of the data of the plane's class is classified as unknown; also, 16% of data from quadrocopter's class and 9% of the class of stationary rotating rotor are misclassified as an unknown target.

For all experiments above we used half of a second of the observation time to classify the target. Next we show what a performance can be achieved when shorter interval is used for decision making. The training set is constructed in the same manner as before (using 0.5 sec as segment's duration); however, for training set, the features are extracted from shorter segments. This shows the robustness of the feature extraction procedure to the duration of the segment.

Fig. 7.10 demonstrates the dependence of the classification rates on the dwell time for 11-classes problem. The following conclusions can be pointed out:

- Both SVM classifiers demonstrate stable result with dwell time longer than 0.25 sec;
- Naive Bayes Classifier provides a decrease of 4% with dwell time of 0.25 sec;
- With dwell time shorter than 0.25 sec, the performance drops significantly with decrease of the dwell time. At dwell time 0.05 sec the following result is achieved: Linear SVM 75%, non-linear SVM 82%, naive Bayes classifier 65%.

Noise can corrupt the signal and degrade the classification performance. We will add white Gaussian noise to experiments from test dataset and examine the performance of the system. To do this we assume that collected radar signal contains no noise and the power of the raw data will be used to calculate Signal to Noise Ratios (SNRs). Additive white Gaussian noise is generated as variable $\epsilon(n)$ in (7.1). It should be noted, that the raw data contains noise, because data collection was performed for all possible ranges, however, we neglect this fact.

Fig. 7.11 demonstrates the dependence of classification rate on SNR, for 11-classes problem. We can conclude the following:

- The proposed approach together with SVM classifier demonstrates robustness to the SNR when it is higher than 30 dB;
- Performance drops to half with SNR = 16 dB, and reaches probability of random guess at 0 dB;

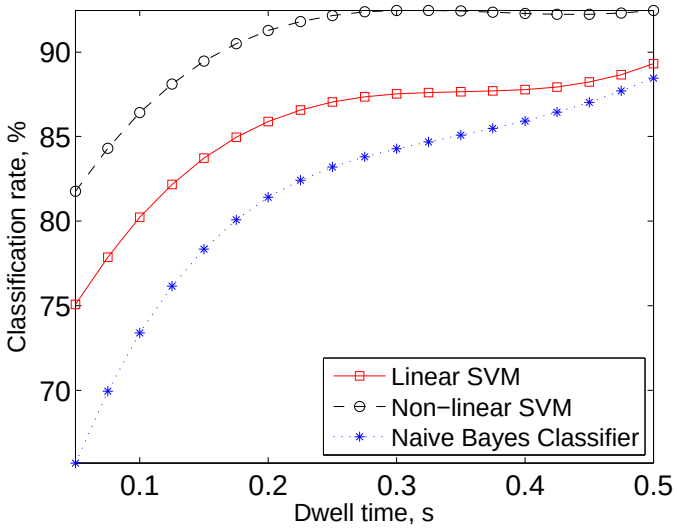

Figure 7.10: Classification rate for 11-class problem depending on the dwell time

- Naive Bayes classifier together with the proposed approach is more sensitive to the SNR; drop to the half of the performance is obtained with 28 dB and than rapidly decreases.

VIII Summary

In this Chapter, a new automatic target recognition system has been proposed for classification of unmanned aerial targets by their micro-Doppler signatures. Preprocessing steps of the signature such as filtering and Doppler alignment have been discussed. New, robust features for target classification based on extraction of bases of the micro-Doppler signature have been introduced. The probability of correct classification of the order of 92% has been achieved. It has been shown that different models of the same type could be distinguished, helicopters with probability of 98%, stationary rotors near 95% and planes with 74.5%. It was shown that system can identify unknown classes as well as classify models of UAVs hidden from the training procedure.

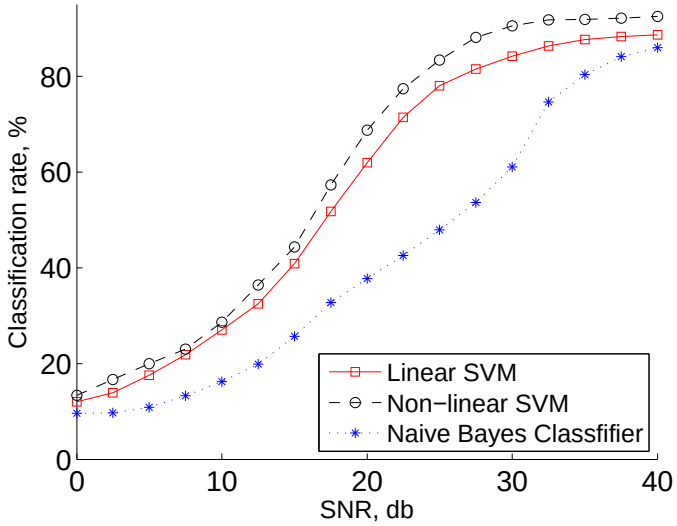

Figure 7.11: Classification rate depending on SNR, 11-classes problem

Chapter 8

Classification of ground moving radar targets by using joint time-frequency analysis

In this Chapter, two novel algorithms for ground moving target classification using additional information features related to the radial velocity time-variability are proposed and studied. These approaches are compared with feature extraction method based on linear prediction model and cepstrum coefficients. Results of computer simulations performed by exploiting real-life radar backscattering signal records with different decision making concepts demonstrate the benefits of the suggested approach.

I Introduction

Nowadays, conventional spectrogram defined as the square modulus of the STFT is widely spread tool used for time-frequency analysis of non-stationary processes. Spectrogram is usually computed by using a sliding window truncating received signal by the sequence of short-time segments and Fourier transform (FT) related to the short-time segmented signals. A larger window length provides higher frequency resolution in the TFD, however, as a consequence, poorer temporal resolution is observed at the same time.

The idea behind this Chapter is in using additional information features related to the radial velocity time-variability for solving target classification problem. Information contained in time variations of radial velocity caused by various human activities (walking, running, crawling) and various classes of objects (one person, group of humans, wheeled, truck, animal, etc.) is used for class label prediction in the algorithms suggested for application in automatic target recognition (ATR) systems.

II Real radar data description

In this Section, we present experimental results by exploiting publicly available database of Doppler radar signatures [6–8] which helps us to demonstrate the efficiency of proposed radar target classification algorithms.

Ground surveillance pulse-Doppler radar operating at the frequency of 16.8 GHz was used for collecting radar data [7]. The radar parameters are: average irradiated power of 5 mW; pulse

width of 15 μsec; average range resolution of 150 m; elevation resolution of 7.5°, and azimuth resolution of 5°. The range between the radar and the targets was rather short (100...1000 m). Amplitude of the raw radar data was within the range of ±1V and the sampling frequency is of 4 kHz.

The backscattered radar signals were recorded by using two different scenarios. The first one is the road of 4 m width and 800 m length. The second one is the rough terrain contained barriers (slews, woods) and small vegetation [6–8].

We are focused on solving target classification problem regarding eight different classes of ground moving targets. Considered classes and the lengths of radar signal records are listed below.

Class #1. Human walking towards/away the radar (388 s);

Class #2. Truck (188 s);

Class #3. Noise (clutter) (360 s);

Class #4. Wheeled (104 s);

Class #5. Human running (124 s);

Class #6. Human crawling (72 s);

Class #7. A group of people walking (496 s);

Class #8. A group of people running (200 s).

III Problem Statement

Let us consider backscattering signal model focusing on the time-dependency of Doppler frequency behavior observed in a human gait analysis. Under assumption of periodical locomotion of a human legs (steps) and arms (swings), multi-component received signal model s(t) can be expressed as the following superposition of phase modulated contributions:

$$s(t) = \sum_{i=1}^{I} \exp(-\frac{j4\pi}{\lambda}(v_i t + \alpha_i \cos(2\pi t\theta_i + \phi_i) + \beta_i)), \tag{8.1}$$

where v_i is averaged velocity of i-th local scattering center; α_i, θ_i and ϕ_i are the parameters related to the radial velocity behavior of i-th local scattering center; β_i is the initial phase; I is the total number of local scattering centers.

Concerning the extraction of classification features, the parameters given in (8.1) can be separated into the following two groups: the *essential* and *inessential* parameters. By *inessential* parameters we mean the parameters contained no information about class label. They are the v_i, ϕ_i and β_i. These parameters are not unique regarding to various target classes. By *essential* parameters we mean the parameters contained unique information about class label: the α_i and θ_i.

One of the most important questions regarding the STFT implementation in real-life noisy scenarios is: what optimal parameters must be selected? Window length must be selected in order to split a total non-stationary noisy signal observation length T into the M segments of length of B samples. Splitting provides both good smoothed spectrogram estimates by averaging over

M segments and required temporal and frequency resolution at the same time. In the case of $M = 1$, whole information is used for target classification with the highest frequency resolution. However, if $M \neq 1$, an optimal window length must be defined.

IV Feature Extraction Algorithms Suggested

In this Section we will introduce feature extraction methods used in this study. As the first method we will consider very robust method based on parametric estimation of the linear prediction model and cepstrum coefficients, we will refer to this method as *Bilik's approach* (BA), it has been originally proposed in [17]. Then we will propose two novel methods for feature extraction from TFD of backscattered radar signals.

A) Bilik's approach

The best probability of classification for personnel targets was obtained and declared by the authors of the paper [17]. Basic idea of Bilik's approach is extraction of classification features in terms of using the values $a \in \mathbb{R}^p$ related to the linear prediction model (LPM) and the cepstral coefficients $c \in \mathbb{R}^Z$ computed by the following recursive algorithm:

$$c_z = \begin{cases} \ln(G), & \text{if } z = 0 \\ a_z + \sum\limits_{k=1}^{z-1} \frac{k-z}{z} a_k c_{z-k}, & \text{if } 1 \leq z \leq p \\ \sum\limits_{k=z-p}^{p} \frac{k-z}{z} a_k c_{z-k}, & \text{if } p \leq z \leq Z \end{cases} \tag{8.2}$$

where G and p are the gain term and LPM order, respectively; Z is the total number of cepstral coefficients.

In our simulations we assume that the LPM order is equal to the number of samples and the parameter Z is selected to be equal to p. As follows, we will refer to the above mentioned technique as Biliks approach (BA).

Finally, feature space obtained by BA can be described as

$$BA = a \cup c \in \mathbb{R}^{2N}. \tag{8.3}$$

B) Time-Frequency Distribution - Direction Features (TFD-DF)

Next we will introduce first of the proposed methods. Assume that the length of a recorded discrete-valued radar signal $s(i)$ is equal to T samples. The spectrogram (SP) is computed by using square STFT of the length of N samples and overlapping with K samples. As a result the $SP \in \mathbb{R}^{N \times q}, q = \frac{T-K}{N-K}$ can be expressed as

$$SP(f,t) = \left| \sum_{l=1}^{N} s\big(l + (t-1)(N-K)\big) e^{-\frac{j2\pi fl}{N}} w(l) \right|^2, \tag{8.4}$$

where $w(l)$ is the smoothing window function, for instance, Hamming window can be exploited; f is the frequency index.

First, we note that SP (8.4) is invariant to the inessential value β_i given in (8.1). In order to make SP (8.4) invariant to the phase ϕ_i and averaged velocity v_i values given in (8.1), we propose performing the following signal processing steps.

1) Fourier transform computed along the time axis one more time for SP row-wise elements of matrix (8.4) by holding the *fixed frequency*. As a result, the following Fourier image is computed as

$$SP'(f,k) = \left| \sum_{t=0}^{q} SP(f,t) e^{-\frac{j2\pi kt}{q}} \right|. \tag{8.5}$$

2) Taking logarithm of the function (8.5) we obtain

$$SP'_{log}(f,k) = \log(SP'(f,k)). \tag{8.6}$$

3) Forming the projections of SP'_{log} into f (frequency) and t (time) domains, respectively, as

$$f\_SP'_{log}(m) = \sum_{g=0}^{q} SP'_{log}(m,g), \tag{8.7}$$

$$t\_SP'_{log}(m) = \sum_{f=0}^{N} SP'_{log}(f,m). \tag{8.8}$$

It should be stressed that even the projection $f\_SP'_{log}$ is invariant to the inessential parameter ϕ_i but it contains the contributions of θ_i and α_i values given in (8.1). At the same time, the projection $t\_SP'_{log}$ is invariant to the parameters ϕ_i, v_i and α_i, even it contains the contributions of θ_i values.

The objective of the suggested approach is to extract robust classification features in an efficient way by means of their few numbers. In order to provide the latter requirement the following feature extraction procedures should be performed

$$FS(m) = \left| \sum_{k=0}^{N} f\_SP'_{log}(k) e^{-\frac{j2\pi mk}{N}} \right|, \tag{8.9}$$

$$FS2(m) = \left| \sum_{k=0}^{q} t\_SP'_{log}(k) e^{-\frac{j2\pi mk}{q}} \right|. \tag{8.10}$$

For providing single feature vector, the feature spaces (8.9) and (8.10) could be joint as follows

$$TFD - DF = FS \cup FS2 \in \mathbb{R}^{N+q}. \tag{8.11}$$

Fig. 8.1 summarizes the *TFD-DF* feature extraction method for a test signal - sinusoidal baseband signal. As a result we obtain two low-dimensional vectors that represent the spectrogram. Most informative are the first coefficients of each vector, nevertheless, feature selection procedure performed on training data will select most informative features, and only they must be computed.

C) Time-Frequency Distribution - Singular Values Decomposition - Fourier Transform (TFD-SVD-FT)

According to the Singular Values Decomposition (SVD) technique, the spectrogram $SP \in \mathbb{R}^{N\times q}$ can be represented by multiplication of three matrices contained left singular vectors $S \in \mathbb{R}^{N\times N}$, singular values $V \in \mathbb{R}^{N\times q}$, and right singular vectors $D^* \in \mathbb{R}^{q\times q}$. In order to make this method

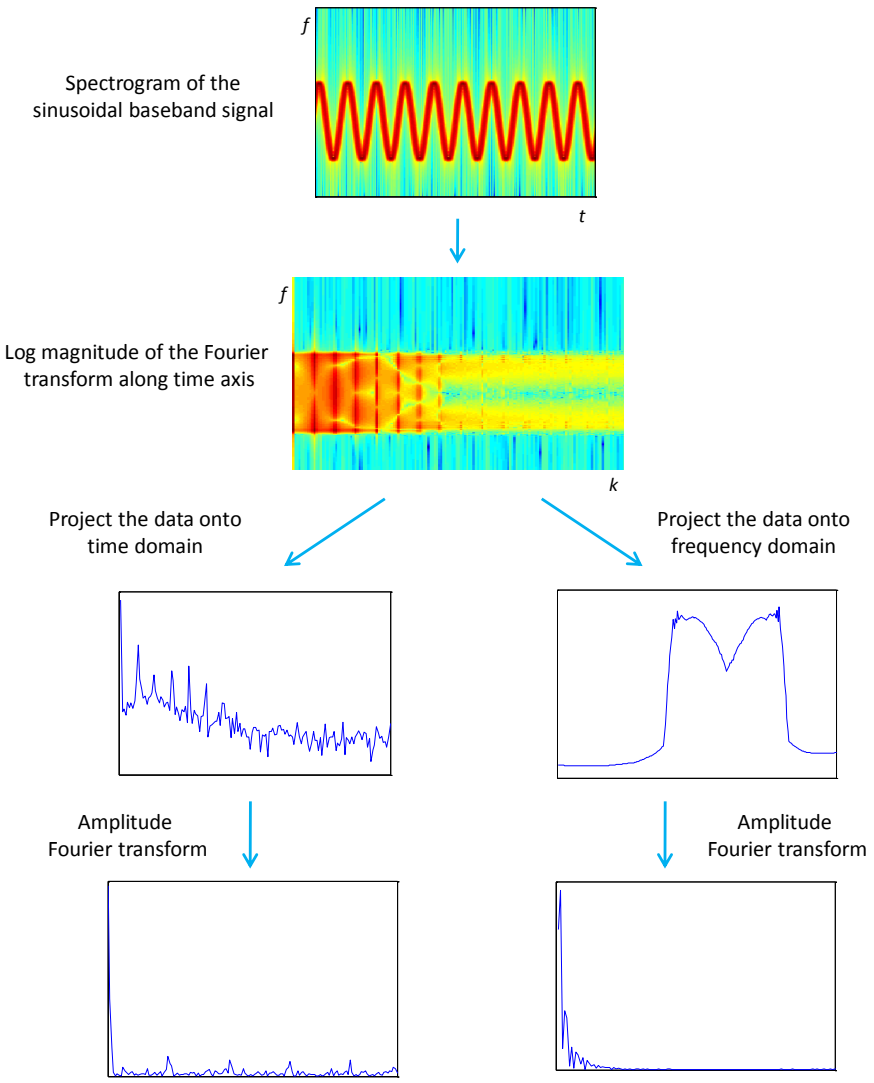

Figure 8.1: General structure of the *TFD-DF* feature extraction method for a test signal - sinusoidal baseband signal. It extracts features that depend on relevant information and parameters of the radar signal and irrelevant to not informative ones.

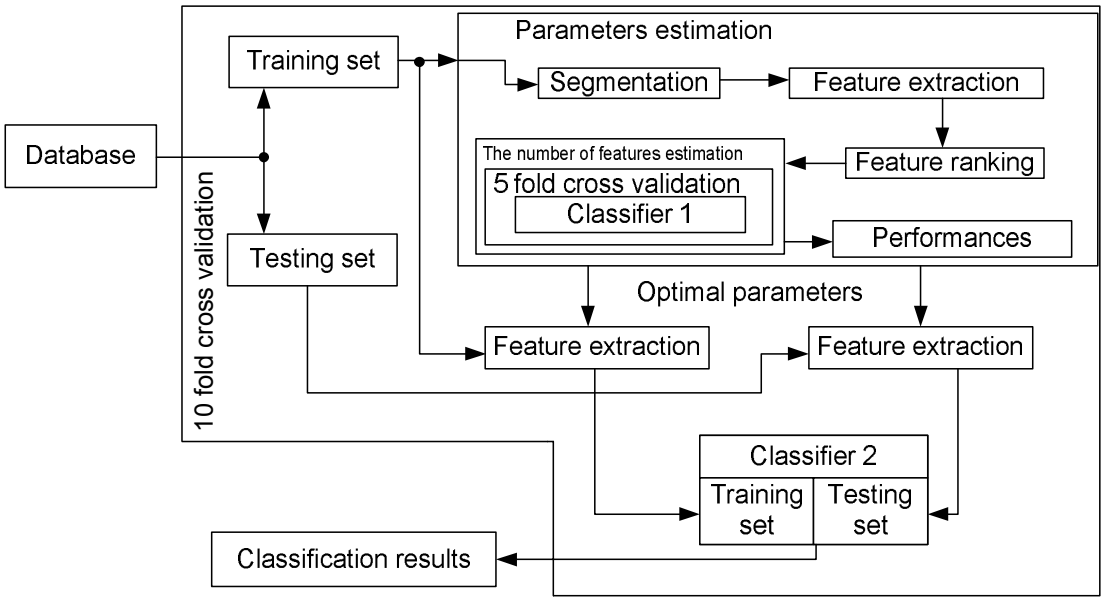

Figure 8.2: Block-scheme of classification algorithm

invariant regarding the averaged target radial velocity each singular vector in the S matrix should be replaced by its magnitude Fourier spectrum values.

Suggested *TFD-SVD-FT* algorithm contains the same signal processing steps as in Chapter 7 Section E), with the only difference that correlation matrix is computed differently because of change of dimensions' order in spectrogram: $\Psi(f_1, f_2) = \sum_{t=1}^{N} SP(t, f_1)SP(t, f_2)$. Then feature vector are formed as $F = \bigcup_{r=1}^{Z}\{y_r, \lambda_r\}$, where y_r is a magnitude of Fourier transform of eigenvectors extracted from Ψ. Eigenvectors of Ψ correspond to left singular vectors of SP if would be decomposed by SVD.

V Experimental setup

The block-scheme of proposed target classification algorithms is represented in Fig. 8.2. The training set is used for parameters estimation of the feature extraction procedures. Assuming that the decision should be made every T seconds, then decision can be made every $B < T$ seconds and can be integrated to T seconds (T/B times) by Majority Voting concept to obtain a single result, or features can be extracted for time interval of T seconds and one decision should be made. The idea of decision making on local segments and then aggregating the decisions by majority voting is shown in Fig. 8.3. The procedure of splitting the received radar signal into the short-time segments is performed in Segmentation block. After that, a set of features is extracted from the segmented data.

Feature ranking procedure is selected to be MIMI, introduced in Chapter 4 Section V. Then, Classifier 1 estimates accuracy of CV with selected parameters. After that, parameters are changed and new performance of classification is evaluated. This procedure repeats for all available set of parameters and decision about optimality is making by the maximum of accuracy obtained by CV procedure.

The number of used features (NF) is estimated by using the following strategy. Starting from

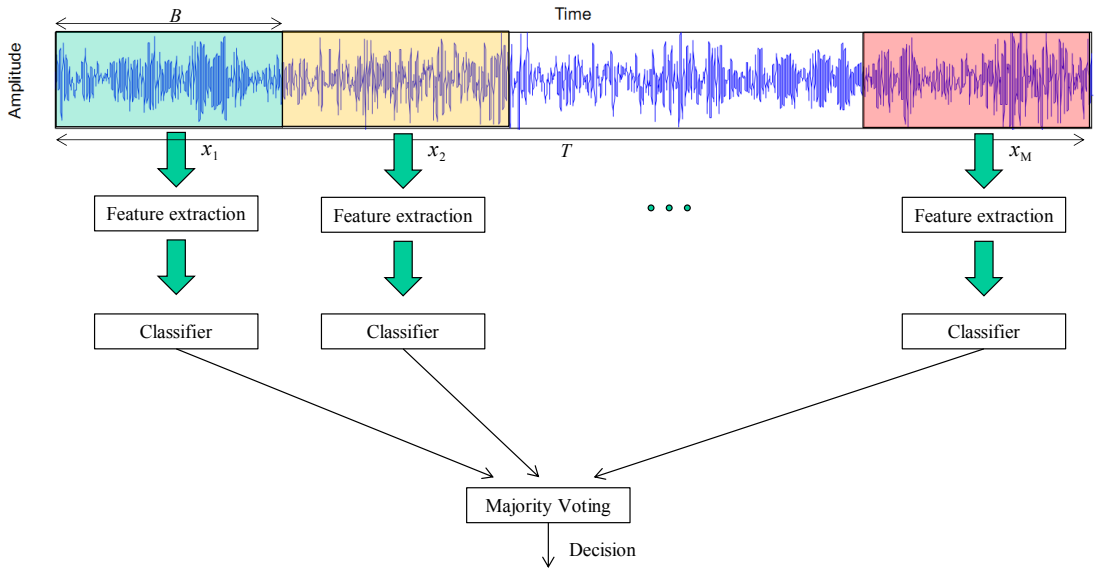

Figure 8.3: The decisions are made on local segments of radar date and then aggregated by majority voting.

$NF = 1$, accuracy is estimated by using CV concept. After that, the number of features increases by one and accuracy is estimated one more time. Procedure repeats until we will obtain the highest accuracy of CV compared to the next studied $V = 10$. For instance, assuming that $V = 4$ and changing number of features NF from 1 to 8 we obtain a vector of accuracies in the form of $L = \{10\ 20\ 30\ 40\ 35\ 33\ 31\ 30\}$. Finally, the procedure stops because each from the last four values $\{35\ 33\ 31\ 30\}$ is smaller than 40 and NF has been selected to be 4.

In order to clarify how the parameter estimation procedure operates, assume that we have a set of possible parameters. For each set of parameters we estimate the accuracy of CV. By evaluating maximum accuracy value we make a decision for which set of parameters is of sub-optimal. For designing a set of parameters we use $B \in G$ samples, where $G = \{2^{6,\ldots,14}\}$. For SP matrix (8.4) with fixed N value we use the same space of values ($N \in G$) and $K = N/2$.

When a set of sub-optimal parameters has been evaluated, it can be used for feature extraction from data contained in the training and testing sets. Finally, classification accuracy of used feature extraction method is estimated.

Decision making time can vary in real-life situation depending on radar characteristics such as radar antenna scanning period and other technical restrictions and requirements. Because of this, we will vary the value of this parameter within rather wide limits from 16 ms to 4 s consecutively multiplying each value by two. Therefore, decision making time is studied for $\tau \in D$, where $D = \{16ms\ 32ms\ 64ms\ 128ms\ 256ms\ 512ms\ 1s\ 2s\ 4s\}$. To make it possible, we assume that new data are collected and accumulated in radar signal processing scheme each 16 ms or more frequently.

In this report, two different classifiers based on the GMM and support vector machine (SVM) technique [68] are studied. Expectation-maximization (EM) algorithm [24] for parameter estimation is used in GMM classifier. Maximum likelihood rule is selected for decision making with GMM. Note that the same strategy has been used by the authors of paper [17]. Implementation of SVM is performed by using LIBSVM libraries described in [27]. The SVM is used with exploiting radial basic functions (RBF) kernel. Parameters of kernel are estimated by 2-fold CV inside the

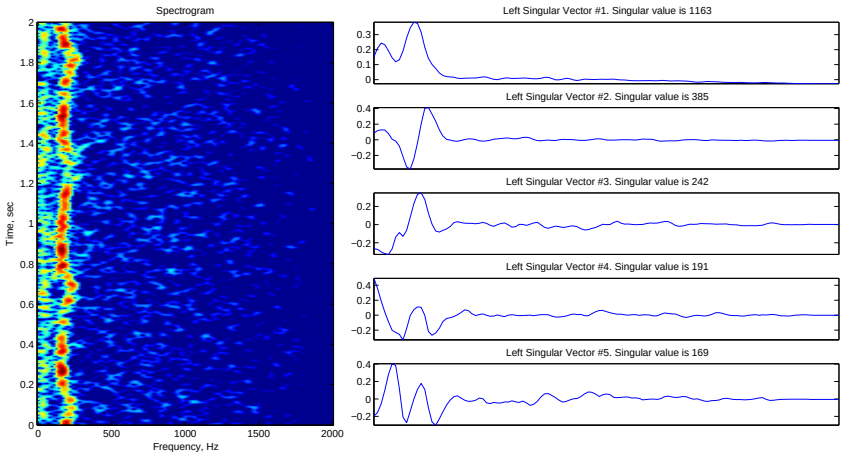

Figure 8.4: Single walking human. Spectrogram (on the left) and first five left singular vectors with singular values (on the right).

Classifier 1 in training set.

The three-fold CV is utilized to obtain optimal parameters related to the GMM order. This GMM-based classifier demonstrates small instability of results because it contains some random procedures, i.e. GMM uses K-means strategy for initialization. Because of this, instead of one involved classifier we use a set of five classifiers with the same parameters. Therefore, all decisions are combined by Majority Voting strategy in order to make and select optimal final decision. We assume that within an arbitrary observation interval, just only one target is located in the radar line-of-sight.

VI Analysis of Experimental Results

Feature vectors are extracted from the spectrogram computed for radar backscattering signal. Spectrogram contains essential information about micro-Doppler phenomenon. Therefore we will study them for eight considered classes together with results of singular value decomposition. They are illustrated in Fig. 8.4-8.11.

Spectrograms and results of singular value decomposition illustrated in Fig. 8.4-8.11 allows us to conclude the following:

- Classes of vehicles produce Doppler shifts at higher frequencies then humans; however, considered methods are invariant to this feature in order to be aplicable in case of moving radar;
- Spectrogram of the walking human is narrow band with curve repetition pattern corresponded to gaits;
- Truck and wheeled classes produce spectrograms of very narrow band, with difference that spectrogram of wheeled class has variation of the amplitude within the time. These variations result in higher values of the second and above singular values as well as in the form of third and above left singular vectors;
- Class of clutter does not contain any particular structure and therefore random left singular vectors;

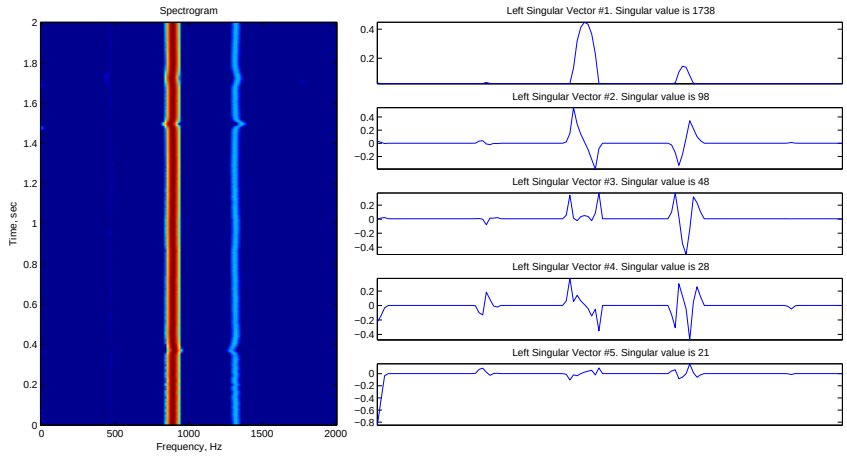

Figure 8.5: Truck. Spectrogram (on the left) and first five left singular vectors with singular values (on the right).

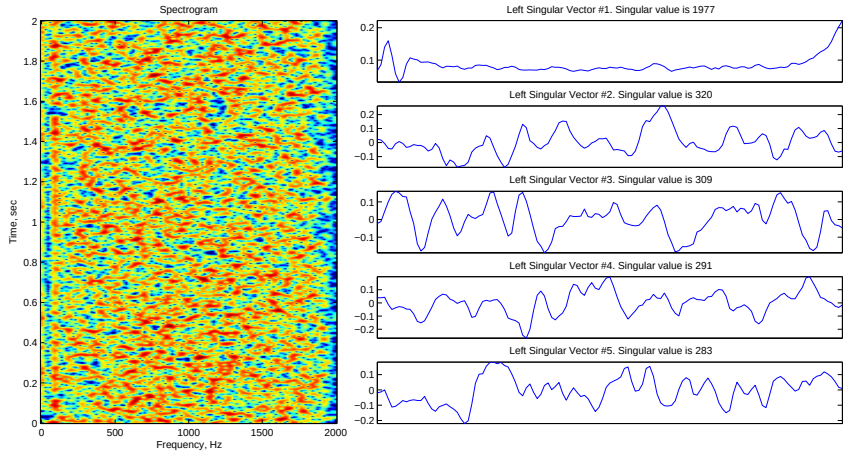

Figure 8.6: Noise (clutter). Spectrogram (on the left) and first five left singular vectors with singular values (on the right).

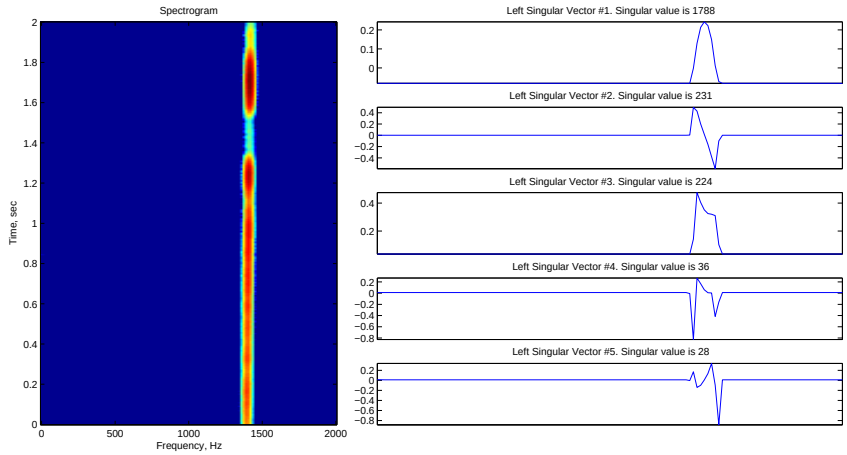

Figure 8.7: Wheeled. Spectrogram (on the left) and first five left singular vectors with singular values (on the right).

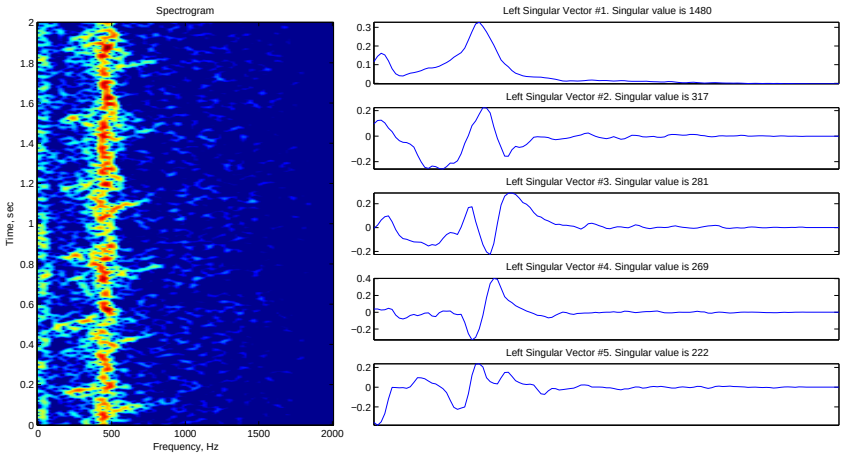

Figure 8.8: Human running. Spectrogram (on the left) and first five left singular vectors with singular values (on the right).

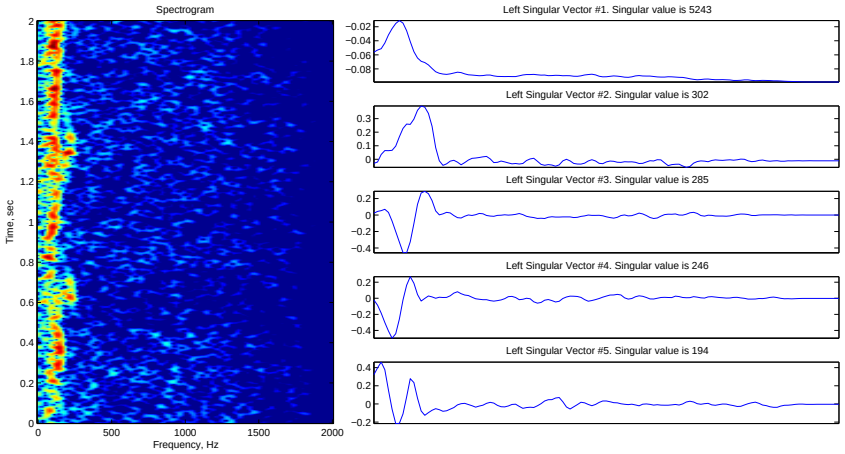

Figure 8.9: Human crawling. Spectrogram (on the left) and first five left singular vectors with singular values (on the right).

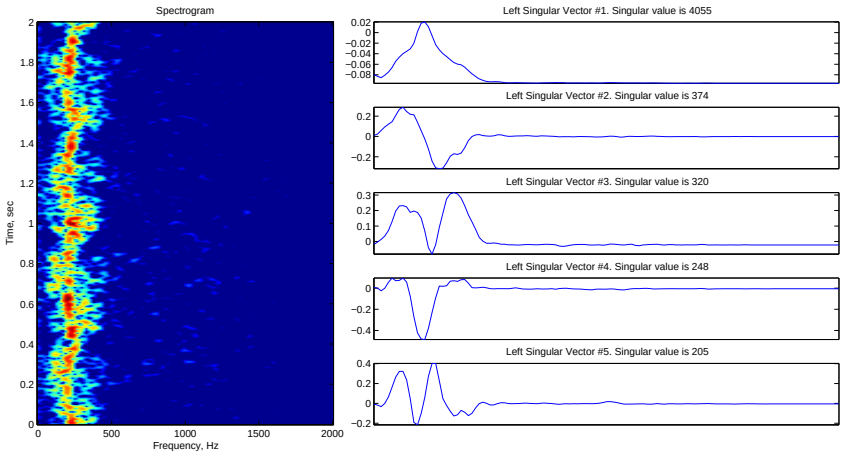

Figure 8.10: A group of people walking. Spectrogram (on the left) and first five left singular vectors with singular values (on the right).

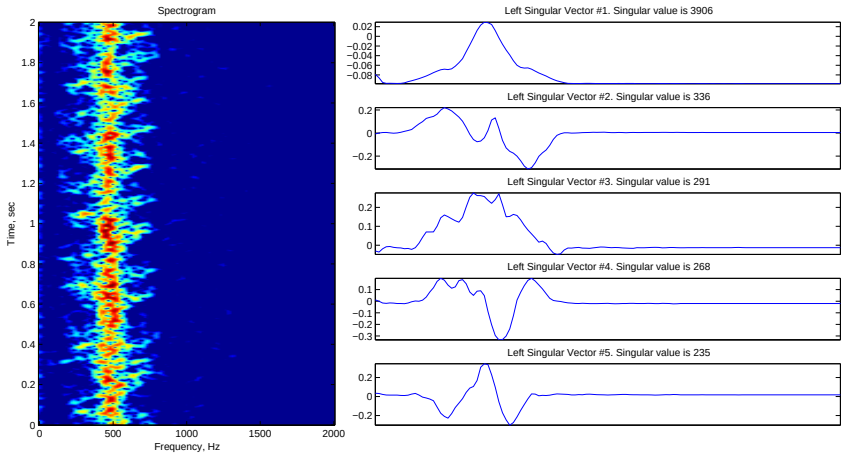

Figure 8.11: A group of people running. Spectrogram (on the left) and first five left singular vectors with singular values (on the right).

- Spectrogram of the running human demonstrate wider spread of the frequencies;
- Spectrogram of the crawling human is similar to walking human, but without strong curve pattern;
- Groups of people produce spectrograms of sophisticated form with wider bandwidth.

For each decision making time interval, the CV procedure was performed. Training set is used for estimation the optimal parameters of the feature extraction procedure. Testing set is used for evaluation classification accuracy.

Note that the length of available radar signal records is not the same for considered eight target classes. In order to compensate the difference between these eight classes, we propose to compute the probability of correct classification as

$$P = \sum_{u=1}^{U} \frac{C_{cor}(u)}{C_{total}(u)} P_a(u), \tag{8.12}$$

where U is the total number of classes available, $C_{cor}(u)$ is the number of correctly classified instances related to the class u, $C_{total}(u)$ is the total number of classified instances related to the class u, $P_a(u)$ is a priori probability related to the class u. Unfortunately, a priori probability is impossible to estimate using available experimental data. Due to, we suppose that a priori probability related to each separate considered class is of the same value equal to $P_a(u) = \frac{1}{U} \vee u$.

First, we consider and analyze the results obtained by GMM classifier. Dependence of classification rate on decision making time and feature extraction technique is illustrated by results given in Table 8.1.

The BA outperforms two proposed algorithms when decision making time less than 128 ms. However, the benefit obtained by BA is less than one percent comparing to the TFD-SVD-FT algorithm for this time interval. It can be explained by the fact that with the small amount of available data the proposed algorithms are not capable to extract completely the parameters of velocity modulation. The TFD-DF approach shows extremely bad results with decision making time within the range of 16 ... 64 ms. However, when decision making time is equal or larger than 256 ms, two suggested algorithms outperform BA performance. With decision making time

Table 8.1: Accuracy of correct classification depending on decision making time. GMM classifier.

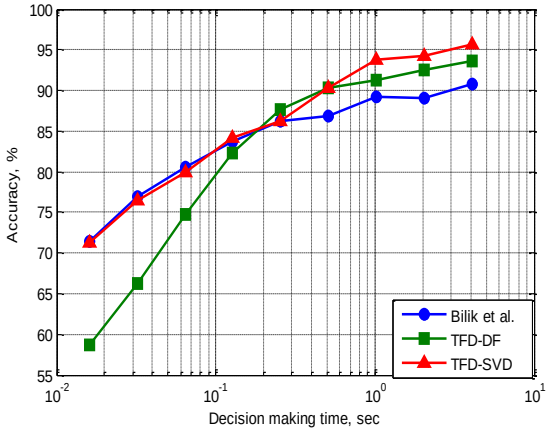

		Feature extraction technique		
		BA	TFD-DF	TFD-SVD-FT
Decision making time	16 ms	**71.45**	58.66	71.30
	32 ms	**76.94**	66.24	76.49
	64 ms	**80.59**	74.72	79.95
	128 ms	83.74	82.23	**84.21**
	256 ms	86.27	**87.71**	86.31
	512 ms	86.79	90.34	**90.37**
	1 s	89.26	91.24	**93.76**
	2 s	89.10	92.45	**94.19**
	4 s	90.82	93.67	**95.69**

Table 8.2: Confusion matrix. TFD-SVD-FT. $\tau = 4sec$. GMM classifier.

Class number	1	2	3	4	5	6	7	8
1	97	0	0	0	1	1	1	0
2	0	100	0	0	0	0	0	0
3	0	0	92	8	0	0	0	0
4	0	0	0	91	0	9	0	0
5	0	0	0	0	96	0	0	4
6	0	0	0	0	0	100	0	0
7	4	0	0	0	0	1	95	0
8	0	0	0	0	6	0	0	94

Table 8.3: Confusion matrix. TFD-DF. $\tau = 4sec$. GMM classifier.

Class number	1	2	3	4	5	6	7	8
1	96	1	0	0	1	1	1	0
2	0	100	0	0	0	0	0	0
3	15	0	77	4	0	4	0	0
4	0	3	0	97	0	0	0	0
5	0	0	0	0	93	0	0	7
6	0	4	0	0	0	96	0	0
7	1	0	0	0	1	1	97	0
8	1	0	0	0	6	0	0	93

equal to 4 seconds, the TFD-SVD-FT provides the classification rate of 95.69%. The latter value is more than 2% better comparing to the TFD-DF and more than 5% comparing to the BA. For decision making time equal to 16 ms, the classification rates computed according to the BA and the TFD-SVD-FT are far from random guess and they are interesting as well.

Confusion matrices computed for three approaches considered and GMM classifier with decision making time equal to 4 seconds are represented in Tables 8.2-8.4.

It is clearly seen from Tables 8.2-8.4 that BA demonstrates bad classification result for group of walking people, i.e. 20% of test signatures from class #7 were misclassified to class of single walking human. At the same time, two proposed algorithms show better ability to distinguish these classes, i.e. only 4 and 1 percents of data from Class #7 were erroneously declared as Class #1 by the TFD-DF and the TFD-SVD-FT, respectively. Note that clutter Class #3 seems to be the most difficult for distinguishing and errorless classification by considered approaches. More specifically, the TFD-DF and BA achieve only 77% of correct classification. However, at the same time, the TFD-SVD-FT provides 92% of correct classification.

Classification rates computed for SVM-based classifier are given in Table 8.5. With decision making time smaller than 256 ms, the BA outperforms two proposed algorithms and the benefit is within the limit of 3%. However, with decision making time equal and higher than 256 ms, the TFD-SVD-FT algorithm consistently exceed the best performance of two other considered

Table 8.4: Confusion matrix. BA. $\tau = 4sec$. GMM classifier.

Class number	1	2	3	4	5	6	7	8
1	96	0	0	0	0	0	4	0
2	0	100	0	0	0	0	0	0
3	15	0	77	8	0	0	0	0
4	0	6	0	91	0	3	0	0
5	0	0	0	0	91	0	0	9
6	0	0	0	0	0	100	0	0
7	20	0	0	0	1	0	79	0
8	2	1	0	0	5	0	1	91

Table 8.5: Accuracy of correct classification depending on decision making time. SVM classifier.

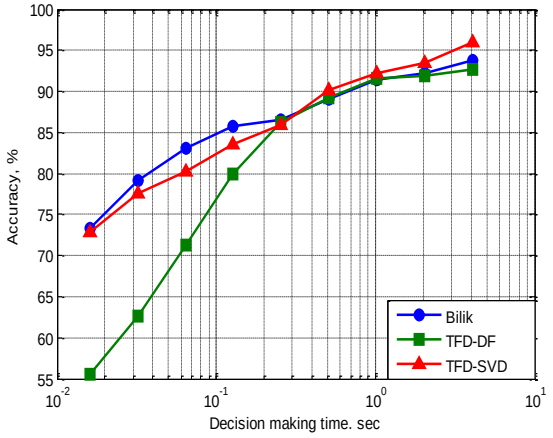

Decision making time	Feature extraction technique: BA	TFD-DF	TFD-SVD-FT
16 ms	**73.37**	55.53	72.83
32 ms	**79.22**	62.67	77.61
64 ms	**83.11**	71.23	80.18
128 ms	**85.74**	79.96	83.55
256 ms	**86.54**	86.18	85.90
512 ms	89.13	89.20	**90.10**
1 s	91.46	91.59	**92.23**
2 s	92.20	91.91	**93.55**
4 s	93.77	92.63	**95.97**

approaches. TFD-DF algorithm demonstrates the worst results and in the best case it reaches the BA performance. When decision making time is equal to 4 seconds, the best classification rate is obtained by the TFD-SVD-FT and differences are approximately equal to 2 and 3 percents comparing to the BA and TFD-DF, respectively.

Confusion matrices computed for SVM classifier and decision making time equal to 4 seconds are represented in Tables 8.6-8.8. The TFD-SVD-FT provides errorless classification for Classes #2, #5, #6, and #7, i.e for truck, running human, crawling human and group of walking humans, respectively. For all three approaches the most problematic issue was to predict clutter class #3 errorless. The worst probability of classification given in Table 8.7 is obtained by TFD-DF algorithm. It can be explained by large misclassification related to the Class #4. From Table 8.7 one can see that probability of correct classification obtained for TFD-DF algorithm is of 84% compared to 95% and 92% that are evaluated for the TFD-SVD-FT and BA, respectively.

Thus, the following conclusions can be formulated for this Section. First, a feature extraction method should be selected according to decision making time. Second, TFD-SVD-FT algorithm demonstrates the benefits comparing it to the other methods when decision making time is higher than 128 ms. Third, TFD-DF algorithm generally does not exceed the TFD-SVD-FT, however, it seems to be interesting for real-life ATR systems, because the computational complexity is much

Table 8.6: Confusion matrix. TFD-SVD-FT. $\tau = 4sec$

Class number	1	2	3	4	5	6	7	8
1	97	0	0	0	0	0	3	0
2	0	100	0	0	0	0	0	0
3	14	0	79	0	0	7	0	0
4	0	0	0	95	0	5	0	0
5	0	0	0	0	100	0	0	0
6	0	0	0	0	0	100	0	0
7	0	0	0	0	0	0	100	0
8	0	0	0	0	3	0	0	97

Table 8.7: Confusion matrix. TFD-DF. $\tau = 4sec$

Class number	1	2	3	4	5	6	7	8
1	99	0	0	0	0	0	1	0
2	0	100	0	0	0	0	0	0
3	11	0	82	7	0	0	0	0
4	2	8	0	84	3	3	0	0
5	0	0	2	4	90	0	0	4
6	4	7	0	0	0	89	0	0
7	1	0	0	0	0	0	99	0
8	1	0	0	0	0	0	0	99

Table 8.8: Confusion matrix. BA. $\tau = 4sec$

Class number	1	2	3	4	5	6	7	8
1	95	0	0	0	0	0	5	0
2	0	100	0	0	0	0	0	0
3	11	0	82	7	0	0	0	0
4	0	5	0	92	0	3	0	0
5	0	0	2	0	90	0	0	8
6	0	0	0	0	0	100	0	0
7	2	0	0	0	0	1	97	0
8	1	0	0	0	4	0	0	95

lower comparing to the other two approaches studied. Fourth, BA permits to achieve the benefit for small time intervals that can be explained by parametric nature of the method.

VII Summary

It has been shown in the Chapter that spectrogram-based time-frequency distributions computed for radar backscattering is useful and effective tool for target classification. Two novel algorithms are proposed and studied for target classification by using radar signals collected by ground surveillance Doppler radar. Both proposed algorithms are based on the classification feature extraction from time-frequency distributions of the radar target returns. Proposed approaches have been compared with state-of-the-art approach developed by Bilik et al [17]; one of the proposed methods, based on SVD of spectrogram overcome it with decision making time longer than 512 s. It was demonstrated that suggested algorithms provide good potential for ground moving target classification. The probability of the correct classification for decision making time equal to 4s peaks at 95.97% for SVM-based strategy. It was shown that it is possible to develop effective ATR radar system by using suggested target classification algorithms. The algorithms suggested in this report are suitable for real-life implementation in the security and battlefield ATR radar systems.

Conclusions and Future Work

Conclusions

Important problem in radar automatic target systems is searching and obtaining robust information features for improving the probability of recognition and enhancement target classification. It has been shown that micro-Doppler contributions allow robust classification of non-rigid moving objects. Moreover, a number of solutions have been suggested to increase robustness of such methods.

Introduction of the problem and motivation for the study have been presented in Chapter 1. Chapter 2 discusses radar basics of CW and FMCW radars, for which most of the results from thesis are applicable.

In Chapter 3, a novel approach to micro-Doppler period estimation has been proposed. In case of a priori uncertainty about the class of the radar target, the correct estimate of a period is achieved for SNR $\geq$ -2 dB. In case of complete determination about moving radar target, the correct estimate of period is observed for SNR $\geq$ -10 dB. Suggested method has been shown to outperform results of common period estimation techniques. During the Chapter 4, a novel approach for feature selection in task of classification has been proposed. The novel method showed advantage over maximum relevance technique and showed comparable results for mRMR approach.

A problem of using higher-order spectral techniques in analysis of micro-Doppler signatures has been considered in Chapter 5. Frequency and phase coupling phenomena have been investigated for radar backscattered signals of human walking, showing applicability of higher-order spectra techniques. Then, it has been shown that bispectrum based signal processing enhances the classification rate of ground moving and aerial flying objects. For this purpose, a novel bispectrum-based feature extraction method from micro-Doppler radar signatures to classify moving radar targets has been proposed. The method has been tested on real radar measurements of one, two and three moving persons, and on simulated aerial radar measurements. For classification of one, two or three moving persons the gain is from 2% to 6% comparing to state-of-the-art method based on parametric cepstrum estimation. For aerial targets, classification performance could be enhanced from 3% to 30% providing better robustness to aspect angle changes. Suggested bispectrum based method has shown robustness to atmosphere turbulence. The study of SNR influence has shown robustness to additive Gaussian noise.

Chapter 6 discusses applications of automotive radar. First, a new idea of joint usage of automotive radars, video coding and vehicle-to-vehicle communication has been presented. Proposed system reallocates the wireless channel resources in favour of the part of captured video frame that contains the oncoming vehicle, which is detected by the automotive radar. The proposed system significantly increases the visual quality of the frame region, which contains the oncoming vehicle. Then, a problem of frequency band invariant pedestrian and vehicle classification by

an automotive radar has been studied. It has been shown that scale invariant features could overcome the problem of multi frequency band invariant radar data classification. Classification accuracy has been shown to be at level of 96%.

In Chapter 7, a new automatic target recognition system has been proposed for classification of unmanned aerial targets by their micro-Doppler signatures. New features based on extraction of bases of the micro-Doppler signature have been introduced. Five different types of aerial targets have been studied including quadrocopters, helicopters, planes, birds and stationary rotors. It has been demonstrated that suggested features outperformed physical features such as rotor diameter. Improvement in terms of classification accuracy is from 40% to 50%. The overall classification probability for designed features is from 92% to 96% depending on the selected classifier. The correct classification probability is above 80% for SNR $\geq$ 22 dB in case of artificially added Gaussian noise to the testing dataset. It has been shown that different models of the same type could be distinguished: helicopters with probability of 98%, stationary rotors near 95% and planes with 74.5%. Suggested system can identify unknown classes and classify models of UAVs hidden from the training procedure.

Spectrogram based features have been introduced in Chapter 8. These features have demonstrated to be suitable for effective classification of ground moving objects by micro-Doppler contributions. Improvement over state-of-the-art frequency profile based features, like parametric cepstrum coefficients, become up to 5%, if target is observed for more than 0.5 s. The overall classification probability for 8 classes of ground moving objects (car, truck, walking, running, crawling human, group of people running, crawling, clutter) is above 95% for the suggested method.

Future Work

The approaches and methods considered in thesis are focused on radar target classification by micro-Doppler contributions. Future work could include combination of developed methods with classification methods based on range profiles, because these domains are completely orthogonal. Another direction of future studies could include further development of bispectrum-based features. In thesis we used phase coupling only for classification of aerial targets. Features extracted from bicoherence estimate could be combined with cepstral based coefficients, because, two methods use different information of short-time Fourier transform: cepstrum uses an amplitude and bicoherence uses a phase.

Design of feature extraction methods and classification schemes based on machine learning are main aims of this thesis. However, classification follows the detection step in the radar processing pipeline. It is assumed, that detection is performed successfully and the problem is to identify, which of predefined classes the target belongs to. Also, target detection problem could be transformed to the classification problem, where noise is considered as a separate class (such approach was used in Chapter 8).

In application of overtaking assistance system with automotive radar, only a theoretical framework has been introduced. Building a real prototype with measuring performance is another direction of the future studies. In the study of frequency-band invariant pedestrian classification, real 24 GHz radar measurements have been used together with simulated 77 GHz radar measurements. Even though, the simulator is realistic, verification of the algorithm on the real radar data is required, and is a purpose of ongoing study.

In the study of UAV classification a novel system has been suggested. It applies eigendecomposition of the correlation matrix for feature extraction. This step is the most consuming of the

overall system. For current computers, it is not a problem. However, for embedded systems it could be a problem, for example in the case of multiple target scenario. The egigendecomposition could be replaced with the calculation of a projection of the spectrogram onto a dictionary. Dictionary could be constructed only once during the training stage and it should contain eigenvectors extracted from the training data.

REFERENCES

[1] T. Ahonen, A. Hadid, and M. Pietikäinen, "Face recognition with local binary patterns," in *Computer Vision-ECCV 2004*. Springer, 2004, pp. 469–481.

[2] T. Ahonen, A. Hadid, and M. Pietikainen, "Face description with local binary patterns: Application to face recognition," *IEEE Transactions on Pattern Analysis and Machine Intelligence*, vol. 28, no. 12, pp. 2037–2041, 2006.

[3] T. Ahonen, J. Matas, C. He, and M. Pietikäinen, "Rotation invariant image description with local binary pattern histogram Fourier features," in *Image Analysis*. Springer, 2009, pp. 61–70.

[4] A. A. Alizadeh, M. B. Eisen, R. E. Davis, C. Ma, I. S. Lossos, A. Rosenwald, J. C. Boldrick, H. Sabet, T. Tran, X. Yu, J. I. Powell, L. Yang, G. E. Marti, T. Moore, J. Hudson, L. Lu, D. B. Lewis, R. Tibshirani, G. Sherlock, W. C. Chan, T. C. Greiner, D. D. Weisenburger, J. O. Armitage, R. Warnke, R. Levy, W. Wilson, M. R. Grever, J. C. Byrd, D. Botstein, P. O. Brown, and L. M. Staudt, "Distinct types of diffuse large B-cell lymphoma identified by gene expression profiling." *Nature*, vol. 403, no. 6769, pp. 503–511, 2000. [Online]. Available: http://dx.doi.org/10.1038/35000501

[5] M. G. Anderson, "Design of multiple frequency continuous wave radar hardware and micro-Doppler based detection and classification algorithms," Ph.D. dissertation, Austin, TX, USA, 2008.

[6] M. Andric, B. Bondzulic, and B. Zrnic, "The database of radar echoes from various targets," 2010. [Online]. Available: http://cid-3aaf3e18829259c0.skydrive.live.com/home.aspx

[7] ——, "The database of radar echoes from various targets with spectral analysis," in *Neural Network Applications in Electrical Engineering (NEUREL), 2010 10th Symposium on*, sept. 2010, pp. 187 –190.

[8] ——, "Feature extraction related to target classification for a radar doppler echoes," in *18th Telecommunications Forum*, November 2010.

[9] J. Astola, K. Egiazarian, G. Khlopov, S. Khomenko, I. Kurbatov, V. Morozov, A. Tepliuk, and A. Totsky, "Time-frequency analysis of ground surveillance Doppler radar echo signals by using short-time cross-bispectrum estimates," in *Proceedings of International Radar Symposium*, vol. 1, 2007, pp. 805–808.

[10] J. Astola, K. Egiazarian, G. Khlopov, S. Khomenko, I. Kurbatov, V. Morozov, and A. Totsky, "Application of bispectrum estimation for time-frequency analysis of ground surveillance Doppler radar echo signals," vol. 57, no. 9, sept. 2008, pp. 1949 –1957.

[11] A. Balleri, K. Chetty, and K. Woodbridge, "Classification of personnel targets by acoustic micro-Doppler signatures," *IET Radar, Sonar and Navigation*, vol. 5, no. 9, pp. 943–951, 2011.

[12] S. Barbarossa and O. Lemoine, "Analysis of nonlinear FM signals by pattern recognition of their time-frequency representation," *IEEE Signal Processing Letters*, vol. 3, no. 4, pp. 112 –115, April 1996.

[13] A. Bartsch, F. Fitzek, and R. H. Rasshofer, "Pedestrian recognition using automotive radar sensors," *Advances in Radio Science*, vol. 10, pp. 45–55, 2012.

[14] R. Battiti, "Using mutual information for selecting features in supervised neural net learning," *IEEE Transactions on Neural Networks*, vol. 5, no. 4, pp. 537–550, 1994.

[15] A. Bazzi, C. Krnfelt, A. Pden, T. Chonavel, P. Galaup, and F. Bodereau, "Estimation techniques and simulation platforms for 77 GHz FMCW ACC radars," *The European Physical Journal Applied Physics*, vol. 57, 1 2012.

[16] E. Belyaev, P. Molchanov, A. Vinel, and Y. Koucheryavy, "The use of automotive radars in video-based overtaking assistance applications," *IEEE Transactions on Intelligent Transportation Systems*, vol. 14, no. 4, pp. 1035 – 1042, 2014.

[17] I. Bilik, J. Tabrikian, and A. Cohen, "GMM-based target classification for ground surveillance doppler radar," *IEEE Transactions on Aerospace and Electronic Systems*, vol. 42, no. 1, pp. 267–278, 2006.

[18] C. M. Bishop, *Neural Networks for Pattern Recognition.* New York, NY, USA: Oxford University Press, Inc., 1995.

[19] S. Bjorklund, T. Johansson, and H. Petersson, "Evaluation of a micro-doppler classification method on mm-wave data," in *IEEE Radar Conference (RADAR)*, 2012, pp. 934–939.

[20] S. Bjorklund, H. Petersson, and G. Hendeby, "On distinguishing between human individuals in micro-Doppler signatures," in *14th International Radar Symposium (IRS)*, vol. 2, 2013, pp. 865–870.

[21] E. Botha, "Classification of aerospace targets using superresolution ISAR images," in *IEEE South African Symposium on Communications and Signal Processing*, 1994, pp. 138–145.

[22] R. Boulic, N. Magnenat-thalmann, and D. Thalmann, "A global human walking model with real-time kinematic personification," *The Visual Computer*, vol. 6, pp. 344–358, 1990.

[23] B. Bullard and P. Dowdy, "Pulse Doppler signature of a rotary-wing aircraft," *IEEE Aerospace and Electronic Systems Magazine*, vol. 6, no. 5, pp. 28 –30, May 1991.

[24] S. Calinon, *Robot Programming by Demonstration: A Probabilistic Approach.* EPFL CRC Press, 2009.

[25] V. Chandran and S. Elgar, "Pattern recognition using invariants defined from higher order spectra- one dimensional inputs," *IEEE Transactions on Signal Processing,*, vol. 41, no. 1, p. 205, January 1993.

[26] V. Chandran and S. L. Elgar, "Pattern recognition using invariants defined from higher order spectra- one dimensional inputs," *IEEE Transactions on Signal Processing*, vol. 41, no. 1, pp. 205–212, 1993.

[27] C.-C. Chang and C.-J. Lin, "LIBSVM: A library for support vector machines," *ACM Transactions on Intelligent Systems and Technology*, vol. 2, pp. 27:1–27:27, 2011, software available at http://www.csie.ntu.edu.tw/~cjlin/libsvm.

[28] V. Chen, "Doppler signatures of radar backscattering from objects with micro-motions," *IET Signal Processing*, vol. 2, no. 3, pp. 291–300, 2008.

[29] ——, "Spatial and temporal independent component analysis of micro-Doppler features," in *IEEE International Radar Conference*, May 2005, pp. 348 – 353.

[30] ——, *The Micro-Doppler Effect in Radar*. London: Artech House, 2011.

[31] V. Chen, F. Li, S.-S. Ho, and H. Wechsler, "Micro-Doppler effect in radar: phenomenon, model, and simulation study," *IEEE Transactions on Aerospace and Electronic Systems*, vol. 42, no. 1, pp. 2 – 21, January 2006.

[32] V. Chen, C.-T. Lin, and W. Pala, "Time-varying Doppler analysis of electromagnetic backscattering from rotating object," in *IEEE Radar Conference*, April 2006, pp. 1–6.

[33] V. Chen and H. Ling, *Time-Frequency Transforms for Radar Imaging and Signal Analysis*, ser. Artech House Radar Library. Artech House, 2002.

[34] A. Cilliers and W. A. J. Nel, "Helicopter parameter extraction using joint time-frequency and tomographic techniques," in *International Conference on Radar*, 2008, pp. 598–603.

[35] L. Cirillo, A. Zoubir, and M. Amin, "Parameter estimation for locally linear FM signals using a time-frequency hough transform," *IEEE Transactions on Signal Processing*, vol. 56, no. 9, pp. 4162 –4175, sept. 2008.

[36] C. Clemente, A. Balleri, K. Woodbridge, and J. Soraghan, "Developments in target micro-Doppler signatures analysis: radar imaging, ultrasound and through-the-wall radar," *EURASIP Journal on Advances in Signal Processing*, vol. 2013, no. 1, p. 47, 2013.

[37] K. Copsey and A. Webb, "Bayesian gamma mixture model approach to radar target recognition," *IEEE Transactions on Aerospace and Electronic Systems*, vol. 39, no. 4, pp. 1201 – 1217, oct. 2003.

[38] E. L. E. Corp. (2013, Nov.) FMCW mono-pulse system basics. [Online]. Available: http://www.epsilonlambda.com/white_paper/files/FMCW%20Mono-pulse%20System%20Basic.pdf

[39] C. Cortes and V. Vapnik, "Support-vector network," *Machine Learning*, vol. 20, pp. 273–297, 1995.

[40] T. Cover and J. Thomas, *Elements of Information Theory*, ser. Wiley Series in Telecommunications and Signal Processing. John Wiley & Sons, 2006.

[41] M. Dakovic, M. Brajovic, T. Thayaparan, and L. Stankovic, "An algorithm for micro-Doppler period estimation," in *20th Telecommunications Forum (TELFOR)*, 2012, pp. 851–854.

[42] S. Davis and P. Mermelstein, "Comparison of parametric representations for monosyllabic word recognition in continuously spoken sentences," *IEEE Transactions on Acoustics, Speech and Signal Processing*, vol. 28, no. 4, pp. 357–366, 1980.

[43] M. de Wit, R. I. A. Harmanny, and G. Prémel-Cabic, "Micro-Doppler Analysis of Small UAVs," in *European Radar Conference (EuRAD)*, oct. 2012, pp. 210 –213.

[44] A. Dempster, N. Laird, and D. Rubin, "Maximum likelihood from incomplete data via the EM algorithm," *Journal of the royal statistical society*, vol. 39, no. 1, pp. 1–38, 1977.

[45] A. P. Dempster, N. M. Laird, and D. B. Rubin, "Maximum likelihood from incomplete data via the EM algorithm," *Journal of the royal statistical society, series B*, vol. 39, no. 1, pp. 1–38, 1977.

[46] D. Dimitriadis, P. Maragos, and A. Potamianos, "Robust AM-FM features for speech recognition," *IEEE Signal Processing Letters*, vol. 12, no. 9, pp. 621–624, 2005.

[47] L. Du, B. Wang, Y. Li, and H. Liu, "Robust classification scheme for airplane targets with low resolution radar based on EMD-CLEAN feature extraction method," *IEEE Sensors Journal*, vol. 1, no. 99, pp. 1–1, 2013.

[48] L. Du, H. Liu, Z. Bao, and M. Xing, "Radar HRRP target recognition based on higher order spectra," *IEEE Transactions on Signal Processing*, vol. 53, no. 7, pp. 2359 – 2368, july 2005.

[49] L. Du, H. Liu, Z. Bao, and J. Zhang, "A two-distribution compounded statistical model for radar HRRP target recognition," *IEEE Transactions on Signal Processing*, vol. 54, no. 6, pp. 2226 – 2238, june 2006.

[50] R. O. Duda, P. E. Hart, and D. G. Stork, *Pattern Classification, 2nd edition.* Wiley, 2001.

[51] K. O. Egiazarian, V. V. Lukin, P. A. Molchanov, A. A. Roenko, A. V. Totsky, and A. A. Zelensky, "Signal detection in additive gaussian noise, doppler frequency shift and propagation fading fluctuations environment by using third-order test statistics."

[52] H. Essen, M. Hagelen, A. Wahlen, K.-H. Bers, M. Jager, and M. Hebel, "Non-cooperative classification of helicopters using millimetre wave radar and ISAR processing," in *International Workshop on Digital Communications - Enhanced Surveillance of Aircraft and Vehicles*, 2008, pp. 1–6.

[53] P. A. Estevez, M. Tesmer, C. A. Perez, and J. M. Zurada, "Normalized mutual information feature selection," *IEEE Transactions on Neural Networks*, vol. 20, no. 2, pp. 189–201, 2009.

[54] R. A. Fisher, "The use of multiple measurements in taxonomic problems," *Annals of Eugenics*, vol. 7, no. 2, pp. 179–188, 1936.

[55] A. Frank and A. Asuncion, "UCI machine learning repository," 2010. [Online]. Available: http://archive.ics.uci.edu/ml

[56] J. Fu, X. Deng, and W. Yang, "Radar HRRP recognition based on discriminant information analysis," *WSEAS Trans. Info. Sci. and App.*, vol. 8, no. 4, pp. 185–201, Apr. 2011.

[57] T. Gandhi and M. M. Trivedi, "Pedestrian protection systems: Issues, survey, and challenges," *Trans. Intell. Transport. Sys.*, vol. 8, no. 3, pp. 413–430, Sep. 2007.

[58] D. Gavrila, M. Kunert, and U. Lages, "A multi-sensor approach for the protection of vulnerable traffic participants the PROTECTOR project," in *IEEE Instrumentation and Measurement Technology Conference*, vol. 3, 2001, pp. 2044–2048 vol.3.

[59] J. Geisheimer, W. Marshall, and E. Greneker, "A continuous-wave (CW) radar for gait analysis," in *Conference on Signals, Systems and Computers*, vol. 1, 2001, pp. 834–838.

[60] E. Gelenbe, R. Lent, and G. Sakellari, "Computer and information sciences II - 26th international symposium on computer and information sciences," in *ISCIS*. Springer, 2011.

[61] P. Gomes, C. Olaverri-Monreal, and M. Ferreira, "Making vehicles transparent through V2V video streaming," *IEEE Transactions on Intelligent Transportation Systems*, vol. 13, no. 2, pp. 930–938, 2012.

[62] R. C. Gonzalez and R. E. Woods, *Digital Image Processing (3rd Edition)*. Upper Saddle River, NJ, USA: Prentice-Hall, Inc., 2006.

[63] S. Gorshkov, S. Leshchenko, V. Orlenko, Y. Shirman, and S. Sedyshev, *Radar Target Backscattering Simulation: Software and User's Manual*, ser. Radar Library. Artech House, 2002.

[64] H. Groll and J. Detlefsen, "History of automotive anticollision radars and final experimental results of a mm-wave car radar developed by the Technical University of Munich," *Transaction Intelligent Transportation System*, vol. 12, no. 8, pp. 15–19, Sep. 1997.

[65] S. Groot, A. Yarovoy, R. Harmanny, and J. Driessen, "Model-based classification of human motion: Particle filtering applied to the micro-Doppler spectrum," in *9th European Radar Conference (EuRAD)*, 2012, pp. 198–201.

[66] H. A. Guvenir, B. Acar, G. Demiroz, and A. Cekin, "A supervised machine learning algorithm for arrhythmia analysis," in *Computers in Cardiology*, 1997, pp. 433–436.

[67] P. Hanchuan, L. Fuhui, and C. Ding, "Feature selection based on mutual information criteria of max-dependency, max-relevance, and min-redundancy," *IEEE Tran. on Pattern Analysis and Machine Intel.*, vol. 27, no. 8, pp. 1226–1238, 2005.

[68] S. Haykin, *Neural Networks: A Comprehensive Foundation*. New York: Macmillan, 1994.

[69] R. v. d. Heiden and F. Groen, "The Box-Cox metric for nearest neighbour classification improvement," *Pattern Recognition*, vol. 30(2), pp. 273–279, 1997.

[70] S. Heuel and H. Rohling, "Two-stage pedestrian classification in automotive radar systems," in *International Radar Symposium (IRS)*, 2011, pp. 477–484.

[71] ——, "Pedestrian classification in automotive radar systems," in *13th International Radar Symposium (IRS)*, May 2012, pp. 39 – 44.

[72] M. Heuer, A. Al-Hamadi, M. Meinecke, and R. Mende, "Requirements on automotive radar systems for enhanced pedestrian protection," in *13th International Radar Symposium (IRS)*, May 2012, pp. 45 –48.

[73] S. Homma, A. Kobayashi, I. Toru, and T. Takagi, "Bi-spectral acoustic features for robust speech recognition," *IEICE Transactions on Information and Systems*, vol. 91, no. 3, pp. 631–634, 2008.

[74] R. Hu and Z. Zhu, "Researches on radar target classification based on high resolution range profiles," in *IEEE National Aerospace and Electronics Conference*, vol. 2, 1997, pp. 951–955 vol.2.

[75] B. Huether, S. Gustafson, and R. Broussard, "Wavelet preprocessing for high range resolution radar classification," *IEEE Transactions on Aerospace and Electronic Systems*, vol. 37, no. 4, pp. 1321 –1332, oct 2001.

[76] M. Inggs and A. D. Robinson, "Ship target recognition using low resolution radar and neural networks," *IEEE Transactions on Aerospace and Electronic Systems*, vol. 35, no. 2, pp. 386–393, 1999.

[77] InnoSent GmbH, "Data sheet IPS-146," 2011.

[78] S. Jacobs and J. O'Sullivan, "Automatic target recognition using sequences of high resolution radar range-profiles," *IEEE Transactions on Aerospace and Electronic Systems*, vol. 36, no. 2, pp. 364 –381, Apr. 2000.

[79] M. Jahangir, K. Ponting, and J. O'Loghlen, "Robust doppler classification technique based on hidden Markov models," *IEE Proceedings Radar, Sonar and Navigation*, vol. 150, no. 1, pp. 33 – 36, Feb. 2003.

[80] A. K. Jain, R. P. Duin, and J. Mao, "Statistical pattern recognition: a review," *IEEE Trans. Pattern Anal. Mach. Intell.*, vol. 22, no. 1, pp. 4–37, 2000.

[81] S.-H. Jeong, J.-N. Oh, and K.-H. Lee, "Design of 24 GHz radar with subspace-based digital beam forming for ACC stop-and-go system," *ETRI Journal*, vol. 32, no. 5, pp. 827 –830, Oct. 2010.

[82] A. Johnson, C. Rupp, B. Wolf, L. Hong, and A. Mitra, "Collision-avoidance radar for bicyclist and runners," in *National Aerospace and Electronics Conference (NAECON)*, July 2010, pp. 84 –91.

[83] G. Karagiannis, O. Altintas, E. Ekici, G. Heijenk, B. Jarupan, K. Lin, and T. Weil, "Vehicular networking: A survey and tutorial on requirements, architectures, challenges, standards and solutions," *IEEE Communications Surveys Tutorials*, vol. 13, no. 4, pp. 584–616, 2011.

[84] D.-H. Kim, D.-K. Seo, and H.-T. Kim, "Efficient classification of ISAR images," *IEEE Transactions on Antennas and Propagation*, vol. 53, no. 5, pp. 1611–1621, 2005.

[85] K.-T. Kim, D.-K. Seo, and H.-T. Kim, "Efficient radar target recognition using the MUSIC algorithm and invariant features," *IEEE Transactions on Antennas and Propagation*, vol. 50, no. 3, pp. 325 –337, Mar. 2002.

[86] Y. Kim and H. Ling, "Human activity classification based on micro-Doppler signatures using a support vector machine," *IEEE Transactions on Geoscience and Remote Sensing*, vol. 47, no. 5, pp. 1328 –1337, May 2009.

[87] K. Kira and L. A. Rendell, "A practical approach to feature selection," in *Proceedings of the ninth international workshop on Machine learning*, ser. ML92. San Francisco, CA, USA: Morgan Kaufmann Publishers Inc., 1992, pp. 249–256.

[88] D. Kok and J. Fu, "Signal processing for automotive radar," in *IEEE International Radar Conference*, 2005, pp. 842–846.

[89] M. Koolhoven, "Ratelband drone plane crash at Binnenhof," http://www.telegraaf.nl/binnenland/20876587/__Ratelband_laat_vliegtuigje_crashen__.html, September 2013.

[90] F. Kruse, F. Folster, M. Ahrholdt, H. Rohling, M. Meinecke, and T.-B. To, "Target classification based on near-distance radar sensors," in *IEEE Intelligent Vehicles Symposium*, 2004, pp. 722–727.

[91] K. Lang, "Newsweeder: Learning to filter netnews," in *Proceedings of the Twelfth International Conference on Machine Learning*, 1995, pp. 331–339.

[92] D. Linzmeier, M. Skutek, M. Mekhaiel, and K. Dietmayer, "A pedestrian detection system based on thermopile and radar sensor data fusion," in *International Conference on Information Fusion*, vol. 2, 2005, pp. 8 pp.–.

[93] H. Liu, E. Dougherty, J. Dy, K. Torkkola, E. Tuv, H. Peng, C. Ding, F. Long, M. Berens, L. Parsons, Z. Zhao, and G. Yu, L.and Forman, "Evolving feature selection," *IEEE Intelligent Systems*, vol. 20, no. 6, 2005.

[94] D. Lowe, "Distinctive image features from scale-invariant keypoints," *International Journal of Computer Vision*, vol. 60, no. 2, pp. 91–110, 2004. [Online]. Available: http://dx.doi.org/10.1023/B%3AVISI.0000029664.99615.94

[95] ——, "Object recognition from local scale-invariant features," in *IEEE International Conference on Computer Vision*, vol. 2, 1999, pp. 1150–1157 vol.2.

[96] I. Lozano Mrmol, "Monopulse range-doppler FMCW radar signal processing for spatial localization of moving targets," Tecnologas de la Informacin y las Comunicaciones, Universidad Politcnica de Cartagena, Tech. Rep., November 2012. [Online]. Available: http://hdl.handle.net/10317/2966

[97] T. Mäenpää, *The Local Binary Pattern Approach to Texture Analysis: Extenxions and Applications*. Oulun yliopisto, 2003.

[98] J. Marple, S.L., "Sharpening and bandwidth extrapolation techniques for radar micro-Doppler feature extraction," in *International Radar Conference*, September 2003, pp. 166 – 170.

[99] J. Martin and B. Mulgrew, "Analysis of the theoretical radar return signal form aircraft propeller blades," in *IEEE International Radar Conference*, May 1990, pp. 569 –572.

[100] A. M. Martinez and A. Kak, "PCA versus LDA," *IEEE Transactions on Pattern Analysis and Machine Intelligence*, vol. 23, no. 2, pp. 228–233, Feb 2001.

[101] A. Martinez and R. Benavente, "The AR face database," *CVC Tech. Report*, vol. 24, 1998.

[102] T. McConaghy, H. Leung, E. Bosse, and V. Varadan, "Classification of audio radar signals using radial basis function neural networks," *IEEE Transactions on Instrumentation and Measurement*, vol. 52, no. 6, pp. 1771 – 1779, dec. 2003.

[103] P. Molchanov, J. Astola, K. Egiazarian, G. Khlopov, V. Morozov, B. Pospelov, and A. Totsky, "Object recognition in ground surveillance Doppler radar by using bispectrum-based time-frequency distributions," in *11th International Radar Symposium*, 2010, pp. 414–417.

[104] ——, "Object recognition in ground surveillance Doppler radar by using bispectrum-based time-frequency distributions," in *11th International Radar Symposium*, 2010, pp. 1–4.

[105] P. Molchanov, J. Astola, K. Egiazarian, and A. Totsky, "Aircraft recognition by radar range profiles," in *Statistical Methods of Signal and Data Processing SMSDP*, 2010, pp. 50–53.

[106] ——, "Ground moving target classification by using DCT coefficients extracted from micro-doppler radar signatures and artificial neuron network," in *Microwaves, Radar and Remote Sensing Symposium (MRRS)*, 2011, pp. 173–176.

[107] ——, "Moving target classification in ground surveillance radar ATR system by using novel bicepstral-based information features," in *2011 European Radar Conference (EuRAD)*, 2011, pp. 194–197.

[108] ——, "Moving target classification in ground surveillance radar ATR system by using novel bicepstral-based information features," in *European Radar Conference (EuRAD)*, 2011, pp. 194–197.

[109] ——, "Target classification by using pattern features extracted from bispectrum-based radar Doppler signatures," in *International Radar Symposium (IRS)*, 2011, pp. 791–796.

[110] ——, "Classification of ground moving radar targets by using joint time-frequency analysis," in *IEEE Radar Conference (RADAR)*, 2012, pp. 366–371.

[111] ——, "Frequency and phase coupling phenomenon in micro-Doppler radar signature of walking human," in *13th International Radar Symposium (IRS)*, 2012, pp. 49–53.

[112] ——, "Classification of ground moving targets using bicepstrum-based features extracted from micro-Doppler radar signatures," *EURASIP Journal on Advances in Signal Processing*, vol. 2013, no. 1, 2013.

[113] ——, "On micro-Doppler period estimation," in *19th International Conference on Control Systems and Computer Science (CSCS)*, 2013, pp. 325–330.

[114] P. Molchanov, J. Astola, K. Egiazarian, A. Totsky, and Z. A., "Multi-frequency encoding technique using phase coupling in wireless communication systems," in *23rd International ConferenceRadioelektronika (RADIOELEKTRONIKA)*, 2010, pp. 261–266.

[115] P. Molchanov, K. Egiazarian, J. Astola, R. Harmanny, and J. de Wit, "Classification of small UAVs and birds by micro-doppler signatures," in *European Radar Conference (EuRAD)*, 2013, pp. 172–175.

[116] P. Molchanov, R. Harmanny, J. de Wit, K. Egiazarian, and J. Astola, "Classification of small UAVs and birds by micro-doppler signatures," *International Journal of Microwave and Wireless Technologies*, vol. 6, pp. 435 – 444, 2014.

[117] P. Molchanov, A. Totsky, J. Astola, K. Egiazarian, S. Leshchenko, and M. Rosa-Zurera, "Aerial target classification by micro-Doppler signatures and bicoherence-based features," in *9th European Radar Conference (EuRAD)*, 2012, pp. 214–217.

[118] P. Molchanov, A. Totsky, S. Leshchenko, P. Jarabo-Amores, K. Egiazarian, and J. Astola, "Classification of aircraft using micro-doppler bicoherence-based features," *IEEE Transactions on Aerospace and Electronic Systems*, vol. 50, no. 2, pp. 1455 – 1467, 2014.

[119] P. Molchanov, A. Vinel, J. Astola, and K. Egiazarian, "Radar frequency band invariant pedestrian classification," in *14th International Radar Symposium (IRS)*, 2012, pp. 19–21.

[120] A. Moreno and M. Rutllan, "Integrated polispectrum on speech recognition," in *Fourth International Conference on Spoken Language*, vol. 2, 1996, pp. 1281–1284.

[121] J. Muoz-Ferraras, F. Perez-Martinez, and M. Burgos-Garcia, "Helicopter classification with a high resolution LFMCW radar," *IEEE Transactions on Aerospace and Electronic Systems*, vol. 45, no. 4, pp. 1373–1384, 2009.

[122] D. Nelson, J. Starzyk, and D. Ensley, "Iterated wavelet transformation and signal discrimination for HRR radar target recognition," *IEEE Transactions on Systems, Man and Cybernetics, Part A: Systems and Humans,*, vol. 33, no. 1, pp. 52 – 57, jan. 2003.

[123] C. Nikias and M. Raghuveer, "Bispectrum estimation: A digital signal processing framework," *Proceedings of the IEEE*, vol. 75, no. 7, pp. 869–891, 1987.

[124] T. Ojala, M. Pietikainen, and T. Maenpaa, "Multiresolution gray-scale and rotation invariant texture classification with local binary patterns," *IEEE Transactions on Pattern Analysis and Machine Intelligence*, vol. 24, no. 7, pp. 971–987, 2002.

[125] K. Onoe, S. Sato, S. Homma, A. Kobayashi, T. Imai, and T. Takagi, "Bi-spectral acoustic features for robust speech recognition," *IEICE - Trans. Inf. Syst.*, vol. E91-D, no. 3, pp. 631–634, 2008.

[126] W. H. Organization, *Global status report on road safety: summary.* World Health Organization, 2009.

[127] I. Orovi, S. Stankovi, and M. Amin, "A new approach for classification of human gait based on time-frequency feature representations," *Signal Processing*, vol. 91, no. 6, pp. 1448 – 1456, 2011.

[128] M. Otero, "Application of a continuous wave radar for human gait recognition," in *Proceedings of SPIE*, vol. 5809, May 2005, pp. 538 – 548.

[129] S. K. Pal and S. Mitra, "Multilayer perceptron, fuzzy sets, and classification," *IEEE Transactions on Neural Networks*, vol. 3, no. 5, pp. 683–697, 1992.

[130] J. Park, H. Lim, and N. Myung, "Analysis of jet engine modulation effect with extended Hilbert-Huang transform," *Electronics Letters*, vol. 49, no. 3, pp. 215–216, 2013.

[131] S. Park, J. P. Hwang, E. Kim, H. Lee, and H. G. Jung, "A neural network approach to target classification for active safety system using microwave radar," *Expert Systems with Applications*, vol. 37, no. 3, pp. 2340 – 2346, 2010.

[132] D. A. Reynolds, T. F. Quatieri, and R. B. Dunn, "Speaker verification using adapted Gaussian mixture models," *Digital signal processing*, vol. 10, no. 1, pp. 19–41, 2000.

[133] D. A. Reynolds and R. C. Rose, "Robust text-independent speaker identification using gaussian mixture speaker models," *IEEE Transactions on Speech and Audio Processing*, vol. 3, no. 1, pp. 72–83, 1995.

[134] H. Rohling, S. Heuel, and H. Ritter, "Pedestrian detection procedure integrated into an 24 GHz automotive radar," in *IEEE Radar Conference*, 2010, pp. 1229–1232.

[135] H. Rohling and M.-M. Meinecke, "Waveform design principles for automotive radar systems," in *2001 CIE International Conference on Radar*, 2001, pp. 1 –4.

[136] H. Rohling, M.-M. Meinecke, S. Heuel, J. Hakli, K. Nummila, and M. Heuer, "Objectives of the ARTRAC initiative in active pedestrian safety," in *14th International Radar Symposium (IRS)*, vol. 2, 2013, pp. 726–731.

[137] H. Rohling and C. Moller, "Radar waveform for automotive radar systems and applications," in *RADAR '08, IEEE Radar Conference*, May 2008, pp. 1 –4.

[138] RT, "German 'Pirates' stage mini-drone stunt at Merkel rally," http://rt.com/news/pirates-drone-stunt-merkel-953/, September 2013.

[139] S. Russell and P. Norvig, *Artificial Intelligence: A Modern Approach*, 3rd ed. Upper Saddle River, NJ, USA: Prentice Hall Press, 2009.

[140] S. Saha and S. Kay, "Maximum likelihood parameter estimation of superimposed chirps using Monte Carlo importance sampling," *IEEE Transactions on Signal Processing*, vol. 50, no. 2, pp. 224 –230, 2002.

[141] T. Sakamoto and T. Sato, "Real-time imaging of human bodies with UWB radars using walking motion," in *International Conference on Ultra-Wideband*, 2007, pp. 26–30.

[142] S. Se, D. Lowe, and J. Little, "Vision-based mobile robot localization and mapping using scale-invariant features," in *IEEE International Conference on Robotics and Automation*, vol. 2, 2001, pp. 2051–2058 vol.2.

[143] P. Setlur, F. Ahmad, and M. Amin, "Maximum likelihood and suboptimal schemes for micro-Doppler estimation using carrier diverse Doppler radars," *IET Signal Processing*, vol. 5, no. 2, pp. 194 –208, April 2011.

[144] P. Setlur, M. Amin, and T. Thayaparan, "Radar waveform for automotive radar systems and applications," in *Eighth International Symposium on Signal Processing and Its Applications*, vol. 2, 28-31, 2005, pp. 639 – 642.

[145] P. Setlur, F. Ahmad, and M. Amin, "Helicopter radar return analysis: Estimation and blade number selection," *Signal Process.*, vol. 91, no. 6, pp. 1409–1424, Jun. 2011.

[146] Y. D. Shirman, S. A. Gorshkov, S. P. Leshchenko, V. M. Orlenko, S. Y. Sedyshev, and O. I. Sukharevskiy, *Computer simulation of aerial targets, radar scattering, recognition, detection, and tracking.* Boston-London: Artech House, 2002.

[147] Y. Shirman, S. Gorshkov, S. Leshenko, and V. Orlenko, "Aerial target backscattering simulation and study of radar recognition, detection and tracking," in *IEEE International Radar Conference*, 2000, pp. 521 –526.

[148] T. Sim, S. Baker, and M. Bsat, "The CMU pose, illumination, and expression database," *IEEE Transactions on Pattern Analysis and Machine Intelligence*, vol. 25, no. 12, pp. 1615 – 1618, dec. 2003.

[149] C. Smith and P. Goggans, "Radar target identification," *IEEE Antennas and Propagation Magazine*, vol. 35, no. 2, pp. 27 –38, april 1993.

[150] G. Smith, K. Woodbridge, and C. Baker, "Radar micro-Doppler signature classification using dynamic time warping," *IEEE Transactions on Aerospace and Electronic Systems*, vol. 46, no. 3, pp. 1078–1096, 2010.

[151] G. Smith, K. Woodbridge, C. Baker, and H. Griffiths, "Multistatic micro-Doppler radar signatures of personnel targets," *IET Signal Processing*, vol. 4, no. 3, pp. 224–233, 2010.

[152] G. E. Smith, K. Woodbridge, and C. J. Baker, "Radar micro-Doppler signature classification using dynamic time warping," *IEEE Transactions on Aerospace and Electronic Systems*, vol. 46, no. 3, pp. 1078 –1096, July 2010.

[153] Y. Sun, S. Todorovic, and S. Goodison, "Local-learning-based feature selection for high-dimensional data analysis," *IEEE Transactions on Pattern Analysis and Machine Intelligence*, vol. 32, no. 9, pp. 1610 –1626, sept. 2010.

[154] I. Tabus and J. Astola, "Gene feature selection," in *Genomic Signal Processing and Statistics*, E. Dougherty, I. Shmulevich, J. Chen, and Z. Wang, Eds. Hindawi Publishing Corporation, 2005, pp. 67–92.

[155] D. Tahmoush and J. Silvious, "Radar stride rate extraction," in *13th International Machine Vision and Image Processing Conference (IMVIP '09)*, September 2009, pp. 128 –133.

[156] ——, "Modeled gait variations in human micro-Doppler," in *11th International Radar Symposium (IRS)*, 2010, pp. 1–4.

[157] P. Tait, *Introduction to Radar Target Recognition*, ser. IEE radar series. Institution of Engineering and Technology, 2005.

[158] ——, "Target classification for air defence radars," in *The Institution of Engineering and Technology Seminar on High Resolution Imaging and Target Classification*, 2006, pp. 3–16.

[159] T. Thayaparan, S. Abrol, E. Riseborough, L. Stankovic, D. Lamothe, and G. Duff, "Analysis of radar micro-Doppler signatures from experimental helicopter and human data," *IET Radar, Sonar Navigation*, vol. 1, no. 4, pp. 289 –299, Aug 2007.

[160] M. Tons, R. Doerfler, M.-M. Meinecke, and M. Obojski, "Radar sensors and sensor platform used for pedestrian protection in the EC-funded project SAVE-U," in *IEEE Intelligent Vehicles Symposium*, 2004, pp. 813–818.

[161] B. Torvik, K. E. Olsen, and H. Griffiths, "K-band radar signature analysis of a flying mallard duck," in *14th International Radar Symposium (IRS)*, vol. 2, 2013, pp. 584–591.

[162] M. Toscano, "Unmanned aircraft systems roadmap to the future," in *7th North Dakota Research Corridor UAS Summit*, May 2013, pp. 569 –572.

[163] A. Totsky, I. Kurbatov, G. Khlopov, S. Khomenko, and V. Morozov, "Time-frequency analysis of radar backscattered signals using phase coupled frequencies extracted from time-varying bispectrum estimates," in *International Conference on Microwaves, Radar Wireless Communications*, 2006, pp. 203–206.

[164] M. P. W. van Breukelen, D. M. J. Tax, and J. E. den Hartog, "Handwritten digit recognition by combined classifiers,," *Kybernetika*, vol. vol. 34, pp. 381–386, 1998.

[165] R. van der Heiden, *PhD. Thesis Aircraft Recognition with Radar Range Profiles.* Universiteit, 1998.

[166] P. van Dorp and F. Groen, "Feature-based human motion parameter estimation with radar," *IET Radar, Sonar Navigation*, vol. 2, no. 2, pp. 135–145, 2008.

[167] P. van Dorp and F. C. A. Groen, "Human walking estimation with radar," *IEE Proceedings Radar, Sonar and Navigation*, vol. 150, no. 5, pp. 356–365, 2003.

[168] P. van Dorp, "Human motion analysis with radar," Ph.D. dissertation, 2010.

[169] V. Vapnik, S. E. Golowich, and A. Smola, "Support vector method for function approximation, regression estimation, and signal processing," *Advances in neural information processing systems*, pp. 281–287, 1997.

[170] V. N. Vapnik, *Statistical learning theory.* Wiley New York, 1998, vol. 2.

[171] S. V. Vaseghi, *Advanced Digital Signal Processing and Noise Reduction.* John Wiley & Sons, 2006.

[172] A. Vinel, E. Belyaev, K. Egiazarian, and Y. Koucheryavy, "An overtaking assistance system based on joint beaconing and real-time video transmission," *IEEE Transactions on Vehicular Technology*, vol. 61, no. 5, pp. 2319–2329, 2012.

[173] C. Wang and J. Xie, "Radar high resolution range profile target recognition based on T-mixture model," in *IEEE Radar Conference (RADAR)*, May 2011, pp. 762 –767.

[174] L. Wang, "Feature selection with kernel class separability," *IEEE Transactions on Pattern Analysis and Machine Intelligence*, vol. 30, no. 9, pp. 1534 –1546, September 2008.

[175] J. Woll, "Monopulse Doppler radar for vehicle applications," in *Proceedings of the Intelligent Vehicles '95 Symposium*, Sep. 1995, pp. 42 –47.

[176] T. Wu, C. Lin, and R. Weng, "Probability estimates for multi-class classification by pairwise coupling," *Journal of Machine Learning Research*, vol. 5, pp. 975–1005, 2003.

[177] S.-H. Yoon, B. Kim, and Y.-S. Kim, "Helicopter classification using time-frequency analysis," *Electronics Letters*, vol. 36, no. 22, pp. 1871–1872, 2000.

[178] Q. Zhang, Y. Luo, D. L. Hu, B.-f. Luo, and Y. S. Zeng, "Avian detection and monitoring using frequency-stepped chirp signal radar," *PIERS Online*, vol. 2008, no. 1, pp. 51–55, 2008.

[179] X.-D. Zhang, Y. Shi, and Z. Bao, "A new feature vector using selected bispectra for signal classification with application in radar target recognition," *IEEE Transactions on Signal Processing*, vol. 49, no. 9, pp. 1875 –1885, sep 2001.

[180] Z. Zhao, F. Morstatter, and S. e. a. Sharma, "Advancing feature selection research ASU feature selection repository," January 2012. [Online]. Available: http://featureselection.asu.edu/

[181] D. Zhou, G. Liu, and J. Wang, "Spatio-temporal target identification method of high-range resolution radar," *Pattern Recognition*, vol. 33, no. 1, pp. 1–7, 2000.

[182] J. Zwart, R. van der Heiden, S. Gelsema, and F. Groen, "Fast translation invariant classification of HRR range profiles in a zero phase representation," *IEE Proceedings Radar, Sonar and Navigation*, vol. 150, no. 6, pp. 411 – 418, dec. 2003.

[183] P. E. Zwicke and I. Kiss, "A new implementation of the Mellin transform and its application to radar classification of ships," *IEEE Transactions on Pattern Analysis and Machine Intelligence*, vol. PAMI-5, no. 2, pp. 191–199, 1983.

[184] A. Zyweck and R. Bogner, "Radar target classification of commercial aircraft," *IEEE Transactions on Aerospace and Electronic Systems*, vol. 32, no. 2, pp. 598 –606, april 1996.

Tampereen teknillinen yliopisto
PL 527
33101 Tampere

Tampere University of Technology
P.O.B. 527
FI-33101 Tampere, Finland

ISBN 978-952-15-3390-7
ISSN 1459-2045